The Swan Song of a Neutron Star Binary

Fundamental physics and astrophysics with gravitational waves
from compact binary coalescence

Michalis Agathos

Promotiecommissie:

Promotor:	Prof. dr. J.F.J. van den Brand
Co-promotor:	Dr. C. Van Den Broeck
Overige Leden:	Prof. dr. Piet Mulders
	Prof. dr. Gijs Nelemans
	Dr. Anna Watts
	Dr. Henk Jan Bulten
	Prof. dr. Stan Bentvelsen

The Swan Song of a Neutron Star Binary

Fundamental physics and astrophysics with gravitational
waves from compact binary coalescence

- What's beyond the sky and stars?
- Well, that's infinity.
- And what's infinity like?
- I don't know...

C

CONTENTS

PREFACE

Over the past 100 years, physicists have come to realize and appreciate the special role of gravity as one of the fundamental actors in nature. Although much weaker than the other known fundamental interactions, gravity conquers the large scales and determines the evolution of the Universe. But apart from the quantitative differences, there is something much deeper about gravity that has been fascinating generations of physicists. The key lies in what is known as the equivalence principle, a postulate that has taken different forms throughout the last four centuries and has been verified so far by a number of precision measurements. In simple words it states that all bodies fall freely in exactly the same way under the effect of gravity. Taking this statement further, while trying to reconcile gravity with the special theory of relativity, Einstein concluded that the trajectories of freely falling bodies are in fact attributes of spacetime itself, having nothing to do with the body in question. With the formulation of Einstein's general theory of relativity in 1915 (followed by decades of dispute), it became clear that gravity is a purely geometric effect: it is the manifestation of the non-trivial geometry of spacetime, which curves in the presence of energy and matter.

Einstein's equations defined the dynamics of spacetime geometry, and since the geometry was now a dynamical entity, it only took him a few months to demonstrate that his equations admitted wave solutions, *e.g.* in the form of perturbations around an empty spacetime. These *gravitational waves* propagate at the speed of light and are generated by accelerating distributions of matter. Strong evidence in favour of their existence was provided many decades later by the observation of the Hulse-Taylor binary pulsar and the accurate measurement of the decay of its orbital period over the course of many years. The binary seemed to be losing energy at exactly the same rate as the power of the emitted gravitational waves that general relativity had predicted. Experimental observation and detailed analysis of gravitational wave signals from a variety of sources of astrophysical and cosmological origin would provide useful insights on *e.g.* the nature of gravity, the physics of black holes and neutron stars, the populations and life cycle of such objects and the evolution of the Universe as a whole, and will probe regimes that were so far inaccessible to us by means of electromagnetic observations. Alas, the weakness of the gravitational coupling had not allowed

for a direct observation of gravitational waves emitted by such strong natural sources (as for instance binary pulsars) that can be found across the Universe. Until now.

I remember being only a few months into my doctoral studies when the first-generation network of ground-based gravitational wave interferometers (Virgo in Italy and two LIGO detectors in the USA) was shut down for decommissioning, before undergoing a major upgrade to their "Advanced" configuration. In more than a decade of operation they had detected no sign of gravitational waves, despite their impressive sensitivity. The upgrade would extend the horizon of the detectors by roughly one order of magnitude, increasing the accessible volume of space, and hence the number of potential sources, by a factor of 1000. Four years later, while this dissertation was close to completion, the two upgraded LIGO detectors were undergoing their last preparatory engineering runs and officially ushering gravitational physics into a new era. Indeed (and quite unexpectedly), within a few days of operation, on September 14, 2015, the two detectors were almost simultaneously perturbed by a gravitational wave that was generated during the coalescence of two stellar-mass black holes, about 1.3 billion years ago. It was a loud, beautiful signal that left no room for doubting the reality of its nature.

We have now unlocked a great new sense to the exploration of the Universe, we can feel the fabric of spacetime itself vibrating, and the purpose of my doctoral work has been to study ways in which we, as physicists, can make useful sense of this unprecedented kind of information that will keep streaming through the output of our detectors. Two main themes can be distinguished in this dissertation, both related to the physics output of gravitational wave detections from coalescing compact binaries: i) testing the dynamics of general relativity in its strong, fully relativistic regime and ii) inferring the neutron star equation of state by analyzing signals from neutron star binaries. The Virgo group at Nikhef has had a leading role in investigating both of the aforementioned topics, in the context of gravitational wave data analysis. Our work in the case of i) has already come to fruition with the analysis of data from the first detection, while binary neutron star coalescences are expected to be detected in the coming years and will provide rich information for ii).

This dissertation is structured in three parts, with a substructure that is outlined below. The main body of my work can be found in Part II and Part III. Part I serves as the introductory part of the dissertation, in which most of the underlying theory and methodology are covered, in a way that the reader has a comprehensive overview of the main analytical and computational tools used in gravitational wave data analysis. First, a brief introduction to general relativity and gravitational wave physics is given in Chapter 1. Next, Chapter 2 covers the basics of post-Newtonian theory of coalescing compact binaries, which will be the main objects of interest in this work. Finally, an introduction to Bayesian inference and computational methods for data analysis in gravitational wave physics is given in Chapter 3.

The subject of Part II is the formulation, development and study of data analysis methodologies for the purpose of testing Einstein's general theory of relativity with data obtained from gravitational wave detections. Chapter 4 gives an introduction and overview of earlier and contemporary tests of general relativity, and provides the motivation for the tests with gravitational waves, that will be developed in the rest of Part II. In Chapter 5, we formulate a generic Bayesian framework for testing general relativity using gravitational waves from compact binaries, under the acronym *TIGER* (Test Infrastructure for GEneral Relativity). In Chapter 6 we provide a proof-of-principle test for TIGER applied on gravitational wave signals emitted by non-spinning binary neutron star inspirals, whereas in Chapter 7 we give a more detailed study of the methods used in a more realistic setting, and take on a series of robustness tests. Next, trial runs using signals from realistic simulated sources injected into real detector noise are explored in Chapter 8 and finally, an outlook on the future of testing GR using gravitational waves from neutron star and black hole binaries concludes Part II in Chapter 9.

In Part III we study the prospects of inferring the internal structure and physical properties (encoded in the equation of state) of neutron stars by analyzing gravitational wave signals from neutron star binaries. An overview of neutron star physics and existing methods for constraining their equation of state is given in Chapter 10, The main part of our work comprises Chapter 11 and Appendix C, where our Bayesian data analysis methods are formulated, developed and tested under a variety of scenarios and increasingly realistic assumptions. Finally, our conclusions and outlook are discussed in Chapter 12.

The work in this dissertation has produced several scientific papers co-authored by myself and other colleagues. The foundations for testing general relativity in Part II were set in [245] and [246] and also featured in the dissertation of T.G.F. Li (2013), while further studies in this direction were published in [32] and [33]. During the course of writing this dissertation, an unexpected discovery took place, namely the first direct detection of gravitational waves by the LIGO-Virgo Collaboration, on September 14, 2015. The first historical results from real gravitational wave signals, constraining violations of general relativity to unprecedented levels, are discussed in Chapter 4 (giving the most stringent constraints on post-Newtonian coefficients) and Chapter 9 (giving the most stringent constraints on a massive graviton dispersion relation); these results feature in [24], a Phys. Rev. D "*highlight*" published in May 2016. Next, a method for testing the no-hair theorem was studied in [259] and is only briefly summarized in the concluding remarks of Part II. The original work of Part III is published in the exploratory studies of [152] and the more detailed investigations of [35], whereas the novel method presented in Appendix C is currently unpublished, in preparation.

Michalis, August 2016

Notation and conventions

In the formulas and calculations that follow, the following choices have been made with regards to the corresponding ambiguities in sign conventions, units, etc.

The Lorentzian signature is taken to be $(-, +, +, +)$, i.e. timelike norms are negative and spacelike are positive. Both in component calculations and whenever the abstract index notation is used, greek lowercase letters denote spacetime indices, whereas latin lowercase letters $(i, j, k, \ldots)$ denote spacelike indices in the corresponding subspace; the Einstein summation convention will be used throughout unless stated otherwise. The definition of the Riemann tensor follows the sign convention of Wald [374], according to Eq. (1.6). Any covariant derivative that enters the calculations is understood to be compatible with the corresponding metric (and decorated accordingly). The spacetime coordinates are given by $x^\mu = (ct, \vec{x})$ wave 4-vector by $k^\mu = (\omega/c, \vec{k})$.

Whenever possible, we shall keep track of dimensionful factors such as powers of G and c. However, there will be cases where, for the benefit of clarity, geometrical units are used by setting $G = c = 1$. For instance, conversions of mass values from SI units of mass [kg] to units of length [m] and time [s] are given by a factor of G/c^2 and G/c^3 respectively, so that one solar mass $1 M_\odot = 1.989 \times 10^{30}$kg equals to 1.477×10^3m or 4.9255×10^{-6}s. Similarly, the dimensionful tidal deformability λ can be converted from the units of $\mathrm{g\,cm^2\,s^2}$ used e.g. in [200] to units of $\mathrm{s^5}$ by multiplying with $10^{-7} \times G/c^5$. In the Bayesian calculations, a capital P is used to denote probabilities, while a lowercase p denotes probability densities and π is reserved for prior probability densities. Finally, for the benefit of the curious reader, whenever an observed stellar object is mentioned in the text, its exact sky coordinates are given explicitly as a footnote.

Useful constants

Constant	Symbol	Value	Unit
Newton's constant	G	6.67384×10^{-11}	$\mathrm{m^3\,kg^{-1}\,s^{-2}}$
Speed of light	c	2.99792458×10^8	$\mathrm{m\,s^{-1}}$
Planck constant	h	$6.62606957 \times 10^{-34}$	$\mathrm{J\,s}$
		4.135668×10^{-15}	$\mathrm{eV\,s}$
Solar mass	$M_\odot$	1.98892×10^{30}	kg
Earth mass	$M_\oplus$	5.9721986×10^{24}	kg
Earth's radius (equatorial)	$R_\oplus$	6378.137	km
Parsec	pc	$3.0856775807 \times 10^{16}$	m
Boltzmann constant	k	1.380658×10^{-23}	$\mathrm{J\,K^{-1}}$
Electron mass	m_e	$9.1093897 \times 10^{-31}$	kg
Proton mass	m_p	$1.67262158 \times 10^{-27}$	kg
Neutron mass	m_n	$1.6749286 \times 10^{-27}$	kg
Nuclear saturation density	n_0	0.1620	$\mathrm{fm^{-3}}$
	ρ_{nucl}	2.8×10^{14}	$\mathrm{g\,cm^{-3}}$
Neutron drip density	ρ_{drip}	4×10^{11}	$\mathrm{g\,cm^{-3}}$

Part I

Introduction
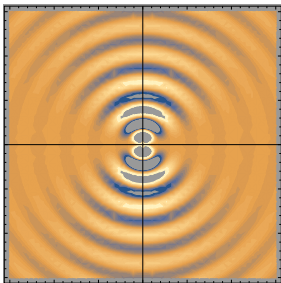
Chapter 1

Gravitational Wave Physics

Gravity's holding us together but don't get too close or it'll tear us apart

<div align="right">Gravity Blues (Unpublished)</div>

In the beginning of the 20th century, Einstein's *Special Theory of Relativity* radically changed our understanding of the notions of space and time. In 1915, Einstein arrived at the formulation of *General Relativity* (GR), a theory that explained gravity as a manifestation of the *curvature* of spacetime, by using the mathematical framework of differential geometry.

In the first section of this Chapter we will briefly recall the basics of GR. For a proper introduction to GR, we direct the reader to any of the numerous textbooks on GR, most notably [374, 265, 326, 377, 120]. We will then proceed to the derivations related to the production, propagation and detection of gravitational waves.

1.1 General Relativity

In GR, spacetime is defined as a mathematical entity $(\mathcal{M}, g)$, a real 4-dimensional *differentiable manifold* $\mathcal{M}$ equipped with a pseudo-Riemannian metric $g_{\mu\nu}$, a symmetric rank-2 tensor field of Lorentzian signature $(-, +, +, +)$ that endows $\mathcal{M}$ with a geometric structure. Locally the manifold is isomorphic to $\mathbb{R}^4$, so locally spacetime can be approximated by the flat Minkowski metric $\eta_{\mu\nu} = \text{diag}(-1, 1, 1, 1)$ within a small enough neighborhood of any point. The metric defines at each point $x \in \mathcal{M}$ an inner product between vectors $g : T_x\mathcal{M} \times T_x\mathcal{M} \to \mathbb{R}$, where $T_x\mathcal{M}$ denotes the tangent space over x, and thus it also defines what vectors or tangent curves are *timelike*, *null* or *spacelike*, depending on whether their norm $\|v\| = g(v, v) = g_{\mu\nu}v^\mu v^\nu$ is negative, zero or positive respectively.

The metric also uniquely defines a connection, or covariant derivative ∇ (a first order derivative operator on tensor fields) by the compatibility requirement

1

$\nabla_\mu g_{\nu\lambda} = 0$. The covariant derivative is also required to reduce to the *differential* d when acting on scalars, i.e. $\nabla f = \mathrm{d}f$ or in an arbitrary coordinate system $\nabla_\mu f = \partial_\mu f$. It is easy to show that in a given coordinate system x^μ, the relation of ∇_μ with the coordinate derivative ∂_μ operator is defined by their action on vector fields as

$$\nabla_\mu v^\nu = \partial_\mu v^\nu + \Gamma^\nu_{\mu\lambda}\, t^\lambda, \tag{1.1}$$

where $\Gamma^\lambda_{\mu\nu}$ are known as the Christoffel symbols and are given by

$$\Gamma^\lambda_{\mu\nu} = \frac{1}{2} g^{\lambda\rho} \left(\partial_\mu g_{\nu\rho} + \partial_\nu g_{\mu\rho} - \partial_\rho g_{\mu\nu} \right). \tag{1.2}$$

For a general tensor field $T^{\mu_1\cdots\mu_p}{}_{\nu_1\cdots\nu_q}$ of rank (p,q), the action of the covariant derivative can be expressed as

$$\nabla_\rho T^{\mu_1\cdots\mu_p}{}_{\nu_1\cdots\nu_q} = \partial_\rho T^{\mu_1\cdots\mu_p}{}_{\nu_1\cdots\nu_q} \quad + \quad \sum_{i=1}^{p} \Gamma^{\mu_i}_{\rho\lambda} T^{\mu_1\cdots\lambda\cdots\mu_p}{}_{\nu_1\cdots\nu_q}$$
$$- \quad \sum_{j=1}^{q} \Gamma^{\lambda}_{\rho\nu_i} T^{\mu_1\cdots\mu_p}{}_{\nu_1\cdots\lambda\cdots\nu_q}. \tag{1.3}$$

Parallel transport   A crucial non-trivial process on (pseudo-)Riemannian manifolds which is trivial for flat space is the *parallel transport* of vectors and tensor fields in general. Having a metric-induced differential operator on $\mathcal{M}$, parallel transport arises as a natural operation that maps the isomorphic but distinct tangent vector spaces $T_x\mathcal{M}$, $T_y\mathcal{M}$ over different points $x, y \in \mathcal{M}$ onto each other. This enables us to compare vectors and tensors at different points. Given a curve $c : [0,1] \to \mathcal{M}$ with tangent vector t^μ, we say that a vector v^μ defined on each point of the curve is parallel-transported along c if $t^\mu \nabla_\mu v^\nu = 0$ at each point along the curve. More generally, the same operator $t^\mu \nabla_\mu$ acting on tensors defines parallel transport of tensors of any kind as

$$t^\mu \, \nabla_\mu T^{\mu_1\cdots\mu_p}{}_{\nu_1\cdots\nu_q} = 0\,. \tag{1.4}$$

.

Geodesics   Parallel transport defines the set of *geodesic curves* that generalize the notion of "straight lines" for generic manifolds with a non-flat metric. In flat space we usually conceive those as a grid of coordinate lines, but since coordinates are merely an artificial construction, geodesics in curved geometries will have to be defined in a geometric, coordinate independent way. The property that defines a geodesic curve on $\mathcal{M}$ is that it parallel-transports its own tangent vector t^μ, *i.e.*

$$t^\mu \, \nabla_\mu t^\nu = 0 \tag{1.5}$$

along the entire curve. The representation of Eq. (1.5) for a coordinate system x^μ with the path of c given by $x^\mu(c(\tau))$, yields a first order ODE and admits a unique

solution, given an initial tangent vector at a point on the curve. A different, non-local property that characterizes geodesic curves is the extremization of the proper length for curves that connect two given points. Timelike geodesics play a special role in GR; they are the word-lines of inertial observers and any freely falling test body follows a timelike geodesic curve. Acceleration is induced by non-gravitational forces with respect to inertial frames and is measured by a non-zero vector on the right hand side of Eq. (1.5). Moreover, *geodesic deviation*, the relative acceleration between two originally parallel curves, is an indication of the presence of *curvature.*

Curvature   Curvature manifests itself as the failure of parallel transport of a vector along a closed curve. It is defined infinitesimally as the non-commutativity of the covariant derivative with itself,

$$(\nabla_\mu \nabla_\nu - \nabla_\nu \nabla_\mu)\omega_\rho = R_{\mu\nu\rho}{}^\sigma \, \omega_\sigma, \qquad (1.6)$$

where $R_{\mu\nu\rho}{}^\sigma$ is a tensor known as the *Riemann tensor*. In terms of the Christoffel symbols, the Riemann tensor can be expressed in its coordinate form as

$$R_{\mu\nu\rho}{}^\sigma = \partial_\mu \Gamma^\sigma_{\nu\rho} - \partial_\nu \Gamma^\sigma_{\mu\rho} + \Gamma^\sigma_{\mu\lambda} \, \Gamma^\lambda_{\nu\rho} - \Gamma^\sigma_{\nu\lambda} \, \Gamma^\lambda_{\mu\rho} \qquad (1.7)$$

This is a (1,3)-tensor from which one gets a (0,4)-tensor $R_{\mu\nu\rho\sigma} = g_{\sigma\lambda} R_{\mu\nu\rho}{}^\lambda$ with the following symmetries in its indices: (i) $R_{\mu\nu\rho\sigma} = -R_{\nu\mu\rho\sigma}$, (ii) $R_{\mu\nu\rho\sigma} = R_{\rho\sigma\mu\nu}$, (iii) the first Bianchi identity $R_{[\mu\nu\rho]\sigma} = 0$ and (iv) the *Bianchi identity* $\nabla_{[\lambda} R_{\mu\nu]\rho\sigma} = 0$. Using these symmetries, one can derive the number of independent components of the Riemann tensor in n dimensions to be $n^2(n^2 - 1)/12$. The *Ricci tensor* $R_{\mu\nu}$ is defined by performing contraction on two of the Riemann tensor indices and the *Ricci scalar* R is obtained by contracting the remaining two,

$$R_{\mu\nu} = R_{\mu\rho\nu}{}^\rho \quad , \quad R = R^\mu{}_\mu \,. \qquad (1.8)$$

Geodesic deviation   Consider a one-parameter family of timelike geodesics $c_s(\lambda)$ indexed by s, tangent to a smooth vector field t^μ and parametrized in such a way that $t_\mu \, t^\mu = -1$ everywhere. Let us also define the v.f. $X^\mu = (\partial/\partial s)^\mu$ as the *deviation vector* that takes us from one geodesic to its neighbor. Its Lie bracket with t^μ is zero, implying

$$t^\nu \nabla_\nu X^\mu = X^\nu \nabla_\nu t^\mu \,. \qquad (1.9)$$

Now, the *deviation velocity* can be defined as $v^\mu = t^\nu \nabla_\nu X^\mu$ and the corresponding *acceleration* as

$$a^\mu = t^\lambda \nabla_\lambda \left(t^\nu \nabla_\nu X^\mu \right) . \qquad (1.10)$$

Using the geodesic equation (1.5) for t^μ, together with the Leibnitz rule and Eq. (1.9), one can easily show that

$$a^\mu = -R_{\lambda\nu\rho}{}^\mu X^\nu \, t^\lambda \, t^\rho \,, \qquad (1.11)$$

1

which implies that in the presence of curvature, and only then, geodesics that are initially parallel to each other deviate from or converge to each other. In more physical terms, test bodies that are initially at rest with each other undergo a relative acceleration which can be interpreted as a *tidal force* of the gravitational field.

The Einstein field equations   For years Einstein was working on what should be the field equations connecting gravity or *geometry* to matter and energy in GR. The crucial property that matter should satisfy is conservation of energy and momentum, expressed by means of the *continuity equation* for the matter *stress-energy tensor* $T_{\mu\nu}$, which in a curved spacetime reads:

$$\nabla^\mu T_{\mu\nu} = 0 \,. \tag{1.12}$$

The only purely geometric tensor of second order in derivatives of the metric that is automatically divergenceless as a consequence of the second Bianchi identity, is the *Einstein tensor*:

$$G_{\mu\nu} = R_{\mu\nu} - \frac{1}{2} g_{\mu\nu} \, R \,. \tag{1.13}$$

The *Einstein field equations* (EFE) are a system of quasilinear coupled second order PDEs, expressed as a tensorial equation which directly relates the geometry of spacetime (via $G_{\mu\nu}$) to its matter content (via $T_{\mu\nu}$) as:

$$G_{\mu\nu} = -\frac{8\pi G}{c^4} \, T_{\mu\nu} \,. \tag{1.14}$$

The main implication here is that curvature is induced by the presence of matter or, in the famous words of John Archibald Wheeler,

> Matter tells spacetime how to curve; spacetime tells matter how to move.

Exact solutions   The infamous complexity and non-linearity of the EFE does not leave much hope for a general solution for the metric to be obtained. However, there are a few example spacetimes which, usually due to certain assumed symmetries, simplify the EFE and can be solved exactly. A first non-trivial example is the Schwarzschild spacetime [327], characterized by spherical symmetry, that describes spacetime around a spherically symmetric body, *e.g.* a non-spinning black hole (BH). Other well studied solutions are the Kerr (spinning BH) [221], Reissner-Nordstrom (charged BH) [311, 274], Kerr-Newman (spinning charged BH) [270, 271, 27] and the Friedman-Lemaitre-Robertson-Walker (homogeneous isotropic universe) [173, 244, 315, 316, 317, 375] metric, to mention a few. For the purposes of this dissertation we shall not deal with exact solutions, but will examine more closely how a *perturbative* solution around an exact background can be derived.

The prediction of gravitational waves (GW) as a direct consequence of general relativity dates as far back as Einstein's 1916 paper [161], in an attempt to solve a linearized version of the differential equations of GR. In contrast with Newtonian gravity, where the gravitational force acts instantaneously at any distance, in GR one obtains that the solutions of small perturbations on the geometry of spacetime propagate like waves at the speed of light.

1.2 The Linearized Einstein Equations

Gravity is known to be the weakest among the four fundamental interactions in nature, a property that can be attributed to the "smallness" of the gravitational constant in SI units, $G \simeq 6.67 \times 10^{-11} \mathrm{m}^3\, \mathrm{kg}^{-1}\, \mathrm{s}^{-2}$. In GR, through Eq. (1.14) this means that the geometry of spacetime is weakly coupled to matter or, in other words, spacetime is a hard thing to bend. In the absence of extremely dense matter that would induce strong gravity, which is almost always the case throughout the universe, GR can be treated perturbatively by expanding the metric tensor $g_{\mu\nu}$ around a fixed *background metric* $\bar{g}_{\mu\nu}$, which in the simplest case is the Minkowski metric $\eta_{\mu\nu}$ of flat spacetime. One may thus decompose

$$g_{\mu\nu}(x) = \bar{g}_{\mu\nu}(x) + h_{\mu\nu}(x) \quad , \; x \in \mathcal{M} \tag{1.15}$$

which defines the small metric perturbation $h_{\mu\nu}$ with the requirement $\|h\| \ll 1$.

One may then proceed with expanding all geometrical quantities of interest[1] to leading order in h and its derivatives,

$$
\begin{aligned}
\Gamma^{\lambda}_{\mu\nu} &= \frac{1}{2}\left[\bar{g}^{\lambda\rho} - h^{\lambda\rho}\right]\left[\partial_\mu \bar{g}_{\rho\nu} + \partial_\mu h_{\rho\nu} + \partial_\nu \bar{g}_{\rho\mu} + \partial_\nu h_{\rho\mu} - \partial_\rho \bar{g}_{\mu\nu} - \partial_\rho h_{\mu\nu}\right] \\
&= \bar{\Gamma}^{\rho}{}_{\mu\nu} + \underbrace{\frac{1}{2}\bar{g}^{\lambda\rho}\left(\bar{\nabla}_\mu h_{\rho\nu} + \bar{\nabla}_\nu h_{\rho\mu} - \bar{\nabla}_\rho h_{\mu\nu}\right)}_{\delta\Gamma^{\lambda}{}_{\mu\nu}} + O(h^2)\,,
\end{aligned}
\tag{1.16}
$$

where all barred quantities like $\bar{\Gamma}$ are obtained by using only the background metric. Note how even though the Christoffel symbols for the full and background metric are not tensors, their difference $\delta\Gamma$ which is *exactly* first order in h is a (1,2)-tensor; this is true for the difference of any two connections on a manifold. In Minkowski space we get $\bar{\Gamma} = 0$ and $\nabla \to \partial$, which simplifies (1.16). We

---

[1] Starting with $g^{\mu\nu} = \bar{g}^{\mu\nu} - h^{\mu\nu} + O(h^2)$ and by using $\bar{g}_{\mu\nu}$ to raise and lower indices.

1

continue with the Riemann, Ricci and Einstein tensors,

$$
\begin{aligned}
R_{\mu\nu\rho}{}^{\sigma} &= \left[\partial(\bar{\Gamma}+\delta\Gamma)\right] + \left[\bar{\Gamma}\,\bar{\Gamma}\right] + \left[\bar{\Gamma}\,\delta\Gamma\right] + \overbrace{\left[\delta\Gamma\,\delta\Gamma\right]}^{h^2} + O(h^2) \\
&= \bar{R}_{\mu\nu\rho}{}^{\sigma} + \left(\partial_\mu\delta\Gamma^{\sigma}{}_{\nu\rho} + \bar{\Gamma}^{\sigma}_{\mu\lambda}\delta\Gamma^{\lambda}{}_{\nu\rho} - \delta\Gamma^{\sigma}{}_{\nu\lambda}\bar{\Gamma}^{\lambda}_{\mu\rho} - \nu\leftrightarrow\mu\right) + O(h^2) \\
&= \bar{R}_{\mu\nu\rho}{}^{\sigma} + \bar{\nabla}_\mu\delta\Gamma^{\sigma}{}_{\nu\rho} - \bar{\nabla}_\nu\delta\Gamma^{\sigma}{}_{\mu\rho} + O(h^2) \qquad (1.17)
\end{aligned}
$$

$$
R_{\mu\nu} = \bar{R}_{\mu\nu} + \bar{\nabla}_\mu\delta\Gamma^{\rho}{}_{\rho\nu} - \bar{\nabla}_\rho\delta\Gamma^{\rho}{}_{\mu\nu} + O(h^2) \qquad (1.18)
$$

$$
R = \bar{R} - h^{\mu\nu}\bar{R}_{\mu\nu} + \bar{\nabla}^\mu\delta\Gamma^{\rho}{}_{\rho\nu} - \bar{\nabla}_\rho\delta\Gamma^{\rho} + O(h^2) \qquad (1.19)
$$

$$
G_{\mu\nu} = \bar{G}_{\mu\nu} + \left(\delta^\lambda_\mu\delta^\rho_\nu - \frac{1}{2}\bar{g}_{\mu\nu}\bar{g}^{\lambda\rho}\right)\left(\bar{\nabla}_\lambda\delta\Gamma^{\sigma}{}_{\sigma\rho} - \bar{\nabla}_\sigma\delta\Gamma^{\sigma}{}_{\lambda\rho}\right) \qquad (1.20)
$$

$$
+ \frac{\bar{R}_{\rho\sigma}}{2}\left(\bar{g}_{\mu\nu}h^{\rho\sigma} - h_{\mu\nu}\bar{g}^{\rho\sigma}\right) + O(h^2)\,, \qquad (1.21)
$$

where in the Ricci scalar we denote $\delta\Gamma^\rho = \bar{g}^{\mu\nu}\delta\Gamma^{\rho}{}_{\mu\nu}$.

We will now specialize the discussion to perturbations around a flat spacetime, *i.e.* we assume that there exists a coordinate system in which we can write $g_{\mu\nu}(x) = \eta_{\mu\nu} + h_{\mu\nu}(x)$ with $\|h\| \ll 1$. By substituting in Eq. (1.14) we then obtain the *linearized Einstein tensor* for the metric perturbation, which reads

$$
G^{(1)}_{\mu\nu} = \frac{1}{2}\left(\partial_\mu\partial_\nu h - 2\partial_{(\mu}\partial^\lambda h_{\nu)\lambda} + \Box h_{\mu\nu} - \eta_{\mu\nu}\Box h + \eta_{\mu\nu}\partial_\rho\partial_\sigma h^{\rho\sigma}\right)\,, \qquad (1.22)
$$

where the superscript "(1)" denotes the order in h and its derivatives. It is now convenient to define the *trace-reversed* perturbation, $\bar{h}_{\mu\nu} = h_{\mu\nu} - \frac{1}{2}\eta_{\mu\nu}h$, with $\bar{h} = -h$ justifying its name. By substituting for $\bar{h}_{\mu\nu}$ we get

$$
G^{(1)}_{\mu\nu} = \frac{1}{2}\left(\Box\bar{h}_{\mu\nu} - 2\partial_{(\mu}\partial^\lambda\bar{h}_{\nu)\lambda} + \eta_{\mu\nu}\partial_\rho\partial_\sigma\bar{h}^{\rho\sigma}\right)\,. \qquad (1.23)
$$

As we shall see below, we can always find a coordinate transformation such that

$$
\partial^\mu\bar{h}_{\mu\nu} = 0\,, \qquad (1.24)
$$

thus fixing the gauge freedom related to infinitesimal diffeomorphism invariance to what is known as the *de Donder gauge*[2]. In this gauge only the first term survives and the Einstein equation (1.14) simplifies to

$$
\Box\bar{h}_{\mu\nu} \simeq -\frac{16\pi G}{c^4}T_{\mu\nu}. \qquad (1.25)
$$

We recall that $\Box = \partial_\mu\partial^\mu = -\frac{1}{c^2}\partial_t^2 + \nabla^2$ is the *d'Alembertian*, a second order elliptical differential operator.

It is clear that Eq. (1.25) is a wave equation sourced by the matter stress energy tensor. The general solution for $\bar{h}_{\mu\nu}$ given an arbitrary matter distribution $T_{\mu\nu}$

---

[2]For a generic background the de Donder gauge is defined as $\partial^\mu\left(\sqrt{-g}g_{\mu\nu}\right) = 0$.

is given by integrating the Green's function of the d'Alembertian operator

$$\Box G(x; x') = \delta^{(4)}(x - x') \quad \Rightarrow \quad G(x; x') = -\frac{\delta\left(t' - \left[t - \frac{|\vec{x} - \vec{x}'|}{c}\right]\right)}{4\pi|\vec{x} - \vec{x}'|} \tag{1.26}$$

throughout the entire space (or at least the support of $T_{\mu\nu}$) in retarded time

$$\bar{h}_{\mu\nu}(t, \vec{x}) = \frac{4G}{c^4} \int d^3\vec{x}' \, \frac{T_{\mu\nu}\left(t - \frac{|\vec{x} - \vec{x}'|}{c}, \vec{x}'\right)}{|\vec{x} - \vec{x}'|} \, . \tag{1.27}$$

In vacuum, where $T_{\mu\nu} = 0$, the metric perturbation can be decomposed into waves that propagate at the speed of light.

Fixing the gauge degrees of freedom On first inspection, Eq. (1.25) due to the symmetry in its indices seems to comprise 10 independent component equations.

Two metric perturbations $h_{\mu\nu}$ and $h'_{\mu\nu}$ represent the same physical perturbation over the same background metric if and only if they are related by the Lie derivative of an infinitesimal diffeomorphism φ.

Diffeomorphism invariance is the fundamental symmetry of GR, which states that physical laws are invariant under general coordinate transformations. This is manifest in the EFE through its purely tensorial form; if a tensorial equation is true in one coordinate system then it is true in any coordinate system. It also implies that solutions of the EFE that are related to each other via a diffeomorphism represent physically identical spacetimes. One needs to lift such ambiguities when counting degrees of freedom.

An arbitrary v.f. ξ^μ on $\mathcal{M}$ generates through its integral curves a one-parameter family of diffeomorphisms $\varphi_\epsilon : \mathcal{M} \to \mathcal{M}$. Under a coordinate transformation $x^\mu \to x'^\mu = x^\mu + \epsilon\xi^\mu$ where ϵ is small enough that it varies weakly ($\epsilon\partial\xi \lesssim \|h\|$), the metric perturbation remains small and to linear order transforms as

$$h'_{\mu\nu} = h_{\mu\nu} - \partial_\mu\xi_\nu - \partial_\nu\xi_\mu \quad , \quad h' = h - 2\,\epsilon\,\partial_\mu\xi^\mu \tag{1.28}$$

The divergence $\partial^\mu\bar{h}_{\mu\nu}$ that we wish to set to zero transforms as

$$\partial^\mu\bar{h}'_{\mu\nu} = \partial^\mu\bar{h}_{\mu\nu} - \epsilon\,\Box\xi_\nu \tag{1.29}$$

which means that going to the de Donder gauge is equivalent to solving the differential equation

$$\Box\,\xi_\mu(x) = f_\mu \, , \tag{1.30}$$

which is always solvable. By fixing the gauge in this way we take away four degrees of freedom from the EFE. The solution however is not unique; any v.f. that satisfies $\Box\zeta^\mu = 0$ can be added to a solution for ξ^μ and still preserve the de

Donder gauge condition. This means that even within the de Donder gauge, we have not restricted $h_{\mu\nu}$ to its purely physical degrees of freedom; we can impose further conditions in order to use up this freedom.

We will do this by imposing the *radiation gauge*:

$$h = 0 \quad , \quad h_{0i} = 0 \, . \tag{1.31}$$

This can be achieved through an initial data problem, solved *e.g.* in [374], and is similar to what is done with the gauge freedom of the vector potential A_μ in electromagnetism. Note that since $h = 0$, we have $\bar{h}_{\mu\nu} = h_{\mu\nu}$. Furthermore, by Eq. (1.31) and (1.24) we get

$$\frac{\partial h_{00}}{\partial t} = 0 \, , \tag{1.32}$$

which turns h_{00} into a non-dynamical variable. This gauge is also known as the *transverse traceless gauge* (TT), in which the EFE reads

$$\Box \, h_{\mu\nu}^{TT} = -\frac{16\pi G}{c^4} T_{\mu\nu} \, . \tag{1.33}$$

Gravitational wave solutions   Let us see how the linearized EFE (1.25) give what can be described as *gravitational wave* solutions. We first consider the linearized EFE in vacuum, *i.e.* $\Box \, h_{\mu\nu} = 0$, in which case we can also set $h_{00} = 0$. Now, the obvious thing to do is to decompose our field into plane waves of wave vector $k^\mu = (\omega/c, \vec{k})$ as

$$h_{\mu\nu}^{TT}(x; k) = C_{\mu\nu}(k) \, e^{i \, k_\rho \, x^\rho} \, , \tag{1.34}$$

where $C_{\mu\nu}$ is a traceless symmetric tensor.

The linearized EFE gives the dispersion relation $k^\mu k_\mu = 0 \Rightarrow \omega = \pm |\vec{k}|/c$, which means that the wave vectors are null or, in other words, the waves propagate at the speed of light. The de Donder gauge translates to $C_{\mu\nu} k^\mu = 0$ which implies transversality of the wave tensor with the direction of propagation. Without loss of generality, we can set $\vec{k} \parallel \hat{z}$ so that the wave propagates along the z-axis; this would imply $k^\mu = \frac{1}{c}(\omega, 0, 0, \omega)$ and $C_{\mu z} = 0$. Moreover, based on the above gauge-fixing discussion we also know that $C_{0\mu} = 0$ so the only surviving components are C_{ij}, $i, j = x, y$. Now, symmetry implies $C_{xy} = C_{yx}$ and tracelessness implies $C_{xx} = -C_{yy}$, so the remaining *physical degrees of freedom* after all the gauge freedom is fixed are only two. We will refer to the two gravitational wave degrees of freedom as the *plus polarization* h_+ and the *cross polarization* $h_\times$, and the plane wave takes the form

$$h_{\mu\nu}^{TT}(x; k) = \underbrace{\begin{bmatrix} 0 & 0 & 0 & 0 \\ 0 & h_+ & h_\times & 0 \\ 0 & h_\times & -h_+ & 0 \\ 0 & 0 & 0 & 0 \end{bmatrix}}_{C_{ij}} \times \, e^{i \, \omega(t - z/c)} \, . \tag{1.35}$$

We introduce the standard decomposition often used for the 3×3 spatial part of the tensor $C_{ij}(k) = h_+(k)\epsilon_{ij}^+(\vec{k}) + h_\times(k)\epsilon_{ij}^\times(\vec{k})$, where for $\hat{u}$ and $\hat{v}$ a chosen basis normal to $\hat{k}$ we define

$$\epsilon_{ij}^+(\hat{k}) = \hat{u}_i\hat{u}_j - \hat{v}_i\hat{v}_j \quad \xrightarrow{\hat{k}=\hat{z}} \quad \begin{pmatrix} 1 & 0 & 0 \\ 0 & -1 & 0 \\ 0 & 0 & 0 \end{pmatrix} , \tag{1.36}$$

$$\epsilon_{ij}^\times(\hat{k}) = \hat{u}_i\hat{v}_j + \hat{v}_i\hat{u}_j \quad \xrightarrow{\hat{k}=\hat{z}} \quad \begin{pmatrix} 0 & 1 & 0 \\ 1 & 0 & 0 \\ 0 & 0 & 0 \end{pmatrix} . \tag{1.37}$$

Plane waves propagating in vacuum are good approximations of gravitational waves coming from far away sources. Within this context, it is useful to define the spatial *TT-projection operator* $\Lambda_{ij}{}^{kl}(\hat{n})$ with respect to a unit vector $\hat{n}$, that projects an arbitrary (0,2)-tensor onto the transverse-traceless subspace. First, the projection operator $P_\mu{}^\nu = \delta_\mu^\nu - n_\mu n^\nu$ projects (dual) vectors onto the hyperplane of co-dimension 1, normal to n. Then the transverse traceless projection operator can be defined as

$$\Lambda_{ij}{}^{kl} = P_i{}^k P_j{}^l - \frac{1}{2}P_{ij}P^{kl} \tag{1.38}$$

and one can readily check that
(i) it is indeed a projection operator, *i.e.* $\Lambda_{ij}{}^{mn}\Lambda_{mn}{}^{kl} = \Lambda_{ij}{}^{kl}$,
(ii) it eliminates longitudinal components $\Lambda_{ij}{}^{kl}n_l = \Lambda_{ij}{}^{kl}n_k = 0$ and
(iii) it eliminates traces $\Lambda^i{}_i{}^{kl} = \Lambda_{ij}{}^k{}_k = 0$.
Note that in this form it is only applicable to spatial unit vectors, and to the spatial part of tensors.

Gravitational wave energy-momentum   As soon as we separate $h_{\mu\nu}$ as an entity in its own right, and we distinguish it from the background geometry, we effectively assign to it physical properties (energy, momentum, *etc.*) that are defined by its interaction with matter and the background geometry. In order to better understand the energy-momentum content of a gravitational wave, we need to see beyond the linearized theory. The splitting of the metric into background plus perturbation is usually done based on a clear classification of spatial and temporal modes. That is, background is the "smooth, slowly varying" part of the metric, on top of which high frequencies at short scales define the perturbation. Following [377] or [253] we can split the exact EFE to low- and high-frequency parts. The low-frequency part to second order in h

$$\bar{R}_{\mu\nu} = -[R_{\mu\nu}^{(2)}]^{\text{Low}} + \frac{8\pi G}{c^4}\left[T_{\mu\nu} - \frac{1}{2}g_{\mu\nu}T\right]^{\text{Low}} \tag{1.39}$$

will tell us how the macroscopic background experiences the effect of the microscopic $h_{\mu\nu}$ (found in the first term on the RHS) through its blurry glasses. Here,

a superscript "Low" refers to a low-frequency part of the quantity in brackets, which can be obtained by cutting off its Fourier decomposition beyond a certain frequency. Note that second order terms of high frequency modes, *e.g.* at f_1 and f_2, have a non-zero "Low" part at their frequency difference $f = f_1 - f_2$. We now introduce an operator $\langle \cdot \rangle$ that takes a spatial average of quantities, over a scale that is small compared to the background variation scales but much larger than the typical wavelengths found in the spectrum of $h_{\mu\nu}$. Applying this to Eq. (1.39), we arrive at the *effective* Einstein equation

$$\bar{G}_{\mu\nu} = \frac{8\pi G}{c^4} \left(\bar{T}_{\mu\nu} + t_{\mu\nu} \right) , \qquad (1.40)$$

where we have defined the *effective stress-energy tensor* of matter $\bar{T}_{\mu\nu}$ through

$$\bar{T}_{\mu\nu} - \frac{1}{2}\bar{g}_{\mu\nu}\bar{T} = \left\langle T_{\mu\nu} - \frac{1}{2}g_{\mu\nu}T \right\rangle \quad , \quad \bar{T} = \bar{g}_{\mu\nu}\bar{T}^{\mu\nu} , \qquad (1.41)$$

and the *gravitational wave stress-energy tensor* $t_{\mu\nu}$ as

$$t_{\mu\nu} = -\frac{c^4}{8\pi G} \left\langle R^{(2)}_{\mu\nu} - \frac{1}{2}\bar{g}_{\mu\nu}R^{(2)} \right\rangle \quad , \quad R^{(2)} = \bar{g}^{\mu\nu}R^{(2)}_{\mu\nu} . \qquad (1.42)$$

The essence of Eq. (1.40) is that from a macroscopic perspective, the metric perturbation acts on the background spacetime as an additional matter field, described by a stress-energy tensor $t_{\mu\nu}$ that we can calculate. A better understanding of this scale-dependent discrimination and definition can be achieved through the study of *effective actions* and *renormalization group transformations* [397, 84].

One can then try to isolate the *physical content* of $t_{\mu\nu}$ and ignore the spurious degrees of freedom (d.o.f.) related to gauge freedom. A consistent expansion of Eq. (1.8) in the flat background limit (away from the source) and to second order in $h_{\mu\nu}$, with subsequent use of the transverse traceless gauge $\partial^\mu h_{\mu\nu} = 0$, $h = 0$ and the vacuum wave equation $\Box h_{\mu\nu} = 0$ gives

$$R^{(2)}_{\mu\nu} = -\frac{1}{4}\partial_\mu h_{\rho\sigma}\partial_\nu h^{\rho\sigma} , \qquad (1.43)$$

and thus we get

$$t_{\mu\nu} = \frac{c^4}{32\pi G} \langle \partial_\mu h_{\rho\sigma}\partial_\nu h^{\rho\sigma} \rangle . \qquad (1.44)$$

One can indeed show that the above expression is invariant to leading order under the residual gauge transformations generated by an arbitrary *vector field* ξ^μ and thus one concludes that $t^{\mu\nu}$ has no dependence on gauge d.o.f. .

1.3 Emission of Gravitational Waves

In this section we will see what are the necessary ingredients for the production of significant amounts of gravitational radiation. Consider a distribution of matter described by the stress-energy tensor $T_{\mu\nu}$, whose support is a compact region of space of size $O(R)$. We want to evaluate the perturbation tensor at an arbitrary point $x = (t, \vec{x})$ outside the source. Using the general solution (1.27) for the Green's function (1.26) and the TT projection (1.38), we obtain the TT gauge solution *outside the source* for the spatial part as

$$h_{ij}^{TT}(t, \vec{x}) = \frac{4G}{c^4} \Lambda_{ij}{}^{kl}(\hat{n}) \int d^3 \vec{x}' \frac{T_{kl}\left(t - \frac{|\vec{x}-\vec{x}'|}{c}, \vec{x}'\right)}{|\vec{x} - \vec{x}'|} \,. \tag{1.45}$$

Figure 1.1: *Green's function is integrated over the source of size R, far from the observer.*

It is useful to study the Fourier decomposition of this solution, where the TT part of the stress energy tensor,

$$T_{\mu\nu}(t_{\text{ret}}, \vec{x}) = \int_{-\infty}^{\infty} \frac{d^n k}{(2\pi)^{n/2}} \, e^{i\left(-\omega t + \omega \frac{|\vec{x}-\vec{x}'|}{c} - \vec{k}\cdot\vec{x}\right)} \tilde{T}_{\mu\nu}\left(\omega, \vec{k}\right), \tag{1.46}$$

sources plane wave solutions in the TT gauge. If the internal motion in the source is non-relativistic, the Fourier modes will only contribute up to an angular velocity $\omega_s \ll c/R$. For far away observers, for which $r/R \ll 1$, we may perform the expansion

$$|\vec{x} - \vec{x}'| = r \sqrt{1 - 2\vec{x}' \cdot \hat{n}/r + (\vec{x}'/r)^2} \simeq r - \vec{x}' \cdot \hat{n}, \tag{1.47}$$

through which the solution integral (1.45) can be expanded as

$$\frac{1}{r} \int d^3 \vec{x}' \int d^4 k \, e^{-i\omega t_{\text{ret}}} \left[1 - i\frac{\omega}{c}\vec{x}' \cdot \hat{n} - \frac{1}{2}\left(\frac{\omega \, \vec{x}' \cdot \hat{n}}{c}\right)^2 + \ldots\right] \tilde{T}_{kl}\left(\omega, \vec{k}\right)$$

$$= \frac{1}{r} \int d^3 \vec{x}' \left[1 + \frac{\vec{x}' \cdot \hat{n}}{c}\partial_0 + \frac{(\vec{x}' \cdot \hat{n})^2}{2c^2}\partial_0^2 + \ldots\right] T_{kl}(t_{\text{ret}}, \vec{x}'). \tag{1.48}$$

Here we used the slow-moving expansion parameter $\frac{\omega}{c}\vec{x}' \cdot \hat{n}$. Moreover, if we expand the $1/|\vec{x} - \vec{x}'|$ factor in *e.g.* Legendre polynomials

$$\frac{1}{|\vec{x} - \vec{x}'|} = \sum_{l=0}^{\infty} \frac{|\vec{x}'|^l}{r^{l+1}} P_l(\hat{x}' \cdot \hat{n}), \tag{1.49}$$

it is clear that for our purposes we only need to keep the $1/r$ term.

13

1

Multipolar expansion   In the *far-zone* and *non-relativisic* expansion of the linear theory, we thus obtain

$$h_{ij}^{TT} = \frac{4G}{r\,c^4}\Lambda_{ij,kl}(\hat{n})\left[S^{kl}(t_{\text{ret}}) + \frac{1}{c}n_m\dot{S}^{kl,m}(t_{\text{ret}}) + \frac{1}{2c^2}n_m n_n\ddot{S}^{kl,mn}(t_{\text{ret}}) + \dots\right].$$
(1.50)

This can be interpreted as an expansion in the source's *multipole moments* of the stress energy tensor, defined as[3]

$$S^{ij,k\cdots l}(t) = \int \mathrm{d}^3x\, T^{ij}(t,\vec{x})\, x^k\cdots x^l\,.$$
(1.51)

It is also useful to define the *mass multipole moments* as moments of $\rho(x) = T^{00}(x)/c^2$,

$$M^{k\cdots l}(t) = \frac{1}{c^2}\int \mathrm{d}^3x\, T^{00}(t,\vec{x})\, x^k\cdots x^l\,,$$
(1.52)

and the *momentum multipole moments* as moments of $T^{0i}(x)/c$,

$$P^{i,k\cdots l}(t) = \frac{1}{c}\int \mathrm{d}^3x\, T^{0i}(t,\vec{x})\, x^k\cdots x^l\,.$$
(1.53)

All the above quantities will be evaluated at the retarded time $t_{\text{ret}} = t - r/c$. By making use of (i) the symmetry $T^{\mu\nu} = T^{\nu\mu}$ and conservation $\partial_\mu T^{\mu\nu}$ of the stress-energy tensor, (ii) integration by parts (and the compactness of the source) and (iii) coordinate derivatives $\partial_\mu x^\nu = \delta_\mu^\nu$ and their commutativity, one can establish identities between moments of the above three types and their derivatives. For instance, one easily finds

$$S^{ij} = \frac{1}{2}\ddot{M}^{ij}\,.$$
(1.54)

These can be used in order to re-express Eq. (1.50) in source-related quantities that are intuitive and easier to calculate,

$$\begin{aligned}
h_{ij}^{TT}(t) &= \frac{4G}{r\,c^4}\Lambda_{ij,kl}(\hat{n})\left\{\frac{1}{2}\ddot{M}^{kl}(t_{\text{ret}})\right. \\
&+ \left.\frac{1}{c}n_m\left[\frac{1}{6}\dddot{M}^{klm}(t_{\text{ret}}) + \frac{1}{3}\left(\ddot{P}^{k,lm} + \ddot{P}^{l,km} - 2\ddot{P}^{m,kl}\right)\right] + O\left(\frac{1}{c^2}\right)\right\}.
\end{aligned}$$
(1.55)

The quadrupole formula   The leading order expression in the multipole expansion (1.55) is known as the *quadrupole formula* [162, 236]

$$h_{ij}^{TT}(t,\vec{x}) = \frac{4G}{r\,c^4}\,\ddot{M}_{ij}^{TT}\left(t - \frac{r}{c}\right) = \frac{4G}{r\,c^4}\,\ddot{Q}_{ij}^{TT}\left(t - \frac{r}{c}\right),$$
(1.56)

where

$$Q_{ij}(t) = \int \mathrm{d}^3x\, \rho(t,\vec{x})(x^i x^j - r^2\delta^{ij}/3)$$
(1.57)

---

[3]In all definitions below, the absense of the $k\cdots l$ indices denotes the zeroth moment, *i.e.* the integral with no x^k factors present. For instance, M is simply the total mass-energy.

is the familiar quadrupole tensor of classical mechanics.

It becomes clear that the emission of gravitational waves requires a source with a strong accelerating quadrupole moment. On the good side, the GW amplitude only falls off as $1/r$ due to its tensorial nature, but again the small pre-factor $\frac{G}{c^4} \sim 8.26 \times 10^{-44} \mathrm{s}^2 \, \mathrm{kg}^{-1} \, \mathrm{m}^{-1}$ predicts that even a dense asymmetric distribution of matter will produce a relatively weak signal. As we shall see in Chapter 2, binary systems of compact astrophysical objects are perfect candidates as sources with a strong oscillating quadrupole moment. These will be the main object of investigation in this dissertation.

Radiated energy Let us point out some basic leading order effects that are derived using the quadrupole formula. First, we can calculate the *energy density* contained in a GW far away from a non-relativistic source, according to the 00 component of Eq. (1.42),

$$t^{00} = \frac{c^2}{16\pi G} \left\langle \dot{h}_{ij}^{TT} \dot{h}_{ij}^{TT} \right\rangle = \frac{c^2}{16\pi G} \left\langle \dot{h}_+^2 + \dot{h}_\times^2 \right\rangle , \qquad (1.58)$$

where in the last equation we used the explicit decomposition in the $+$ and $\times$ polarizations. The *energy flux*, *i.e.* the time derivative of the energy in a sphere that encloses the source, $\dot{E}_S = -c \int_{\partial S} \mathrm{d}A \, t^{00}$ gives the *power* of the source. Then the GW differential *power* emitted per solid angle, by a non-relativistic source in the quadrupole approximation gives

$$\frac{\mathrm{d}P_{\mathrm{gw}}}{\mathrm{d}\Omega} \simeq \frac{G}{8\pi c^5} \Lambda_{ij,kl}(\hat{n}) \left\langle \dddot{Q}_{ij} \dddot{Q}_{kl} \right\rangle , \qquad (1.59)$$

where now the averaging process occurs in the (retarded) time dependence of Q for a few GW periods. We see that the radiation is anisotropic, depending on the orientation of the quadrupole moment. The *total radiated GW power* is the integral of Eq. (1.59) across a sphere that surrounds the source (the angular dependence lies in $\Lambda_{ij,kl}(\hat{n})$),

$$P_{\mathrm{gw}} \simeq \frac{G}{5c^5} \left\langle \dddot{Q}_{ij} \dddot{Q}_{ij} \right\rangle . \qquad (1.60)$$

Radiated angular momentum If one treats the linear theory as a field theory of the spin-2 tensor field h_{ij} living on the background spacetime, then one finds the kinematic Lagrangian density in the TT gauge

$$\mathcal{L}_{\mathrm{gw}} = -\frac{c^4}{64\pi G} \partial_\mu h_{ij}^{TT} \partial^\mu h_{ij}^{TT} . \qquad (1.61)$$

Under spatial rotations, one then obtains the Noether conserved quantity

$$J_{\mathrm{gw}}^i = \frac{c^2}{32\pi G} \int \mathrm{d}^3 \vec{x} \, \varepsilon^{ijk} \underbrace{\left[\dot{h}_{lm}^{TT} x^j \partial_k h_{lm}^{TT} - 2 \underbrace{\dot{h}_{lj}^{TT} h_{lk}^{TT}}_{S_{jk}} \right]}_{L_{jk}} = L_{\mathrm{gw}}^i + S_{\mathrm{gw}}^i , \qquad (1.62)$$

1

which is interpreted as the total *angular momentum* carried by the gravitational wave. A system that radiates GWs will lose angular momentum based on the above expression. The loss rate $\dot{\vec{J}}$ is calculated as the outflow of GW angular momentum through a surface that encloses the source and in the quadrupole approximation one gets

$$\frac{\mathrm{d}L^i_{\mathrm{gw}}}{\mathrm{d}t} = \frac{2G}{15c^5}\varepsilon^{ijk}\left\langle \ddot{Q}_{jl}\,\dddot{Q}_{kl}\right\rangle , \quad \frac{\mathrm{d}S^i_{\mathrm{gw}}}{\mathrm{d}t} = \frac{4G}{15c^5}\varepsilon^{ijk}\left\langle \ddot{Q}_{jl}\,\dddot{Q}_{kl}\right\rangle . \tag{1.63}$$

One thus gets a total flux of angular momentum

$$\frac{\mathrm{d}J^i_{\mathrm{gw}}}{\mathrm{d}t} = \frac{\mathrm{d}L^i_{\mathrm{gw}}}{\mathrm{d}t} + \frac{\mathrm{d}S^i_{\mathrm{gw}}}{\mathrm{d}t} = \frac{2G}{5c^5}\varepsilon^{ijk}\left\langle \ddot{Q}_{jl}\,\dddot{Q}_{kl}\right\rangle . \tag{1.64}$$

1.4 The post-Newtonian formalism

So far we have seen how gravitational wave production can be approximated in a slow-moving expansion within the context of the linear theory. However, in self-gravitating systems, such as compact binaries, an expansion in v/c also implies one in the strength of the gravitational field, or the *compactness* GM/Rc^2 of the source (the ratio between the Schwarzschild radius and the size of the system). This is a direct consequence of the virial theorem for bound orbits, that relates $(v/c)^2 \sim GM/Rc^2 \sim \epsilon$, which in the case of quasi-circular orbits is an exact equality. Thus, one should not ignore deviations from a flat metric close to the source, when performing a systematic expansion to obtain the equations of motion and, eventually the gravitational waveform. Instead, one needs to employ a post-Minkowskian (PM) or weak-field expansion of the metric in powers of G,

$$\sqrt{-g}g^{\mu\nu} = \eta_{\mu\nu} + \epsilon h^{(1)}_{\mu\nu} + \epsilon^2 h^{(2)}_{\mu\nu} + \dots , \tag{1.65}$$

based on which one will look for a perturbative solution to an order-by-order expansion of the EFE, with the appropriate source on the RHS.

An iterative perturbation method for the non-linear theory, known as the *post-Newtonian formalism* [92, 87, 353] has been developed by Blanchet and Damour, in order to treat non-solvable problems in GR, such as the two body problem of a coalescing compact binary [88, 176]. This will be valid assuming post-Newtonian sources, *i.e.* sources that are *weakly gravitating*, *slowly moving* and *weakly stressed*. For distances much smaller than a typical wavelength $r \ll \lambda/2\pi$, the metric can be treated as a static field that evolves slowly, together with the source. This regime exists for post-Newtonian sources, since $R \sim (v/c)\lambda/2\pi$, and defines the region of validity for the post-Newtonian (PN) expansion. The outside of the source can be conveniently expressed by a post-Minkowskian expansion in vacuum and far away from the source, a multipolar expansion like Eq. (1.50) gives the solution for the linear theory [118, 353]. For finite-sized sources, spacetime is thus separated into four (overlapping) regions:

Source interior: the region of spacetime where the source's stress-energy tensor is non-zero, that extends to a world tube of radius R. Here PN is valid but (vacuum) PM is not; formally the latter diverges at $r \to 0$.

Source exterior: the complement of the source interior. PM is valid throughout.

Near zone: the region encompassing the source, where the gravitational field varies "in phase" with the source. This extends out to distances much smaller than the shortest wavelength. PN is valid throughout, while PM only in the exterior part.

Far zone: the region where the gravitational field is weak enough to be treated in the linear theory. It is part of the exterior, so PM is valid, and the multipolar expansion is convenient here, while PN diverges.

In a sense the PN expansion in the near zone and the PM expansion outside the source are complementary, not only because their domain of validity fills up the entire space, but also because the latter can provide the correct boundary conditions to the former (no incoming radiation from null infinity), which in turn provides the source multipoles. The theorems stated below [88], together with a set of matching conditions in the overlapping regions, will eventually yield the solution that covers the entire spacetime. A different approach that gives consistent results was pioneered by Will and Wiseman [383, 387] and is based on the direct integration of the relaxed Einstein equations (DIRE).

To solve the EFE perturbatively in the near zone, one needs to expand the metric $g_{\mu\nu}$ (as in Eq. (1.65)) and the stress-energy tensor $T_{\mu\nu}$ in powers of ϵ, keeping in mind that the time derivatives of the metric are of an additional $O(\epsilon)$ order smaller than the spatial derivatives. The following theorem gives the form of its general solution to arbitrary order.

Theorem 1 (near-zone PN). *The expression of the post-Newtonian field[4] in the near zone of a post-Newtonian source, satisfying no-incoming-radiation boundary conditions at infinity reads*

$$\bar{h}^{\mu\nu} = \frac{16\pi G}{c^4} \left[\mathcal{FP}\Box_{ret}^{-1} \left[\bar{\tau}^{\mu\nu} \right] + \sum_{l=0}^{\infty} \frac{(-1)^l}{l!} \partial_L \left\{ \frac{\mathcal{R}_L^{\mu\nu}(t_{\mathrm{ret}}) - \mathcal{R}_L^{\mu\nu}(t_{\mathrm{adv}})}{2r} \right\} \right] . \quad (1.66)$$

The first term represents a particular solution of the hierarchy of post-Newtonian equations, while the second one is a homogeneous multipolar solution of the wave equation, of the "anti-symmetric" type that is regular at the origin $r = 0$ located in the source.

The inverse d' Alembertian $\Box_{ret}^{-1}$ is simply the Green's function of the d'Alembertian evaluated at retarded time $t_{ret} = t - r/c$ and $\mathcal{FP}$ denotes the *finite part*

---

[4]Here $\bar{h}^{\mu\nu} = \sqrt{-g}g^{\mu\nu}\eta_{\mu\nu}$.

1

operator that removes its singular behavior for point-like sources [92]. The index L is a multi-index of rank l.

The PN expansion is developed at two levels: first at the conservative level, where radiation emission is not taken into account and the source's equations of motion are calculated; then at the dissipative level where GW emission back-reacts on the dynamics of the system. The latter does not enter until the next-to-next-to-leading order (1.5PN), so in an order-by-order perturbative treatment of the EFE, one can gradually introduce dissipative effects that are calculated from lower-order solutions of the equations of motion.

Theorem 2 (near-zone PM)**.** *The general structure of the expansion of the post-Minkowskian exterior metric in the near-zone is of the type*

$$h^{(n)}_{\mu\nu}(t, \vec{x}) = \sum \hat{n}_L r^m (\ln r)^p \, F_{L,m,p,n}(t) + o\left(r^N\right) \, , \qquad (1.67)$$

where $m \in \mathbb{Z}$, with $m_0 \leq m \leq N$, $p \in \mathbb{N}$, $p \leq n - 1$. The functions $F_{L,m,p,n}$ are multilinear functionals of the source multipole moments $I_L, \ldots, Z_L$.

This theorem establishes a structure with which one can match the near-zone PM expansion which is singular at $r \to 0$, with the source multipoles derived in the PN expansion that are regular. Details of the explicit derivations can be found for example in [88, 176] and references therein. A matching condition is thus applied in the overlapping region of the near-zone where both PN and PM are valid. Some explicit expressions for the source multipoles and radiation multipoles are given in [88] both in their general form and in particular for point-mass binaries. Finally, the PM solution can be re-expanded in the far-zone expansion.

Theorem 3 (far-zone PM)**.** *The most general multipolar-post-Minkowskian solution, stationary in the past, admits some radiative coordinates $(t, \vec{x})$, for which the expansion at future null infinity, $r \to \infty$, with $t_{\mathrm{ret}} \equiv t - r/c = const$, takes the form*

$$H^{(n)}_{\mu\nu}(t, \vec{x}) = \sum \frac{\hat{N}_L}{r^k} K_{L,k,n}(t_{\mathrm{ret}}) + O\left(\frac{1}{r^N}\right) \, . \qquad (1.68)$$

The functions $K_{L,k,n}$ are computable functionals of the source multipole moments. In radiative coordinates the retarded time t_{ret} is a null coordinate in the asymptotic limit. The metric is asymptotically simple [290, 291], perturbatively to arbitrary order.

The actual calculations in the PN formalism are technically difficult and extremely laborious, so derivations beyond next-to-leading order are not easy to obtain. However, the necessity for a high-PN-order modeling of compact binaries becomes clear when one calculates the phase of the waveform, to be used by the data analysis algorithms (for searches, *etc.*). During the time that the waveform spends in-band, the modeled phase needs to match the true signal up to a fraction of a cycle, in order to make the matched filtering algorithms efficient enough. It appears that the template waveforms need to be modeled with post-Newtonian effects up to at least 2.5PN.

1.5 Detection of Gravitational Waves

In order to fully understand the operational principles of gravitational wave detection we will first look into the leading order effects of their interaction with matter. The most instructive way to study such effects is in terms of the geodesic deviation of nearby test particles, since only the *relative motion* of freely falling particles can give away a time varying perturbation in the metric. For simplicity, let us assume a monochromatic plane wave as in Eq. (1.35) with wave vector $k^\mu = (\omega, 0, 0, \omega)$.

Going back to the geodesic deviation equation (1.11), for freely falling particles $u^\mu = t^\mu = (1, 0, 0, 0)$ at rest in the TT frame, we find the Riemann tensor components

$$R_{\mu\nu\rho\sigma} = \frac{1}{2} \left(\partial_\rho \partial_\nu h_{\mu\sigma} + \partial_\sigma \partial_\mu h_{\nu\rho} - \partial_\sigma \partial_\nu h_{\mu\rho} - \partial_\rho \partial_\mu h_{\nu\sigma} \right) . \tag{1.69}$$

It is important to note that the linear expression for the Riemann tensor (1.69) is *invariant* under the infinitesimal diffeomorphisms of Eq. (1.28); we choose to calculate it in the TT gauge once and for all

$$R_{0\mu0\sigma} = -\frac{1}{2\,c^2} \frac{\partial^2}{\partial t^2} h_{\mu\sigma}^{TT} \tag{1.70}$$

which, given that $t = \tau$, induces a local relative acceleration $\ddot{\delta x}^i$ of neighboring geodesics and a local apparent (tidal) force F^i on a test mass m given by

$$c^2\, a^i = \ddot{\delta x}^i = -\frac{1}{2} \ddot{h}_{ij}^{TT}\, \delta x^j \quad , \quad F^i = \frac{m}{2} \ddot{h}_{ij}^{TT}\, \delta x^j . \tag{1.71}$$

In terms of the two polarizations $\{+, \times\}$ of a plane wave, the corresponding deviations vary according to

$$\begin{pmatrix} \ddot{\delta x} \\ \ddot{\delta y} \end{pmatrix}_+ \simeq \begin{pmatrix} -\delta x_0 \\ \delta y_0 \end{pmatrix} \frac{\omega^2\, h_+}{2}\, \sin(\omega\, t) \quad \Rightarrow \quad \begin{pmatrix} \delta x \\ \delta y \end{pmatrix}_+ = \frac{h_+}{2} \begin{pmatrix} \delta x_0 \\ -\delta y_0 \end{pmatrix} \sin(\omega\, t) , \tag{1.72}$$

$$\begin{pmatrix} \ddot{\delta x} \\ \ddot{\delta y} \end{pmatrix}_\times \simeq \begin{pmatrix} \delta y_0 \\ \delta x_0 \end{pmatrix} \frac{\omega^2\, h_\times}{2}\, \sin(\omega\, t) \quad \Rightarrow \quad \begin{pmatrix} \delta x \\ \delta y \end{pmatrix}_\times = \frac{h_\times}{2} \begin{pmatrix} \delta y_0 \\ \delta x_0 \end{pmatrix} \sin(\omega\, t) . \tag{1.73}$$

The force fields, together with the apparent motion of test masses in a circular arrangement on the x-y plane around the origin, are drawn in Fig. 1.2, at different times within a wave period, that correspond to phases $\phi = 0$, $\pi/2$, π, $3\pi/2$. In a ground-based detector frame however, the reference points of the apparatus are neither in a TT frame nor in free fall. The first point is taken care of by means of the detector's antenna pattern function described below, while the second point is shown to introduce a negligible effect [253].
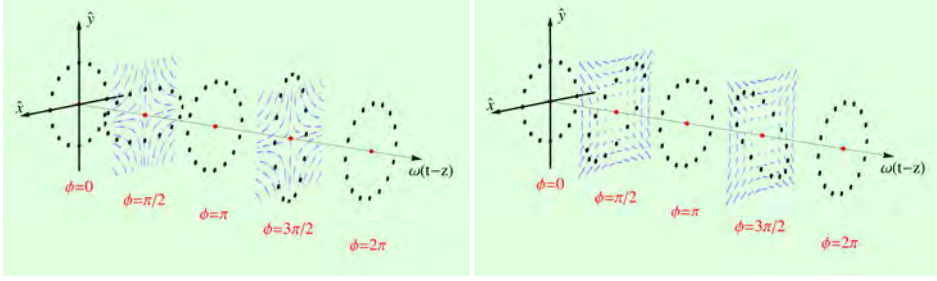
Figure 1.2: *Motion of test masses in a circular arrangement on a plane around the origin, under the influence of a passing GW that propagates in a direction perpendicular to the plane. The arrow lines represent the force vector field. The left (right) plots show the effect of a pure + (×) polarization.*

A generic *gravitational waveform* from a far away source, can then be expressed as a superposition of plane waves that propagate along a given direction $\hat{n}$ as

$$h_{ij}(t, \vec{x}) = \sum_{P=+,\times} \epsilon_{ij}^P(\hat{n}) \int_{-\infty}^{\infty} \mathrm{d}f \, \tilde{h}_P(f) \, e^{-2\pi i f(t - \hat{n} \cdot \vec{x})/c}. \qquad (1.74)$$

Antenna pattern for GW interferometers In order to translate a passing gravitational wave into detector output, one needs to transform from the TT frame defined by the source, to the proper detector frame, where the effect on the apparatus is best described, and subsequently apply a mapping from the perturbation tensor to the *gravitational wave strain* scalar. Since $h_{\mu\nu}$ transforms as a tensor under Lorentz transformations, its spatial part h_{ij} transforms as a regular (0,2)-tensor under rotations $R \in SO(3)$, which can be represented as 3x3 matrices parametrized by three angles (*e.g.* Euler angles). The mapping from the new $h_{\mu\nu}$ to the strain $h(t)$ is given by a (2,0)-tensor known as the *detector tensor* D^{ij}, which can be decomposed into the plus and cross *detector pattern functions*, the projections of the detector tensor on the polarization basis tensors,

$$h(t) = F_+(\hat{n}) \, h_+(t) + F_\times(\hat{n}) \, h_\times(t), \qquad (1.75)$$

$$F_P(\hat{n}) = D^{ij} \, \epsilon_{ij}^P(\hat{n}) \quad , \, P = +, \times. \qquad (1.76)$$

More specifically, here we are only interested in interferometric GW detectors, whose geometric properties are determined by the two unit vectors $\hat{x}$ and $\hat{y}$ that define the detector's arms. In particular, we will consider *L-shaped* detectors, whose arms are perpendicular to each other. We will also assume that length L of the detector is much smaller than the typical wavelengths of the signal, $\omega_{gw} L / c \ll 1$, so that the perturbation applies uniformly across the entire detector. Let θ and ϕ be the spherical angles between the proper detector frame and the TT frame, *i.e.* the direction of propagation is expressed as $\hat{n} = (\theta, \phi)$ in spherical

coordinates in the detector frame $\hat{x}, \hat{y}, \hat{z}$ and let ψ be the *polarization angle*, the angle that defines the orientation of the source with respect to the detector plane.

As a gravitational wave passes through the interferometer, it stretches and squeezes the spatial dimensions perpendicular to its direction of propagation in an oscillatory fashion. As a result, the paths that light travels along the two arms change relative to each other, creating an oscillating bright pattern on the dark fringe. The action of an interferometric detector's tensor D^{ij} returns a scalar that measures the integrated path difference between the light rays that travel along the two arms in $\hat{x}$ and $\hat{y}$, and so

$$D^{ij} = \frac{1}{2}(\hat{x}_i\hat{x}_j - \hat{y}_i\hat{y}_j)\,. \tag{1.77}$$

The spatial perturbation matrix h_{ij} of Eq. (1.35) transforms under a general rotational transformation

$$R(\hat{n}) = R_z(\phi)\,R_y(\theta)\,R_z(\psi)\,, \tag{1.78}$$

here in the $z - y' - z''$ sequence, as

$$h'_{ij} = (R\,h\,R^T)_{ij} = R_{ik}\,R_{jl}\,h_{kl}\,. \tag{1.79}$$

Originally, the TT gauge choice restricts h to the 2×2 subspace x-y which is invariant under R_z rotations. This implies that the two polarizations will mix with each other but the form of Eq. (1.35) will be preserved. Now, if we substitute R with the rotation matrix that transforms $(\hat{X}, \hat{Y}, \hat{Z})$ to $(\hat{x}, \hat{y}, \hat{z})$ we find

$$F_+(\hat{n}) = \frac{(1 + \cos^2\theta)}{2}\cos 2\phi \cos 2\psi - \cos\theta \sin 2\phi \sin 2\psi\,, \tag{1.80}$$

$$F_\times(\hat{n}) = \frac{(1 + \cos^2\theta)}{2}\cos 2\phi \sin 2\psi + \cos\theta \sin 2\phi \cos 2\psi\,. \tag{1.81}$$

The L-shaped detectors' antenna pattern functions are shown in the parameterized surface plots of Fig. 1.3, in which the functions are encoded in the radial coordinate $r - 2$, as functions of (θ, ϕ), so that their range $[-1, 1]$ is fully mapped in the space between the spheres $r = 1$ and $r = 3$. A large absolute value (closer to the red end of the color bar) indicates high sensitivity to GWs coming from the given direction and vice versa.

1.6 Second generation ground-based interferometers

The Virgo (Cascina, Italy) and two LIGO (Hanford, WA and Livingston, LA) interferometric GW detectors started operating in 2007, 2002 and 2002 respectively.

1
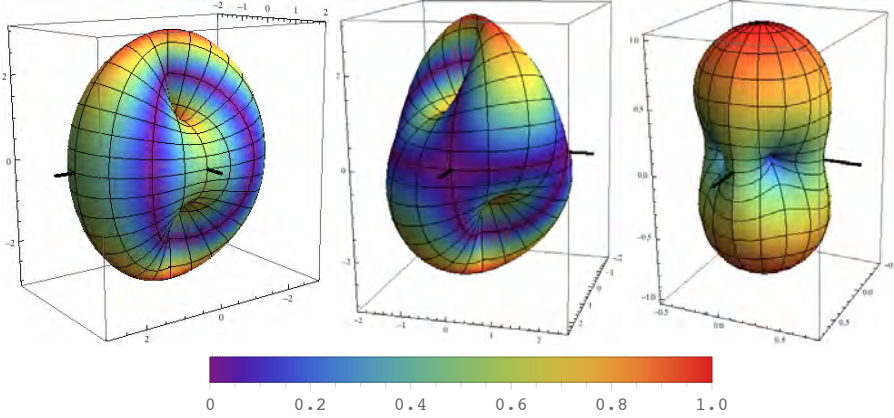
Figure 1.3: F_+ *(left) and $F_\times$ (center) antenna pattern functions for a GW interferometer for $\psi = 0$, plotted as the radial coordinate of the surface, with the zero section being mapped on the sphere of $r = 2$ (purple intersection). Color represents the absolute value. Detector arms are shown in black for reference. The right plot shows $\sqrt{F_+^2 + F_\times^2}$. Overall, an L-shaped interferometer is more sensitive to GWs coming from right above or below the detector's plane. For waves coming from the side, the sensitivity maximizes when the direction is aligned with either of the detector's axes.*

These are laser interferometers of 3 km (Virgo) and 4 km (LIGO) arm-length, in a 90° (L-shaped) configuration.

The detectors' sensitivity is described by the spectrum of noise present in the output (the photo-diode readout on the dark fringe), to which sources of noise of different nature contribute (seismic noise, radiation pressure noise, thermal noise, shot noise, Newtonian noise, *etc.*). As a stochastic process, the noise can be modeled by measuring its *auto-corellation function* in time

$$R(\tau) \equiv \langle n(t + \tau)\, n(t) \rangle \equiv \frac{1}{2} \int_{-\infty}^{\infty} \mathrm{d}f\, S_n(f) e^{-i2\pi f\tau}\,, \qquad (1.82)$$

where the Fourier decomposition in the second equation defines the function $S_n(f)$, that has units of $1/\sqrt{\mathrm{Hz}}$ and is called the *noise power spectral density* (PSD). Assuming that the process is Gaussian (and that it averages to zero), the auto-correlation completely characterizes the noise; furthermore, if it does not change in time we say that the noise is *stationary*. Equivalently, in the frequency domain, Gaussian stationary noise will be uncorrelated in frequency space and characterized by its root mean square on each frequency bin. The autocorrelation function for $\tilde{n}$ reads

$$\langle \tilde{n}^*(f)\tilde{n}(f') \rangle = \frac{1}{2}\delta(f - f')\, S_n(f)\,. \qquad (1.83)$$

Of course, it is not always the case that noise satisfies the assumptions of being
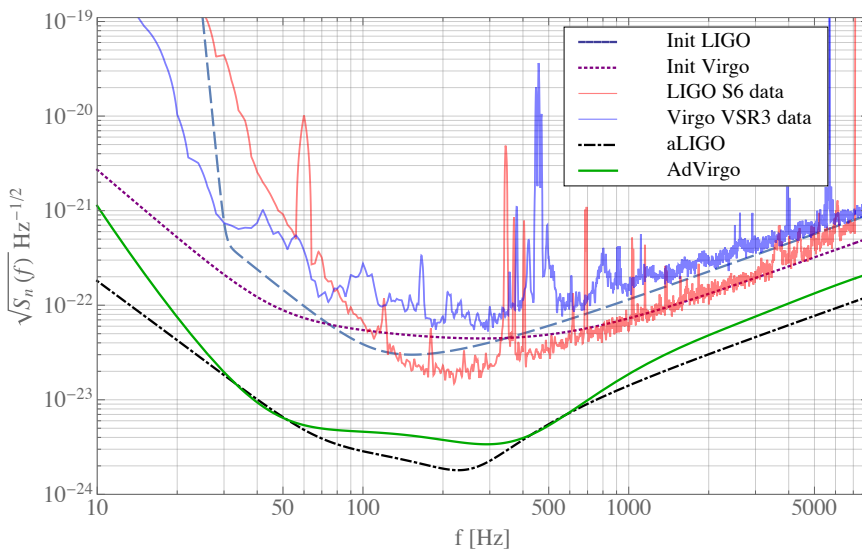
Figure 1.4: *Initial LIGO and Virgo sensitivities plotted from analytical estimates (dark blue, purple) and real data measurements (blue, red) and compared against the design sensitivities in their advanced configuration (black and green).*

Gaussian and stationary, and this may become important in our analysis, as we shall see in Chapter 8.

The VSR3 science run of Virgo and S6 of LIGO ended in 2011, with a maximum sensitivity that reached $\sqrt{S_n(f)} \sim 7 \times 10^{-23} \mathrm{Hz}^{-1/2}$ and $\sim 4 \times 10^{-23} \mathrm{Hz}^{-1/2}$ respectively and an absolute horizon for *binary neutron star* (BNS) signals for the network of three detectors at ~ 40 Mpc. After the network of initial LIGO and Virgo detectors shut down, the instruments were disassembled and started being upgraded to bring the interferometers to their advanced configuration, towards a sensitivity improvement of roughly an order of magnitude. Given the $1/r$ behaviour of the GW amplitude, this implies an order of magnitude improvement in horizon distance, which means a factor of 1000 more accessible volume, or about an equally large improvement in detection rates. Results of measurements of the noise PSDs in the initial Virgo and LIGO detectors are shown in Fig. 1.4, together with idealized curves that model the expected PSDs of AdVirgo and aLIGO at *design sensitivity*. Notice the uniform improvement by roughly an order of magnitude on top of an already impressive $\sqrt{S_n(f)} \sim 10^{-22} \mathrm{Hz}^{-1/2}$ across almost 2 decades of frequency. The wide high sensitivity band (commonly known as "the bucket"), within which one has the most chances of detecting a GW signal, ranges between a few 10s and a few 100 Hz, making coalescing neutron-star or black-hole binaries ideal candidates for detection. The evolution of AdVirgo and aLIGO sensitivity during the first few years of operation is shown in Fig. 1.5.

1
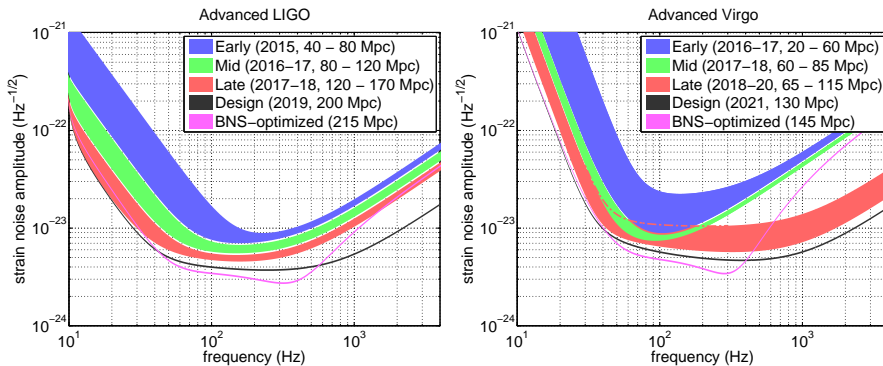
Figure 1.5: *Scheduled sensitivity for aLIGO (left) and AdVirgo (right) detectors for different commissioning phases during their first five years of operation. The angle-averaged horizon distance for binary neutron star signals is quoted in the legend in Mpc. Taken from [5].*

1.7 The first direct detection of gravitational waves

During the writing of this dissertation, the first science run of aLIGO, *O1* was succesfully completed, with the two aLIGO detectors at Hanford and Livingston reaching a BNS horizon distance of ~ 80 Mpc. On the 14th of September, 2015, at 09:50:45 UTC, a loud event triggered both aLIGO detectors almost simultaneously with a relative delay of 7 ms, and a duration of ~ 0.2 s, yielding a signal-to-noise ratio of 24, with a peak gravitational wave strain at 1.0×10^{-21} [21]. Subsequent on-line (low-latency) and off-line analyses on the event, later to be named *GW150914*, indicated and eventually verified that what perturbed the detectors was in fact a real gravitational wave, that originated from the coalescence of a stellar-mass black hole binary; the first to be detected by man kind, on the centenary of Einstein's theory of general relativity. The component black hole masses were estimated at $m_1 = 36^{+5}_{-4} \, M_\odot$, $m_2 = 29^{+4}_{-4} \, M_\odot$ (uncertainties define 90% confidence intervals), while the location of the binary was in the general direction of the southern hemisphere at a luminosity distance of $D_L = 410^{+160}_{-180}$Mpc. All relevant properties of the binary coalescence were estimated and presented in detail in [23], while futher information on the analyses performed can be found in [24, 16, 12, 22, 25, 17, 14, 15, 18, 20, 30]. A couple of weeks before the official end of O1, on the 26th of December, 2015 at 03:38:53 UTC, a second significant event, *GW151226* was registered and verified as a GW detection [19], with a signal-to-noise ratio of 13. Its duration as a signal within the frequency band of aLIGO detectors was ~ 1 s, much longer than *GW150914*, since it was emitted by a black hole binary of lower mass, $m_1 = 14.2^{+8.3}_{-3.7} \, M_\odot$, $m_2 = 7.5^{+2.3}_{-2.3} \, M_\odot$. Part of the author's work related to these discoveries will be discussed in Sec. 4.5 and 9.2 and can also be found in [24, 13].
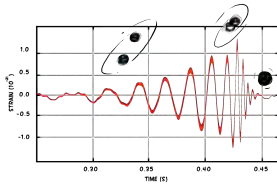
Chapter 2

Coalescing Compact Binaries

Nothing happens until something moves.

Albert Einstein

2.1 Generalities

 In this chapter we will particularize the discussion to the main subject of this dissertation, which is the study of GW signals from compact binary coalescence (CBC). Among the possible candidate sources for ground-based GW interferometers, the coalescence of neutron star (NS) or black hole (BH) binaries is the most promising type. Indeed, the first direct GW detection came with the observation of a *binary black hole* (BBH) coalescence. These systems have evolved over the course of millions of years, during which their orbits gradually circularize and shrink, due to the emission of gravitational waves. The three features that characterize the final stage of this process are all key ingredients that raise the expectations for detection with Advanced Virgo and LIGO:

Compact: a high compactness of the component bodies is necessary for the binary to achieve coherent gravitational wave emission, all the way up to the last stable orbit, where the radiated energy flux is the highest. Binaries including less compact objects like white dwarfs (WD) merge into a single object in a much earlier stage, when the GW signal is still too weak to be detected and the GW frequency is far below the high sensitivity band of ground-based interferometers.

Binary: gravitational wave generation requires a strong oscillating/accelerating quadrupolar moment, an ingredient that cannot easily be obtained by single astrophysical objects with a spherical mass distribution. A *binary system* is an ideal setup for this requirement and yields a characteristic *chirp* GW signal.

Image credits: Nutsinee Kijbunchoo, LIGO.

Coalescence: as the binary orbit shrinks towards the innermost stable circular orbit (ISCO), a prodigious amount of GWs is emitted with an increasing amplitude. For NS and stellar-mass BH systems the frequency band where most of the GW power is released largely overlaps with the high-sensitivity band of ground-based interferometers.

Intrinsic parameters   Assuming for a moment that the two component bodies can be treated as point masses, the system is defined by the following *intrinsic parameters*:

- Two mass parameters: these can simply be the component masses[1] m_A, $A = 1, 2$, or equivalently any pair of independent combinations of those, such as the total mass $M = m_1 + m_2$, the mass difference $\delta m = m_1 - m_2$ and *fractional mass difference* $\delta = \frac{m_1 - m_2}{m_1 + m_2}$, the *chirp mass* $\mathcal{M}_c = \frac{(m_1 \, m_2)^{3/5}}{(m_1 + m_2)^{1/5}}$, the *reduced mass* $\mu = \frac{m_1 \, m_2}{m_1 + m_2}$ and one of the symmetric or asymmetric mass ratios $\eta = \frac{m_1 \, m_2}{(m_1 + m_2)^2}$ or $q = m_1/m_2$. Note that the dimensionless variables q, η are linearly dependent through the relation $\eta = \frac{q}{(1+q)^2}$ (this is also true for any other dimensionless combination). Another useful relation is $\mathcal{M}_c = M \, \eta^{3/5}$.

- Two spin vectors: $\vec{S}_A$, $A = 1, 2$ or their dimensionless counterparts $\vec{\chi}_A = \frac{\vec{S}_A}{m_A^2}$; these define the internal angular momentum of each component body, due to rotation in the case of a NS, or Kerr spin parameter in the case of a BH. Depending on the problem at hand, these can also be re-parametrized into convenient combinations (effective spin parameters, effective precessing spin, *etc.* [220, 191, 304]), among which we shall only deal with the *symmetric* and *anti-symmetric spins* $\vec{\chi}_s = \frac{\vec{\chi}_1 + \vec{\chi}_2}{2}$ and $\vec{\chi}_a = \frac{\vec{\chi}_1 - \vec{\chi}_2}{2}$. The component spin vectors are often parametrized in spherical coordinates with respect to a preferred frame, that is, in terms of their norm χ_A, a polar angle κ_A and azimuth angle γ_A.

As two simplified cases, we consider systems where (i) both spins are zero, (ii) both spin vectors are *aligned* with the orbital angular momentum $\vec{L} = \vec{r} \times \vec{p}$. In the latter case, the spins will remain aligned throughout the entire evolution of the binary. The *total angular momentum* of the binary is denoted as $\vec{J} = \vec{L} + \vec{S}_1 + \vec{S}_2$. Note that the spins $\vec{S}_A$, as well as the orbital $\vec{L}$ and total $\vec{J}$ angular momentum of the binary, are instantaneous quantities, *i.e.* they are not conserved but actually evolve with time.[2] We shall return to this in Sec. 2.4.2. In particular, this means that in order to define the system, one also needs to define the instance at which the spins take a given value.

---

[1] We will adopt the convention that $m_1 > m_2$.

[2] The reason why $\vec{J}$ is not conserved in principle is that the outgoing GWs also carry angular momentum (see Eq. (1.64)), however the quantity $\vec{J}_{\text{tot}} = \vec{J} + \vec{J}_{\text{gw}}$ is indeed conserved.

The orbital evolution can be qualitatively split into three stages: (i) the *inspiral*, during which the component bodies are far enough from each other that the binary can be described as a post-Newtonian source that loses energy through copious emission of GWs; (ii) the *merger*, which comes roughly when the orbital separation becomes smaller than the last stable orbit (LSO) and briefly extends up to the point when the two objects have merged into a single excited spinning BH; (iii) the *ringdown*, during which the final BH radiates away its excessive moments by means of GW emission, until it finally settles into a quiescent state as a Kerr BH. The evolution of a binary system driven predominantly by gravitation is the infamous two-body problem in general relativity, which admits no known analytical solution. However, a number of perturbative techniques have been developed in order to derive approximate solutions to this problem. During the inspiral, the PN formalism, allows for a systematic expansion of the orbital quantities of interest, in terms of the small parameter $(v/c)^2$, where $v = |\vec{v}_1 - \vec{v}_2|$ is the instantaneous orbital velocity of the system. In second generation interferometers the inspiral enters the sensitivity band at roughly 10 Hz and lasts up to LSO or, for circularized orbits, the ISCO frequency which is inversely proportional to the mass,

$$f_{\text{ISCO}} \simeq \frac{1}{\pi} \sqrt{\frac{M}{(6M)^3}} = \frac{1}{6^{3/2}\pi M} \, , \tag{2.1}$$

and for a typical $(1.4 - 1.4)M_\odot$ BNS system is at $\sim 1600\,\text{Hz}$. For BNS systems however and depending on the component masses and the *NS equation of state* (EoS), the inspiral orbit may be terminated earlier due to *tidal disruption* or physical *contact* between the two finite-sized neutron stars. Both of the above will spoil the coherence of the GW emission and introduce sudden changes in the waveform. A short overview of PN methods applied to compact binaries and their results will be discussed in Sec. 2.3. The late inspiral and merger stage cannot be accurately treated perturbatively, and have been the objects of studies using numerical relativity (NR) simulations where the entire spacetime geometry in the vicinity of the binary is being evolved [63, 334, 164]. Finally, the ringdown stage can be modeled in terms of the perturbation equations around a Kerr spacetime [352, 301, 242]. The ringdown GW signal is modeled as a superposition of damped sinusoids, that correspond to the different eigen-frequencies of the BH's quasi-normal modes, and in practice lasts a small fraction of a second. The main focus of this dissertation is on the study of the inspiral stage.

Extrinsic parameters The intrinsic parameters of a compact binary completely define the evolution of spacetime, and the gravitational waves that are emitted by it. However, for the purposes of GW data analysis one needs to also be concerned with the source's *extrinsic parameters* relative to the observer. These will introduce additional transformations on the waveform and will give the GW signal its final form with which it will appear in the detector output.

We define the following extrinsic parameters of the source with respect to an observer/detector frame on Earth:

- Distance to the source: the *luminosity distance* $D = D_L$ is most commonly used, since this is the quantity that appears in the inverse distance law of the waveform. Since detectable sources may reach distances out to cosmological scales (close to 1Gpc), a careful treatment of the different types of distances may be required, depending on the calculation one wishes to perform. Also, at cosmological scales, the waveform undergoes the standard cosmological redshift, which induces a rescaling of the *observed masses* relative to the *intrinsic masses*.

- Sky location of the source: is defined in terms of the polar ϑ and azimuth φ angles of the source with respect to the detector frame $(\hat{X}, \hat{Y}, \hat{Z})$ (which for L-shaped interferometers is defined by its X-arm, Y-arm and the vertical). In practice, the *right-ascension* α and *declination* δ angles on the celestial sphere are used instead, which can be directly translated into (φ, ϑ), given the location of the detector on the Earth and the Earth's orientation during the time of coalescence.

- Orientation of the source: is described by the *inclination angle ι* and *polarization angle ψ*. ι is defined as the angle between the orbital axis and the line of sight, while ψ is the angle between the major axis of the apparent orbital ellipse and the detector plane.

- Time of coalescence: t_c is defined as the time when the gravitational wave front of peak amplitude arrived at the detector. When a network of detectors is considered, one often uses the time of arrival (TOA) at the center of the Earth, which can then be translated to the TOAs at each individual detector.

- Phase at coalescence: φ_c is the phase of the GW at peak amplitude.

To conclude, a typical CBC gravitational wave signal is characterized by 15 independent parameters, a choice of which is

$$\vec{\theta}_{CBC} = \left(m_1, m_2, \vec{S}_1, \vec{S}_2, D, \alpha, \delta, \iota, \psi, t_c, \varphi_c \right) . \tag{2.2}$$

Detection rates Apart from the aforementioned attractive physical features of compact binaries, one also needs to take into account the abundance of such systems in the universe. If the rate of coalescing compact binaries within our detectors' reach were too low, then one would not be guaranteed to make a detection within a reasonable amount of time. We can safely assume that the density of compact binaries throughout the universe is roughly uniform. Since systems of different masses radiate up to different frequencies and with different amplitudes, the horizon of a given detector can only be defined per type of source

population. *Binary neutron star* (BNS) systems, in which both components are neutron stars, are known to be of low mass [314, 226, 356, 227], with a typical total mass $M \sim 2.7 M_\odot$, thus radiating up to 1600 Hz before crossing their ISCO. A typical BNS system will spend a few minutes within the LIGO/Virgo sensitivity band. On the other hand, higher-mass NS-BH or BH-BH binaries will emit stronger gravitational radiation (as we will see in Sec. 2.2, GW amplitude at a given frequency scales as $M^{5/6}$), but will sweep the in-band frequencies much faster and will terminate at a lower ISCO frequency (see Eq. (2.1)).

For a given detector of a certain sensitivity and a given population of sources of a certain lifetime and density, one can estimate the rate at which binaries of this population will coalesce and the rate at which their GW signals will reach us with signal-to-noise ratios (SNR) above a certain threshold (usually set to the "detectability threshold" of SNR = 8). Since no direct observation of a BH was available before the first science run of aLIGO (O1), the density estimates for BH binaries were subject to large uncertainties [219, 67, 280, 83], with no definite lower bound. There are however direct observations of a few BNS

IFO	Source	$\dot{N}_{\text{low}} \, (yr^{-1})$	$\dot{N}_{\text{re}} \, (yr^{-1})$	$\dot{N}_{\text{high}} \, (yr^{-1})$
	NS-NS	2×10^{-4}	0.02	0.2
Initial	NS-BH	7×10^{-5}	0.004	0.1
	BH-BH	2×10^{-4}	0.007	0.5
	NS-NS	0.4	40	400
Advanced	NS-BH	0.2	10	300
	BH-BH	0.4	20	1000

Table 2.1: *Expected detection rates for the network of initial Virgo–LIGO and AdVirgo–aLIGO detectors at design sensitivity, based on pessimistic (low), realistic (re) and optimistic (high) estimates for binary populations and merger rates, according to a variety of astrophysical models on the population of compact binaries. Table adapted from [9]. In the light of the recent GW detections during O1, the detection rate was also estimated as a probability distribution on the* sensitive time-volume $\langle VT \rangle$ *in [25].*

systems [280, 226, 282, 227, 157], for which the *coalescence rate* estimates range between 10^{-6} and 10^{-3} per Gyr per Milky Way Equivalent Galaxy (MWEG) [9]. These can be directly translated into *detection rate* estimates, given the observed density of galaxies and the $1/r$ scaling in the GW amplitude. A conservative but realistic estimate for the detection rate gives around 40 BNS signal detections per year, with a network of 3 second generation detectors at design sensitivity. A summary of the expected detection rates for BNS, NS-BH and BBH systems with AdVirgo and aLIGO is given in [9] and shown in Table 2.1, in comparison with the initial LIGO–Virgo network. After the completion of O1, and with the detection of two GW signals at high significance, the BBH merger rate was estimated to lie in the range $6 - 400 \, \text{Gpc}^{-3} \text{yr}^{-1}$. Based on these merger rates, it is expected that a few more BBH signals will be detected within the upcoming science run O2 and more than 10 in O3 [25]. Table 2.2 shows the expectations for BNS detections in particular, during the science runs scheduled with advanced

detectors.

Scheduled Run		BNS Range (Mpc)		Number of	% BNS localized in	
Epoch	Duration	aLIGO	AdVirgo	BNS Detections	$5\deg^2$	$20\deg^2$
2015	3 months	40–80	–	0.0004–3	–	–
2016–17	6 months	80–120	20–60	0.006–20	2	5–12
2017–18	9 months	120–170	60–85	0.04–100	1–2	10–12
2019 +	(per year)	200	65–130	0.2–200	3–8	8–28
2022+	(per year)	200	130	0.4–400	17	48

Table 2.2: *Expected BNS range, detection rates and localisation resolution, with the network of aLIGO and AdVirgo detectors during the first few years of operation. LIGO India (IndIGO) is added to the network from 2022 onwards (bottom row); KAGRA is not considered in this study but it is expected to improve the quoted figures from 2017 onwards. The corresponding sensitivity curves are given earlier, in Fig. 1.5.*

2.2 The quadrupole formula

Before diving into the complexity of the PN formulation for the two-body problem, let us first derive the leading order expressions for the generation of GWs from a compact binary in a quasi-circular orbit. The Newtonian or zeroth order conservative equation is simply Kepler's law

$$\omega^2 = \frac{G\,M}{R^3}\,. \tag{2.3}$$

The quadrupole formula Eq. (1.56), whose key ingredient is the time-varying quadrupole mass moment $\ddot{Q}$, can be used directly. First, we model the mass-energy density $T^{00}(t,\vec{x}) = \rho(t,\vec{x})c^2$ as a sum of delta functions centred on the locations of the two component masses $\vec{x}_1$ and $\vec{x}_2$, whose orbit in the non-relativistic limit obeys Kepler's laws,

$$\rho(t,\vec{x}) = m_1\,\delta^{(3)}(\vec{x} - \vec{x}_1(t)) + m_2\,\delta^{(3)}(\vec{x} - \vec{x}_2(t))\,, \quad \vec{x}_A(t) = \pm\frac{\mu}{m_A}R(t)\hat{e}(t)\,, \tag{2.4}$$

$$\hat{e}(t) = \left(\cos\frac{\Phi(t)}{2}, \cos\iota\sin\frac{\Phi(t)}{2}, \sin\iota\sin\frac{\Phi(t)}{2}\right)\,, \tag{2.5}$$

in a frame where the orbit has an inclination angle ι with respect to the z-axis, and intersects the $x-y$ plane along the y-axis. For simplicity let us first assume that the energy loss affects the orbit at a timescale much larger than its period, so that practically $\Phi(t) = \omega t$. The TT projection for an observer sitting along the z-axis (*i.e.* $\hat{n} = \hat{z}$), will only preserve the $x-y$ components of the mass moments, which we can calculate from Eq. (2.4) and (1.52) as

$$M_{ij}(t) = \frac{1}{c^2}\int \mathrm{d}^3\vec{x}\,\rho(t,\vec{x})\,x^i x^j = \left(\frac{\mu^2 R}{m_1} + \frac{\mu^2 R}{m_2}\right)\hat{e}^i\hat{e}^j\,. \tag{2.6}$$

Performing the TT projection $\ddot{M}_{ij}^{TT} = \Lambda_{ij}^{kl} \ddot{M}_{kl}$ we find

$$\ddot{M}_{xx}^{TT} = -\ddot{M}_{yy}^{TT} = \frac{1}{2}\left(\ddot{M}_{xx} - \ddot{M}_{yy}\right) = 2\left(\frac{1}{m_1} + \frac{1}{m_2}\right)\mu R^2\omega^2\cos 2\omega t, \quad (2.7)$$

$$\ddot{M}_{xy}^{TT} = \ddot{M}_{yx}^{TT} = \ddot{M}_{xy} = 2\left(\frac{1}{m_1} + \frac{1}{m_2}\right)\mu R^2\omega^2\sin 2\omega t, \quad (2.8)$$

with which we get the waveform to leading order

$$h_+(t) = \frac{4}{r}\left(\frac{G\mathcal{M}_c}{c^2}\right)^{5/3}\left(\frac{\omega}{c}\right)^{2/3}\left(\frac{1 + \cos^2\iota}{2}\right)\cos(2\omega t_{\text{ret}} + \varphi_0), \quad (2.9)$$

$$h_\times(t) = \frac{4}{r}\left(\frac{G\mathcal{M}_c}{c^2}\right)^{5/3}\left(\frac{\omega}{c}\right)^{2/3}\cos\iota\,\sin(2\omega t_{\text{ret}} + \varphi_0). \quad (2.10)$$

Here we used Kepler's law and the definition of the chirp mass $\mathcal{M}_c = M\eta^{3/5}$.

2.3 Compact binaries in the post-Newtonian expansion

We briefly outline the results of applying the post-Newtonian formulation on the problem of modeling the evolution of compact binaries [88, 176], up to the late inspiral. In the derivation of the quadrupole formula above, we saw how the conservative equation (Kepler's law) gave the leading order equations of motion, according to which the multipoles that source the emitted GWs are calculated. Kepler's law Eq. (2.3) is valid only as a leading-order equation and needs to be corrected for relativistic effects, based on PN calculations. Each iteration in the PN expansion will give an additional correction to the equations of motion (the acceleration vectors in terms of the position and velocity vectors). The equations of motion in the center-of-mass frame, calculated based on the metric expanded up to 3.5PN [215, 97, 272] take the form

$$\frac{\mathrm{d}\vec{v}}{\mathrm{d}t} = -\frac{GM}{\|\vec{x}\|^2}\left[\,(1 + A)\hat{x} + B\,\vec{v}\,\right] + O\left(\frac{1}{c^8}\right), \quad (2.11)$$

where $\hat{x} = \vec{x}/\|\vec{x}\|$ $\vec{v} = \mathrm{d}\vec{x}/\mathrm{d}t = \vec{v}_1 - \vec{v}_2$ ($\vec{x} = \vec{x}_1 - \vec{x}_2$ being the separation vector between the two bodies) and where the quantities A and B are explicitly written out in Appendix A. One may then distinguish between corrections of odd and even order in v/c; the even order terms (Newtonian or 0PN, 1PN, 2PN, 3PN) give rise to time-reversible equations, and thus make up the *conservative* sector of the PN expansion, whereas the odd terms (2.5PN, 3.5PN), starting at $(v/c)^5$, act as non-reversible contributions that make up the *dissipative* sector.

Conservative sector   If one keeps the conservative terms alone, the equations of motion admit a conserved energy E per total mass, which for circular binaries in the center-of-mass frame reads

$$E = -\frac{\mu c^2 \epsilon}{2} \left\{ 1 + \left[-\frac{7}{4} + \frac{1}{4}\eta \right] \epsilon + \left[\frac{-7}{8} + \frac{49}{8}\eta + \frac{1}{8}\eta^2 \right] \epsilon^2 \right. \tag{2.12}$$
$$\left. + \left[-\frac{235}{64} + \left(\frac{46031}{2240} - \frac{123}{64}\pi^2 + \frac{22}{3} \ln\frac{r}{r_0'} \right) \eta + \frac{27}{32}\eta^2 + \frac{5}{64}\eta^3 \right] \epsilon^3 \right\} + O(\epsilon^4) \,,$$

where η is the symmetric mass ratio and ϵ is the expansion parameter introduced in Section 1.4. Once the dissipative effects enter, this quantity is no more conserved and one gets its time derivative $\mathrm{d}E/\mathrm{d}t$ purely from the dissipative sector.

Dissipative effects   The "driving force" in the inspiral evolution of the binary is the outward flux of energy in the form of gravitational radiation. We can make use of Eq. (2.12) in order to obtain the GW energy flux to 3.5PN order and then apply the *energy balance equation*

$$\frac{\mathrm{d}v}{\mathrm{d}t} = \frac{\dot{\mathcal{E}}}{\mathcal{E}'(v)} = -\frac{\mathcal{F}(v)}{M \, E'(v)} \tag{2.13}$$

in order to obtain the orbital evolution using dissipative GW effects to leading order. Here, E is the energy per total mass, while $\mathcal{E}$ is the total energy. In Eq. (2.18) we directly give the expression for the GW energy flux expanded in terms of the orbital parameter x (or equivalently v).

Orbit circularization   Radiation of gravitational waves is known to remove angular momentum from the system in a way that, in the long term, circularizes the orbit [293]. The majority of astrophysical binary systems that are close to coalescence have most likely undergone a long evolution process since their birth, during which they have lost their orbital eccentricity. We can safely assume that the systems to be observed with aLIGO and AdVirgo will have practically circular orbits.

2.3.1   3.5PN evolution of quasi-circular orbits

The PN orbital evolution can be better understood in a Newtonian-like picture, where we make use of the variable

$$x \equiv \left(\frac{G \, M \, \omega}{c^3} \right)^{2/3} \sim O\left(\frac{v^2}{c^2} \right) \sim O(\epsilon) \,, \tag{2.14}$$

which is a dimensionless version of the instantaneous orbital angular velocity and defines the PN order in the expansions. When considering circularized orbits, *i.e.*

$\dot{r} = \hat{n} \cdot \vec{v} = 0$ up to 2.5PN when radiation reaction terms come in, the expressions of Eq. (A.2) and (A.3) greatly simplify. Now, the equivalent of Kepler's law is the PN expansion of the orbital angular velocity ω in the center-of-mass frame,[3] which reads

$$\omega^2 = \frac{GM}{r^3} \left\{ 1 + (-3+\eta)\epsilon + \left(6 + \frac{41}{4}\eta + \eta^2 \right)\epsilon^2 \right. \tag{2.16}$$

$$\left. + \left[-10 + \left(-\frac{75707}{840} + \frac{41}{64}\pi^2 + 22\ln\frac{r}{r_0'} \right)\eta + \frac{19}{2}\eta^2 + \eta^3 \right]\epsilon^3 \right\} + O(\epsilon^4) .$$

After inverting this equation to obtain ϵ in powers of x, one finds the energy per total mass E up to 3.5PN order [141, 148, 140, 93, 97, 213][4]

$$E(x) = -\frac{M\eta x}{2} \left\{ 1 + \left[-\frac{3}{4} - \frac{1}{12}\eta \right] x + \left[-\frac{27}{8} + \frac{19}{8}\eta - \frac{1}{24}\eta^2 \right] x^2 \right. \tag{2.17}$$

$$\left. + \left[-\frac{675}{64} + \left(\frac{34445}{576} - \frac{205}{96}\pi^2 \right)\eta - \frac{155}{96}\eta^2 - \frac{35}{5184}\eta^3 \right] x^3 \right\} + O\left(\frac{1}{c^8} \right) .$$

Furthermore, the *energy flux* $\mathcal{F}(x)$ has been calculated to 3.5PN [99, 96, 94, 98, 95]

$$\mathcal{F}_{3.5}(x) = \frac{32}{5}\eta^2 x^5 \left\{ 1 - \left(\frac{1247}{336} + \frac{35}{12}\eta \right) x + 4\pi x^{3/2} - \left(\frac{44711}{9072} - \frac{9271}{504}\eta - \frac{65}{18}\eta^2 \right) x^2 \right.$$

$$- \left(\frac{8191}{672} + \frac{583}{24}\eta \right)\pi x^{5/2} + \left[\frac{6643739519}{69854400} + \frac{16}{3}\pi^2 - \frac{1712}{105}\gamma_E \right.$$

$$+ \left(\frac{41}{48}\pi^2 - \frac{134543}{7776} \right)\eta - \frac{94403}{3024}\eta^2 - \frac{775}{324}\eta^3 - \left. \frac{856}{105}\log(16x) \right] x^3$$

$$- \left(\frac{16285}{504} - \frac{214745}{1728}\eta - \frac{193385}{3024}\eta^2 \right)\pi x^{7/2} \right\} , \tag{2.18}$$

where $\gamma_E = 0.577216\ldots$ is the Euler–Mascheroni constant.

Using the energy balance equation (2.13) in the adiabatic approximation, one gets the PN expressions for the orbital phase $\phi(x)$ and time $t(x)$ from the integrals

$$\omega = \frac{d\phi}{dv}\frac{dv}{dt} = \frac{v^3}{M} \quad \Leftrightarrow \quad \phi(v) = \phi_0 + \int_v^{v_0} dv\, v^3 \frac{E'(v)}{\mathcal{F}(v)} \tag{2.19}$$

---

[3]Technically speaking, ω is the coefficient of the conservative part in the PN-expansion of the relative acceleration

$$\vec{a} = -\omega^2\vec{x} - \left[\frac{32G}{5c^5}\frac{M^3\eta}{r^4} + O\left(\frac{1}{c^7} \right) \right]\vec{v} \tag{2.15}$$

.

[4]Note that from here onwards, we drop the G and c factors and express quantities in geometric units ($G = c = 1$). If we were to reinstate the constants, then E would get a pre-factor c^2 and $\mathcal{F}$ would get a $\frac{c^5}{G}$.

and

$$\frac{\mathrm{d}v}{\mathrm{d}t} = -\frac{\mathcal{F}(v)}{ME'(v)} \quad \Leftrightarrow \quad t(v) = t_0 + \int_v^{v_0} \mathrm{d}v \, \frac{E'(v)}{\mathcal{F}(v)} \, . \tag{2.20}$$

Depending on the exact way one chooses to perform the expansion in the above expressions, one obtains slightly different results, which will diverge from each other as the small parameter x, or v/c, approaches unity. This in particular means that the different models which will be outlined below, will exhibit slightly inconsistent behaviour towards the end of the inspiral.

2.4   Post-Newtonian waveform approximants

2.4.1   Non-spinning point-particle waveforms

In this section we will go through the different PN-based waveform models that are most often used in GW data analysis, focusing on the two that we shall use the most (TaylorF2, TaylorT4) in the following chapters. For simplicity, in this section we assume waveforms from quasi-circular binaries with zero-spin, point-mass components. In general, waveform models can be divided into ones that are generated in the time domain and ones that are directly generated in the frequency domain. As will become clear, for the purposes of GW data analysis the signal is treated in the frequency domain, which means that the time-domain waveforms need to undergo a Fourier transform (FT). Even though there exist efficient FT algorithms [110, 300, 174, 192], the additional step may actually contribute a significant part of the computational cost, so frequency-domain waveforms (if accurate enough) are always preferred.

TaylorT1   This approximant preserves the original form of the differential equations (2.19), (2.20) with rational functions on the RHS and solves them numerically. The initial conditions are defined at a reference GW frequency f_0 (or equivalently $v_0 = (\pi M f_0)^{1/3}$) at which we can choose $t_0 = 0$, while the phase at that frequency can also take an arbitrary value. These initial values eventually determine the time and phase at coalescence parameters t_c and φ_c. The 3.5PN model waveform is obtained by using the expansion of E to 3PN and $\mathcal{F}$ to 3.5PN.

TaylorT2   The TaylorT2 waveforms are generated by first expanding the rational fractions that appear as the integrands of Eq. (2.19), (2.20). Then, the integration is performed analytically, to consistent PN order in the resulting polynomials. The resulting functions take the parametric form

$$\phi_{3.5}(v) = \phi_0 - \frac{1}{32\eta v^5} \sum_{k=0}^{7} \hat{\phi}_k^v v^k, \quad t_{3.5}(v) = t_0 - \frac{5M}{256\eta v^8} \sum_{k=0}^{7} \hat{t}_k^v v^k \, . \tag{2.21}$$

This is a set of algebraic equations that can be solved numerically to give the time domain waveform $\phi(t)$. First, Eq. (2.21) is inverted and solved for discrete values of t, to obtain $v(t)$, which is then substituted in (2.21) to obtain $\phi(t)$.

TaylorT3   In the TaylorT3 approximants the equations (2.21) of TaylorT2 are further worked out. After inverting the latter to solve for the GW frequency $F(t) = v^3(t)/(\pi M)$ as an expansion

$$F_{3.5}(t) = \frac{\Theta^3(t)}{8\pi M} \sum_{k=0}^{7} \hat{F}_k^t \Theta^k(t) \quad , \quad \Theta(t) = \left[\frac{\eta(t_0 - t)}{5M}\right]^{-1/8} , \qquad (2.22)$$

we can substitute into the former to get the waveform phase $\phi(t)$ at 3.5PN

$$\phi_{3.5}(t) = \phi_0 - \frac{1}{\eta\Theta^5(t)} \sum_{k=0}^{7} \hat{\phi}_k^t \Theta^k(t) . \qquad (2.23)$$

Integration constants are determined by requiring that at $t = 0$, F takes a given value F_0 and solving for t_0.

TaylorT4   This is the time-domain waveform approximant that we will use in our investigations and it is known to have the best matching with NR simulated waveforms, among all PN approximants. The TaylorT4 waveform is generated by means of numerical integration of $\dot{\omega}$ ($\omega = v^3/M$) in Eq. (2.20), in which the rational function $\frac{\mathcal{F}(\omega)}{ME'(\omega)}$ to be integrated is first expanded to consistent PN order,

$$\dot{\omega} = \frac{d\omega}{dv}\frac{dv}{dt} = \frac{96\,\mathcal{M}_c^{5/3}}{5}\omega^{11/3} \sum_{k=0}^{7} \left[\xi_k + \xi_k^{(l)} \log(M\omega)^{\frac{1}{3}}\right](M\omega)^{k/3} , \qquad (2.24)$$

where the coefficients ξ_i and $\xi_i^{(l)}$ depend on the intrinsic parameters[5]. For non-spinning point-particle binaries these read

$$\xi_0 = 1 , \quad \xi_1 = 0 , \quad \xi_2 = \left(\tfrac{743}{336} + \tfrac{11}{4}\eta\right) , \quad \xi_3 = 4\pi ,$$
$$\xi_4 = \tfrac{34103}{18144} + \tfrac{13661}{2016}\eta + \tfrac{59}{18}\eta^2 , \quad \xi_5 = -\left(\tfrac{4159}{672} + \tfrac{189}{8}\eta\right)\pi ,$$
$$\xi_6 = \tfrac{16447322263}{139708800} + \tfrac{16}{3}\pi^2 - \tfrac{1712}{105}\gamma_E + \left(\tfrac{451}{48}\pi^2 - \tfrac{56198689}{217728}\eta + \tfrac{541}{896}\eta^2 - \tfrac{5605}{2592}\eta^3\right)$$
$$\xi_7^{(l)} = -\tfrac{1712}{105} , \quad \xi_7 = -\left(\tfrac{4415}{4032} - \tfrac{358675}{6048}\eta - \tfrac{91495}{1512}\eta^2\right)\pi . \qquad (2.25)$$

A second numerical integration of $\omega(t) = \dot{\phi}(t)$ then gives the phase evolution $\phi(t)$ to 3.5PN order.

---

[5]Note that there is only one non-zero logarithmic coefficient that appears at 3PN.

TaylorF2   The *stationary phase approximation* (SPA) is a common method in complex integration, which in this case allows us to approximate a Fourier transform (FT) analytically and calculate the gravitational waveform directly in the frequency domain. Based on the fact that the integration takes place over a fast oscillating complex function like $e^{i[g(t)x]}$ over t, the FT gets its dominant contribution from the values around which the phase is stationary, *i.e.* $dg/dt = 0$. When performing the FT of a waveform $h(t) = A(t)e^{i\Phi(t)}$ the SPA may be used to derive an analytical approximation of the frequency domain waveform $\tilde{h}(f)$. Now, the main contribution at each value of the Fourier variable f comes from the *saddle point* time $t_s(f)$, defined implicitly by the stationary phase condition $\dot{\Phi}(t_s(f)) - 2\pi f = 0$, or $F(t_s(f)) = f$, *i.e.* the time when the GW frequency $F = \omega/\pi$ coincides with the value of the Fourier variable. Intuitively this makes sense, since it matches the rationale of an adiabatic quasi-circular orbit, during which the GW signal can be considered as "instantaneously monochromatic". In TaylorF2, and by using only the quadrupole formula for the amplitude, one can then Taylor expand the exponent $2\pi f - \Phi(t)$ around $t_s(f)$ and arrive at

$$\tilde{h}(f) \simeq \sqrt{\frac{\pi}{2}} \frac{A(t_s(f))}{\sqrt{\ddot{\Phi}(t_s(f))}} e^{i\Psi(f)}, \quad \Psi(f) = 2\pi f t_s(f) - \Phi(t_s(f)) - \frac{\pi}{4}, \quad (2.26)$$

where the proportionality constant has an explicit dependence on the extrinsic anglular parameters $(\theta, \phi, \iota, \psi)$, as described in Sec. 1.5. After performing the expansion $t(v(f))$ as in Eq. (2.21) of TaylorT2 and substituting everything in Eq. (2.26), the (mass quadrupole) *amplitude* reads

$$|\tilde{h}(f)| = \frac{\mathcal{A}(\theta, \phi, \iota, \psi)}{r} \sqrt{\frac{5\pi}{96}} \mathcal{M}_c^{5/6} (\pi f)^{-7/6}, \ \mathcal{A} = \sqrt{F_+^2 [1 + \cos^2 \iota]^2 + F_\times^2 4 \cos^2 \iota} \tag{2.27}$$

and the *phase* takes the form

$$\Psi_{3.5}(f) = 2\pi f t_c - \varphi_c - \frac{\pi}{4} + \frac{3}{128\eta\, v^5} \sum_{k=0}^{7} \left[\psi_k + \psi_k^{(l)} \log v \right] v^k, \quad v(f) = (\pi M f)^{1/3}, \tag{2.28}$$

where the reference time $t_0 = t_c$ is taken at coalescence and the *TaylorF2 PN phase coefficients* depend on the masses and are calculated up to 3.5PN

$$\psi_0 = 1, \quad \psi_1 = 0, \quad \psi_2 = \frac{20}{9} \left(\frac{743}{336} + \frac{11}{4}\eta \right), \tag{2.29}$$

$$\psi_3 = -16\pi, \quad \psi_4 = 10 \left(\frac{3058673}{1016064} + \frac{5429}{1008}\eta + \frac{617}{144}\eta^2 \right),$$

$$\psi_5 = \pi \left(\frac{38645}{756} - \frac{65}{9}\eta \right) (1 - 3\log(v_{\mathrm{LSO}})), \quad \psi_5^{(l)} = \pi \left(\frac{38645}{252} - \frac{65}{3}\eta \right),$$

$$\psi_6 = \frac{11583231236531}{4694215680} - \frac{640}{3}\pi^2 - \frac{6848}{21} [\gamma_E - \log(4)]$$

$$+ \left(-\frac{15335597827}{3048192} + \frac{2255}{12}\pi^2 \right) \eta + \frac{76055}{1728}\eta^2 - \frac{127825}{1296}\eta^3, \quad \psi_6^{(l)} = -\frac{6848}{21},$$

$$\psi_7 = \pi \left(\frac{77096675}{254016} + \frac{378515}{1512}\eta - \frac{74045}{756}\eta^2 \right). \tag{2.30}$$

These are the expressions for the restricted GW signal from a non-spinning point-particle circularized binary. The phase coefficients defined above will eventually

have additional spin contributions, as we shall see in Sec. 2.4.2, as well as contributions from finite-size effects that will be studied in Sec. 2.6.

Number of GW cycles Once the explicit expression for the orbital or GW phase is known, it is interesting to estimate the *total number of cycles* that the waveform spends in band. Moreover, a good figure of merit for assessing the impact of a particular effect on a waveform is the induced modification of the phase, and more specifically, the number of additional cycles that are due to that effect alone. We thus define

$$N_{\text{tot}} = \int_{f_1}^{f_2} \mathrm{d}f \, \frac{\mathrm{d}N}{\mathrm{d}f} = \int_{f_1}^{f_2} \mathrm{d}f \, \frac{1}{2\pi} \frac{\mathrm{d}\Psi}{\mathrm{d}f} \, , \tag{2.31}$$

where $\mathrm{d}N = \mathrm{d}\Psi/2\pi$, Ψ is the GW phase (or the contribution of a particular effect), and f_1, f_2 define the frequency range (usually the detector's low frequency cutoff and ISCO respectively). For a compact binary whose ISCO frequency falls within the detector's sensitivity band, the total number of cycles is given by

$$N_{\text{tot}} = \frac{(\pi M f_s)^{-5/3}}{32\pi\eta} \, . \tag{2.32}$$

However, this does not fully exploit one's knowledge of the importance of a phase modification at different frequencies, pertaining to the detector's noise spectrum. The natural way to incorporate this information is by performing the integration by using a different measure, weighted by the ratio of signal and noise amplitudes. Thus, we will also define the *number of useful cycles* as the integral

$$\mathcal{N}_{\text{use}} = \int_{f_1}^{f_2} \mathrm{d}f \, w(f) \frac{\mathrm{d}N}{\mathrm{d}f} \, , \quad w(f) = \frac{a^2(f)}{f^2 S_n(f)} \, , \tag{2.33}$$

where $a(f)$ is the "bare" amplitude in the frequency domain (without the $1/\sqrt{\dot{F}}$ factor). Occasionally, one only needs to estimate the effect that the *shape* of a noise curve has on the measurability of a certain waveform or effect, in which case one needs to quote the *normalized number of useful cycles*, introduced by Damour, Iyer and Sathyaprakash [139] as

$$N_{\text{use}} = \frac{\int_{f_1}^{f_2} \mathrm{d}f \, w(f) \frac{\mathrm{d}N}{\mathrm{d}f}}{\int_{f_1}^{f_2} \mathrm{d}f \, w(f)} \, . \tag{2.34}$$

2.4.2 Spin effects

So far we have considered particles with no intrinsic angular momentum. The inclusion of spins in the point-particle CBC waveforms introduces additional terms that affect the evolution of the system [224, 223, 182, 178, 183, 180,

262, 384, 344, 281, 166, 89, 90, 91], based on the theory of spinning particles in GR [287, 133, 61, 62]. The spins themselves are dynamical variables which also evolve and undergo *precession* via the differential equation

$$\frac{\mathrm{d}\vec{S}_A}{\mathrm{d}t} = \vec{\Omega}_A \times \vec{S}_A, \quad A = 1, 2 \quad , \tag{2.35}$$

where at 1.5PN we define

$$\vec{\Omega}_A = \omega_{\mathrm{orb}}^{5/3} \left[\frac{3}{4} + \frac{\eta}{2} + (-1)^A \frac{3}{4}\delta \right] \hat{L}_N + O\left(\frac{1}{c^4}\right), \tag{2.36}$$

and by $\hat{L}_N$ we denote the unit vector of the (instantaneous) orbital angular momentum. In turn, the orbital angular momentum also precesses in a way that compensates for the precession of the component spin vectors, and to leading order

$$\frac{\mathrm{d}\hat{L}_N}{\mathrm{d}t} = -\frac{v}{\eta} \frac{\mathrm{d}(\vec{S}_1 + \vec{S}_2)}{\mathrm{d}t}. \tag{2.37}$$

This effect causes the inclination angle ι to change throughout the inspiral which will be seen as an *amplitude modulation* in the polarizations of the signal. A characteristic illustration of this behaviour is given in Fig. 2.1, where we plot waveforms from i) a BBH system with zero spins (top) and ii) the same system where the two BHs have misaligned spins that induce precession (bottom). Finally, the orbital frequency evolution is modified by effects that come from:

- Spin-Orbit (S-O): The coupling of each spin with the orbital angular momentum, entering at 1.5PN, linear in spins and known up to 3.5PN [182, 384, 344, 281, 166, 90, 91, 256].

- S1-S2: The coupling between the two component spins, entering at 2PN, quadratic in spins [224, 223, 103].

- SSelf: The *self-interaction* coupling for each component spin, also entering at 2PN and quadratic in spins [180, 262].

With all the above effects taken into account, the conservative energy of Eq. (2.17) is modified by the *additional* S-O, S1S2 and SSelf terms,

$$\delta E_{\mathrm{SO}}(x) = -\frac{M\eta}{2}x \left[\left(\frac{14}{3}S_l + 2\delta\,\Sigma_l \right) x^{3/2} + \left(\frac{99 - 61\eta}{9}S_l + \frac{9 - 10\eta}{3}\delta\,\Sigma_l \right) x^{5/2} \right.$$
$$\left. + \left(\frac{405 - 1101\eta + 29\eta^2}{12}S_l + \frac{27 - 156\eta + 5\eta^2}{4}\delta\,\Sigma_l \right) x^{7/2} + O\left(\frac{1}{c^8}\right) \right], \tag{2.38}$$

$$\delta E_{\mathrm{S1S2}}(x) = -\frac{M\eta}{2}x\,\eta \left[\vec{\chi}_1 \cdot \vec{\chi}_2 - 3\left(\vec{\chi}_1 \cdot \hat{L}\right)\left(\vec{\chi}_2 \cdot \hat{L}\right) \right] x^2, \tag{2.39}$$

$$\delta E_{\mathrm{SSelf}}(x) = -\frac{M\eta}{2}x\frac{1}{4}\sum_{A=1,2} \left[1 - 2\eta + (-1)^A\delta \right] \left[\chi_A^2 - 3\left(\vec{\chi}_A \cdot \hat{L}\right)^2 \right] x^2, \tag{2.40}$$

the dissipative energy flux(2.18) is modified by the *additional* terms

$$
\delta\mathcal{F}_{\text{SO}} = \frac{32\,\eta^2}{5}x^5 \left\{ -\left[4S_l + \frac{5}{4}\delta\,\Sigma_l\right]x^{3/2} + \left[\frac{-81 + 544\,\eta}{18}S_l - \frac{13 - 172\,\eta}{16}\delta\Sigma_l\right]x^{5/2} \right.
$$
$$
- \left[16\pi S_l + \frac{31\pi}{6}\delta\,\Sigma_l\right]x^3 + \left[\left(\frac{476645}{6804} + \frac{6172}{189}\eta - \frac{2810}{27}\eta^2\right)S_l\right.
$$
$$
+ \left(\frac{9535}{336} + \frac{1849}{126}\eta - \frac{1501}{36}\eta^2\right)\delta\,\Sigma_l\right]x^{7/2} + \left[\left(-\frac{3485}{96} + \frac{13879}{72}\eta\right)\pi\,S_l\right.
$$
$$
\left. + \left(-\frac{7163}{672} + \frac{130583}{2016}\eta\right)\pi\,\delta\,\Sigma_l\right]x^{7/2} + O\left(\frac{1}{c^8}\right)\right\}, \qquad (2.41)
$$
$$
\delta\mathcal{F}_{\text{S1S2}}(x) = \frac{32\,\eta^2}{5}x^5\eta\left[-\frac{103}{24}\vec{\chi}_1\cdot\vec{\chi}_2 + \frac{289}{24}\left(\vec{\chi}_1\cdot\hat{L}\right)\left(\vec{\chi}_2\cdot\hat{L}\right)\right]x^2,
$$
$$
\delta\mathcal{F}_{\text{SSelf}}(x) = \frac{32\,\eta^2}{5}x^5\frac{x^2}{192}\sum_{A=1,2}\left[1 - 2\eta + (-1)^A\delta\right]\left[89\chi_A^2 + 287(\vec{\chi}_A\cdot\hat{L})\right], \quad (2.42)
$$

and finally, the expansions of the differential equations (2.19) and (2.20) for the orbital evolution will get modified accordingly. The spin quantities S_l and Σ_l are defined as

$$
S_l = \frac{1}{M^2}\left(\vec{S}_1 + \vec{S}_2\right)\cdot\hat{L}, \quad \Sigma_l = \frac{1}{M^2}\left(\frac{M}{m_2}\vec{S}_2 - \frac{M}{m_1}\vec{S}_1\right)\cdot\hat{L}, \qquad (2.43)
$$

and will need to be calculated at each step in the evolution, since they vary with time as the system precesses. The spin-orbit and spin-spin interactions will also affect the evolution of the orbital and total angular momentum vector and the spin vectors, by contributing to the differential equations (2.35), (2.37). The explicit expressions for the corresponding 2PN terms are given in [179]. Furthermore, an additional spin-related effect enters at 2PN, caused by a quadrupole moment of each component body, induced by its spin. This quadrupole is known for BHs [353], but varies for finite-sized stars, depending on the mass and the matter EoS. Thus it will be treated as a matter effect in Sec. 2.6.2.

SpinTaylorT4 For example, in the time domain we will use the TaylorT4 approximant, whose phase coefficients ξ_i of Eq. (2.25) take the additional spin

terms

$$\xi_3 \to \xi_3 - \frac{47}{3} S_l - \frac{25}{4} \delta \, \Sigma_l \,,$$

$$\xi_5 \to \xi_5 + \left(-\frac{5861}{144} + \frac{1001}{12} \eta \right) S_l + \left(-\frac{809}{84} + \frac{281}{8} \eta \right) \delta \, \Sigma_l \,,$$

$$\xi_6 \to \xi_6 - \frac{188}{3} \pi S_l - \frac{151}{6} \pi \delta \, \Sigma_l \,,$$

$$\xi_7 \to \xi_7 + \left(-\frac{4323559}{18144} + \frac{436705}{672} \eta - \frac{5575}{27} \eta^2 \right) S_l$$

$$+ \left(-\frac{1195759}{18144} + \frac{257023}{1008} \eta - \frac{2903}{32} \eta^2 \right) \delta \, \Sigma_l \,. \tag{2.44}$$

This generic spin extension of TaylorT4 is commonly referred to as *SpinTaylorT4*.

SpinTaylorF2 The same effects cannot be directly encoded into the SPA approximant TaylorF2, which we shall use in the frequency domain, due to the additional differential evolution equations (2.35) and (2.37). If however, one restricts to the aligned-spin case, there is no precession, since all cross products vanish. Thus, we are able to extend TaylorF2 in order to accommodate aligned spins and we find that the corresponding PN phase coefficients of Eq. (2.29) are modified by

$$\psi_3 \to \psi_3 + 4\beta_s \,, \quad \psi_4 \to \psi_4 - 10\sigma_s \,, \quad \psi_5 \to \psi_5 - \gamma_s \,, \tag{2.45}$$

$$\psi_5^{(l)} \to \psi_5^{(l)} - 3\gamma_s \,, \quad \psi_6 \to \psi_6 + \frac{\pi}{3} (3760 S_l + 1490 \delta \, \Sigma_l) \,,$$

$$\psi_7 \to \psi_7 - \left(\frac{8980424995}{762048} - \frac{6586595}{756} \eta + \frac{305}{36} \eta^2 \right) S_l$$

$$- (\frac{170978035}{48384} - \frac{2876425}{672} \eta - \frac{4735}{144} \eta^2) \delta \, \Sigma_l \,,$$

where we "overloaded" the notation with $\psi_k = \psi_k(m_1, m_2, \vec{S}_1, \vec{S}_2)$ to depend on both masses and spins. The spin-related coefficients $\beta_s, \sigma_s, \gamma_s$, are calculated as

$$\beta_s = \left(\frac{113}{12} - \frac{192268}{3} \eta \right) \vec{\chi}_s \cdot \vec{L}_N + \frac{113}{12} \delta \, \vec{\chi}_a \cdot \vec{L}_N \,, \tag{2.46}$$

$$\sigma_s = \eta \left\{ \frac{721}{48} \left[\left(\vec{\chi}_s \cdot \vec{L}_N \right)^2 - \left(\vec{\chi}_a \cdot \vec{L}_N \right)^2 \right] - \frac{247}{48} \left(\chi_s^2 - \chi_a^2 \right) \right\}$$

$$+ (1 - 2\eta) \left\{ \frac{719}{96} \left[\left(\vec{\chi}_s \cdot \vec{L}_N \right)^2 + \left(\vec{\chi}_a \cdot \vec{L}_N \right)^2 \right] - \frac{233}{96} \left(\chi_s^2 + \chi_a^2 \right) \right\}$$

$$+ \delta \left[\frac{719}{48} \left(\vec{\chi}_s \cdot \vec{L}_N \right) \left(\vec{\chi}_a \cdot \vec{L}_N \right) - \frac{233}{48} \vec{\chi}_s \cdot \vec{\chi}_a \right] \,, \tag{2.47}$$

$$\gamma_s = \left(\frac{681145}{2268} - \frac{138140}{567} \eta - \frac{260}{21} \eta^2 \right) \vec{\chi}_s \cdot \vec{L}_N + \left(\frac{681145}{2268} + \frac{3860}{63} \eta \right) \delta \, \vec{\chi}_a \cdot \vec{L}_N \,. \tag{2.48}$$
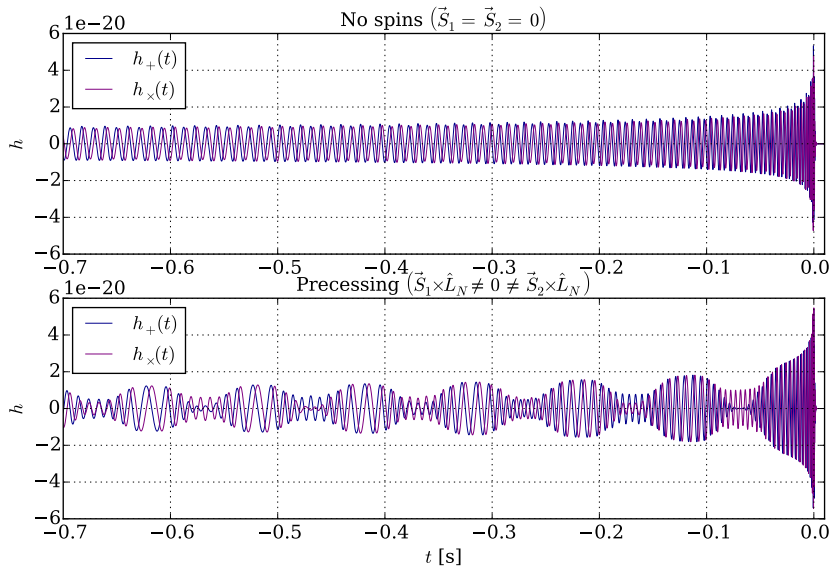
Figure 2.1: *Example of a time-domain inspiral waveform without (top) and with (bottom) amplitude modulation due to strong spin-induced precession.*

Note that the above expressions for TaylorF2 hold for (anti-)aligned spins only, where no precession takes place. Recently, there have been investigations on how to incorporate precession effects in frequency-domain waveforms and in particular a single-spin precessing version of TaylorF2 has been derived in closed form by Lundgren and O'Shaughnessy [250].

2.5   The Effective-One-Body formalism

In Newtonian gravity, the two-body problem admits a simple solution when re-expressed as the problem of a single mass (reduced mass) μ moving in an *effective potential* V_{eff}. In GR this is not directly applicable due to the complexity of the field equations. It is however reasonable to seek a solution in such a framework; in fact, during the last decade, this kind of *effective-one-body* (EOB) approach has shown to be rather successful in modeling the dynamics of binary evolution [115, 142, 143, 116, 392, 60, 57, 59, 146, 349, 284, 58], especially during the late inspiral towards and beyond the LSO, where perturbative PN approaches fail.

In the EOB framework [113], the binary evolution is mapped to the motion of a single body under the influence of an effective metric

$$g_{\mu\nu} = \text{diag}(-A(r), D(r)/A(r), r^2, r^2 \sin^2\theta)\,, \qquad (2.49)$$

41

(which to leading order agrees with a Schwarzschild metric), with an EOB Hamiltonian H^{real} on the phase space (r, ϕ, p_r, p_ϕ) based on the test particle action under the EOB metric

$$H^{\mathrm{real}}(r, p_r, p_\phi) = \mu \hat{H}^{real} = M \sqrt{1 + 2\eta \left(\frac{H^{\mathrm{eff}} - \mu}{\mu} \right)}, \qquad (2.50)$$

$$H^{\mathrm{eff}}(r, p_r, p_\phi) = \mu \hat{H}^{\mathrm{eff}} = \mu \sqrt{A(r) \left[1 + \frac{A(r)}{D(r)} p_r^2 + \frac{p_\phi^2}{r^2} + 2(4 - 3\eta)\eta \frac{p_r^4}{r^2} \right]}. \quad (2.51)$$

The *effective potentials* $A(r)$ and $D(r)$ defining the asymmetric-mass-ratio dependent deformations of the Schwarzschild metric are expanded in $1/r$ as $A_k(r) = \sum_{j=0}^{k+1} \frac{a_j(\eta)}{r^j}$ and $D_k(r) = \sum_{j=0}^{k+1} \frac{d_j(\eta)}{r^j}$; their expansion coefficients have been calculated up to 3.5PN. The equations of motion are given by Hamilton's equations

$$\frac{\mathrm{d}r}{\mathrm{d}\hat{t}} = \frac{\partial \hat{H}^{\mathrm{real}}}{\partial p_r} \quad , \qquad \frac{\mathrm{d}p_r}{\mathrm{d}\hat{t}} = -\frac{\partial \hat{H}^{\mathrm{real}}}{\partial r} ,$$

$$\frac{\mathrm{d}\phi}{\mathrm{d}\hat{t}} = \frac{\partial \hat{H}^{\mathrm{real}}}{\partial p_\phi} \quad , \qquad \frac{\mathrm{d}p_\phi}{\mathrm{d}\hat{t}} = -\frac{\partial \hat{H}^{\mathrm{real}}}{\partial \phi} = \hat{\mathcal{F}}_\phi , \qquad (2.52)$$

where $\hat{t} = t/M$ is the reduced (dimensionless) time. Higher order "pseudo"-PN terms in the potentials can be artificially introduced, by matching them with accurate numerical relativity simulated spacetimes. The gravitational waveform that is produced, and is reliable up to merger, is then smoothly attached to a appropriate ringdown signal that can be generated analytically based on the system's parameters.

The EOB framework is also convenient for studying finite-size effects and in particular effects of tidal deformations which we will elaborate on in Sec. 2.6.1.

2.6   Neutron Star Binaries and Matter Effects

2.6.1   Tidal deformations

Towards the end of the evolution of a BNS system, and as the two neutron stars get closer to each other, the tidal tensor of one star's gravitational field gets strong enough to induce a significant tidal deformation on the other. Vines *et al.* [369] have shown that, to leading order within an adiabatic approximation, where the tidal deformation instantaneously follows the gravitational field's tidal tensor,

$$Q_{ij} = -\lambda \mathcal{E}_{ij} , \qquad (2.53)$$

the effect on the gravitational waveform enters at 5PN in the phase. When calculated in the SPA (TaylorF2) the next-to-leading order, as shown in [368],

comes at a fractional 1PN order, that is at 6PN in the phase. Damour, Nagar and Villain [147], by using the effective-one-body (EOB) formalism [145, 144], calculated the tidal corrections up to a fractional 2.5PN order; in Eq. (2.56) we explicitly show the corresponding terms in the GW phase of TaylorF2, at 5PN, 6PN, 6.5PN, 7PN and 7.5PN order, as a function of the orbital velocity v.

The proportionality parameter λ in Eq. (2.53), known as the *tidal deformability parameter*, is a function of the NS mass, determined by the EoS, *i.e.* $\lambda_A = \lambda^{EOS}(m_A)$. More explicitly, λ can be expressed in terms of the second Love number k_2 and the NS radius R as $\lambda = (2/3)k_2 R^5$ [170, 199, 85]. With this in mind, one should point out that, even though in Eq. (2.56) tidal deformation appears as a high-order effect in the phase, its overall contribution is expected to be significant, due to the large pre-factor that is of the order $(R_i/m_i)^5$. The ratio R/m (*i.e.* the diameter measured in Schwarzschild radii) for a typical NS of $m = 1.4M_\odot$ and $R = 10$km is as high as ~ 4.8, which gives a factor of $\simeq 2.65 \times 10^3$ to the pre-factor of the tidal terms.

In the EOB approach of [147], the EOB Hamiltonian of Eq. (2.50), valid up to merger, is augmented with tidal corrections (*e.g.* for $l = 2$)

$$A_{tidal}^{(2)}(r) = -3\frac{3}{r^5}\sum_{A=1,2}\lambda_A\left(1 + \frac{\bar{\alpha}_1^{(2)}}{r} + \frac{\bar{\alpha}_2^{(2)}}{r^2} + \ldots\right), \qquad (2.54)$$

on the radial potential $A(r) = A^0(r) + A^{tidal}(r)$. Here $A^0(r)$ is a Padé-resummed quantity for the point-particle calculated in [145] and $\alpha_n^{A(l)}$ are polynomial functions of η or equivalently X_A. The new Hamiltonian is used in order to derive, in the adiabatic approximation, the tidal part of the orbital function $Q_\omega(\omega) = \omega^2/\dot{\omega}$, which may then be recast in a PN-expanded form (see Eq.(B1-B7) in [147]). Finally, the tidal contribution to the waveform $\Psi_{tidal}(f)$ is calculated in the stationary phase approximation

$$\frac{d^2\Psi_{tidal}(\omega)}{d\omega^2} = \frac{Q_\omega^{tidal}}{\omega^2} . \qquad (2.55)$$

The leading and next to leading order terms in the phase agree with [368], and together with the next three terms up to fractional 2.5PN order, the tidal part

of the SPA phase reads

$$
\begin{aligned}
\Psi_{tidal}^{2.5PN}(v) = &+\frac{3}{128\,\eta}\left(\frac{v}{c}\right)^{-5}\sum_{A=1,2}\frac{\lambda_A}{M^5 X_A}\left[-24\left(12-11X_A\right)\left(\frac{v}{c}\right)^{10}\right.\\
&-\frac{5}{28}\left(3179-919X_A-2286X_A^2+260X_A^3\right)\left(\frac{v}{c}\right)^{12}\\
&+24\,\pi\left(12-11X_A\right)\left(\frac{v}{c}\right)^{13}-24\left(\frac{39927845}{508032}-\frac{480043345}{9144576}X_A\right.\\
&\left.+\frac{9860575}{127008}X_A^2-\frac{421821905}{2286144}X_A^3+\frac{4359700}{35721}X_A^4-\frac{10578445}{285768}X_A^5\right)\left(\frac{v}{c}\right)^{14}\\
&\left.+\frac{\pi}{28}\left(27719-22127X_A+7022X_A^2-10232X_A^3\right)\left(\frac{v}{c}\right)^{15}\right],
\end{aligned}\tag{2.56}
$$

where $X_A = m_A/M$. At this point, we should point out that the above calculations ignore i) contributions from higher order multipoles as these are estimated to give small corrections (see discussion in Appendix A2 of [147]) and ii) a number of yet uncalculated functions, β_2^{22}, β_1^{21}, β_1^{31}, β_1^{33} that appear in the 7PN phase term (fractional 2PN order in Q_ω^{tidal}). In the majority of recent studies, only the 5PN and 6PN tidal terms were taken into account. The overall contribution of the three new higher-order corrections to the phase is of opposite sign with respect to the two leading terms and will thus slightly weaken the effect of tidal deformations on the waveform. However, in the presence of the full 7PN term which is so far unknown, this may no longer be the case.

2.6.2   Spin-induced quadrupoles

Another finite-size effect that takes place during the inspiral is the contribution of the spin-induced mass quadrupole moments of each NS to the GW emission and binary evolution. If a NS is spinning, its equilibrium is achieved under an oblate matter distribution, rather than a spherical one. Assuming an axisymmetric mass distribution with respect to the axis of rotation, the deformation can be expressed to leading order by means of a dimensionless quadrupole moment parameter q,[6] defined in the context of GR as [232]

$$
q = -\frac{5}{2}\lim_{r\to\infty}\left(\frac{r}{M}\right)^3\int_{-1}^{1}\nu(r,\theta)P_2(\cos\theta)\mathrm{d}\cos\theta,\tag{2.57}
$$

where $P_2(x) = (3x^2-1)/2$ is the second Legendre polynomial, and ν is a potential related to the metric of a stationary axially symmetric body; more specifically, the line element in the form introduced by Komatsu-Eriguchi-Hachisu [230] reads

$$
\mathrm{d}s^2 = -e^{-2\nu}\mathrm{d}t^2 + r^2\sin^2\theta\,e^{2\beta}\left(\mathrm{d}\phi-\omega\mathrm{d}t\right)^2 + e^{2\alpha}\left(\mathrm{d}r^2+r^2\mathrm{d}\theta^2\right),\tag{2.58}
$$

---

[6]Not to be confused with the asymmetric mass ratio.

where the undetermined α, β, ν are all functions of (r, θ). The quadrupole moment q is the leading-order $(1/r^3)$ coefficient of the second multipole in the asymptotic expansion of $\nu(r, \theta)$ and can be calculated numerically. This quantity is the general-relativistic equivalent of the Newtonian mass quadrupole moment.

Since a stiffer EoS implies a larger NS radius for a given mass, the quadrupole moment increases in absolute value with the stiffness of the EoS. Examples of q estimates for different EOS were calculated numerically in [232] based on the expressions of Ryan [320, 321]. These demonstrated the dependence on the dimensionless spin χ, which for a fixed NS mass can be fit very well up to the maximum spin value $\chi_{\max} \simeq 0.65$ (also dependent on the EOS) by a quadratic rule

$$q \simeq -a\chi^2 \,, \tag{2.59}$$

where $a = a_{EOS}(m)$ is a mass-dependent parameter. The corresponding behaviour in the limiting case of a spinning black hole is shown to be exactly $a_{BH} = 1$ [353]. Further evidence to support the quadratic relation (2.59) is given in [289, 288]. The authors of [289, 172] also point out a spin correction in the identification of multipole moments that was previously overlooked; this correction preserves the quadratic spin behaviour of Eq. (2.59), and vanishes in the slow-rotation limit. Assuming that this relation will hold for any EOS, we will only be concerned with the spin-independent parameter a which, similarly to the tidal deformability parameter λ, has a functional dependence on the neutron mass that is determined by the EOS. More details will follow in Chapter 11.

The effect of such a quadrupole moment on the gravitational waveform emitted by a binary system was analytically derived in [294]. To Newtonian order, this introduces an additional coupling in the effective gravitational potential, between the mass quadrupole of each spinning NS and the mass of its companion, leading to a modification of the energy flux

$$\dot{E}_{QM} = \frac{32}{5}\eta^2 v^{14} \sum_{A=1,2} p_A \left[3\left(\hat{S}_A \cdot \hat{J}\right) - 1 \right] \,, \tag{2.60}$$

where, following the standard notation, we introduced the variables

$$p_A = \frac{q_A m_A^2}{M^2} \,. \tag{2.61}$$

In particular, if we only consider NS with spin aligned with the orbital angular momentum, we obtain $\hat{S}_A \cdot \hat{J} = 1$, and

$$\dot{f} = \frac{96\eta}{5\pi M^2} v^{11} \left[\cdots - \frac{5}{2} v^4 \sum_{A=1,2} p_A \left(3\left(\hat{S}_A \cdot \hat{J}\right)^2 - 1 \right) \right] \,, \tag{2.62}$$

in which case, the phase evolution of the binary (denoted by the dots) will be modified by an additional term. We define the *quadrupole-monopole* (QM) related

45

2PN parameter σ_{QM} as

$$\sigma_{QM} = -\frac{5}{2} \sum_{A=1,2} p_A \left[3 \left(\hat{S}_A \cdot \hat{J} \right)^2 - 1 \right] . \tag{2.63}$$

In the SPA waveform TaylorF2, the additional contribution to the GW phase due to the QM interaction reads

$$\Psi_{QM}(v) = -\frac{30}{128\eta} \sigma_{QM} \left(\frac{v}{c} \right)^{-1} . \tag{2.64}$$

Overall, the QM effect has the potential to introduce a few additional cycles to the GW phase in the very early part of the inspiral (where the detector sensitivity is relatively low), but only in the case of fast-spinning NSs characterized by a stiff EoS. Typically, the number of *useful cycles* introduced by the QM term will be negligible and therefore for much of the analysis that follows in Part II, this EoS-dependent correction will not be taken into account.

2.6.3 Magnetic effects

Decades of observations of neutron stars in the electromagnetic (EM) spectrum have shown that NSs often exhibit strong EM activity, most prominently in their outer layers, which is what makes them visible to us as *pulsars*. Especially during the early stages after their birth, the surface of newborn NSs hosts powerful magnetic fields, whose strength can reach up to 10^{15} G; these highly active NSs are also known as *magnetars*.

Huge amounts of energy may be stored in the form of an EM field around a NS and therefore it makes sense to pose the following questions: Are the EM properties of each NS important parameters of the two-body problem? What effect may the EM interaction between the two components of the binary have on the orbital evolution, the emitted GW and the final product of the merger? These questions have been the subject of a number of studies (both analytical and numerical in nature), but for the purposes of the current dissertation it is sufficient to quote the analytical leading-order result in the PN approximation of the GW emission, originating from [206].

Treating each NS as a magnetic dipole is a realistic approximation to the morphology of the fields away from the NS surface. Similar to the QM effect of Sec. 2.6.2, the interaction between the magnetic dipoles of the two NSs, denoted by $\vec{d}_A$, $A = 1, 2$ introduces a 2PN term in the GW phase evolution

$$\Psi_{\mathrm{DD}}(v) = -\frac{30}{128\eta} \sigma_{\mathrm{DD}} \left(\frac{v}{c} \right)^{-1} , \tag{2.65}$$

which is proportional to d_1 and d_2

$$\sigma_{\mathrm{DD}} = -\frac{5}{\eta\mu^4} d_1 d_2 \left[3 \left(\hat{L} \cdot \hat{d}_1 \right) \left(\hat{L} \cdot \hat{d}_2 \right) - \hat{d}_1 \cdot \hat{d}_2 \right] . \tag{2.66}$$

The last factor depends on the relative orientation of the two magnetic dipoles (see [362] for the detailed calculation). It is now easy to show that the effect can only contribute a phase difference in the order of a GW cycle only when the magnetic fields take values in the order of 10^{16}G. Although not theoretically impossible, in practice one does not expect newly born NSs with so strong magnetic fields to be taking part in binary NS coalescence. We thus consider EM interaction effects to be negligible in practically all BNS sources.

2.7 Numerical Relativity

In this chapter we introduced and presented a series of results in the analytical post-Newtonian approximation of the two-body problem in GR. These results came about after decades of tedious work by some of the brightest relativists of our time. *Numerical relativity* (NR) comprises a completely different approach to the problem, by means of numerical evolution of the spacetime geometry under the Einstein equations of GR. The evolution of spacetime in general relativity can be formulated as an initial-value problem in a "$3+1$" decomposition of GR, as was first done by Arnowitt, Deser and Misner [47] (in what is known as the ADM formalism), whereby one defines the metric and extrinsic curvature on an initial spacelike slice (Cauchy hypersurface) and then lets the geometry evolve in a timelike direction, as dictated by the full Einstein equations. This process can be cast in a discretized form and applied to a 4-dimensional grid of spacetime points so that the Einstein equations can be solved numerically on a computer, to a precision that is in principle only restricted by our computational resources.

Numerical relativity is an entire field in its own right, which has seen radical development in the last decade [63, 37, 333]. The critical milestone that exploded the field was the first simulation in which Pretorius [302] successfully evolved a circular BBH system for a few orbital cycles. Since then, various numerical methods were developed in order to make the process faster, more stable and more accurate.

The main advantage of NR simulations is the fact that the full Einstein equations are solved, without being truncated to any finite order. This provides an ideal setting to test the predictions of the PN theory against gravitational waveforms that are generated by NR simulations. Indeed, for the regime where PN theory is expected to be reliable, namely the binary *inspiral* up to a few cycles before merger (beyond which the different PN approximants even disagree with each other), an excellent agreement with NR waveforms has been verified. Apart from the verification of PN results, NR allows us to explore territory that was previously unaccessible by perturbative methods, most notoriously, binary evolution close to and during the *merger* of the binary. Finally, NR simulations of CBC systems in the final *ringdown* stage are in good agreement with the predictions of black-hole perturbation theory [352, 301, 242].

There is however a major cost to this approach: numerical evolution of a dynamical $(3+1)$-dimensional spacetime is a technically challenging computational task. It requires a combination of advanced numerical methods and cutting-edge hardware technology, in order to produce a single waveform within a reasonable amount of time (currently in the order of weeks when running on a modern supercomputer). But even though NR cannot be used directly for the analysis of GW signals due to computational constraints, the information contained in the set of available NR waveforms has been incorporated in hybrid waveform models, where it fine-tunes and complements the analytical formulas of PN theory and EOB models. As soon as the intrinsic parameter space of compact binaries is populated sufficiently densely by NR-generated gravitational waveforms, one may then obtain waveform families that are both close to the accurate NR waveforms (thus arguably close to the true GR solution), and at the same time as fast to generate as PN waveforms. This is an ongoing effort, especially in the regime of spinning BBH systems, for which the merger and ringdown fall within the sensitive band of AdVirgo/aLIGO. In the case of NS binaries, NR simulations have also given us a more accurate picture of how NS matter (given a pre-defined EoS) behaves in a finite-size two-body setting, where tidal fields may deform or even disrupt the two bodies, and where the interaction of strong magnetic fields may lead to rich EM radiation output. Since the primary focus of this dissertation is on BNS systems, and since no assumption can be made on the EoS of NS matter, NR-tuned hybrid waveform models will not be employed throughout most of the exploratory studies presented here.

Chapter 3

Data Analysis Methods

> *Science is not about what's true. It's about what people with originally diverse viewpoints can be forced to believe by way of public evidence.*
>
> Lee Smolin

The biggest challenge in experimental gravitational wave physics is reaching a sensitivity that is high enough for detecting a GW signal. The second generation ground-based GW interferometers are expected to reach those levels of sensitivity within the next few years. Even so, the amplitude of even the loudest events is expected to be much smaller than the amplitude of the noise. Gravitational wave data analysis is an interesting case of signal processing where the signal of interest is weak compared to the noise. However, since the data are in the form of a time sequence $d(t)$, the presence of a signal that lasts sufficiently long will statistically manifest itself as a deviation from pure-noise behaviour. Furthermore, assuming that both the signal space and the noise spectrum are well modeled, one can make use of sophisticated statistical data analysis methods, in order to extract as much information out of the data as possible.

3.1 Introduction to Gravitational Wave Data A-nalysis

The data output of a detector is represented as a time series $d(t)$, which can be decomposed into a random noise part $n(t)$ with the characteristic properties defined in Sec. 1.6, plus a potential GW signal $h(t)$, that comes from applying the transfer function of the instrument onto the GW strain. Since the properties of the noise as a stochastic process are better defined in frequency space, we prefer to work with the Fourier transformed data and by using that the FT is a linear

operation, we can write

$$\tilde{d}(f) = \tilde{n}(f) + \tilde{h}(f) \,. \tag{3.1}$$

Given a known noise PSD $S_n(f)$, the *noise frequency series* $\tilde{n}$ can be treated as a random variable with the underlying distribution for each f (or for each frequency bin f_i in the discrete case) modeled as a Gaussian distribution with standard deviation $\sigma_f^2 = \frac{1}{2}S_n(f)$,

$$p(\tilde{n}(f)) = \mathcal{N}(0, \sigma_f) = \frac{1}{\sqrt{\pi S_n(f)}} e^{-\frac{|\tilde{n}(f)|^2}{S_n(f)}} \,. \tag{3.2}$$

To determine the apparent strength of a signal, also taking into account the noise PSD, a norm can be constructed, where the signal amplitude scaled by the PSD is integrated across the frequency space. This is equivalent to defining (the real part of) an *inner product* $(\cdot|\cdot)$ in the space of signals; for two (time series) signals a and b with FTs $\tilde{a}$ and $\tilde{b}$ their inner product is defined as

$$(a|b) \equiv \Re \left\{ \int_{-\infty}^{\infty} \mathrm{d}f \frac{\tilde{a}^*(f)\tilde{b}(f)}{\frac{1}{2}S_n(f)} \right\} \,. \tag{3.3}$$

Matched filtering   One of the most commonly used techniques in signal processing to dig out a weak signal buried in noise, is by correlating a model signal or *template* against the data. When the form of the signal is more or less known one can optimize the signal analysis process by constructing what is known as a *Wiener filter*. A functional of the data $\hat{d} = \int_{-\infty}^{\infty} \mathrm{d}t d(t)K(t)$ can be constructed by choosing a trial *filter* K to be the kernel. Then, the *signal-to-noise ratio* (SNR) ρ_K for that filter K is defined as

$$\rho_K = \frac{S}{N} \equiv \frac{\langle \hat{d} \rangle}{\sqrt{\langle \hat{d}^2 \rangle - \langle \hat{d} \rangle^2}} = \frac{\int_{-\infty}^{\infty} \mathrm{d}f \, \tilde{d}(f)\tilde{K}^*(f)}{\sqrt{\int_{-\infty}^{\infty} \mathrm{d}f \, \frac{1}{2}S_n(f)\tilde{K}(f)\tilde{K}^*(f)}} = (d|\hat{K}) \,, \tag{3.4}$$

where $\hat{K}$ is the filter given by $\bar{K}(f) = \frac{1}{2}S_n(f)\tilde{K}(f)$, normalized with respect to the inner product. In the penultimate equation, we used Parseval's theorem and the stochastic properties of n discussed in Sec. 1.6. Thus, if one wants to maximize the SNR, then one finds that, up to a normalizing constant, this is done by the filter $\tilde{K}(f) = \frac{\tilde{h}(f)}{S_n(f)}$. Now, given that the CBC parameter space is at least 9-dimensional, the form of the signal is highly uncertain, so one needs to use many trial waveforms and look for the one that yields the highest SNR; this defines a filter space $\tilde{K}(\vec{\theta}) = \frac{\tilde{h}(f;\vec{\theta})}{S_n(f)}$ related to a parametrized template family

$h(t; \vec{\theta})$ and also defines the *optimal SNR* [1]

$$\rho_{\text{opt}} = \max_{\vec{\theta}} \frac{\left(d | K(\vec{\theta})\right)}{\sqrt{\left(K(\vec{\theta}) | K(\vec{\theta})\right)}} \, . \tag{3.5}$$

Naturally, if the real signal is exactly described by one of the members of the template family $h(t; \vec{\theta})$, for some of its parameters $\vec{\theta}_0$, then it can be shown that the filter given by normalizing $\frac{\tilde{h}(f; \vec{\theta}_0)}{S_n(f)}$ yields the optimal filter. By using such filtering methods, when the noise colouring and signal form are known, one can recover signals that are orders of magnitude weaker than the noise.

3.2 Bayesian Inference

When interpreting the output of a set of experiments like Virgo and LIGO into quantitative scientific results, performing a thorough statistical treatment of the data is of the utmost importance. Two main schools of statistical inference are commonly encountered in modern science: the *orthodox* or *frequentist* paradigm and the *Bayesian* paradigm. The former gives simple rules for getting error-analysis and confidence-level type of results, while the latter is in principle a more fundamental and philosophically profound one, that answers precise probabilistic questions with precise probabilistic statements, but may often entail significant technical difficulties. Nevertheless, Bayesian inference has been gaining much ground in many branches of science, especially with the development of numerical algorithms and the proliferation of computational resources designated for scientific purposes. Some excellent textbooks where the interested reader can find a more detailed introduction to probability theory and statistical inference are [149, 216, 218, 136, 252, 335]; a more advanced reader will enjoy [212, 137, 196, 228, 104, 109, 336].

A *probability space* for a random experiment is defined as a triple $(\Omega, \mathcal{F}, P)$, where

- Ω is the *sample space*, defined as the space of all possible outcomes;

- $\mathcal{F}$ is the space of *eventualities*, which has the structure of a σ-algebra[2] on the sample space Ω;

- P is a *probability measure* on the σ-algebra $\mathcal{F}$: a measure that satisfies (i) $P(A) \in [0, 1]$, $\forall A \in \mathcal{F}$, with $P(\Omega) = 1$ and $P(\emptyset) = 0$, and (ii) additivity for countable unions $P(\bigcup_i A_i) = \sum_i P(A_i)$.

---

[1]It should be noted that for a network of detectors the combined SNR ρ_{net} can be calculated from the individual detectors' SNRs added in quadrature.

[2]A σ-algebra can be roughly understood as a set of subsets of a given set X, that includes X itself. The σ-algebra must be closed under the operations of complementation $X \backslash A$ and countable unions $A_1 \cup A_2 \cup \ldots$ defined on X.

Bayes' theorem   Bayes' theorem is one of the simplest, yet most powerful laws of probability theory, whose importance becomes evident when interpreted in the context of statistical inference. Given a *probability space* $(\Omega, \mathcal{F}, P)$ and two eventualities $A, B \in \mathcal{F}$ we may re-express the joint probability $P(A, B)$, which is symmetric in A and B, in two ways:

$$P(A, B) = P(A|B)\, P(B) = P(B|A)\, P(A), \tag{3.6}$$

where $P(A|B)$ denotes the *conditional probability* of A, given that B is true. The last equality is Bayes' theorem, which can be recast in its most common form as

$$P(A|B) = \frac{P(B|A)\, P(A)}{P(B)}. \tag{3.7}$$

Data analysis interpretation   In data analysis we want to perform statistical inference on quantities and hypotheses, given a set d of measured data. In other words, we wish to derive explicit probabilities (for discrete random variables or hypotheses) and probability density functions (for continuous random variables). The entire analysis is based on certain assumptions or *background information* that we shall collectively denote by $\mathcal{I}$, which is always a given. For instance, a simple inference problem would be to determine the probability of an eventuality A being true, in the light of some measured data d; this is expressed by the quantity $P(A|d, \mathcal{I})$. Now, it often is the case that one can calculate the probability of obtaining a set of data, assuming that A is true; this is expressed by the quantity $P(d|A, \mathcal{I})$, which we will refer to as the *likelihood* of the data d given A. When A is left undetermined, *e.g.* when it takes the form of a continuous parameter, one may speak of the *likelihood function* of the data d. By applying Bayes' theorem (3.7), one obtains

$$P(A|d, \mathcal{I}) = \frac{P(d|A, \mathcal{I})\, P(A|\mathcal{I})}{P(d|\mathcal{I})}, \tag{3.8}$$

which contains the likelihood $P(d|A, \mathcal{I})$, the *prior probability* $P(A|\mathcal{I})$ of A, and $P(d|\mathcal{I})$. The prior probability of A can be directly interpreted as the probability that we had assigned to A before the data d were observed. The quantity $P(d|\mathcal{I})$ is a likelihood of the data irrespective of any assumptions other than $\mathcal{I}$; here, it can be seen as a normalization constant, but we shall return to this soon. This particular form of Eq. (3.7) is often referred to as *Bayes' rule*.

Bayesian inference in GW data analysis   We can now particularize the general Bayesian inference problem to the specifics of GW data analysis. The data will simply be a detector output like the one described by Eq. (3.1) and the eventuality A will take the form of either a hypothesis H or a continuous parameter $\vec{\theta}$. When treating discrete random variables or hypotheses we shall denote the probability by using capital 'P', whereas for the probability densities of continuous random variables we shall use lowercase 'p'.

An important quantity that we can explicitly define is the *likelihood* for some data $d(t)$ that we observed as the output of a detector with a known PSD. We start with the following building block: For an arbitrary frequency bin f_i, the observed value of the data $d(f_i)$, assuming pure noise (no GW signal), is an *independent identically distributed random variable* (i.i.d.) and its likelihood is given according to Eq. (3.2)

$$p(d(f_i)|H_{\text{noise}}, \mathcal{I}) = \frac{1}{\sqrt{\pi S_n(f)}} e^{-\frac{|\tilde{d}(f)|^2}{S_n(f)}} . \qquad (3.9)$$

This extends to defining the likelihood of an arbitrary noise realization $n(t)$ as

$$p(d|H_{\text{noise}}, \mathcal{I}) = \mathcal{N} \exp\left[-\int_{-\infty}^{\infty} df \frac{|\tilde{d}(f)|^2}{S_n(f)}\right] = \mathcal{N} e^{-\frac{(d|d)}{2}} , \qquad (3.10)$$

where $\mathcal{N}$ is a normalization constant and in the last step we have made use of the inner product given in Eq. (3.3).

This is readily extended to more general cases that do not assume pure noise. For instance, under the assumption H_h that a particular waveform $h(t)$ is present in the data as a signal, we can define the likelihood $P(d|H_h, \mathcal{I})$. By observing that the time series $d(t) - h(t)$ by Eq. (3.1) is a realization of pure noise under the current assumption, we find

$$p(d|H_h, \mathcal{I}) = p(d - h|H_{\text{noise}}, \mathcal{I}) = \mathcal{N} e^{-\frac{(d-h|d-h)}{2}} . \qquad (3.11)$$

More generally, if we do not know the exact parameters of the source but we do assume *e.g.* the presence of a CBC signal in the data, then we define the *likelihood function* of d on the CBC parameter space Σ_{CBC} as

$$L(d; \vec{\theta}) \equiv p(d|\vec{\theta}, \mathcal{I}) = p(d - h_{\vec{\theta}}|H_{\text{noise}}, \mathcal{I}) = \mathcal{N} \exp\left[-\int_{-\infty}^{\infty} df \frac{|\tilde{d}(f) - \tilde{h}(f; \vec{\theta})|^2}{S_n(f)}\right] . \qquad (3.12)$$

An interesting optimization problem that immediately arises is whether one can get a *maximum likelihood estimator*, that is, whether one can implement an algorithm that finds the parameter vector $\vec{\theta}_{\text{maxL}}$ that maximizes $L(d; \vec{\theta})$ for the given data. Better yet, one should be able to obtain the entire *posterior* probability distribution function on Σ_{CBC}, that incorporates the new information encoded in the data. Additionally, one can also calculate the *evidence* for the H_{CBC} hypothesis by marginalizing the likelihood function over the entire parameter space

$$p(d|H_{\text{CBC}}, \mathcal{I}) = \int_{\Sigma_{\text{CBC}}} d\vec{\theta} \, \pi(\vec{\theta}) \, L(d; \vec{\theta}), \quad \vec{\theta} \in \Sigma_{\text{CBC}} , \qquad (3.13)$$

where we denote the *prior probability density function* by $\pi(\vec{\theta}) = p(\vec{\theta}|\mathcal{I})$. The importance of knowing the evidence in any problem of Bayesian inference, is stressed in [337].

In the simulations results we will present in the following chapters, we will try to *recover* a CBC signal that is simulated and artificially added into detector noise. The numerical algorithms described in Sec. 3.3 will be used in order to sample the parameter space Σ_{CBC} and obtain the Likelihood function, evidence and posterior p.d.f., by using the models described in Sec. 2.4 as template waveforms.

3.3 Numerical algorithms

3.3.1 Monte Carlo sampling

Bayesian analysis is performed numerically by dedicated algorithms that attempt to explore the (high-dimensional) parameter space as efficiently as possible. Monte Carlo methods are designed to do exactly that. The requisites for our analysis are: (i) a sampling method for exploring the parameter space, (ii) a way to extract the posterior p.d.f., (iii) a way of calculating the integral of the likelihood over the parameter space to get the evidence.

There are many different random walk methods for sampling from a target probability distribution. The one that we will be using, known as *Markov Chain Monte Carlo* (MCMC) is based on the construction of a Markov chain whose *equilibrium distribution* is the target distribution. A Markov chain is a stochastic process $X_t : t \in \mathbb{N}$ described by a state space S, a transition function $T : S \times S \to [0, 1]$ and the property that its random variables satisfy the Markov property, *i.e.* the transition probability to a new state only depends on the current state, or more formally

$$P(X_{n+1} = x | X_1 = x_1, \dots, X_n = x_n) = P(X_{n+1} = x | X_n = x_n),\qquad (3.14)$$

for any allowed chain up to n. This means that the stochastic process has no memory; furthermore, we will assume time-homogeneity, that is, the transition probabilities do not change with time. Such processes admit a measure (or probability distribution) π that is invariant under the action of the transition function[3]; this is called the equilibrium distribution and is the one to which any chain will converge. In our case, the state space $S = \Sigma$ is (a discretized version of) the parameter space to be sampled, and the equilibrium distribution will by construction be the prior p.d.f. The process also needs to be *ergodic*, meaning that any state can be accessible from any other state within a finite number of steps.

After a few MCMC steps, the chain samples the prior correctly, which does not sound very interesting at this point; its usefulness will become clear in the following section. A clever way of making use of a MCMC will allow us to retrieve

---

[3]The continuous version of this statement is invariance under the transition *kernel*

$$\int_S \mathrm{d}x_n \, T(x_n; x_{n+1}) \, \pi(X_n = x_n) = \pi(X_{n+1} = x_{n+1}) \,. \qquad (3.15)$$

the posterior p.d.f. Finally, the calculation of the evidence is the less trivial of tasks, especially in high-dimensional spaces where standard integration methods cannot sample densely enough; to this end we shall focus on a particular algorithm called nested sampling.

3.3.2 Nested Sampling

Description Among the many sampling algorithms that currently exist, we choose to work with a relatively recent one, developed by J. Skilling in 2006, under the name *nested sampling* [337]. The reason behind this preference is that nested sampling manages to produce both the posterior p.d.f. $p(\vec{\theta}|d, \mathcal{I})$ *and* the evidence $Z = p(d|\mathcal{I})$ in one go. The main idea is the following: The algorithm starts by sprinkling a set of N_{live} initial points, sampled from the given prior p.d.f. on Σ.

Then, step by step, the point of the lowest likelihood is replaced by a new point, sampled from the prior by a MCMC, that is however required to yield a higher likelihood value than the original point. This way, the set of *live points* gradually climbs up the likelihood function in the parameter space as shown schematically in Fig. 3.1. At the same time, the MCMC is restricted to sample only an ever shrinking part of the prior volume, where the likelihood is larger than a certain value.
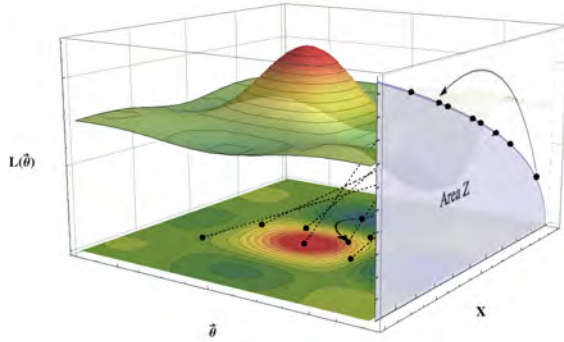
Figure 3.1: *Mapping the likelihood function $L(\vec{\theta})$ (z-axis) on the parameter space (x-y plane) to the prior mass X (side plot). The lowest L point is updated to a new sample (arrow).*

An intuitive way to formalize this is by defining the *prior mass X* as

$$X(\bar{L}) = \int_{\Sigma_{\bar{L}}} \pi(\theta) \, \mathrm{d}\theta \quad , \qquad \Sigma_{\bar{L}} = \{\theta \in \Sigma : L(\theta) > \bar{L}\}, \qquad (3.16)$$

as a function of the likelihood; this represents the prior volume of the region whose likelihood is greater than $\bar{L}$. It will always be the case that $X(\bar{L} = L_{min}) = 1$ and $X(\bar{L}_{\max}) = 0$ and that the function is monotonic, as shown in the side plot of Fig. 3.1. Now, $\mathrm{d}X$ represents the prior volume of an infinitesimal shell of likelihood $\bar{L} \leq L < \bar{L} + \delta L$ and gives us a 1-dimensional integral for the evidence,

$$Z = \int_0^1 \tilde{L}(X) \, \mathrm{d}X \,, \qquad (3.17)$$

where $\tilde{L}$ is the inverse of the monotonic function $X(\bar{L})$

$$\tilde{L}(X(\bar{L})) = \bar{L}\,. \tag{3.18}$$

To get the integral (3.17) numerically (since we do not know a priori what is $X(\bar{L})$ or its inverse), all we need to do is find a way to sample from the prior mass and calculate the area under the $\tilde{L}(X)$ curve. Typically, the bulk of the posterior mass $dP(\vec{\theta}) = p(\vec{\theta}|\mathcal{I})\,d\vec{\theta}$ that dominates the evidence lies within a narrow region, whose size e^{-H} as a fraction of the prior volume defines the *information* H of the data as

$$H = \int \log\left(\frac{dP}{dX}\right) dP\,. \tag{3.19}$$

In practice, due to the highly peaked posterior, it is more convenient to sample in $\log X$.

Prior mass estimate In general, the form of the likelihood function can be complex, especially in high-dimensional spaces, with many local extrema and features in different scales. Thus, it is difficult to assign a prior mass to a given likelihood value and vice versa; however, this can be done statistically. Sampling the prior mass can be understood as asking the question "What fraction of prior volume has likelihood larger than some $\bar{L}$?"; this can be statistically determined by sampling the prior $\pi(\vec{\theta})$. The sampling is done by running the MCMC with the restriction $L > \bar{L}$. We need to do this for many different values of $\bar{L}$ that reach as close as possible to the peak $L_{\max}$. This is done by gradually increasing the $\bar{L}$ threshold as the algorithm progresses.

When drawing N samples $\vec{\theta}_i$, $i = 1,\dots,N$ uniform in the prior and therefore in X, the probability density of the highest $X_i = X(L(\vec{\theta}_i))$ being equal to X^* is

$$p\left(\max_{i=1,\dots,N} X_i = X^*\right) = \frac{\partial(X^{*N})}{\partial X^*} = N\,X^{*\,N-1}\,, \quad X^* \in [0,1]\,. \tag{3.20}$$

Thus, at each evolution step, the prior mass statistically shrinks by a factor t following $t \sim N_{\mathrm{live}}\,t^{N_{\mathrm{live}}-1}$, which we call the *shrinkage ratio*. To have a better control over the statistical variance of the shrinking ratio, we can *e.g.* sample this process 100 times at each step.

Implementation Here we give an explicit description of the nested sampling algorithm in pseudo-code. The main body is a loop indexed by i, during which a set of N_{live} objects, indexed by k, moves around the parameter space.

Initialization: We start with an initial set of N_{live} points $\theta_1,\dots,\theta_{N_{\mathrm{live}}}$ sampled from the prior. We initialize $i = 0$, $Z = 0$, $X_0 = 1$ and $H = 0$.

Evolution: While the termination condition is not met, we increment
    i++ and:
    -record the parameter vector $\vec{\Theta}_i = \vec{\theta}_{k_i}$ of the point k_i with the
    lowest likelihood value L_i
    -sample the shrinking ratio and estimate X_i
    -estimate prior mass in the likelihood shell around L_i with
    trapezoidal rule $w_i = (X_{i-1} - X_{i+1})/2$
    -increment the evidence by $\mathrm{d}Z = L_i w_i$ and the information by
    $\mathrm{d}H = \log(L)Lw_i$
    -run MCMC to sample the prior $\pi(\vec{\theta})$ restricted by $L(\vec{\theta}) > L_i$ and
    move the k_i point to the new location

Termination: Once our chosen termination condition is met, we stop
    the evolution of the chain and increment the estimated
    evidence by the residual $\mathrm{d}Z = \sum_{k=1}^{N_{\text{live}}} L(\vec{\theta}_k) X_i / N_{\text{live}}$.

We can chose the termination condition to be *e.g.* the completion of a fixed
number of steps (when the required number is more or less known and pre-defined
runtime is preferred), the evidence increment $\mathrm{d}Z$ from each step contributing less
than an absolute or relative amount to the total Z, a combination of the above
or other. The last $\mathrm{d}Z$ increment at termination adds the evidence corresponding
to the live points at the time of termination. Here we will use a threshold on this
$\mathrm{d}Z$ estimate as a termination condition, *i.e.* once the additional evidence of the
current live points gets lower than a certain value, the code will terminate.

Getting the evidence The evidence is being calculated at every step during
the evolution and its calculation concludes with the residual increment upon
termination, as described above.

Getting the posterior An additional by-product of nested sampling is the
possibility of producing a sampling of the posterior p.d.f. We have already stored
the *chain* $\vec{\Theta}_i$, $i = 1, \ldots, n$, that is however not sampled uniformly in the posterior
but rather from a fraction of the prior with $X_i \simeq e^{-i/N_{\text{live}}}$ Thus, the p.d.f. of
drawing $\vec{\Theta}_i = \vec{\theta}$ on the i-th iteration is given by $\frac{\pi(\vec{\theta})}{X_i}$. On the other hand, the
posterior p.d.f. by Bayes' rule 3.8 reads

$$p(\vec{\theta}|d, \mathcal{I}) = \frac{L(\vec{\theta})\pi(\vec{\theta})}{Z} . \tag{3.21}$$

Therefore, each point in the chain needs to be assigned a weight $\frac{L_i X_i}{Z}$ in order
to represent the posterior p.d.f. We can use this weight to resample and get
posterior points as a trivial post-processing step.

3.4 Bayesian methods

Having the necessary toolkits for numerically calculating the posterior and evidence, we now turn to the basic methods where the Bayesian framework is applied.

3.4.1 Bayesian model selection

One of the main applications of Bayesian statistics is a rigorous *model selection* (MS) method for assigning posterior probabilities to competing hypotheses. Let us consider two candidate models M_1, M_2, which compete in explaining the outcome of a random experiment, and whose validity is postulated by two respective hypotheses H_1, H_2. Each model/hypothesis may encompass its own parameter space $\Sigma_{H_1}, \Sigma_{H_2}$ and the two do not even need to be of the same dimensionality. Now, the *posterior probability* for hypothesis H_i being true, given the data d, is given by

$$P(H_i|d,\mathcal{I}) = \frac{P(d|H_i,\mathcal{I})\, P(H_i|\mathcal{I})}{P(d|\mathcal{I})}\,. \tag{3.22}$$

When comparing hypotheses we are interested in their relative posterior probabilities, given by the *odds ratio*

$$O^{H_1}_{H_2}(d) = \frac{P(H_1|d,\mathcal{I})}{P(H_2|d,\mathcal{I})} = \frac{P(H_1|\mathcal{I})}{P(H_2|\mathcal{I})}\frac{P(d|H_1,\mathcal{I})}{P(d|H_2,\mathcal{I})}\,, \tag{3.23}$$

where we see that the normalization factor $P(d|\mathcal{I})$ conveniently cancels out. The odds ratio then factors out as the ratio of the hypotheses' prior probabilities $P(H_i|\mathcal{I})$ times the ratio of their *evidences* of the data $P(d|H_i,\mathcal{I})$, also known as the *Bayes factor*

$$B^{H_1}_{H_2}(d) = \frac{P(d|H_1,\mathcal{I})}{P(d|H_2,\mathcal{I})}\,. \tag{3.24}$$

The hypotheses priors are probabilities assigned to each hypothesis based on the scientist's best knowledge before the experiment (or its analysis) takes place and represent the degree of prior belief on each hypothesis. In the second fraction, the *evidence*, or *marginal likelihood* of the data for a hypothesis H_i, is calculated as an integral of the likelihood across the hypothesis' parameter space, as in Eq. (3.13).

The likelihood integration usually requires numerical techniques such as the Nested Sampling algorithm described in Sec. 3.3.2, that for CBC analysis may take hours or even days to converge to a result with good accuracy. There are ways to minimize the number of trials in such algorithms by *e.g.* using smart jump proposals for evolving the chain of live points, that keep the acceptance ratio as high as possible. Additionally, parallel computing makes use of multiple computer cores at the same time to distribute the workload when possible, and to minimize the computational time. There have been extensive studies tailored to GW data analysis with CBC, and the corresponding computational

algorithms are incorporated in the `LALInference` package, which is part of the `LIGO Algorithm Library` (LAL). For a detailed description, see [364] and references therein.

Being able to calculate all the ingredients on the RHS of (3.23), one may use available stretches of data from GW interferometers to extract scientific results. For instance, one may try to infer the probability for a CBC signal being present in the data; in this case one compares the H_{CBC} hypothesis against the H_{noise} hypothesis, where the data consists of pure noise. If a GW event is identified, one can also test different hypotheses that model the nature of the GW sources; *e.g.* whether the source is made of black holes or neutron stars, or whether the detected properties of a population of CBC events are in best agreement with one stellar evolution model or another [328]. An inquiry that is one of the main subjects of this dissertation is testing GR itself; usually the hypothesis that GR is the underlying theory of gravity is considered as given and is implicitly included in the background information $\mathcal{I}$. One may instead decide to separate it as $\mathcal{H}_{\text{GR}}$ and treat it as a testable hypothesis.

Of course some of the most interesting problems in GW data analysis have to do with inferring the values of certain (continuous) parameters. These types of problems are the subject of Bayesian parameter estimation (PE) which is covered below.

3.4.2 Bayesian parameter estimation

The purpose of most statistical inference methods is to estimate the value and the respective errors of one or more parameters introduced by the working model. More importantly, given a prior p.d.f. $p(\vec{\theta}|\mathcal{I}) = \pi(\vec{\theta})$ on the parameter space Σ, and a set of measured data d, we would like to calculate the *posterior probability density function* $p(\vec{\theta}|d,\mathcal{I})$ on the parameters $\vec{\theta}$ of the working model. Again, using Bayes' rule (3.8) we can re-express the posterior p.d.f. as

$$p(\vec{\theta}|d,\mathcal{I}) = \frac{p(d|\vec{\theta},\mathcal{I})\,p(\vec{\theta}|\mathcal{I})}{p(d|\mathcal{I})}\,. \tag{3.25}$$

Often we are only interested in measurements in some p-dimensional *subspace* Σ_A of the q-dimensional $\Sigma \simeq \Sigma_A \oplus \Sigma_B$, and wish to consistently calculate the posterior p.d.f. on that subspace, without of course disregarding possible correlations between the parameters of interest and the nuisance ones. This calculation is given by the process of *marginalization*, which involves integrating out the nuisance components of $\vec{\theta} = (\underbrace{\theta_1,\ldots,\theta_p}_{\vec{\vartheta}\in\Sigma_A},\theta_{p+1},\ldots,\theta_q)$, using a measure defined by the prior on Σ:

$$p(\vec{\vartheta}|d,\mathcal{I}) = \int_{\Sigma_B} \mathrm{d}\theta_{p+1}\cdots\mathrm{d}\theta_q\, p(\vec{\theta}|d,\mathcal{I}) = \frac{\int_{\Sigma_B} \mathrm{d}\theta_{p+1}\cdots\mathrm{d}\theta_q\, \pi(\vec{\theta})\,p(d|\vec{\theta},\mathcal{I})}{p(d|\mathcal{I})}\,. \tag{3.26}$$

3

59

Here, our sample space is the parameter space of our working model $\Omega = \Sigma$, and one can actually calculate the *evidence* of the data $p(d|\mathcal{I})$ by marginalizing the likelihood across the entire parameter space

$$Z = p(d|\mathcal{I}) = \int_\Sigma \mathrm{d}\theta_1 \cdots \mathrm{d}\theta_q \, \pi(\vec{\theta}) \, p(d|\vec{\theta}, \mathcal{I}) \,, \tag{3.27}$$

which comes from the requirement that the posterior p.d.f. always has to integrate to unity. In particular, the *marginalized posterior* of a single component parameter θ_i of $\vec{\theta}$ is given by

$$p(\theta_i|d, \mathcal{I}) = \frac{\int \prod_{i \neq j=1}^{q} \mathrm{d}\theta_j \, \pi(\vec{\theta}) \, p(d|\vec{\theta}, \mathcal{I})}{\int_\Sigma \mathrm{d}\theta_1 \cdots \mathrm{d}\theta_q \, \pi(\vec{\theta}) \, p(d|\vec{\theta}, \mathcal{I})} \,. \tag{3.28}$$

Furthermore, any observable that one wishes to obtain can be estimated as an expectation value of a function of $\vec{\theta}$ with respect to the posterior p.d.f. For example, the *mean* of a component parameter θ_i is defined as

$$\langle \theta_i \rangle = \frac{\int_\Sigma \mathrm{d}^q \vec{\theta} \, \theta_i \, \pi(\vec{\theta}) \, p(d|\vec{\theta}, \mathcal{I})}{\int_\Sigma \mathrm{d}^q \vec{\theta} \, \pi(\vec{\theta}) \, p(d|\vec{\theta}, \mathcal{I})} \,, \tag{3.29}$$

its variance as the expectation value of $\theta_i^2 - \langle \theta_i \rangle^2$, *etc.*

More specifically for GW data analysis, given a prior p.d.f. $\pi(\vec{\theta})$ on Σ_{CBC}, and a set of measured data d, one would be able to calculate the posterior p.d.f. $p(\vec{\theta}|d, \mathcal{I})$ on the intrinsic and extrinsic parameters $\vec{\theta}_{\mathrm{CBC}}$ of the source binary system. Applications of Bayesian PE for testing GR and inferring the neutron star equation of state will be studied in Part II and Part III.

3.4.3 Combining information from independent data sets

An important feature of Bayesian inference methods is that information from multiple independent sets of data can be combined in a straightforward way. Thus, the calculated posterior probabilities are being successively updated as more and more data becomes available (from one or more experiments). As we shall see in Part II and Part III, this can significantly enhance the inference power of a Bayesian method, whether that is model selection (MS), parameter estimation (PE) or non-parametrics (NP). Given a set of data sets $\{d_i\}_{i=1,\ldots,n}$, and assuming that the different data sets d_i are mutually independent, that is

$$p(d_i, d_j|\mathcal{I}) = p(d_i|\mathcal{I}) \, p(d_j|\mathcal{I}) \,, \quad \forall i \neq j \in \{1, \ldots, n\} \,, \tag{3.30}$$

we can make use of the multiplicative probability rule recursively on the likelihood of the entire collection of data

$$p(\{d_i\}_{i=1,\ldots,n}|\mathcal{I}) = \prod_{i=1}^{n} p(d_i|\mathcal{I}) \,. \tag{3.31}$$

In a sense, we already did this when going from the point-wise (by frequency bin) likelihood to the one for an entire time series in Eq. (3.10) The above rule also holds for likelihoods where more things are assumed at the "givens" side, as long as these do not affect the independence of data sets.

In model selection Applying Eq. (3.31) to Bayesian model selection, we directly obtain by Eq. (3.24) the *combined Bayes factor* for n sources as

$$^{(n)}B^{H_1}_{H_2}(\{d_i\}_{i=1,\ldots,n}) = \frac{P(\{d_i\}_{i=1,\ldots,n}|H_1,\mathcal{I})}{P(\{d_i\}_{i=1,\ldots,n}|H_2,\mathcal{I})} = \prod_{i=1}^{n} \frac{P(d_i|H_1,\mathcal{I})}{P(d_i|H_2,\mathcal{I})} , \qquad (3.32)$$

which gives the *combined Odds ratio*

$$^{(n)}O^{H_1}_{H_2} = \frac{P(H_1|\mathcal{I})}{P(H_2|\mathcal{I})} \prod_{i=1}^{n} \frac{P(d_i|H_1,\mathcal{I})}{P(d_i|H_2,\mathcal{I})} . \qquad (3.33)$$

In most problems, the evidences take values that range up to large numbers; it is therefore convenient to express results in terms of *logarithmic* Bayes factors and odds ratios. From the above calculations we see that the combined $\log O$ is expected to scale linearly with the number of available sources.

In parameter estimation Similarly in Bayesian parameter estimation, one can combine information from different data sets in order to infer the underlying value of a parameter vector $\vec{\theta}$ that is *globally defined*, *i.e.* whose value is assumed to be universal in all of the available data. We shall refer to these as *global parameters*; in our case of CBC signals, these will be source-independent parameters such as the cosmological parameters, parameters that define the NS EoS, parameters of population synthesis models, *etc.* The posterior p.d.f. for the global parameter $\vec{\theta}$ given a set of n data sets is given by

$$p(\vec{\theta}|\{d_i\}_{i=1,\ldots,n},\mathcal{I}) = \frac{p(\{d_i\}_{i=1,\ldots,n}|\vec{\theta},\mathcal{I})\,p(\vec{\theta}|\mathcal{I})}{p(\{d_i\}_{i=1,\ldots,n}|\mathcal{I})} = p(\vec{\theta}|\mathcal{I}) \prod_{i=1}^{n} \frac{p(d_i|\vec{\theta},\mathcal{I})}{p(d_i|\mathcal{I})}$$

$$= p(\vec{\theta}|\mathcal{I}) \prod_{i=1}^{n} \frac{p(\vec{\theta}|d_i,\mathcal{I})\,p(d_i|\mathcal{I})}{p(d_i|\mathcal{I})\,p(\vec{\theta}|\mathcal{I})}$$

$$= p(\vec{\theta}|\mathcal{I}) \prod_{i=1}^{n} \frac{p(\vec{\theta}|d_i,\mathcal{I})}{p(\vec{\theta}|\mathcal{I})} , \qquad (3.34)$$

where in the second and third equation we used Bayes' rule Eq. (3.8) forth and back. This gives a straightforward way of obtaining the *combined posterior p.d.f.* of a global parameter. An interesting "timeline" interpretation of this is that our prior is in fact *updated* with each new set of data that comes to light. More specifically, starting with our initial prior $\pi(\vec{\theta})$, the posterior after the i-th experiment becomes the prior of the $(i+1)$-th experiment.

Part II

Testing General Relativity

<div align="right">
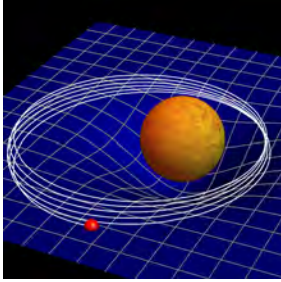
Chapter 4

</div>

Tests of General Relativity

> *Here, on the edge of what we know, in*
> *contact with the ocean of the unknown,*
> *shines the mystery and beauty of the*
> *world. And its breathtaking.*

<div align="right">

Carlo Rovelli

</div>

Formally born in 1915, the general theory of relativity has managed in its 100 years of existence, to establish itself as one of the most successful theories in physics. The exceptional beauty of GR lies not only in the fact that it provided a new elegant geometrical paradigm for fundamental physics, thus radically changing the notions of space and time, but that it would also survive experimental testing for an entire century. Even though with very few exceptions, experimental gravitational physics has been a dormant field for many decades in the mid-20th century, the validity of its predictions has been tested in various different ways. Sec. 4.3 provides a brief overview of the different types of experimental tests of GR performed to date, the first three having been proposed by Einstein himself. It is interesting however to realize how the many different tests are all restricted to the regime of weak gravitational fields generated by non-relativistic sources. Regarding the field strength, a good dimensionless figure of merit is the *compactness* $\mathcal{C} = GM/Rc^2$ of the source, M being the total mass and R being the size of the source, while its characteristic internal velocity v/c sets the relativistic scale. As we shall see, the most stringent tests, coming from observations of pulsar binaries, are characterized by $\mathcal{C} = \mathcal{O}(10^{-6})$ and $v/c = \mathcal{O}(10^{-3})$. In comparison, compact binaries that are close to coalescence and emit strong gravitational radiation, will reach a compactness of $\mathcal{C} \sim 0.2$ and an orbital velocity $v/c \sim 0.4$ during their last stable orbit. These systems are the ideal natural laboratories for us to probe GR in its fully relativistic strong-field regime.

Putting quantitative details aside for a moment, one finds in the conceptual basis

of GR the notion of the equivalence principle. This comes in three different versions in a strict hierarchy that will be briefly outlined below, all of which are satisfied by GR. Any alternative theory of gravity may not comply with one or more of the three and its general structure can be characterized based on this compliance.

4.1 Equivalence principles

Origins and the weak equivalence principle   An early notion of an *equivalence principle* between gravitational effects and non-inertial frames is already present since the days of Galileo. Within the context of 16th century classical mechanics this states that all bodies undergo the same acceleration under the effect of a gravitational field. Later on, this was interpreted in the context of Newtonian physics as the principle that the gravitational content of a body is proportional to its inertial content, or that "gravitational mass is equivalent to inertial mass".

The *weak equivalence principle* (WEP) is essentially Newton's equivalence principle that identifies the property of inertial mass with the gravitational mass or *weight*. More precisely it states that: "The inertial mass of an object is directly proportional to its weight." thus establishing gravity as a kinematic force. The above statement directly implies through Newton's 2nd law that all bodies will follow the same trajectory when performing free fall, irrespective of their mass or composition.

In 1907 Albert Einstein first formulated the equivalence principle with relation to gravity, by establishing an equivalence between *the presence of a gravitational field* and *accelerated reference frames*. Inertial observers were then identified as observers in free fall.

Einstein's and strong equivalence principle   *Einstein's equivalence principle* is stronger than the WEP and consists of a set of three requirements: (i) The WEP is true for test bodies. (ii) Positional invariance holds for all non-gravitational experiments. (iii) Lorentz invariance holds for all non-gravitational experiments.

The *strong equivalence principle* (SEP) is an even stronger one than the EEP, and consists of the same three statements as the EEP, extended to self-gravitating bodies (not only test bodies) and gravitational experiments.

Some of the experimental tests that will be described below do not challenge GR per se, but rather one or more of the statements of the SEP. It is crucial to distinguish between the two cases, since the SEP may be a built-in principle of GR, but is not an exclusive property of the theory. For instance, any geometric theory of gravity, whose observables are constructed using the same metric structure as

in GR, but whose dynamics are not necessarily driven by the Einstein-Hilbert action, can still conform with the SEP.

4.2 Alternative theories of gravity

Since the formulation of GR and the verification of both its qualitative and quantitative differences from Newtonian gravity, a number of alternatives have been put forward, many of which were designed so as not to violate the philosophy that GR introduced. In this discussion we will restrict to such *relativistic* theories of gravity, which can be formulated by the definition of an action principle in 4-dimensional spacetimes involving a symmetric metric tensor and possibly other fields. One may classify the set of alternative theories of gravity in different ways, based on their structural characteristics, extra parameters or fields they entail, their accordance with different principles, such as the EEP or SEP, their phenomenological consequences or main motivation.

Let us proceed with a rather structural overview; we first recall the essence of GR as an action principle, the Einstein-Hilbert action: $S_{\mathrm{E-H}} = \frac{c^4}{16\pi G} \int \mathrm{d}^4 x \sqrt{-g} R$. This is the gravitational part of the *total action*, which includes all matter fields and takes the form

$$S[g, A^{(I)}] = S_{\mathrm{E-H}} + S_m = \int \mathrm{d}^4 x \sqrt{-g} \left[\frac{c^4}{16\pi G} R - \mathcal{L}_m \right], \qquad (4.1)$$

where the metric $g_{\mu\nu}$ has a Lorentzian signature $(-, +, +, +)$ and all matter fields $A^{(I)}$ are described by the matter Lagrangian density $\mathcal{L}_m$ yielding the stress-energy tensor $T_{\mu\nu} = -\frac{2}{\sqrt{-g}} \frac{\delta(\sqrt{-g}\mathcal{L}_m)}{\delta g^{\mu\nu}}$. Most alternative theories are formulated in this context, modifying the structural form of the action. They are subject to theoretical restrictions such as causality constraints, the absence of ghost modes or other instabilities, but also experimental bounds from solar system, astrophysical and cosmological observations.

4.2.1 Metric theories

The class of *metric theories* of gravity includes those relativistic theories for which the symmetric Lorentzian metric tensor field $g_{\mu\nu}$ is the only field that defines the equations of motion for the matter fields. Some still conform with the EEP, but have the freedom to introduce additional *gravitational fields*. This means that matter and non-gravitational fields are restricted to evolve under the influence of the metric tensor alone. The extra gravitational fields only participate in the way non-gravitational fields and matter configure the metric tensor field.

Tensor theories   This class includes theories similar to GR but with *e.g.* higher order curvature terms in the Lagrangian ($f(R)$ theories) [112, 121, 340, 74] or a function of the topological Gauss-Bonnet term ($f(G)$ theories) which is non-trivial at higher dimensions [273, 131]. Another set of higher-dimensional extension of GR is provided by Lovelock gravity [249], where the most general form of an action that yields second order tensorial equations and conserves the matter fields in higher dimensions is preserved. Purely tensor theories may be consistent with the SEP but still be distinguishable from GR in their quantitative predictions. "New massive gravity" [71] is a version of gravity with massive modes (currently in $2+1$ dimensions), that is free from known pathologies like ghosts or the vDVZ (van Dam-Veltman-Zakharov) discontinuity that often appears when trying to recover the massles limit [359, 395].

Scalar-Tensor theories   These theories are characterized by an additional scalar field ϕ which apart from entering the matter Lagrangian with its kinetic and potential terms, also has a scalar coupling with the Ricci scalar in the E-H term (*e.g.* minimally coupled: ϕR) [52, 106, 373, 175, 184]. The matter equations of motion (ϕ being part of it) are still governed by the variation w.r.t. the metric tensor alone, in the usual way of Eq. (4.1). Scalar-Tensor (ST) theories have a long history (since the days of Einstein himself); for example, Kaluza-Klein (in 5 dimensions) can be reduced to 4-dimensional gravity plus a scalar field [46] and thus has a ST representation. Brans-Dicke theory [106, 40] is a representative example, minimally coupled with gravity and with only a kinetic term of the form $-\omega \frac{\partial_\mu \phi \partial^\mu \phi}{\phi}$. Here, ω is the extra free parameter of the theory, which is bounded to $\omega \geq 4.3 \times 10^4$ by measurements of the PPN parameter $\gamma = \frac{\omega+1}{\omega+2}$ with the Cassini spacecraft [82].

Vector-Tensor theories   Similarly to ST theories, the Vector-Tensor (VT) theories are described by the presence of an additional *vector field* which only interacts with matter through the metric by its coupling in the gravitational part of the action. This new dynamical quantity defines a preferred direction throughout the entire spacetime and thus breaks Lorentz invariance. The main motivation behind these theories was the exploration of relativistic theories that predict violation of Lorentz invariance and closely connect to the development of the PPN formalism by Will and Nordtvedt [386, 277]. After being marginalized for a couple of decades these models recently attracted attention as natural candidates for dark energy [68, 69, 70]. Another typical example of a VT theory is Einstein-Aether theory, where the vector field is constrained to be of unit norm [214].

Scalar-Vector-Tensor theories   Naturally, a third class that includes all three types of fields is conceivable and goes under the name Scalar-Vector-Tensor theories (SVT). Here too, the presence of a preferred frame breaks Lorentz invari-

ance and possibly local positional invariance. A characteristic case is TeVeS, the relativistic formulation of Milgrom's theory of *modified Newtonian dynamics* (MOND), whose main motivation was to explain the anomalous galactic rotation curves without the introduction of dark matter [263, 66]. TeVeS contains, apart from a metric tensor, an additional vector field and two scalar fields, that participate in the gravitational action. Another interesting case is MOdified Gravity (MOG) developed by Moffat that introduces one vector field and three scalar fields and that can explain various astrophysical and cosmological observations without the need for dark matter [266].

4.2.2 Other alternative theories

Non-metric theories   This is a different set of theories in which gravity is not directly associated to a metric field. The two most popular members of this set are Cartan gravity [195], in which gravity is interpreted as a Yang-Mills type of theory with non-vanishing torsion, and Teleparallel gravity [38], in which the fundamental structure is a tetrad field and gravity is interpreted as a torsion effect, rather than curvature which in this case vanishes.

Quantum gravity inspired theories   Apart from theories that are formulated as field modifications in the standard GR action Eq. (4.1), others have been devised motivated by arguments related to quantum gravity. The necessity for such a theory stems directly from the well established fact that matter (present in the EFE) behaves in a way dictated by quantum mechanics. A first non-trivial requirement imposed upon candidate theories is that they recover GR in their low-energy limit, and a fundamental obstacle that appears in the quantization process of the latter is the appearance of ultraviolet (UV) divergences when renormalizing the theory with higher order loop corrections [378]. A recent candidate that attempts to overcome such issues is Hořava-Lifshitz gravity [201], which provides a UV completion of GR, treating divergences in the quantum integrals via the introduction of scaling rules for space and time that differentiate at high energies. This is an interesting case for studying parametrized effects in GW signals [101]. On the other hand, Noncommutative Geometry (NCG) introduces an entirely different mathematical framework, based on the spectral algebraic properties of spacetime geometry. This generalized definition of a geometric space, where functions do not need to commute, has all the necessary structure of quantum theory built-in. Observable modifications in gravitational wave physics are investigated in [269], where the existence of additional massive graviton modes is predicted. Another promising example is Loop Quantum Gravity (LQG) [319] which introduces a granular picture of quantum spacetime, providing a non-perturbative theory whose spacetime solutions are superposition of discrete "spin networks" (quantum foam). Causal Dynamical Triangulations (CDT) [43, 42, 31] take a bottom-up approach and attempt to interpret spacetime as the continuum limit of a regularized "geometrical path integral" of piecewise

flat geometries. Higher dimensional gravity [268, 310], supergravity [380, 151], string theory [296] and twistor theory [292, 205] can also be classified in this group of quantum-inspired theories. These and other candidates for quantum gravity have so far not developed to the point where they can give robust predictions for GW phenomenology.

4.2.3   Exceptionally interesting cases

Many of the aforementioned alternative theories of gravity are highly constrained by existing observations. Nevertheless, models exist, where the predicted modification to the GW signal does not manifest itself until the source becomes relativistic or gravity becomes strong enough, *e.g.* shortly before a binary merger. In such cases, even the most stringent existing bounds, like binary pulsar observations, do not effectively constrain the strength of an observable GW effect in the late inspiral. For instance, in some scalar-tensor models studied by Damour and Esposito-Farese [138] and more recently by Pani *et al.* [286], a phase transition of *spontaneous scalarization* takes place in the interior of the neutron star above a critical density; in a different model, studied by Berti *et al.* [81, 40], featuring a light scalar, a discontinuous modification in the binary evolution may enter at high frequencies; finally, Hořava-Lifshitz gravity, with its running critical exponent for the scaling of time, could in principle show a similar behaviour at high energies.

4.2.4   The PPN formalism

There are infinitely many ways in which a theory like GR may be violated. A wealth of theories of gravity have been proposed as alternatives or high-energy completions to GR throughout the last few decades, among which only few survived theoretical and experimental scrutiny. As a consequence, the need of a parametrised, sufficiently general and unified treatment of GR violations becomes evident. The most successful attempt towards such a treatment is known as the parametrized post-Newtonian (PPN) formalism [386].

The PPN formalism defines ten parameters

$$(\gamma, \beta, \xi, \alpha_1, \alpha_2, \alpha_3, \zeta_1, \zeta_1, \zeta_2, \zeta_3, \zeta_4) \ , \tag{4.2}$$

each of which corresponds to a different physical quantity[1]. For example γ physically corresponds to the "curvature per unit rest mass", with a normalization such that in GR one gets $\gamma = 1$. Given an arbitrary alternative theory of gravity one can calculate the new values for the PPN parameters, some of which may deviate from their GR-predicted values. In GR $\gamma = \beta = 1$ and all the rest are zero.

---

[1]See [381, 385] for a detailed overview.

In the light of experimental data one may be able to measure a subset of the PPN parameters and obtain bounds for the competing theories of gravity. Current bounds for the PPN parameters, are summarised in Table 4 of [385]. These include limits derived from observations of pulsars, either solitary (PSR B1937+21[2]) or in binary systems (PSR 1913+16), which however should have been treated in a strong-field formulation, since neutron stars are strongly self-gravitating bodies. The reader should note that the standard version of the PPN formalism is only appropriate for weakly gravitating sources. For the purposes of this dissertation, we shall introduce a simple parametrized formalism which is also based on post-Newtonian theory, specifically tailored for coalescing binaries, but which is however unrelated to what is known as PPN.

4.3 Overview of current tests and bounds

Gravitational redshift and time dilation   Special relativity introduced for the first time the notion of time being relative to the observer's reference frame. In general relativity, an explicit realisation of time dilation occurs as a direct effect of the geometrical nature of gravity: observers at different locations where the gravitational field is different will not measure the passing of time with the same rate.

As an example, consider the Earth's gravitational field, which we assume to be spherically symmetric and thus is expressed by the Schwarzschild metric above the Earth's surface

$$\mathrm{d}s^2 = -\left(1 - \frac{2M}{r}\right)\mathrm{d}t^2 + \left(1 - \frac{2M}{r}\right)^{-1}\mathrm{d}r^2 + r^2\mathrm{d}\Omega^2 \,, \qquad (4.3)$$

where the Earth's mass $M = M_\oplus \simeq 4.43 \times 10^{-3}$m sets the scale. In the Newtonian limit, the gravitational field can be approximated by

$$\phi_N \simeq -\frac{1}{2}(1 + g_{00}) = -\frac{M}{r} \,. \qquad (4.4)$$

Now the proper time $\mathrm{d}\tau_A$ of an observer A whose world line follows the above coordinate system at constant radius r_A, neglecting angular coordinates, will be proportional to $\sqrt{1 + 2\phi}\,\mathrm{d}t$, where from the same argument it follows that the coordinate time $\mathrm{d}t$ coincides with the proper time of an observer at infinity. When comparing the lapse in proper times τ_A and τ_B measured by the clocks of two observers A and B located at different altitudes $r_A < r_B$, for a coordinate time lapse $\mathrm{d}t$, we see that

$$\frac{\mathrm{d}\tau_A}{\mathrm{d}\tau_B} = \sqrt{\frac{1 + 2\phi(r_A)}{1 + 2\phi(r_B)}}, \qquad (4.5)$$

---

[2]ra: $19^h39^m38^s.560210(2)$, dec: $21^o34'59''.14166(6)$

which implies that time will run slower for observer A who sits at a lower altitude (*i.e.* she will age faster than B for the same coordinate time). For instance, if A is located on the surface of the Earth and B at an altitude equal to that of the International Space Station ($\sim 420\,\text{km}$), then the magnitude of time dilation will be roughly 2 parts in 10^{11}. Even though this kind of deviation is tiny – it will take more than 700 years before the proper time difference reaches 1 second– experiments using accurate atomic clocks have managed to measure this effect [125], even for meter-scale height differences! So far the magnitude of this effect has been shown to be consistent with GR.

A direct consequence of gravitational time dilation is the effect of gravitational redshift, according to which a light source in a gravitational potential seems to be redshifted when viewed by an observer at a weaker (less negative) potential. In 1959 this effect was observed by R. Pound and G. A. Rebka [297, 298]. In the homonymous experiment, a moving source of excited nuclei generates blueshifted light due to the relativistic Doppler effect, with respect to a receiver of the same nature at a higher altitude (about $22.5\,\text{m}$ higher). When the relative velocity takes a value for which the Doppler blueshift exactly cancels the gravitational redshift, a narrow absorption reasonance should be achieved. This was indeed observed verifying the predictions, initially to within a 10% accuracy and later on to 1%. More sophisticated tests using hydrogen maser clocks followed, that brought the measurement accuracy down to 2×10^{-4} [367].

Precession of the perihelion of Mercury   Unlike Newtonian gravity, GR does not predict closed elliptical orbits in an isolated 2-body system, even for one of a test mass orbiting a much heavier object and without taking gravitational radiation effects into account. For instance, within our solar system, one can consider the orbit of Mercury around the Sun, with a mass-ratio of $\mathcal{O}(10^7)$.

The conservation of energy and angular momentum for the Schwarzschild metric in GR, expressed as the first integrals of the Lagrangian $L = g_{\mu\nu}\dot{x}^\mu \dot{x}^\nu = 1$ read

$$\epsilon = (1 - \frac{2M}{r})\dot{t} \quad \text{and} \quad J = r^2 \dot{\phi}, \tag{4.6}$$

which lead to the differential equation

$$\left(\frac{\mathrm{d}u}{\mathrm{d}\phi}\right)^2 = 2Mu^3 - u^2 + \alpha u + \beta, \tag{4.7}$$

where we used the transformation $u = 1/r$ and defined the constants of motion $\alpha = \frac{2M}{J^2}, \beta = \frac{\epsilon^2 - 1}{J^2}$. After observing that in a bound orbit there are two values u_1 corresponding to the perihelion and u_2 corresponding to the aphhelion, for which $\frac{\mathrm{d}u}{\mathrm{d}\phi} = 0$, we obtain the general solution

$$\phi - \phi_0 = \int_{u_0}^{u} \frac{\mathrm{d}u'}{\sqrt{(u' - u_1)(u_2 - u')(1 - 2M(u_1 + u_2 + u'))}} \ . \tag{4.8}$$

In particular this implies that after a full equatorial orbit, the azimuthial angle will advance to leading order by

$$\Delta\phi \simeq 2\pi + 3\pi M(u_1 + u_2). \tag{4.9}$$

For the orbit of Mercury around the Sun, this gives a perihelion advance of $\Delta\phi_p \sim 3 \times 10^{-6}$ radians per orbit.

The perihelion advance of Mercury was first observed in 1859 by Le Verrier [241]. Corrections due to the presence of other planets in the solar system were not enough to accurately explain this discrepancy in the Newtonian theory. Two of the first reactions to this apparent anomaly were to assume that there was either a planet yet to be discovered on an even tighter orbit, or that the Sun may have been much more oblate than expected, having a much higher quadrupole moment. As it turned out, the residual advance by ~ 43 arcsec/century is exactly consistent with the correction that GR predicts [160]. Further measurements of increasing accuracy have been performed over the years, verifying the GR prediction with half-arcsecond precision [130, 381]. Similar tests have been performed using observations from other planets in the solar system [130, 86], as well as periapsis advance measurements in pulsar binaries [379], all of which have corroborated consistency with GR.

Light deflection and gravitational lensing As a geometric theory of gravity, GR predicts the effect of light trajectories being bent in the vicinity of a gravitating body. More accurately, light follows null geodesics which are defined by the geometry of spacetime. As a result, light that is emitted by a distant source may undergo deflection and lensing effects, if a massive body intervenes between the source and an observer.

More explicitly, the unbound null geodesics of in a Schwarzschild spacetime now satisfy the differential equation

$$\left(\frac{\mathrm{d}u}{\mathrm{d}\phi}\right)^2 = 2Mu^3 - u^2 + \beta, \tag{4.10}$$

with a perihelion $r_1 = 1/u_1$ satisfying $\frac{\mathrm{d}u}{\mathrm{d}\phi} = 0$. The general solution now reads

$$\phi - \phi_0 = \int_{u_0}^{u} \frac{\mathrm{d}u'}{\sqrt{(u_1 - u')(u_1 + u' - 2M(u_1^2 + u_1 u' + u'^2))}}, \tag{4.11}$$

and to leading order, the angular difference from end to end is

$$\Delta\phi = \pi + 4Mu_1, \tag{4.12}$$

where π corresponds to the zero-deflection part. One then can numerically estimate that a light ray passing right off the surface of the Sun ($r_1 = R_\odot = 6.955 \times 10^8\,\mathrm{m}$) will undergo a deflection by an angle $\sim 8.51 \times 10^{-6}$ radians.[3]

---

[3]If on the other hand one considered a corpuscular theory of light travelling in a Newtonian Universe, the corresponding leading order deflection angle would be smaller by exactly a factor of 2.

Measuring such an effect was the objective of the famous observation in 1919, during which a total solar eclipse was photographed by Sir Arthur Eddington in order to verify or invalidate the predictions of the freshly formulated theory of gravity. The precise apparent locations of the stars surrounding the eclipse were then compared against their true locations and the measured deflection angles matched with what GR had predicted [159, 158]. This was enough to shift a significant part of the scientific community towards favouring general relativity over Newtonian gravity. Since then, various measurements of light deflection have consistently shown agreement with GR [243, 332], with the most notable ones made by the Cassini spacecraft, that measured light geodesics in the solar system [82].

The Lense-Thirring effect   An effect that can be observed in Kerr spacetimes induced by rotating bodies, where the metric is only axisymmetric, is that of *frame-dragging*. Kerr spacetimes are rather common in GR since, apart from describing spinning black holes, they also feature as for example the exterior of spherically symmetric matter distributions that rotate around a given axis. In particular, rotational frame-dragging, also known as the *Lense-Thirring* effect, is a manifestation of the dt-$d\phi$ mixing in the components of the metric, which makes inertial frames get carried along with the rotation of the source. Spacetime itself thus appears to be co-rotating with the source, an effect which is stronger at smaller radii and at polar angles θ closer to the equator.

The gravitational field in the Earth's exterior can be approximated by a Kerr spacetime. Experimental tests of the Lense-Thirring effect involve measuring nodal precession of test masses in orbit or gyroscopic. One expects the effect of frame dragging on orbiting satellites to be very weak, since the orbital radius is 10^9 times the Earth's Schwarzschild radius. In the latest experimental attempt, Gravity Probe B [163] orbiting at an altitude of 642 km, measured a frame-dragging drift of 37.2 ± 7.2 mas/yr, which is consistent with the GR prediction of 39.2 mas/yr. During the same experiment the geodetic effect (the effect of curvature on parallel transport of vectors) was also measured and was found to be consistent with GR, with a drift rate of 6601.8 ± 18.3 mas/yr to be compared against the theoretical prediction of 6606.1 mas/yr.

Eötvös-like experiments and the Nordtvedt effect   The aim of the well known torque balance experiments by Eötvös in the late 19th century was to test whether two masses A and B of different type, behave differently under effects that depend on their inertial m_i or gravitational m_g mass, essentially challenging the WEP [161, 102]. Experiments of this kind continued to evolve into high precision measurements of the Eötvös parameter $\eta(A, B) = 2\frac{(m_g/m_i)_A - (m_g/m_i)_B}{(m_g/m_i)_A + (m_g/m_i)_B}$, by Dicke [318], Braginsky [105] and the Eöt-Wash group [343, 29]; the current bound is set in [55] to $\eta(A, B) < 10^{-13}$. A similar idea was put forward by Nordtvedt [275, 276], whose goal was to test whether the Earth and the Moon

fall freely in the same way, in the Sun's gravitational field, which, as a gravitational experiment, constitutes a test of the SEP. Since the Earth and the Moon have significantly different gravitational binding energies and compositions, their relative accelerations in their binary orbits could be a direct measurement of the Nordtvedt effect. The Earth-Moon distance has been traced to millimetre accuracy using lunar laser ranging (LLR), experiments where laser light from Earthbound labs is shone upon reflectors mounted on the Moon's surface [388]. These experiments have set upper bounds on the relative acceleration at 5^{-13} [388], and on the *Nordtvedt parameter* $\eta_N = 4\beta - \gamma - 3$ of the order 3×10^{-4}.

Orbital motion of pulsar binaries   The EM observation and study of pulsars in binary systems, and most significantly the ones in tight relativistic orbits, can yield valuable information on the orbital parameters and their consistency with GR, through the outstanding precision of the pulses' times of arrival (TOA). Most of the observed systems are wide and slow enough to be accurately described using Kepler's laws; however a few of them are relativistic enough to exhibit observable deviations from Kepler's laws, which are measured in terms of the so-called *post-Keplerian* (PK) parameters. Several different relativistic effects modify the Keplerian prediction of a perfectly regular pulse (relative to the Solar system barycentre), among which are

- the periastron advance (similar to what was described earlier for the perihelion of Mercury), which results in a non-zero PK parameter $\dot{\omega}(P_b)$;

- the gravitational wave emission, and corresponding loss of binding energy leading to a non-zero PK parameter $\dot{P}_b$ and a fixed relation $\dot{P}_b(P_b)$;

- the Einstein delay, accounting for the overall time delay (and redshift) that the emitted light undergoes by escaping the gravitational potential of the binary and entering that of the observer's environment. This is expressed by the PK parameter γ;

- the Shapiro delay, which is an additional time delay that can be observed in edge-on systems and occurs when the companion passes close to the line of sight that connects the pulsar and the observer. It is the companion's gravitational well that imposes a sharp time delay in the pulse, which can be measured in terms of the PK parameters $r \propto m_c$ (the companion's mass) and s, the Shapiro parameter.

More detailed information on the post-Keplerian formulation and data analysis of pulsar binaries can be found *e.g.* in [54, 108, 248]. Each of the above effects overlays a different signature on the observed TOA data and can potentially be disentangled from other effects and estimated using Monte Carlo methods.

Binary pulsar observations have given some of the most stringent tests of GR to date and, thanks to the compactness of these systems, have probed the most relativistic, strong-field regime that any gravitational experiment has ever reached.
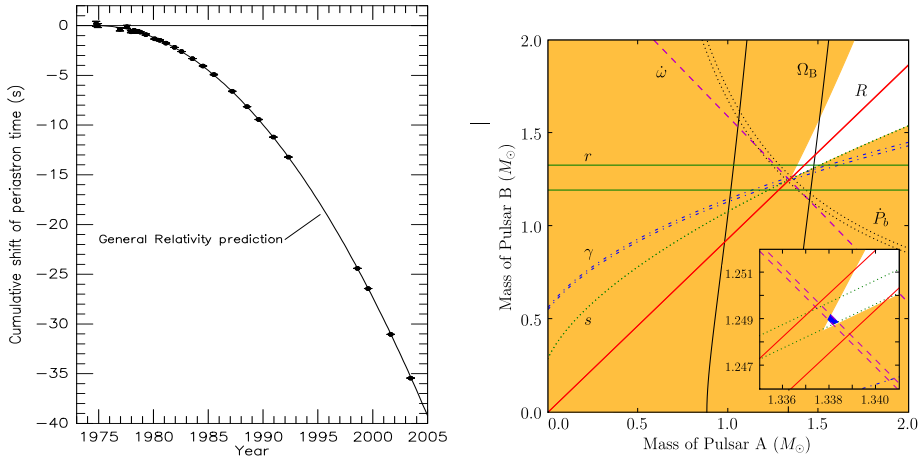
Figure 4.1: *Left: The observed data (black dots) showing the shift in the periastron time for the Hulse Taylor binary pulsar until 2003, together with the curve predicted by GR (taken from [379]). Right: The consistency plot for six measured post-Keplerian parameters of the double pulsar PSR J0737-3039A/B in the m_1-m_2 plane (taken from [108]).*

Most notably, the first observation of a binary pulsar, namely the *Hulse-Taylor binary pulsar*[4] PSR B1913+16 in 1974, led to the first indirect evidence for the existence of gravitational radiation. A more than a decade-long observation of the orbital period decay was astonishingly consistent with the GR predictions for the energy loss in gravitational waves and earned Hulse and Taylor the Nobel Prize in 1993. The measured cumulative shifts in periastron time until 2003 are shown in the left panel of Fig. 4.1, in a plot by Weisberg & Taylor with actual error bars which are however too small to see. Notice how accurately the theoretical $\dot{P}_b(P_b)$ prediction by GR (using the quadrupole approximation alone) matches the observations.

A more recent and even more stringent test of GR comes from the observations of the *double pulsar*[5] PSR J0737-3039A/B, a binary neutron star system where both components were visible as pulsars [117, 251, 108, 231, 107]. As can be seen in the right panel of Fig. 4.1, seven different post-Keplerian parameters were measured at the same time, each of which gave a confidence band in the m_1-m_2 parameter space. All seven bands (5 of which are redundant d.o.f.) overlap with remarkable accuracy, giving consistency with GR, but also a precise measurement of the component NS masses. Similar analyses have been also taken out for other pulsar binaries. Most notably, the NS-WD binary PSR J1738+0333[6], thanks to the large number (17376) and precision ($< 5\mu$s) of TOA measurements and

---

[4]ra: $19^h13^m12^s.4655$, dec: $16^o01'08.189''$

[5]ra: $07^h37^m51^s.247$, dec: $-30^o39'40.74''$

[6]ra: $17^h38^m53^s.9658386(7)$, dec: $03^o33'10''.86667(3)$

its high asymmetry, gave the most stringent bounds to date for a matter-scalar coupling α_0-β_0 parameter space ($\alpha_0^2 < 10^{-5}$) in ST theories (Jordan-Fierz-Brans-Dicke) and SVT theories (TeVeS) [45, 171].

The equivalence principle tested with triple systems   In late 2013 the first millisecond pulsar in a triple system was observed[7], with a mass of $1.4378(13)M_\odot$, while the masses of the two white dwarf companions were estimated to $0.19751(15)$ $M_\odot$ and $0.4101(3)M_\odot$ [306]. The configuration of the triple system is hierarchical, with the NS and the lighter companion closely orbiting each other with a period of 1.63 days. Together they orbit the heavier white dwarf at an outer orbit with a period of 327.26 days.

This setup provides an ideal laboratory for testing the SEP, much the same way as the Earth-Moon-Sun system for the Nordtvedt experiment [276]. A violation thereof would cause the strongly self-gravitating NS to fall differently than its less compact WD companion, under the gravitational field of the heavy WD. Such an investigation with currently available data is under way by the authors of [306], but a discussion can already be found in [190], whose authors claim a constraint of the Nordtvelt parameter $\eta_N = 4\beta - \gamma - 3 < 10^{-4}$, beating the lunar laser ranging bound by a factor of ~ 4.

4.4   Future prospects of testing GR

Improvement on existing experiments   Further investigations on the Lense-Thirring effect are scheduled, with the expectation that ESA's currently operating satellite LARES [129, 128] will perform measurements of the effect to a 1% accuracy.[8]   Improved accuracy is also expected in astrometry experiments such as GAIA or the proposed GAME that (among other duties) will bring the accuracy of measurements of the PPN γ parameter down to $\sim 10^{-7}$ or less [363, 177].

Observing the black hole horizon   Based on evidence from astronomical observations, a supermassive black hole known as Sagittarius A^* (Sgr A^*)[9] is believed to reside in the center of the Milky Way [260]. The *Event Horizon Telescope* is a proposed project to combine data from an array of large telescopes around the globe, so that sufficient resolution is reached to observe EM radiation emitted from close to the event horizon of Sgr A^*. This kind of observations will directly probe the geometry of the Kerr metric that is expected to describe the BH and may provide new tests for GR in the strong field of a SMBH [165, 156, 111, 41].

---

[7]ra: $03^h 37^m 43^s.82589(13)$, dec: $17^o 1514.828(2)$

[8]This has ignited a heated debate between physicists on the realistic expectations for LARES that is still ongoing [207, 208, 312, 209]. First results from analysis on LARES data are shown in [313]

[9]ra: $17^h 45^m 40^s.0409$, dec: $-29^o 0' 28''.118$

Tests of cosmology with Euclid   Euclid is ESA's future M3 space mission, whose objective will be to map the (dark) matter distribution and the geometry of the Universe at cosmological scales. This will be done by means of high-resolution imaging and spectroscopy, redshift measurements and analysis on weak and strong gravitational lensing effects, in light coming from billions of distant galaxies and quasars [240, 323]. The mapping is expected to be so detailed that the data will allow reconstructing "snapshots" of the cosmological evolution of our Universe and we will therefore be able to test the validity of the standard model of FLRW cosmology. This will provide yet another indirect test of GR, this time at large scales [257].

Testing the no-hair conjecture   The no-hair conjecture states that BH space-times are completely characterized by three parameters: a mass M, an angular momentum a and a charge Q [210, 211, 122, 193, 194]; astrophysical BHs are expected to have no charge and are therefore described by the 2-parameter Kerr metric. Although the no-hair conjecture is yet to be proven for GR [127], no counter-example that violates it has been constructed either. It is widely accepted that tests of the no-hair theorem can be considered as tests of GR itself. Such tests can be devised by using observations of BH systems through detection of either EM [111] or GW [186, 259] radiation.

Direct gravitational wave detection   Prior to September 2015, gravitational waves had been the only remaining missing block of our current model of fundamental physics, and their direct detection was rightfully considered as the holy grail of modern experimental gravity for the last 100 years. It goes without saying that the information that GW detections can yield on the nature of gravity is invaluable and qualitatively unique. Again, one only needs to notice that most, if not all, of the aforementioned experiments are performed in the weak-field non-relativistic regime of GR, in order to realize how qualitatively exceptional it would be to detect and analyze a GW signal from a coalescing compact binary. In this part of the dissertation, I will formulate and demonstrate the performance of tests of GR, based on data analysis of GW signals emitted by binary neutron star systems and detected by the aLIGO and AdVirgo network of ground-based interferometers. I will also show how much of an improvement these bring in measuring violations of GR, in comparison with pulsar binary measurements.

4.5   Testing GR with direct gravitational wave detection

The first step towards testing the dynamics of GR with gravitational waves is the detection itself. Recently, the first detection came from a BBH coalescence (and quite unexpectedly so), but GWs from systems including at least one NS

are yet to be detected. Assuming the validity of the expected merger rates for BNS and NSBH systems [9], a non-detection after a few years' operation of the network of second generation detectors at design sensitivity could indicate an inconsistency in our GR-based model. A possible interpretation in such a case would be that GR is so strongly violated in the presence of dense matter fields that any GW signals that are emitted from coalescing NS binaries are too far from the manifold of waveforms that we use as templates in our search pipelines. It is true that such a scenario cannot be discarded, since the highly relativistic regime of CBC signals is a completely experimentally uncharted territory, while at the same time our search pipelines require rather accurate modelling in order to be efficient.[10]

Since the waveform being in phase throughout the entire inspiral is so important for achieving a high fitting factor, we expect the most sensitive measurements of GR violations to come from effects in the GW phase evolution. Many interesting alternative theories of gravity induce non-GR effects in the phase evolution by modifying the conservative and/or dissipative sector. For example, to leading order, the effect for Brans-Dicke theory shows as a -1PN term in the phase, for Quadratic Curvature as a modification at 2PN, for Massive Gravity at 1PN, for dynamical Chern-Simons at 4.5PN also with a modified amplitude, *etc.* Further information of the leading-order effects of alternative theories of gravity can be found in [134] and references therein.

Once the first few GW signals are detected, one then hopes to check for consistency of the detected waveforms against the predictions of GR. Given the strong contribution of the noise and the richness of the 15-dimensional space spanned by CBC waveforms, the task of establishing the consistency of the detected signals with GR, or a violation thereof, is a rather challenging one. One therefore needs to make use of the most sophisticated, reliable and efficient data analysis tools at one's disposal.

4.5.1 Previous efforts

Over the last two decades, an increasing interest has grown in GW data analysis, motivated by the good prospects for the first detection in the near future. This has led to a number of studies proposing tests of GR with GW signals [51]. Compact binary coalescence holds a prominent place among the studied sources, being the best modelled type of source, with a high estimated chance for detection.

A Fisher matrix approach for testing the consistency of the phase of a CBC signal with GR was studied in [49, 264]. Its basic idea, similarly to the PK-parametrized test for binary pulsars [231], is to measure three or more of the PN coefficients ψ_i in the waveform's phase, and check the consistency of the measured values with

---

[10]Moreover, as argued *e.g.* in [79], a number of promising alternative theories of gravity may manifest their GR-violating nature only in the presence of matter and still appear indistinguishable from GR in *e.g.* the pure-spacetime vicinity of a black hole.

the GR predictions on the m_1-m_2 plane. An optimization of the above method using singular-value decomposition in the CBC signal is performed in [283]. Other Fisher matrix investigations, this time on performing BH spectroscopy with the LISA space-based GW detector, can be found in [75, 76, 77, 78]. More recently, a first Bayesian study, targeted to test GR against a simple massive graviton theory, was performed in [154].

4.5.2   Towards a generic Bayesian method

Given the dominant role of noise in the data and the high dimensionality of the signal parameter space, it is clear that a Bayesian approach is imperative for the purpose of GW data analysis. Furthermore, a good candidate method for testing GR with GW signals should feature a number of desiderata that are listed below.

Desiderata

- The method needs to be *theory independent*, in the sense that its assumptions should not be inspired by any particular alternative theory of gravity.

- The required formulation of a negation to the GR hypothesis needs to be parametrizeable, but at the same time sufficiently generic, and should allow for a computationally feasible analysis.

- Any methodologies and algorithms used should yield reliable results for signals of low SNR (close to the detection threshold), as will be the case for the majority of detections.

- It should be straightforward to combine information from multiple independent detections.

- The method should be adaptable and not tied to a particular waveform approximant.

- The method should be robust against uncontrollable sources of systematic errors, such as waveform modelling inadequacies and instrumental calibration errors.

In 2011, a new Bayesian model selection method for testing GR using CBC signals was put forward by Li et al. [245, 246], which seems to be satisfying all of the above criteria. It is based on the formulation of a *modGR hypothesis*, that exploits the sensitivity of the CBC signals in small changes in the evolution of the phase accumulating over the entire in-band duration of the inspiral. As we will show in Chapters 5, 6, 7 and 8, this has developed into a mature and robust computational pipeline, that will be used in the science runs of the upcoming GW experiments aLIGO and AdVirgo [32, 33, 34, 2].

The expectations for such a Bayesian analysis are enormous, if one even naively compares its sensitivity with bounds coming from the most stringent tests that are currently available. If the *double pulsar* measurements [251, 231] for the orbital period decay PK parameter $\frac{\dot{P}_b}{P_b}$ are naively translated into the amplitude and phase *ppE* parameters $\{\alpha, a\}, \{\beta, b\}$ (see [393]),

$$|\alpha| \leq \frac{\delta}{2\eta^c (\pi \mathcal{M}_c f)^a} \quad , \quad |\beta| \leq \frac{5}{48|b||b-1|} \frac{\delta}{\eta^d (\pi \mathcal{M}_c f)^{b+5/3}} \tag{4.13}$$

then bounds on the latter can be derived, based on the uncertainty $\delta \simeq 0.017$ of the measurement. Setting $\eta = 0.249703$, $\mathcal{M}_c = 1.12525 M_\odot$ and $f = 2.263842976 \times 10^{-4}$ Hz, which are the observed values for the double pulsar, and neglecting eccentricity, one obtains the excluded region for the phase amplitude $|\beta|$ as a function of the phase exponent b to be the grey shaded region of Fig. 4.2. As we shall see in the following chapters, the phase sensitivity of GW detections is so high, that a similar bound for BNS will fall several orders of magnitude below these double pulsar bounds. The coloured circles in Fig. 4.2 represent the estimated single-source sensitivity of TIGER, the Bayesian pipeline that will be described in Chapter 5, assuming a network of two aLIGO and one AdVirgo detectors at design sensitivity. These bounds are estimated in Sec. 6.5 for violations of GR in the 0.5PN, 1PN, 1.5PN, 2PN and 3PN level, and will get even tighter as information from more than one detected sources is combined. The exact meaning of the quoted $\delta\chi_i$ parameters will become clear in the next chapter. On the lower left panel of Fig. 4.2 the same bounds are plotted directly in the $\delta\chi$ parametrization. Results of our analysis on the first detection, the high-mass BBH signal *GW150914* [24], are also shown in a similar plot (bottom right) as the orange squares and, for 0.5PN onwards, represent (by orders of magnitude) the most stringent constraints on violations of GR to date.

Notice how this BBH event tends to outperform the expected single-source BNS bound at high PN order, but can still be significantly improved at low PN order with the detection of BNS signals (the Newtonian order bound is actually weaker than the binary pulsar tests). Indisputably, this is due to the fact that BNS systems are observeable since much earlier in their inspiral, and for a longer time at low frequencies and slow orbital velocities; therefore these yield considerably more information on the low-PN regime.
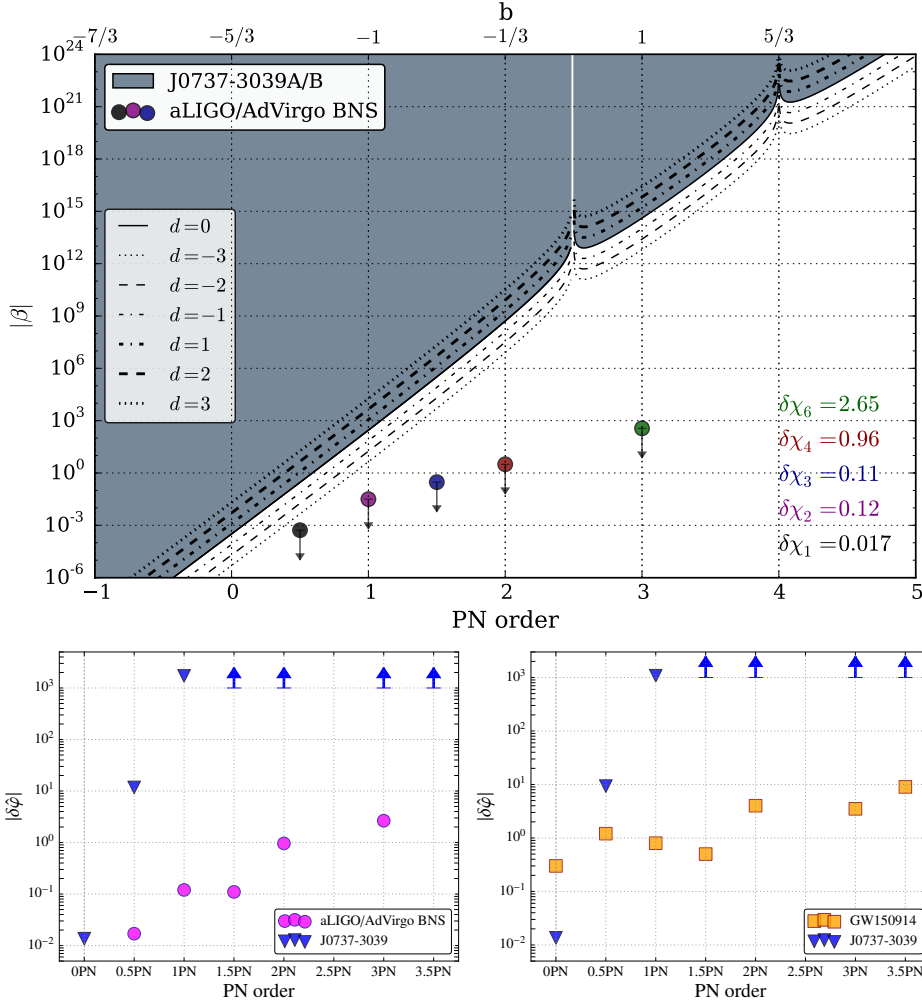
Figure 4.2: *Top: Parameterized violations of GR: shaded region is excluded based on observations of the double pulsar (reconstructed from [393]). Black curves represent bounds for different values of d in Eq. (4.13). Colored circles show estimated bounds from a single BNS detection and analysis with TIGER, for GR-violations at $0.5PN$ (black), $1PN$ (purple), $1.5PN$ (blue), $2PN$ (red) and $3PN$ (green) order in the phase. Quoted $\delta\chi_i$ values correspond to relative shifts in the PN phase terms, $i = 3b + 5$. Bottom: (left) the same bounds in a parametrization based on the post-Newtonian inspiral phase coefficients; (right) our recent analysis on GW150914 resulted in the bounds shown in orange squares [24]. Due to the small number of inspiral cycles observed, we still cannot beat the binary pulsar tests at Newtonian order, but already at $0.5PN$ our new bound is a factor of 10 better than the existing bound, but the ones at higher orders are beating pulsar binaries by many orders of magnitude ($\sim 10^9$ in the case of 3PN).*
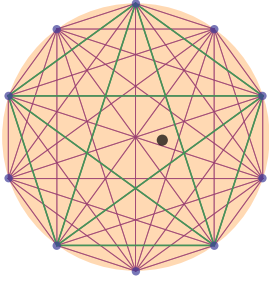
TIGER: Test Infrastructure for GEneral Relativity

What is especially striking and remarkable is that in fundamental physics a beautiful or elegant theory is more likely to be right than a theory that is inelegant.

Murray Gell-Mann

Given a set of GW signals from compact binary coalescence, one would like to test the consistency of the observed data with GR. In the absence of a particular preferred alternative theory, it is a challenging task to attempt to compare GR against "anything else" in a realistic and computationally feasible way. It is however possible, given the knowledge of the family of signals considered, to devise a test of the *GR hypothesis*, against a *modGR hypothesis* that is generic enough to accommodate the important features of virtually any promising alternative.

In the post-Newtonian approximation discussed earlier, the dominant (22)-mode of the gravitational waveform is given by an evolving amplitude and a PN-expanded expression for the phase evolution. Here (22) refers to the $l = 2$, $m = 2$ eigenfucntion, in the (-2)-spin-weighted spherical harmonic decomposition $-2Y^{l,m}$ of the GW tensor field [353]. Any alternative theory of gravity will predict a modified expression for the evolution of the amplitude and/or phase.

Here one should note that the amplitude as an observable explicitly depends on the extrinsic parameters of the system (distance, inclination, sky location, polarization) with respect to the detectors. This introduces a number of degeneracies within a common pre-factor, as can be seen in Eq. (2.9). In addition, during the evolution of a binary with non-aligned spins, the observed inclination and polarization angles may change due to precession, which will introduce modulations in the amplitude (see *e.g.* Fig. 2.1). Further information that would un-correlate the

different parameters that enter the GW amplitude could in principle be obtained by measuring the higher order modes [360, 361, 279]. It is however unlikely that such a measurement will be significant with second generation GW detectors, and for stellar-mass coalescences, since the amplitude of the leading 0.5PN correction due to a factor of v/c is roughly one order of magnitude smaller for most of the visible inspiral.

The phase evolution on the other hand, gives a rich structure to the waveform, and as an observable is a quantity that follows the rapid angular evolution of the binary orbit (in fact, the 22 phase grows twice as fast as the orbital phase). In terms of detection methods based on optimal filtering and Bayesian inference methods for both model selection and parameter estimation, the accurate description of the phase evolution up to the highest available post-Newtonian order is crucial, since the matching between waveforms is very sensitive to de-phasing. It is important to keep the total number of GW cycles accurate to the level of $O(1)$ cycles.

We thus choose to build our modGR hypothesis on deviations from the GR-predicted phase evolution. For PN waveforms, it is straightforward to devise a parametrization of possible deviations, by modifying the GR-predicted values of the phase PN-expansion coefficients $\{\psi_i\}$. We parametrize these deviations by the *relative shifts* $\delta\chi_i$

$$\psi_i^{GR} \to \psi_i = \psi_i^{GR}(1 + \delta\chi_i) \tag{5.1}$$

in any of the i-th PN phase coefficients.

Alternatively, a different choice could be a phase-only version of the more general ppE parametrization, where one or more additional terms of the form $\psi_{ppE} = \psi^{\mathrm{GR}}(1 + \beta\eta^d(\pi\mathcal{M}_c f)^b)$ are introduced in the phase, with arbitrary magnitude β and frequency and η exponents b, a. This is a generic model which can in fact accommodate a huge variety of alternative models, it is however too generic to be used as a realistic model for data analysis, since each such term introduces 3 additional free parameters.

5.1   The 'I' of the TIGER

We now move to a more technical discussion regarding the details of the TIGER method. Since this is essentially a Bayesian model selection method, it is necessary to carefully

- define the competing hypotheses and express them in terms of well defined model hypotheses,

- define the parameter manifold Σ_H for each model hypothesis H,

- assign prior probability densities $p(\theta|H,\mathcal{I})$ on each parameter space,

- define the likelihood function $p(d|\theta, H, \mathcal{I})$, for each model hypothesis,

- assign a prior probability $P(H|\mathcal{I})$ to each hypothesis.

5.1.1 Definition of the hypotheses

Even though TIGER is not tied to a particular waveform model and can in principle be formulated with any parametrized family, it will be instructive for the purposes of the current work to quote the general class of inspiral post-Newtonian waveforms as a working example.

Waveform model The model waveform for the GR hypothesis should ideally be the best CBC template that is available to us. However, given the computational budget that a Bayesian analysis with expensive template waveforms would require, one needs to settle for less accurate but sufficiently realistic waveforms. In the current study the stationary phase approximation is employed and this is shown to be good enough for BNS systems (cf. Sec. 2.4). It is a frequency-domain template family, often referred to as *TaylorF2* and falls within the general class of PN inspiral templates. Regarding the spin parameters, TaylorF2 can only accommodate aligned spins, as shown explicitly in Eq. (2.45) and thus does not feature amplitude modulations or any other precession-related effects.

In terms of the order in the post-Newtonian framework, the GW amplitude will be restricted to Newtonian order [1], while the phase will be expanded to the highest known order which is currently 3.5PN, unless stated otherwise. The former truncation means in particular that higher harmonics will not be considered here and the signal consists of the dominant (22) mode alone. For a discussion on higher harmonics see *e.g.* [48] and references therein.

$\mathcal{H}_{\mathrm{GR}}$

The *GR hypothesis* postulates that the data of each detector comprises noise $\tilde{n}(f)$, which is described by a random variable (independent identically distributed with respect to time) in $\mathbb{R}^{n_{\mathrm{bins}}}$ following a p.d.f. that is defined by a given noise power spectral density as explained in Sec. 1.6, plus a GW signal $\tilde{h}_{\mathrm{GR}}(f)$ coming from a CBC of undetermined parameters, which is described by a GR waveform. The parameter space $\Sigma_{\mathcal{H}_{\mathrm{GR}}}$ for $\mathcal{H}_{\mathrm{GR}}$ is the standard 15-dimensional space for CBC (see p. 26), parametrized by

$$\vec{\theta}_{GR} = \{m_1, m_2, \vec{s}_1, \vec{s}_2, D, \alpha, \delta, \iota, \psi, t_c, \phi_c\}. \tag{5.2}$$

The data are then modelled in the frequency domain for each detector as

$$\tilde{d}(f) = \tilde{n}(f) + \tilde{h}_{\mathrm{GR}}(f; \vec{\theta}_{\mathrm{GR}}), \tag{5.3}$$

---

[1]This is also known as *restricted TaylorF2*.

while it is understood that the noise $\tilde{n}(f)$ is independent among non-co-located detectors. Moreover, even though the intrinsic part of the signal is common in all detectors, the final GW strain waveform $\tilde{h}_{GR}(f; \vec{\theta}_{GR})$ itself is derived through a transformation according to the detector's antenna pattern and the extrinsic parameters of the source, as in Eq. (1.75), (1.80).

Considering for example SPA waveforms, $\tilde{h}_{GR}(f)$ takes the form of Eq. (2.28) where all post-Newtonian phase coefficients have the GR-predicted functional dependence on the intrinsic parameters of the system, as in Eq. (2.29) and (2.45).[2]

$\mathcal{H}_{\mathrm{modGR}}$

The *modGR hypothesis* postulates that the data of each detector comprise noise $\tilde{n}(f)$, which is described in the same way as in $\mathcal{H}_{\mathrm{GR}}$, plus a GW signal coming from a CBC of undetermined parameters, whose waveform is modelled by an extended version of the GR template, where an arbitrary subset of the test coefficients *do not* have the GR-predicted functional dependence on the intrinsic parameters.

The latter statement can be translated into the corresponding relative shifts $\delta\chi_i$ being non-zero. The word "arbitrary" in the above definition is of great significance and implies that the modGR hypothesis is not tied to a model waveform with a fixed number of extra parameters. This flexibility overrides the danger of our modGR hypothesis being penalized by Occam's razor, without sacrificing our sensitivity to GR violations. If one gave the modGR hypothesis a fixed large number of free parameters, a Bayesian model selection analysis would penalize the large prior volume of the unnecessary degrees of freedom and would favour the much simpler GR hypothesis, even with a slightly worse match. On the other hand, if one decided to use a particular extension of the parameter space that is too minimal, one may lose sensitivity to possible violations of GR. Instead, we chose to formulate the modGR hypothesis as a composite one with parameter spaces of different dimensionalies being explored.

The parameter space is extended by subsets of N_T additional free parameters which will from now on be referred to as the *test coefficients*. These are the relative shifts $\delta\psi_i$ in the PN coefficients of the phase mentioned in Eq. (5.1). It is not defined here, what the number of test coefficients should be and which subset of the known phase PN coefficients should be let free to shift. These choices

---

[2]The reader should recall that for TaylorF2 in particular, the dimensionality of the parameter space is reduced to $d = 11$, since only (anti-)aligned spins can be considered. In this case the spin vectors Eq. (5.2) should be replaced by spin amplitudes s_1, s_2. Moreover, in part of the investigations that follow, for simplicity non-spinning binaries are considered, in which cases the parameter space will be the restricted 9-dimensional

$$\vec{\theta}_{\mathrm{restr}} = \{m_1, m_2, D, \alpha, \delta, \iota, \psi, t_c, \phi_c\}. \tag{5.4}$$

will be further discussed in Sec. 6.3. For now, we can proceed with the general formulation where the above details are not yet specified.

The reader should keep in mind that currently the number of PN phase coefficients is 7, that is, the most general deviation from GR within the current truncated expansion has 7 additional degrees of freedom. This would significantly enlarge the parameter space Σ' and give a lot of redundant freedom to the waveform. Again, choosing to use an unnecessarily large parameter space for defining an alternative hypothesis is usually not a good idea, since even though it has a bigger chance of closely representing the true signal , the actual gain in knowledge on the nature of the signal will be poor. In more technical terms, the extra contribution in the evidence, coming from the region of the parameter space in $\Sigma'\backslash\Sigma_{\mathcal{H}_{\mathrm{GR}}}$ where the likelihood takes values larger than what was obtained on the peak of $\Sigma_{\mathcal{H}_{\mathrm{GR}}}$, will be diffused away due to the large integration volume. So even if the augmented model fits the data slightly better for some values of the extra parameters, the simpler model with less degrees of freedom will still be preferred if the difference is not significant enough. This is a realization of Occam's razor in Bayesian model selection.

With this in mind one would prefer to opt for a rudimentary extension of the GR model. On the other hand the modGR hypothesis still needs to remain generic enough to fit as much of the infinitely many possible violations of GR as possible. This highlights the importance of letting the subset of test coefficients that are postulated to violate GR be arbitrary.

We now split the modGR hypothesis –with a set of N_T test coefficients $\{\delta\chi_1,\ldots,\delta\chi_{N_T}\}$– into a complete set of logically disjoint sub-hypotheses as

$$\mathcal{H}_{\mathrm{modGR}} = \bigvee_{I\in\mathcal{P}^{\{1,\ldots,N_T\}}} H_I \tag{5.5}$$

where $I = i_1 i_2 \cdots i_k$ is a collective index with i_m corresponding to a test coefficient index and $\mathcal{P}^X$ denotes the *power set* (the set of all subsets) of X.[3]

In the above expression the *model* corresponding to each of the sub-hypotheses H_I extends the GR model by a subset I of the test coefficients. For instance, in the SPA approximation this is thus described by the model waveform

$$\begin{aligned}
\tilde{h}_{H_I}(f;\vec{\theta}_{H_I}) &= \mathcal{A}\, e^{i\Psi_{H_I}(f;\vec{\theta}_{H_I})} \\
\Psi_{H_I}(f;\vec{\theta}_{H_I}) &= \Psi_{\mathrm{GR}}(f;\vec{\theta}_{\mathrm{GR}}) + \frac{3}{128\eta}\sum_{i\in I}\psi_i\,\delta\chi_i(\pi M f)^{\frac{i-5}{3}}
\end{aligned} \tag{5.6}$$

where $\vec{\theta}_{H_I} = \vec{\theta}_{GR}\otimes(\delta\chi_{i_1},\ldots,\delta\chi_{i_k})$ belongs to the extended parameter space $\Sigma_{H_I}\simeq\Sigma_{\mathcal{H}_{\mathrm{GR}}}\times\mathbb{R}^k$.

A similar definition for the $\mathcal{H}_{\mathrm{modGR}}$ hypothesis and for the models of its sub-hypotheses can be made for time-domain PN waveforms using the corresponding phase PN coefficients.

---

[3]For example, if $N_T = 2$, then $\mathcal{P} = \{\{1\},\{2\},\{12\}\}$ and the $\mathcal{H}_{\mathrm{modGR}}$ decomposes to $H_1\vee H_2\vee H_{12}$. Note that we exclude the empty set, which would simply correspond to $\mathcal{H}_{\mathrm{GR}}$.

5.1.2 Likelihood and Evidence

One of the central ingredients for setting up a proper statistical analysis is the definition of the likelihood function. The explicit form encodes our best guess about the noise, or in other words about the behaviour of our instrument and its environment. For each individual detector I, the likelihood for the observed data $\tilde{d}_I$ to occur in the frequency domain, given a system with parameters $\vec{\theta}_H$ within the model hypothesis H, is given by Eq. (3.12), *i.e.*

$$p(d|\vec{\theta}_H, H, \mathcal{I}) = e^{-\frac{1}{2}(\tilde{d}_I - \tilde{h}_H | \tilde{d}_I - \tilde{h}_H)} = e^{-2\Re\left\{\int_0^\infty df \frac{\tilde{h}_H^* \tilde{d}_I^*}{S_n(f)}\right\}}, \qquad (5.7)$$

where H will be $\mathcal{H}_{\mathrm{GR}}$ or any of the H_I. The likelihood of the noise being the only component of the data is of course derived by setting the signal to zero.

In Sec. 3.4.1 we saw how the evidence for a hypothesis is obtained from the likelihood function. For $\mathcal{H}_{\mathrm{GR}}$ the calculation of the evidence

$$P(d|\mathcal{H}_{\mathrm{GR}}, \mathcal{I}) = \int_{\Sigma_{\mathcal{H}_{\mathrm{GR}}}} d\vec{\theta}_{\mathcal{H}_{\mathrm{GR}}} \, p(d|\vec{\theta}_{\mathcal{H}_{\mathrm{GR}}}, \mathcal{I}) \, p(\vec{\theta}_{\mathcal{H}_{\mathrm{GR}}}|\mathcal{H}_{\mathrm{GR}}, \mathcal{I}) \qquad (5.8)$$

is performed by means of a numerical integration over the standard parameter space $\Sigma_{\mathcal{H}_{\mathrm{GR}}}$ using *e.g.* the nested sampling algorithm described in Sec. 3.3.2.

For $\mathcal{H}_{\mathrm{modGR}}$ on the other hand, the evidence will in practice have to be calculated for each sub-hypothesis H_I individually as

$$P(d|H_I, \mathcal{I}) = \int_{\Sigma_{H_I}} d\vec{\theta}_{H_I} \, p(d|\vec{\theta}_{H_I}, \mathcal{I}) \, p(\vec{\theta}_{H_I}|H_I, \mathcal{I}), \quad I \in \mathcal{P}^{\{1,\ldots,N_T\}} \qquad (5.9)$$

where the numerical algorithm samples the extended parameter space Σ_{H_I} using the appropriate model waveforms Eq. (5.6).

5.1.3 The odds ratio

For the purpose of model selection, evidences of different hypotheses are compared and together with the prior ratio form the odds ratio for model selection. In this section we will work towards explicitly defining the odds ratio for TIGER which will be our main statistic that we can actually calculate.

Recall from Sec. 3.4.1 that the odds ratio between our competing hypotheses $\mathcal{H}_{\mathrm{GR}}, \mathcal{H}_{\mathrm{modGR}}$, given a set of data d, is defined by the ratio of the hypotheses' posterior probabilities:

$$O_{\mathrm{GR}}^{\mathrm{modGR}} = \frac{P(\mathcal{H}_{\mathrm{modGR}}|d, \mathcal{I})}{P(\mathcal{H}_{\mathrm{GR}}|d, \mathcal{I})}. \qquad (5.10)$$

Since $\mathcal{H}_{\mathrm{modGR}}$ is decomposed into a set of disjoint sub-hypotheses, we can re-express the odds ratio as

$$O_{\mathrm{GR}}^{\mathrm{modGR}} = \frac{P(\bigvee_{I \in \mathcal{P}^{\{1,\dots,N_T\}}} H_I | d, \mathcal{I})}{P(\mathcal{H}_{\mathrm{GR}} | d, \mathcal{I})} = \sum_{I \in \mathcal{P}^{\{1,\dots,N_T\}}} \frac{P(H_I | d, \mathcal{I})}{P(\mathcal{H}_{\mathrm{GR}} | d, \mathcal{I})}. \qquad (5.11)$$

This is a sum of $2^{N_T} - 1$ terms, since the empty-set sub-hypothesis corresponds to $\mathcal{H}_{\mathrm{GR}}$ and is not taken into account.

Using Bayes' law Eq. (3.8), one may recast Eq. (5.11) as

$$O_{\mathrm{GR}}^{\mathrm{modGR}} = \sum_{I \in \mathcal{P}^{\{1,\dots,N_T\}}} \frac{P(d | H_I, \mathcal{I})}{P(d | \mathcal{H}_{\mathrm{GR}}, \mathcal{I})} \frac{P(H_I | \mathcal{I})}{P(\mathcal{H}_{\mathrm{GR}} | \mathcal{I})}, \qquad (5.12)$$

turning the odds ratio into a sum of likelihood ratios or *Bayes factors* times *prior ratios*. The prior ratios may be further simplified if we agree on assigning the same prior probability to each of the GR-violating sub-hypotheses, *i.e.* setting

$$\frac{P(H_I | \mathcal{I})}{P(\mathcal{H}_{\mathrm{GR}} | d, \mathcal{I})} = \frac{P(H_J | \mathcal{I})}{P(\mathcal{H}_{\mathrm{GR}} | d, \mathcal{I})} = \frac{\alpha}{2^{N_T} - 1}, \quad \forall I, J \in \mathcal{P}^{\{1,\dots,N_T\}}, \qquad (5.13)$$

while still keeping the overall prior ratio $\frac{P(\mathcal{H}_{\mathrm{modGR}} | \mathcal{I})}{P(\mathcal{H}_{\mathrm{GR}} | d, \mathcal{I})} = \alpha$ arbitrary. Then the common prior ratio drops out as a prefactor and we obtain

$$O_{\mathrm{GR}}^{\mathrm{modGR}} = \frac{\alpha}{2^{N_T} - 1} \sum_{I \in \mathcal{P}^{\{1,\dots,N_T\}}} B_{\mathrm{GR}}^I, \qquad (5.14)$$

which is an average of Bayes factors times an arbitrary scale α that quantifies our prior belief that GR is violated in a measurable way. It is useful to already note here that our final results will be invariant with respect to this arbitrary constant (see discussion on background and efficiency in Sec. 6.2.2). This is the general form of our odds ratio, which will become more explicit through the calculation of Bayes factors for a single source or multiple sources in the following sections.

Single source

The data for a single detected source s consists of a set of n data-streams $\{d_s^A\}_{A \in \{1,\dots,n_{IFO}\}}$ (one for each interferometer A), which for simplicity will be collectively denoted by d_s. The odds ratio for a single source is then calculated as in Eq. (5.14), where the Bayes factors read

$$B_{\mathrm{GR}}^I = \frac{P(d | H_I, \mathcal{I})}{P(d | \mathcal{H}_{\mathrm{GR}}, \mathcal{I})} = \frac{\int_{\Sigma_{H_I}} \mathrm{d}\vec{\theta}_{H_I} \, p(d | \vec{\theta}_{H_I}, H_I, \mathcal{I}) \pi_{H_I}(\vec{\theta}_{H_I})}{\int_{\Sigma_{\mathcal{H}_{\mathrm{GR}}}} \mathrm{d}\vec{\theta}_{\mathcal{H}_{\mathrm{GR}}} \, p(d | \vec{\theta}_{\mathcal{H}_{\mathrm{GR}}}, \mathcal{H}_{\mathrm{GR}}, \mathcal{I}) \pi_{\mathcal{H}_{\mathrm{GR}}}(\vec{\theta}_{\mathcal{H}_{\mathrm{GR}}})}. \qquad (5.15)$$

Catalogue of n sources

One of the strongest virtues of TIGER, and of Bayesian data analysis in general, is the straightforward way in which data from different events may be combined into a single overall result. Consider the scenario where after a certain time of our instruments being operating, our detection algorithms suggest that a number n of individual sources $\{s_1, \ldots, s_n\}$ were detected at different times, with sufficiently high confidence. Based on the above calculations, we know how to calculate the odds ratio for each source individually; we now wish to derive the odds ratio between $\mathcal{H}_{\mathrm{GR}}$ and $\mathcal{H}_{\mathrm{modGR}}$ for a *catalogue* of n sources.

Let us denote entire observed data by $^{(n)}d$ and the stretch of data related to each individual source by $d_{s_i}, \forall i \in \{1, \ldots, n\}$. The evidence of the data being measured under a hypothesis H is then given by a joint probability

$$P(^{(n)}d|H, \mathcal{I}) = P(d_{s_1}, \ldots, d_{s_n}|H, \mathcal{I}). \tag{5.16}$$

Assuming that the data from the individual sources s_i are *pairwise independent* from each other[4], one can make use of the multiplication rule of independent events, turning the joint probability $P(d_{s_1}, \ldots, d_{s_n}|H, \mathcal{I})$ of the entire observed data (evidence) into a product of single-source evidences

$$P(^{(n)}d|H, \mathcal{I}) = \prod_{i=1,\ldots,n} P(d_{s_i}|H, \mathcal{I}). \tag{5.17}$$

We thus define the *multi-source odds-ratio for a catalogue of n sources* as

$$^{(n)}\mathcal{O}_{\mathrm{GR}}^{\mathrm{modGR}} = \frac{P(\mathcal{H}_{\mathrm{modGR}}|\{d_{s_i}\}_{i=1,\ldots,n}, \mathcal{I})}{P(\mathcal{H}_{\mathrm{GR}}|\{d_{s_i}\}_{i=1,\ldots,n}, \mathcal{I})} = \frac{\alpha}{2^{N_T} - 1} \sum_{I \in \mathcal{P}^{\{1,\ldots,N_T\}}} {}^{(n)}B_{\mathrm{GR}}^I. \tag{5.18}$$

The catalogue Bayes factors are defined as

$$^{(n)}B_{\mathrm{GR}}^I = \frac{P(\{d_{s_i}\}_{i=1,\ldots,n}|H_I, \mathcal{I})}{P(\{d_{s_i}\}_{i=1,\ldots,n}|\mathcal{H}_{\mathrm{GR}}, \mathcal{I})} = \prod_{i=1,\ldots,n} \frac{P(d_{s_i}|H_I, \mathcal{I})}{P(d_{s_i}|\mathcal{H}_{\mathrm{GR}}, \mathcal{I})} \tag{5.19}$$

where we made use of Eq. (5.17). We can now recast Eq. (5.18) as

$$^{(n)}\mathcal{O}_{\mathrm{GR}}^{\mathrm{modGR}} = \frac{\alpha}{2^{N_T} - 1} \sum_{I \in \mathcal{P}^{\{1,\ldots,N_T\}}} \prod_{i=1,\ldots,n} \frac{P(d_{s_i}|H_I, \mathcal{I})}{P(d_{s_i}|\mathcal{H}_{\mathrm{GR}}, \mathcal{I})} \tag{5.20}$$

---

[4]That is, the sources themselves are un-correlated and the time of arrival of the GW signals are well apart from each other. The former assumption is practically a trivial one, while the latter will most likely be satisfied for second generation GW detectors, as the rate of CBC detections is expected to be too low for signals to overlap [9].

Example   As a simple example scenario, consider the case where we use $N_T = 2$ test coefficients, $\delta\chi_1$ and $\delta\chi_2$, and we want to derive the odds ratio for a catalogue of $n = 4$ independent sources $\{s_1, s_2, s_3, s_4\}$. The modGR hypothesis is then decomposed into the set of sub-hypotheses $\mathcal{H}_{\mathrm{modGR}} = H_1 \vee H_2 \vee H_{12}$, and the multi-source odds ratio for the *four* sources yields

$$
\begin{aligned}
^{(3)}\mathcal{O}_{\mathrm{GR}}^{\mathrm{modGR}} \;=\; & \frac{\alpha}{3} \sum_{I \in \{1,2,12\}} \prod_{i=1,2,3,4} \frac{P(d_{s_i}|H_I, \mathcal{I})}{P(d_{s_i}|\mathcal{H}_{\mathrm{GR}}, \mathcal{I})} \qquad\qquad (5.21)\\[2mm]
=\; & \frac{\alpha}{3}\left[\frac{P(d_{s_1}|H_1,\mathcal{I})}{P(d_{s_1}|\mathcal{H}_{\mathrm{GR}},\mathcal{I})} \frac{P(d_{s_2}|H_1,\mathcal{I})}{P(d_{s_2}|\mathcal{H}_{\mathrm{GR}},\mathcal{I})} \frac{P(d_{s_3}|H_1,\mathcal{I})}{P(d_{s_3}|\mathcal{H}_{\mathrm{GR}},\mathcal{I})} \frac{P(d_{s_4}|H_1,\mathcal{I})}{P(d_{s_4}|\mathcal{H}_{\mathrm{GR}},\mathcal{I})} \right.\\[2mm]
+\; & \frac{P(d_{s_1}|H_2,\mathcal{I})}{P(d_{s_1}|\mathcal{H}_{\mathrm{GR}},\mathcal{I})} \frac{P(d_{s_2}|H_2,\mathcal{I})}{P(d_{s_2}|\mathcal{H}_{\mathrm{GR}},\mathcal{I})} \frac{P(d_{s_3}|H_2,\mathcal{I})}{P(d_{s_3}|\mathcal{H}_{\mathrm{GR}},\mathcal{I})} \frac{P(d_{s_4}|H_2,\mathcal{I})}{P(d_{s_4}|\mathcal{H}_{\mathrm{GR}},\mathcal{I})}\\[2mm]
+\; & \left.\frac{P(d_{s_1}|H_{12},\mathcal{I})}{P(d_{s_1}|\mathcal{H}_{\mathrm{GR}},\mathcal{I})} \frac{P(d_{s_2}|H_{12},\mathcal{I})}{P(d_{s_2}|\mathcal{H}_{\mathrm{GR}},\mathcal{I})} \frac{P(d_{s_3}|H_{12},\mathcal{I})}{P(d_{s_3}|\mathcal{H}_{\mathrm{GR}},\mathcal{I})} \frac{P(d_{s_4}|H_{12},\mathcal{I})}{P(d_{s_4}|\mathcal{H}_{\mathrm{GR}},\mathcal{I})} \right].
\end{aligned}
$$

5.2   Sensitivity in modified phase coefficients

Let us now estimate the changes in the waveform that a relative shift in one of the phase PN coefficients would induce, for a typical BNS system with zero spins. This will give us a rough estimate on the sensitivity of TIGER with respect to the different phase PN coefficients. First we observe the special properties of some of the terms in the expansions of Eq. (2.29) and 5.6:

- The 0.5PN term is zero in GR ($\psi_1 = 0$). This does not trivially hold for alternative theories of gravity. It is thus impossible to parametrize a *relative* shift in this term, so one needs to define a shift in absolute value, if necessary.

- The 2.5PN term is the turning point in the expansion where the frequency dependence $f^{\frac{i-5}{3}}$ switches from negative powers of f to positive powers. The term itself ($i = 5$) is an overall constant and is thus completely *degenerate with the phase at coalescence* parameter ϕ_c in the SPA.

- Tail effects, which will give the first hints of GR non-linear self-interaction that have ever been measured, enter at 1.5PN in ψ_3 [389, 100]. This is the same order in which the leading order spin-orbit effects appear, as discussed in Sec. 2.4.2.

- At 2PN, the leading order spin-spin effects appear, as well as the spin-induced "*quadrupole-monopole*" (QM) terms; both of them however are expected to be very small for slowly spinning neutron star components.

- The first unknown term is at 4PN order, the would-be ψ_8. This however is again not measurable, since it goes as $\sim f$ and would be completely

degenerate with the $2\pi f t_c$ term in the SPA Eq. (2.29), that is with the *time of coalescence* parameter. The consideration or GR-violating shift of such a term would only result to a bias in the estimation of the arrival time of the signal to $\mathcal{O}(1)$ ms (assuming a value of the order ψ_6).

- Leading order tidal effects, due to the NS's finite-sized matter distribution, enter at 5PN with a very large pre-factor (see Sec. 2.6.1) which makes them a potentially measurable source of bias for TIGER if not accounted for. The point-particle 5PN contribution is not yet known. The impact of tidal effects as nuisance in our TIGER analysis will be studied in Sec. 7.2, while a dedicated analysis on the measurement of tidal effects will be the subject of Part III.

With a closer examination of Eq. (5.6) one observes that modifying different phase coefficients with the same relative shift will induce effects of different sizes in the waveform. This occurs both because of the differences in the values of the PN coefficients themselves, and the differences in the frequency dependence for each term in the expansion. The plot in Fig. 5.1 summarizes the rate at which the total number of GW cycles changes, with a modification of any of the phase PN coefficients, as a function of η. The total number of cycles N_{tot} is calculated as in Eq. (2.31) starting from 20 Hz and going up to the frequency of LSO, and has a linear dependence on each of the relative shifts $\delta\chi_i$. For example, this means that, according to the first plot of the sequence, a 10% deviation in the 1PN coefficient ψ_2 will modify N_{tot} by ~ 11 cycles. The result scales with the chirp mass as $\mathcal{M}_c^{\frac{i-3}{5}}$ and here we have fixed it to the value of a typical BNS system $\mathcal{M}_c = 1.22 M_\odot$.

It is clear that the waveform is more sensitive to modifications of phase coefficients of lower PN order. The overall sensitivity of a post-detection analysis to such modifications will most essentially depend on how much the waveform changes "in the bucket", that is, in the frequency range where the detector is the most sensitive. This is more appropriately illustrated by a change in the *number of useful cycles*, given by Eq. (2.33) where the density of waveform cycles is weighted by a signal amplitude-over-noise measure.
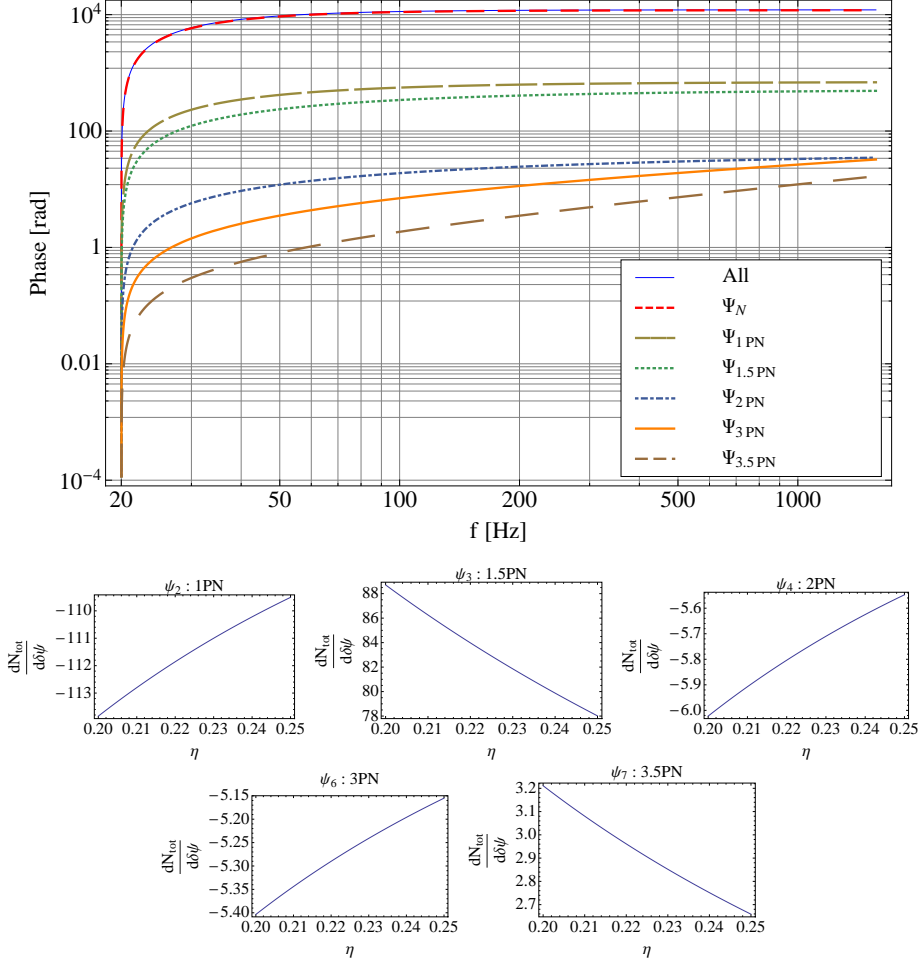
Figure 5.1: *(a) Evolution for the phase terms of different PN order with frequency, for a BNS system of $(1.4, 1.4)M_\odot$. (b) The change in the total number of GW cycles N_{tot} per unit (100%) deviation of each phase PN coefficient ψ_i, starting from $f_{min} = 20$ Hz and going up to $f_{max} = f_{LSO} = \frac{1}{\pi 6^{3/2} M}$. The chirp mass is fixed to $1.22 M_\odot$ and the results scale as $\mathcal{M}_c^{\frac{i-3}{5}}$.*

5

Performance of TIGER with BNS signals

6

As a proof of principle, we now turn to assessing the performance of the TIGER method under a simplified scenario, involving the analysis of data from a set of detected binary neutron star signals, with a network of three second generation GW interferometers. Our preference towards analyzing signals from BNS inspirals in particular is twofold: on the one hand, based on astrophysical observations we are certain that these sources do exist and we have good reasons to believe that they will be among the most frequently observable kinds (see expected detection rates in Sec. 2); on the other hand, we know that the available post-Newtonian waveform models are reliable and accurate enough (with good *faithfulness* and *effectualness* as defined in [114]) within the region of parameter space that covers BNS systems. The expected distribution of NS masses, according to the available population of pulsars falls within a narrow range, which restricts the mass ratio parameter to comparable-mass values. Furthermore, there is observational evidence that neutron stars are slowly spinning objects (in comparison with a typical black hole), with $\chi < 0.02$ in existing measurements [248] and a strict theoretical upper bound of $\chi \lesssim 0.7$ [188, 187]. This too allows us to restrict to a well behaved region of the spin parameter space where existing waveform models can be safely used as templates. Possible issues may however arise due to matter effects of unknown magnitude, since the properties of NS matter are largely uncertain. This discussion is postponed to Chapter 7.

6.1   Construction of a background of GR sources

6.1.1   Motivation

In spite of the rigour with which the above Bayesian analysis has been set up, one will in practice need to be extra careful when claiming an apparent consistency of the data with GR or a discrepancy thereof. If one takes the raw numbers calculated for the odds ratios at face value, one's analysis is sure to be vulnerable to systematic errors introduced by a number of uncontrollable factors. This is particularly evident in the case of CBC data analysis, where the high dimensionality of the parameter space requires sophisticated algorithms that may sacrifice some accuracy in favour of computational efficiency. It is clear from Eq. (5.15) that the calculation of the odds ratio itself involves numerical integration processes over high-dimensional spaces. This fact alone introduces a sizeable error [365] estimated to be of order $\mathcal{O}(1)$ in the *logarithm* of $O_{\mathrm{GR}}^{\mathrm{modGR}}$. Furthermore, the complexity of the problem of solving the two-body problem in GR does not lead to a single accurate analytical description but is treated perturbatively as in the PN formulation, where different approaches lead to different balances between computational speed and accuracy. Since the analysis implicitly assumes that the noise spectrum is given, additional sources of systematics may be present, related to features in the instrumental noise that are difficult to understand and may vary with time. A number of such effects will be studied extensively in Chapters 7, 8.

For the moment it is enough for the reader to realize the necessity of constructing a *background distribution* for our statistic $O_{\mathrm{GR}}^{\mathrm{modGR}}$, populated by a number of sources that are consistent with GR. Knowing what TIGER would yield if GR was the true underlying theory will help with assessing the significance of a real-life measured value for the odds ratio. The reader should also observe that the waveforms used as simulated signals (*injection* waveforms) do not need to (and in principle should not) belong to the same waveform family that is optimally used for analysis (*recovery* waveforms). The background will then pick up any waveform discrepancy as a potential violation of its GR approximation, which will have an impact on the width and shape of the distribution. One is therefore free to choose the most realistic set of waveforms available, however computationally expensive, to be used for simulating the true waveform as accurately as possible, and leave any potential disagreements with the recovery waveforms to feature in the background distribution.

6.2 Statistical assessment of a measurement

6.2.1 Definition of the false alarm probability and significance

In Sec. 6.3 and 6.3.1 we will establish a simple background distribution for our statistic $O_{\mathrm{GR}}^{\mathrm{modGR}}$, against which a real measurement can be compared. One may then move on to simulating sets of BNS sources within a scenario where the true underlying theory of gravity gives a phase evolution different from GR. After calculating an odds ratio for a catalogue of such sources, we may then contrast the result against the pre-calculated background and see whether we can indeed classify –with good confidence– our observed sources as non-GR.

We will quantify our confidence for a non-GR measurement by means of a *false alarm probability* (FAP), which is calculated as the fraction of the background that lies above a given catalogue's calculated value. This is essentially the same procedure as calculating a p-value in a frequentist analysis. In particular, for a measured log-odds ratio $\overline{^{(n)}\mathcal{O}_{\mathrm{GR}}^{\mathrm{modGR}}}$ of a catalogue of n sources, the *significance* β, or the *false alarm probability* (FAP) $1-\beta$ for it to be interpreted as a GR violation is defined as

$$1 - \beta \;\; = \;\; \int_{\overline{O_{\mathrm{GR}}^{\mathrm{modGR}}}}^{\infty} \mathrm{d}O_{\mathrm{GR}}^{\mathrm{modGR}} \; P(O_{\mathrm{GR}}^{\mathrm{modGR}}|\kappa,\mathcal{I}) \tag{6.1}$$

$$= \;\; \int_{\ln \overline{O_{\mathrm{GR}}^{\mathrm{modGR}}}}^{\infty} \mathrm{d}\ln O_{\mathrm{GR}}^{\mathrm{modGR}} \; P(\ln O_{\mathrm{GR}}^{\mathrm{modGR}}|\kappa,\mathcal{I}) \tag{6.2}$$

Given a finite number of simulations, there will always exist a value above which the measured FAP is exactly zero. Theoretically however, in the limit of infinitely many measurements, the tails of the background distribution should extend to infinity. For reasons of scientific consensus it is customary to agree upon a FAP threshold, in the order of $\sim 1\%$ or less, or equivalently a significance of $\sim 99\%$ or more. This threshold β_0 can be mapped to a threshold $\mathcal{O}_0$ in the odds ratio statistic, defined implicitly by

$$1 - \beta_0 = \int_{\ln \mathcal{O}_0}^{\infty} \mathrm{d}\ln O_{\mathrm{GR}}^{\mathrm{modGR}} \; P(\ln O_{\mathrm{GR}}^{\mathrm{modGR}}|\kappa,\mathcal{I}). \tag{6.3}$$

The chosen β_0 threshold is usually referred to as the *significance level* at which the measurement or non-measurement of a violation is quoted. Any measurement lying above (below) the threshold value $\mathcal{O}_0$ will be quoted to be violating (consistent with) GR at a β_0 significance level, or with FAP less than $1 - \beta_0$. This is depicted schematically in Fig. 6.1.

6.2.2 Measurability of a GR-violating scenario

In the above discussion we were concerned with contrasting a real measurement against a populated background. Let us now assess how measurable a *given* type
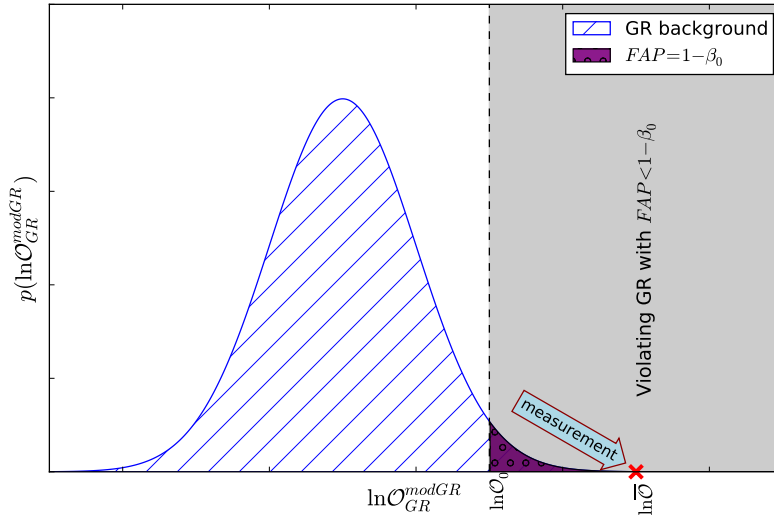
Figure 6.1: *Schematic description of a* background distribution *for* $\ln O_{\mathrm{GR}}^{\mathrm{modGR}}$ *(solid curve bounding hatched region). A FAP of* $1-\beta_0$ *(represented by the purple shaded area under the curve), defines a threshold value* $\mathcal{O}_0$ *for the odds ratio (dashed vertical line). The red X marks a measurement* $\overline{\mathcal{O}}$ *that falls beyond the threshold (grey region) and therefore does violate GR at a* β_0 *significance.*
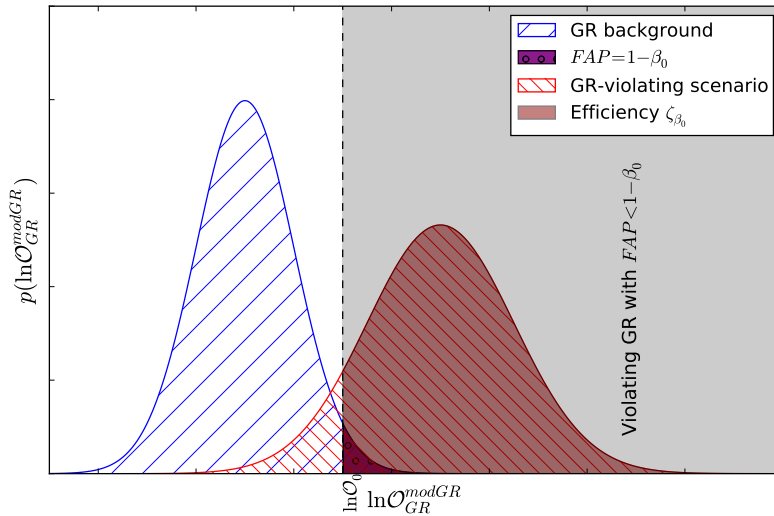
Figure 6.2: *Schematic plot similar to Fig. 6.1, but now showing the efficiency* ζ_{β_0} *(red shaded region) of a GR-violating* foreground distribution *(red solid curve bounding hatched region) with respect to the background and for a given FAP* $1-\beta_0$*. The foreground represents the probability density of measuring a* $\mathcal{O}_{\mathrm{GR}}^{\mathrm{modGR}}$ *value, assuming that the underlying theory gives a particular violation of GR.*

of deviation from GR will be, at some significance level β_0. By populating a *foreground* of simulated catalogues we can estimate the probability of classifying a catalogue of this nature as a non-GR catalogue with FAP less than a given threshold $1 - \beta_0$. This probability will be referred to as *the efficiency ζ* for a type of GR violation and is a feature of both the background and the type of GR-violation.

Formally, we define the *efficiency ζ_{β_0}* at a FAP $1 - \beta_0$, given a background GR population κ that defines the threshold $\mathcal{O}_0$, and a foreground GR-violating population κ' as:

$$\zeta_{\beta_0} = \int_{\ln \mathcal{O}_0}^{\infty} d \ln \mathcal{O}_{\mathrm{GR}}^{\mathrm{modGR}} P(\ln \mathcal{O}_{\mathrm{GR}}^{\mathrm{modGR}} | \kappa', \mathcal{I}) \tag{6.4}$$

This quantity will be calculated for a few individual scenarios of GR violations listed below (without however referring to any particular alternative theory of gravity), and is represented schematically by the shaded area under the red foreground in Fig. 6.2. It is also of interest to see how the efficiency for a given scenario evolves with the number of sources per catalogue. Naturally, the expected behaviour is that of an increasing efficiency with catalogue size, reaching the value 1 in the limit of infinitely many sources and assuming no significant biases being present. More explicit results will be shown towards the end of this chapter.

6.3 Setting up a simple background

In what follows we construct a simple background for the TIGER odds-ratio which we eventually compare against values calculated for sets of GR-violating sources. For the moment our configuration will be minimal, as we will work in a restricted 9-dimensional parameter space, setting the component spins to zero. For BNS systems this is not too far from reality; according to the population of observed NS in binaries to date, the dimensionless spin parameter at the time of coalescence should fall within a narrow range around zero, with the fastest-spinning known case estimated to have $\chi \simeq 0.02$ [248]. However, neutron star spins introduce additional features in the waveform that cannot be matched with restricted templates; we shall return to spinning systems in Chapter 7.

Let us assume a population of sources with an astrophysically realistic set of characteristic properties, such as mass distribution, location, *etc*, which we will collectively denote by κ. Each simulated source that enters our analysis is considered to be an i.i.d. random variable sampled from the population described by κ. When constructing a background, we also assume κ to be consistent with GR, *i.e.* that the GW signals emitted by those sources are described by our best guess of a GR waveform model. The background distribution for $\ln O_{\mathrm{GR}}^{\mathrm{modGR}}$ pertaining to a κ population can then be formally expressed as the real p.d.f. $P(\ln O_{\mathrm{GR}}^{\mathrm{modGR}} | \kappa, \mathcal{I})$.

In practice we numerically populate the background distribution by simulating data from a large enough set of sources (or catalogues of sources) that complies with κ and estimating the odds ratio $\ln O_{\text{GR}}^{\text{modGR}}$ (or $\ln {}^{(n)}\mathcal{O}_{\text{GR}}^{\text{modGR}}$) for each of these datasets. Let us now describe the properties of the first simple background that we will populate and use as the minimal example that demonstrates the performance of TIGER. Apart from the algorithm that will be used, which is the nested sampling algorithm implemented in `LAL` as described in Sec. 3.3.2, what also needs to be defined are the assumptions to be used for generating the *simulated signals* (injection) and the *analysis template waveforms* (recovery).

Simulated signals Here we describe the properties κ of the set of simulated sources that will populate the GR background. In this study we shall only consider zero-spin BNS sources, with component masses ranging in $m_i \in [1, 2]M_\odot$. In principle there is no reason why neutron stars of mass as high as $\sim 3M_\odot$ should not exist, and in fact there is recent evidence of an observed pulsar with a mass marginally larger than $2M_\odot$ [155, 239]. [1] However, hardly any among the candidate models for NS matter allows for the existence of even more massive NS. On the other hand, theoretical limits on the *lowest* possible NS mass may be as low as $0.1M_\odot$, but the lowest *observed* value that is relatively precise (in a binary) is currently $1.05^{+0.45}_{-0.11}M_\odot$ for PSR J1518+4904B[2] [167, 282, 227]. The component masses m_1, m_2 will be sampled from a *uniform mass distribution* in $[1, 2]M_\odot$.

Regarding the distance parameter r the sources will be distributed *uniformly in volume*, in other words, $p(r)\mathrm{d}r \propto \mathrm{d}V = 4\pi r^2 \mathrm{d}r$ and so $p(r) \propto r^2$. The distance range will be set to $[100, 400]$ Mpc, so that a) overly optimistic events at distances smaller than 100 Mpc and for which the expected rate is $< 0.5 \mathrm{yr}^{-1}$ are excluded, and b) the volume that is covered extends approximately to the absolute horizon for BNS, that is expected to be reached by a second generation network of aLIGO and AdVirgo detectors at design sensitivity.

Having excluded the possibility of a BNS system coalescing within the Milky Way neighbourhood (rate estimated at $R_{BNS} \sim 10^{-8} - 10^{-5}\mathrm{Mpc}^{-3}\mathrm{yr}^{-1}$ or $R_{BNS} \sim 10^{-6} - 10^{-3}\mathrm{yr}^{-1}$ per MWEG [9]), there is no reason to prefer one particular direction in the sky over another. Therefore, we sample the sky location angular parameters (θ, ϕ) from a distribution that is uniform in the celestial sphere, *i.e.* $\cos\theta$ is uniform in $[0, 1]$ and ϕ is uniform in $[0, 2\pi]$.

A different educated way of distributing the sources in both distance and sky location, would be by making use of galaxy catalogues, whereby observed galaxy sky-locations and redshifts contribute as δ-functions to the angular distribution

---

[1] PSR J0348+0432 discovered in 2007 at ra: $03^h 48^m 43^s.639$, dec: $+04^o 32' 11.458''$. Its mass was measured at $2.01 \pm 0.04 M_\odot$ by using radio timing and white dwarf spectroscopy on its companion.

[2] ra:$15^h 18^m 16^s.799084(16)$, dec:$+49^o 04' 34.25119''(16)$

and distance respectively[3]. There are two main reasons why one may find this to be a waste of effort: 1) the galaxy catalogue is only partially complete at such large distances and 2) for the sky-resolution of second generation interferometers the galaxy distribution is effectively smeared out to a more or less uniform one.

As for the remaining binary parameters, the inclination and polarization angles (ι, ψ) are also sampled uniformly in the 2-sphere that they parametrize and the phase at coalescence is distributed uniformly in $[0, \pi)$ [4]. There is no need to define a particular time distribution, other than requiring that the different simulated signals do not overlap with each other and may thus be processed independently. Given the expected rates for aLIGO and AdVirgo this is a realistic assumption.

The waveform model that will be used for simulating the signals will be the SPA based TaylorF2 approximant described in Sec. 2.4, which is generated analytically in the frequency domain. Only the dominant (22)-mode will be simulated, since it is known that higher-order modes will not contribute significantly in the case of BNS systems. This would not trivially hold if we considered for example BBH systems [360] where higher order harmonics may play a crucial role in the context of Bayesian analysis (if a secondary mode is excited with a significant amplitude *e.g.* larger than 10% of the (22)-mode, then a single-mode analysis would yield systematically biased results). We only consider Newtonian order in the amplitude but we include all terms up to 2PN in the phase expansion. An overview of the set-up for simulated injections is given in Table 6.1.

Parameter	Range	Unit	P.D.F.	Topology
m_1	$[1, 2]$	$M_\odot$	$1 M_\odot^{-1}$	linear
m_2	$[1, 2]$	$M_\odot$	$1 M_\odot^{-1}$	linear
r	$[100, 400]$	Mpc	$\propto r^2$	linear
θ	$[0, \pi]$	rad	$\propto \sin\theta$	spherical
ϕ	$[0, 2\pi]$	rad	$\frac{1}{2\pi}$	
ι	$[0, \pi]$	rad	$\propto \sin\iota$	spherical
ψ	$[0, 2\pi]$	rad	$\frac{1}{2\pi}$	
φ_c	$[0, \pi]$	rad	$\frac{1}{\pi}$	circular

Table 6.1: *Summary of population priors used for generating the simulated sources.*

Analysis template and priors For the purpose of analyzing the data, we need to specify the details of the template waveforms that will be used by nested sampling, as well as the parameter space and prior p.d.f. defined over it. As with the simulated signals we shall employ the frequency domain TaylorF2 approximant expanded up to 2PN order in the phase and to leading order in amplitude.

---

[3]Here the best available estimate for the cosmological parameters can be taken into account, in order to translate redshift into luminosity distance. However, the BNS horizon is at $z \simeq 0.1$ which only gives a minor correction compared to the measurement uncertainty.

[4]Note that the range of ϕ_c only covers half a circle. A system with ϕ_c is degenerate to the same system with $\phi_c \to \phi_c + \pi$ and $m_A \leftrightarrow m_B$

The parameter space Σ_{GR} will be the 9-dimensional space spanned by the set of restricted (zero-spin) CBC parameters given in Eq. (5.4). As for the prior p.d.f. $\pi(\vec{\theta}) = p(\vec{\theta}|\mathcal{I})$, $\vec{\theta} \in \Sigma_{\mathrm{GR}}$ it will be defined as the product of nine one-dimensional prior p.d.f.s on the individual components; that is, the different components of $\vec{\theta}$ will be treated as independent parameters. In particular

- for the component masses m_A, $A = 1, 2$ we use a fixed range $m_A \in [1, 34] M_\odot$, a Jeffreys prior[5] on the chirp mass, $\pi(\mathcal{M}_c) \propto \mathcal{M}_c^{-11/6}$ and a uniform prior on the symmetric mass ratio η. This choice is fairly wide and only reflects the fact that the detection pipeline should have already tagged the event as a low-mass CBC trigger;

- for the distance r we choose to use a prior uniform in volume $\pi(r) \propto r^2$ in the range $[1, 1000]$ Mpc, which encloses the entire detectability region of an aLIGO-AdVirgo network for the chosen mass range;

- for the sky-location angles (θ, ϕ) we use a prior uniform in the sphere;

- for the orientation angles ι, ψ (inclination and polarization), we use a prior uniform in the sphere;

- for the phase at coalescence φ_c we use a uniform prior $\pi(\varphi_c) = \frac{1}{\pi}$ and finally,

- for the time of coalescence t_c we use a uniform prior $\pi(t_c) = 10\, s^{-1}$ with a range of 0.1 seconds around the true time of coalescence. This is slightly wider than the time resolution with which the detection pipelines are expected to output trigger data from a BNS event. It is also much wider than the largest possible time lapse within the LIGO-Virgo network $\delta t_{\mathrm{LV}} \simeq 27$ ms, or between any two detectors located anywhere on Earth, $\delta t_{max} \simeq 42.6$ ms.

Technical details Finally, let us describe the technical details behind the numerical computations. The main computational framework on which TIGER is based and developed is the LIGO Algorithm Library (LAL) and its implementation of Nested Sampling and other inference algorithms, an updated version of which is thoroughly described in [364]. The properties of a network of the three detectors (longitude, latitude, orientation of the two arms and antenna pattern), are faithfully simulated based on the actual aLIGO Hanford, aLIGO Livingston and AdVirgo Cascina detectors and summarized in Table 6.3. The noise part of the data output for each detector is simulated in the frequency domain using synthetic Gaussian noise, according to the estimated noise PSDs of the zero-detuning

---

[5]The *Jeffreys prior* is a non-informative choice of prior, which has the desireable quality of being invariant under reparameterizations [217, 216].

Parameter	Prior Range	Unit	Prior P.D.F.	Topology
m_1	$[1, 34]$	$M_\odot$	$\pi(\mathcal{M}_c) \propto \mathcal{M}_c^{-11/6}$	linear
m_2	$[1, 34]$	$M_\odot$	$\pi(\eta) = const$	linear
r	$[1, 1000]$	Mpc	$\propto r^2$	linear
θ	$[0, \pi]$	rad	$\propto \sin\theta$	spherical
ϕ	$[0, 2\pi]$	rad	$\frac{1}{2\pi}$ rad^{-1}	
ι	$[0, \pi]$	rad	$\propto \sin\iota$	spherical
ψ	$[0, 2\pi]$	rad	$\frac{1}{2\pi}$ rad^{-1}	
φ_c	$[0, \pi]$	rad	$\frac{1}{\pi}$ rad^{-1}	circular
t_c	$[t_{inj} - 0.05, t_{inj} + 0.05]$	s	$10\ s^{-1}$	linear

Table 6.2: *Summary of parameter priors used for the Monte Carlo analysis with Nested Sampling.*

high-power (ZDHP) configuration of aLIGO and the signal-recycling (SR) configuration of AdVirgo shown in Fig. 1.4. The signal waveform is also generated directly in the frequency domain (TaylorF2). In both cases, the sampling rate used for the datasets was $f_s = 4096$ Hz which is one fourth of the actual sampling rate of the interferometers' hardware. This particular power of 2 was chosen as a golden mean between computational cost and resolution, since: i) computational cost scales linearly with number of bins and ii) the Nyquist frequency for this sampling rate is $f_N = \frac{f_s}{2} = 2048$ Hz, which is high enough to prevent aliasing in a CBC signal. The calculation of the signal starts at $f_{low} = 20$ Hz and terminates at $f_{high} = f_{LSO}$, cutting off any contribution from the merger or ringdown stage. The signal is then added coherently to the three output data-streams after calculating its time of arrival (TOA) at each detector and transforming it by the corresponding antenna pattern Eq. (1.80). The TOAs of the signal are calculated by individually shifting its nominal time of coalescence t_c by the wavefront's time lapse between each detector and the center of the Earth. As for the Bayesian analysis algorithm itself, we use nested sampling with 1024 live points and 100 MCMC points, and a termination condition on the evidence difference d$Z < 0.1$. An overview of the set-up for the simulations is given in Table 6.4.

6.3.1 Simple Background: numerical results

A total of 1422 sources were simulated and are represented by their signal-to-noise ratio and their (logarithmic) TIGER odds ratio in the scatter plot of Fig. 6.3, among which 1267 survived the SNR cut-off of $\rho_{\text{net}} > 8$. In terms of the odds ratio they yield the background distribution histogram illustrated in the central panel of Fig 6.3 that approximates $P(\ln O_{\text{GR}}^{\text{modGR}}|\kappa, \mathcal{I})$ for single sources. Note that a significant part of the background distribution falls within positive values, despite being populated by GR-consistent GW signals. This large pool of sources was partitioned into 15-source catalogues, whose combined odds ratios Eq. (5.18)
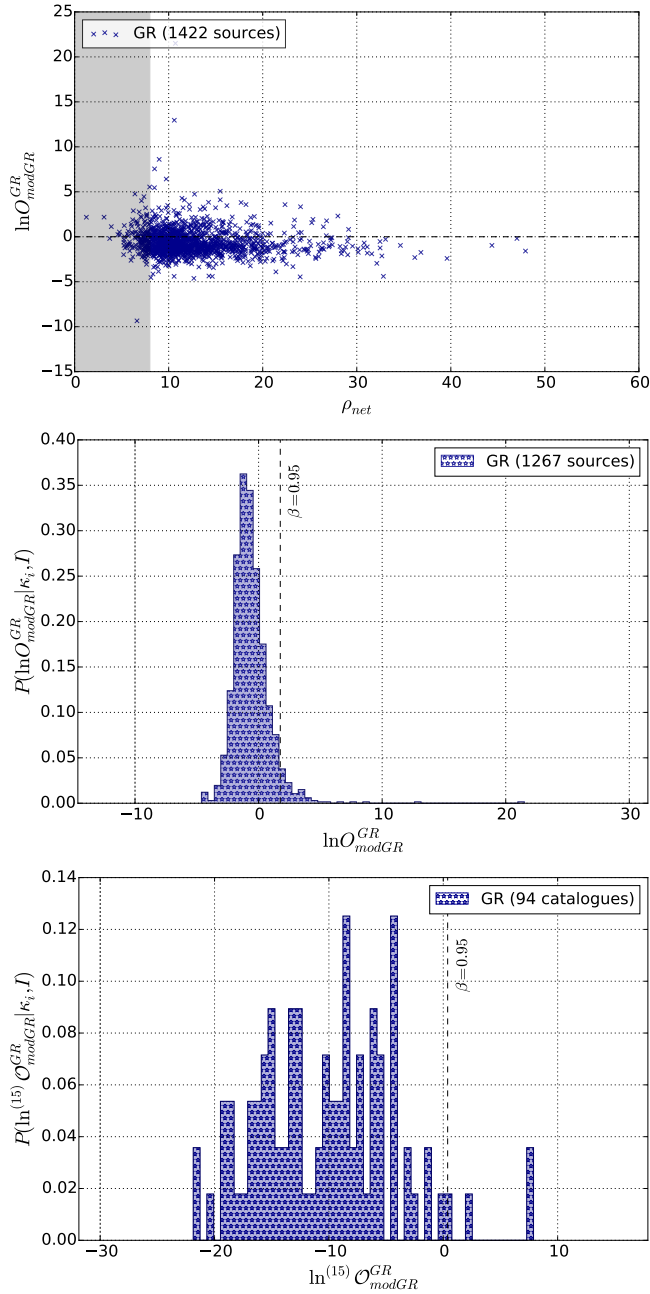
Figure 6.3: *Top: Scatter plot showing the SNR and log-odds-ratio for 1422 GR sources. The shaded area includes the rejected events beneath the network SNR threshold $\rho_{\mathrm{net}} = 8$. Center: Histogram for the single-source odds ratio background distribution $P(\ln O_{\mathrm{GR}}^{\mathrm{modGR}}|\kappa, \mathcal{I})$. Bottom: Histogram for the multi-source odds ratio background distribution $P(\ln^{(15)} \mathcal{O}_{\mathrm{GR}}^{\mathrm{modGR}}|\kappa, \mathcal{I})$ for catalogues of 15 sources each. In both histograms, the vertical line shows the log-odds threshold for a FAP of 5% ($\beta = 0.95$).*

IFO	PSD	λ [deg]	φ [deg]	ϑ [deg]
H	ZDHP	-119.407656	46.455144	126
L	ZDHP	-90.774242	30.562894	-18
V	SR	10.5050	43.631389	71

Table 6.3: *Location and orientation of aLIGO Hanford (H), aLIGO Livingston (L) and AdVirgo (V) detectors. Here, λ represents the longitude, φ is the latitude and ϑ is the angle between the detector's Y-axis and the local meridian.*

f_s	f_N	f_{low}	f_{high}	N_{live}	N_{MCMC}	Termination
4096 Hz	2048 Hz	20 Hz	f_{LSO}	1024	100	$dZ < 0.1$

Table 6.4: *Parameter choices used in the Nested Sampling algorithm.*

were calculated and yield the corresponding background distribution histogram shown in the bottom panel of Fig. 6.3, that approximates $P(\ln {}^{(15)}\mathcal{O}_{\mathrm{GR}}^{\mathrm{modGR}}|\kappa, \mathcal{I})$. The expected widening of the background distribution is observed and by the end of this chapter we will have witnessed how combining information from multiple sources makes a decisive difference in detecting a violation of GR.

6.4 Results

6.4.1 Measuring a 1.5PN violation of 10%

As a first GR-violating example, we consider a parameter-independent deviation $\delta\chi_3 = 0.1$, that is a relative shift of 10% in the 1.5PN phase coefficient ψ_3. We will refer to this scenario as *Alt1*. It is an interesting scenario in its own right, since 1.5PN is the leading order in which one encounters contributions of tail effects. These are induced by the scattering of waves off the approximately Schwarzschild background metric close to the source. Our ability to measure GR violations at this level will signify the first test of the non-linear dynamics of GR.

A set of 851 individual BNS sources with $\boxed{\delta\chi_3 = 0.1}$ is simulated and coherently added in detector noise for the same network of 3 detectors (HLV). Similarly to the population of the background, the prior distribution on the source parameter space is a product of the priors listed in Table 6.1. Here too, sources with $\rho_{\mathrm{net}} < 8$ are excluded from the analysis.

6.4.2 Some more GR-violating scenarios

Following the exact same steps as in Sec. 6.4.1, we will now examine the performance of TIGER under several different deviations from GR:
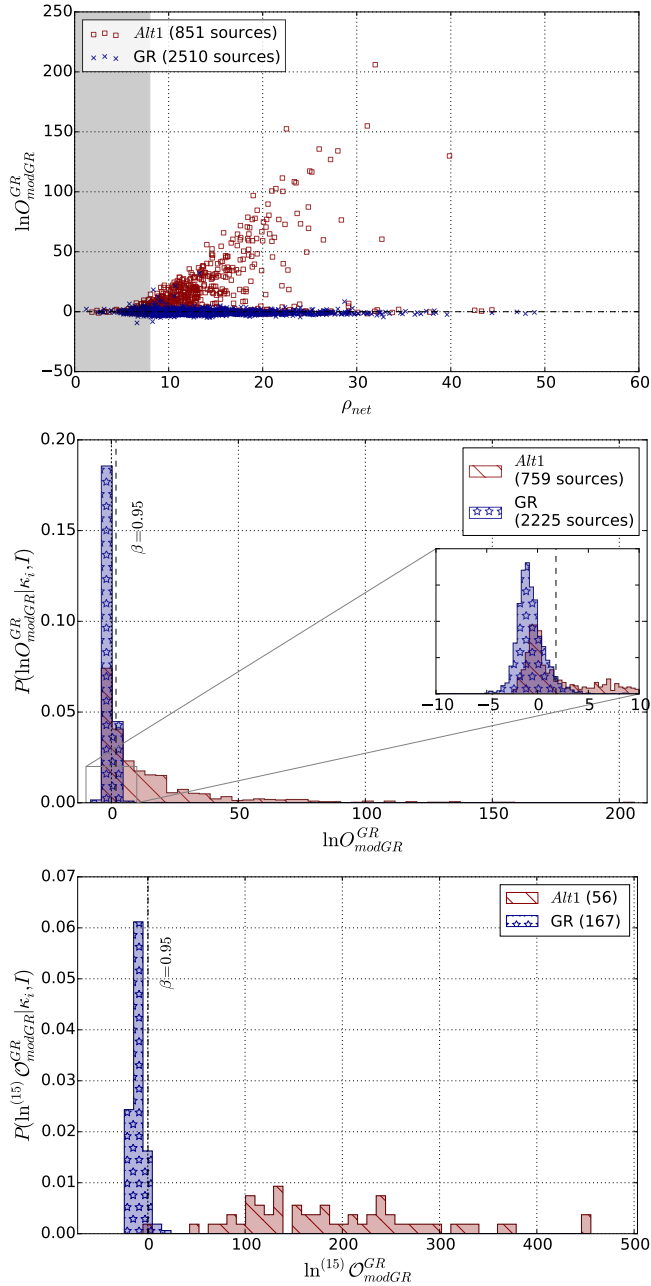
Figure 6.4: *Same as Fig. 6.3, but now comparing the background (blue) against the corresponding distributions for the GR-violating scenario* Alt1 *(red), where the 1.5PN phase coefficient ψ_3 is increased by 10%. The resulting efficiency $\zeta_{0.95}$ at 0.95 significance level is 0.89 for the single-source distribution and practically 1.0 for catalogues of 15 sources (see Fig. 6.6 for error bars).*

- *Alt2*: a parameter-independent (constant) shift of 2.5% at 1.5PN, *i.e.* $\boxed{\delta\chi_3 = 0.025}$ (this is the same as *Alt1* of Sec. 6.4.1 only 4 times smaller)

- *Alt3*: a constant shift of 20% at 2PN, *i.e.* $\boxed{\delta\chi_4 = 0.2}$. This particular modification mimics the effect of gravity theories with a quadratic curvature correction [394].

- *Alt4*: an additional parameter-independent phase term that does not belong to the standard PN-expansion and has a frequency dependence of $(\pi M f)^{-5/6}$. This can be translated as a "1.25PN" term and is given a coefficient $\boxed{\psi_{2.5} = -2.2}$ so that the induced phase shift at 150 Hz in the waveform is of a similar magnitude to that of *Alt1* (~ 6 rad).

- *Alt5*: a non-PN term with a *parameter dependent* frequency exponent $\boxed{(\pi M f)^{-2+\frac{M}{3M_\odot}}}$ that spans a behaviour from 0.5PN (when $M = 2M_\odot$) up to 1.5PN (when $M = 4M_\odot$). This too is given a pre-factor such that its effect on the phase has roughly the same magnitude as *Alt1*.

The five foreground distributions Alt1-Alt5 for the single-source odds ratio are plotted against the single-source background in the left panels of Fig. 6.5. Furthermore, Fig. 6.5 shows the foreground and background distributions for $^{(15)}\mathcal{O}_{\mathrm{GR}}^{\mathrm{modGR}}$, the combined odds ratio for catalogues of 15 sources each. Observe how the difference between the magnitude of the GR-violation in *Alt1* (dark red) and *Alt2* (green) is translated into their distinguishability from GR.

Finally, the efficiencies of each foreground at a threshold $\beta_0 = 0.95$ and $\beta_0 = 0.99$ (FAP of 5% and 1% respectively) are plotted as a function of catalogue size in Fig. 6.6. The error bars represent the statistical error estimated by sampling 1000 different realizations of partitioning the set of available sources into (mutually disjoint) catalogues. At a 95% significance level, most of these GR-violating scenarios are almost perfectly distinguishable from GR after combining information from the detection of roughly 10 sources. The exception is *Alt2*, where the 2.5% shift in ψ_3 is too weak; many more sources will be required in this case in order to have a confident result that favours a violation of GR. If one raises one's requirements for a stronger significance of 99%, then one would need roughly 30 sources to decisively identify *Alt3* as a GR-violation.

6.5 Expected bounds on parametrized deviations

Since a generic GR violation will not give a constant deviation across all sources, in any parametrization scheme, parameter estimation is not a safe approach in a testing GR setting. Nevertheless, we *are* interested in estimating how accurately a parametrized deviation from GR can be measured using a single source alone. Moreover, if TIGER gives no indication of GR being violated, one can start
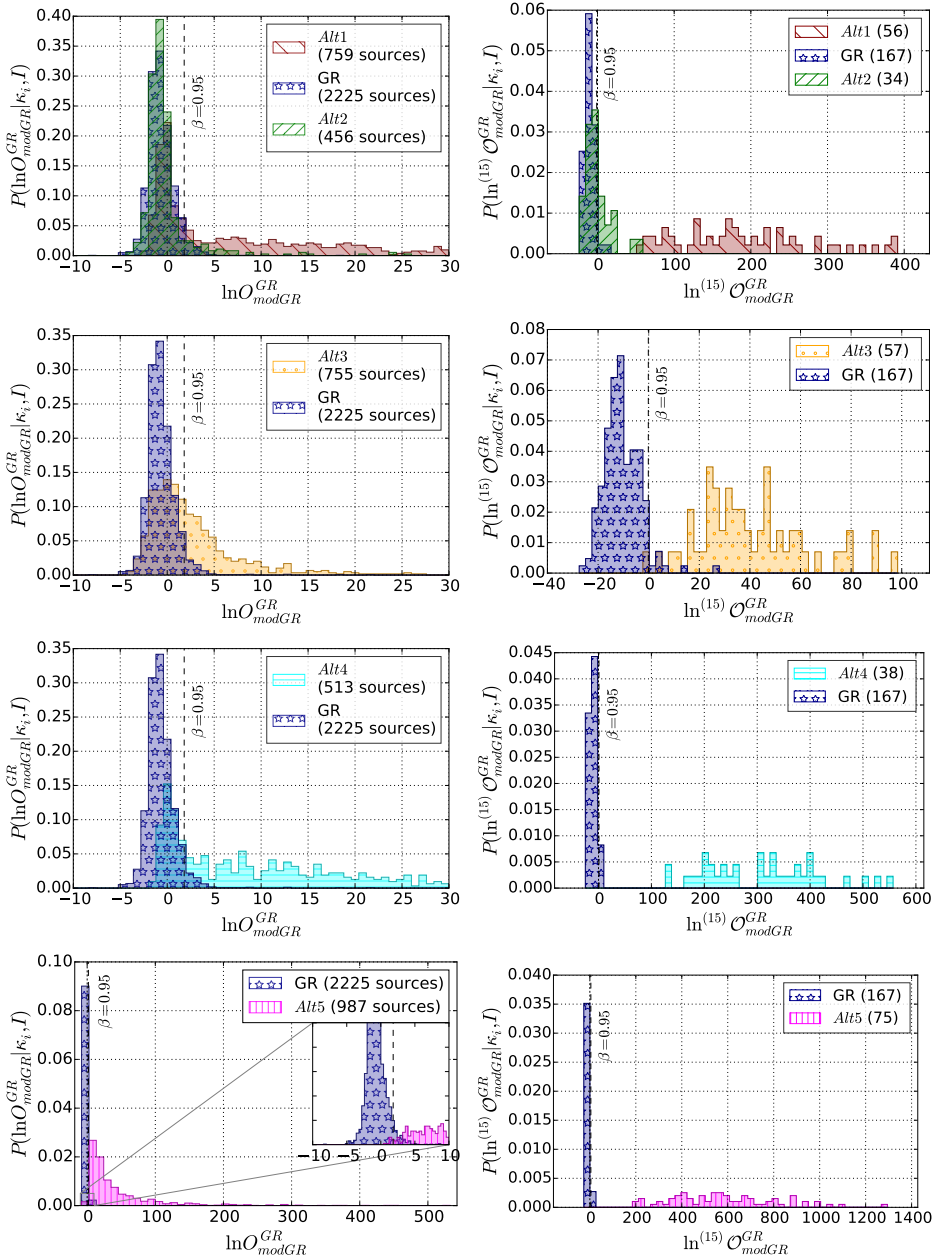
Figure 6.5: *Comparison between the simple GR background of Sec. 6.1 and the 4 different GR-violating scenarios Alt2-Alt5 (top to bottom). Left: single-source distributions for $P(\ln O_{\mathrm{GR}}^{\mathrm{modGR}}|\kappa, \mathcal{I})$ (blue) and $P(\ln O_{\mathrm{GR}}^{\mathrm{modGR}}|\kappa_{AltX}, \mathcal{I})$. Right: distributions for $P(\ln {}^{(15)}\mathcal{O}_{\mathrm{GR}}^{\mathrm{modGR}}|\kappa, \mathcal{I})$ (blue) and $P(\ln {}^{(15)}\mathcal{O}_{\mathrm{GR}}^{\mathrm{modGR}}|\kappa_{AltX}, \mathcal{I})$, for catalogues of 15 sources each.*

Figure 6.6: *The efficiency at a significance level $\beta_0 = 0.95$ (top) and $\beta_0 = 0.99$ (bottom) as a function of catalogue size. The error bars show the 95% confidence intervals for 1000 realizations of partitioning the available set of sources into catalogues. We notice that the efficiency reaches 100% with 10-20 sources, for all GR-violating scenarios except for Alt2, for which we see a slowly ascending trend.*

considering putting upper and lower bounds on the non-GR parameters $\delta\chi_i$. This is also a heuristic way of estimating the discriminatory power of GW data analysis, and comparing it against earlier measurements, such as bounds set by pulsar binaries.

In Fig. 6.7 we show results from a series of simulations in the network of AdVirgo and aLIGO, where the signals are consistent with GR (*i.e.* the true values of all non-GR parameters are zero), and where the template waveforms used for recovery have one additional free parameter $\delta\chi_i$, indicated in the legend. To match the expectation for the first years of operation, we use the early advanced sensitivity curves of Fig. 1.5 and we restrict the analysis to relatively weak signals, of optimal SNR between 10 and 15. We perform this test for $\delta\chi_1$, $\delta\chi_2$, $\delta\chi_3$, $\delta\chi_4$, and $\delta\chi_6$ (but not $\delta\chi_5$, due to its known degeneracy with φ_c, see Sec. 5.2). The results show figure-of-merit estimates on the resolution of such a PE analysis on a single source, with $\delta\chi_1$ being measurable to ~ 0.02 (absolute deviation) and the relative deviations $\delta\chi_2$, $\delta\chi_3$, $\delta\chi_4$ and $\delta\chi_6$ being measurable to a $\sim 10\%$, $\sim 10\%$, $\sim 100\%$ and $\sim 300\%$ level respectively. The distribution of effect-size errors based on the median of the posterior samples in each case, i.e. the offset from zero divided by the 1-σ posterior error width $\Delta\delta\chi_i$, are also shown in the right panels. These crude estimates allow us to fill in the corresponding points in Fig. 4.2.

parameter	68% CI width	95% CI width	effect size
$\delta\chi_1$	0.009	0.017	0.21
$\delta\chi_2$	0.065	0.12	0.01
$\delta\chi_3$	0.07	0.11	-0.98
$\delta\chi_4$	0.63	0.96	0.60
$\delta\chi_6$	1.37	2.65	0.54

Table 6.5: *Median values for* 68% *and* 95% *confidence interval (CI) width and effect size error (p.d.f. median/standard deviation) for the five relative shift parameters.*

6.6 Outlook

In this chapter we have established a proof of principle for our Bayesian model selection framework of testing GR with gravitational wave signals from compact binaries and in particular BNS systems. In the presence of noise, it is not guaranteed that the right model will always be favoured, so a careful statistical study is required. This was done with the construction of a GR background distribution, against which a given set of observations will be compared. Finally, a set of GR-violating scenarios were simulated and the efficiency of TIGER in distinguishing them from GR was evaluated. Overall, we conclude that, even for violations that cannot be faithfully described by the freedom in the waveform models of the modGR subhypotheses, a non-GR scenario is correctly identified, provided (as a

rule of thumb) that its cumulative effect on the waveform phase is in the order of a few radians. This happens because the free extra parameters will rearrange themselves in order to accomodate the peculiarity of the signal in an optimal way, one that the pure GR model fails to match. Furthermore, we have observed that the sensitivity increases as expected with the number of detected signals.

There are however many challenges that so far remain unexplored. In all of the above simulations we have restricted ourselves to non-spinning, point-particle, SPA inspiral signals, embedded in perfectly Gaussian and stationary detector noise. In the following chapters, we will proceed with evaluating the performance of TIGER in increasingly realistic scenarios, before establishing TIGER as a working pipeline for GW data analysis in the advanced detector era.

6
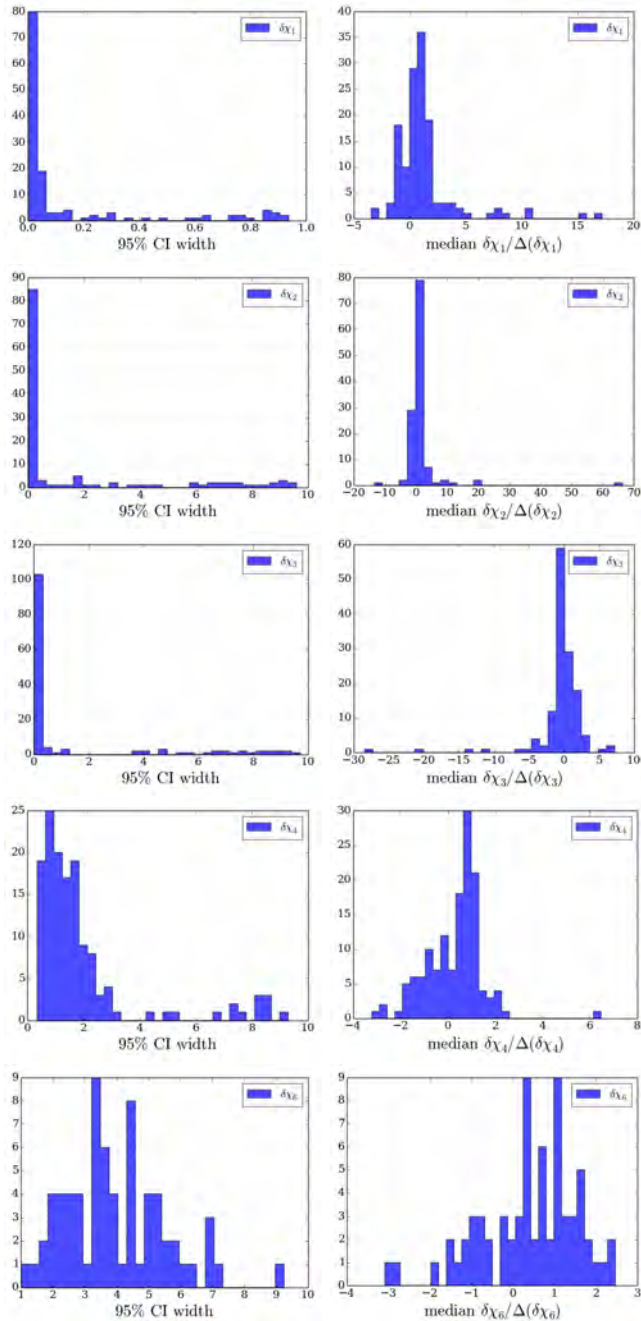
Figure 6.7: *Distribution of the width of* 95% *confidence intervals (left) and effect size errors (right) for sets of GR runs, where in the recovery templates a single relative shift parameter* $\delta\chi_i$ *is left free to vary.*
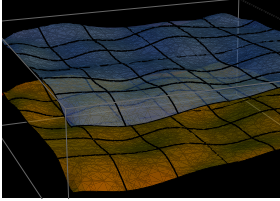
Chapter 7

TIGER in a realistic setting

You can prove anything you want by coldly logical reason—if you pick the proper postulates.

<div align="right">

Isaac Asimov - I, Robot

</div>

7.1 Introduction

In the previous chapter we established a *proof of principle* for TIGER by constructing a simple background for GW signals from BNS sources and assessing the measurability of a few different GR-violating scenarios. We will now study the performance of TIGER in an increasingly realistic setting where a number of different effects will be taken into account in the simulated signals. The purpose of this chapter is to test the robustness of the TIGER method against a number of uncontrollable effects of fundamental, astrophysical or instrumental nature, that could bias our inference if not accounted for.

In particular, in addition to what was described in Sec. 6.1, the behaviour of the background under the following effects will be studied in turn:

- *Waveform discrepancies*: Even for binary neutron star coalescence, there are small differences between the various waveform approximants that are available. Since TIGER is specifically designed to find anomalies in the signals, we must make sure that these discrepancies, however minor, are not mistaken for violations of GR.

- *Post-Newtonian truncation*: Post-Newtonian waveforms are only available up to 3.5PN in phase. What might be the effect of unknown PN contributions?

- *Neutron star spins*: The dimensionless spins of neutron stars in binaries are generally expected to be quite small, but the resulting spin-orbit and spin-spin effects will nevertheless need to be taken into account, at least to leading order in both the simulated signals and the recovery templates. Ignoring the effects of neutron star spins in the phase evolution will prove to have a severe impact on the efficiency of TIGER.

- *Tidal deformations*: In the final stages of inspiral, neutron stars get deformed because of each others tidal fields. This has an effect on the orbital motion, which gets imprinted onto the GW signal waveform. The size of these tidal effects is determined by the equation of state (EoS) of neutron star matter, about which currently not much is known. Can we avoid mistaking unknown tidal effects for a violation of GR?

- *Instrumental calibration errors*: The calibration of the instruments will be imperfect, leading to frequency dependent uncertainties in the interpretation of amplitudes and phases. What will their impact be?

- *Non-Gaussian, non-stationary noise*: So far we have assumed that our synthetic Gaussian noise, based on a given design PSD, is a faithful representation of the real behaviour of interferometric noise. In reality, noise will neither be perfectly Gaussian, nor will its features be constant over time. Will our performance be vulnerable to real-life features of the noise?

In the next few sections the above effects will be treated one by one and all will ultimately be considered in combination. We will be mostly concerned with how the background distribution is modified by each of the above. In particular, the last kind of effects, related to real noise will be treated separately in Chapter 8 due to its technical peculiarities. But first, a minimal background needs to be defined and used as a benchmark against which the results from all the additional effects will be compared.

7.1.1 Preliminaries

We will first set up a set of simulations in order to populate a benchmark background distribution. This will be only slightly different from the one used in the proof-of-principle simulations of Sec. 6.1 in the following ways:

- Both the injection waveforms and the recovery templates will be generated by using all currently available terms in the PN phase expansion, namely up to and including 3.5PN. This will minimize possible systematic errors related to the truncation of our PN models at finite order. In Sec. 7.4 we shall see whether this is sufficiently good for the purpose of TIGER.

- Our analysis will be terminated with a high-frequency cut-off at $f_{high} = 400$ Hz. The reasons for this have to do with abolishing nuisance matter effects

of unknown magnitude, such as tidal deformation or tidal disruption. These will become more clear in Sec. 7.2.

- For a more reliable inference and a better estimate of the evidence, we double the number of MCMC points for nested sampling to $N_{MCMC} = 200$.

- Finally, apart from the optimal SNR cut $\rho_{net} > 8$, an additional condition will be imposed on the recovered Bayes factor for $\mathcal{H}_{GR}$, which is now required to satisfy $\ln B_{noise}^{GR} > 32$. Although in reality the optimal SNR of a detection candidate will be unknown, this Bayes factor value is to leading order equivalent with an optimal SNR of 8 which places the source at the threshold of detectability [366].
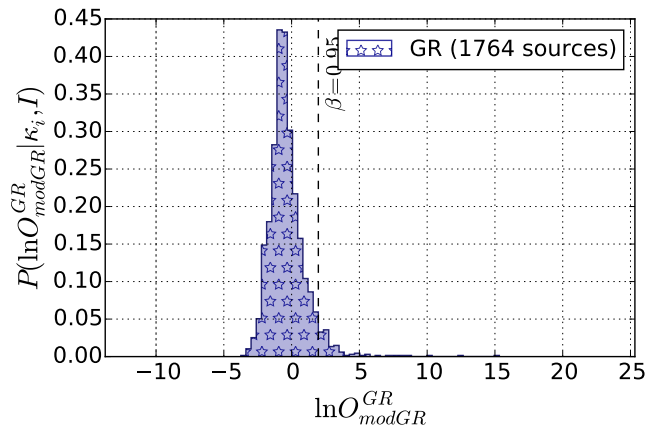
Figure 7.1: *The new GR background based on TaylorF2 waveforms at 3.5PN in phase with a high-frequency cut-off at 400 Hz.*

The parameters used to simulate the population were drawn from the same set of probability densities on the parameter space that were listed in Table 6.1. Moreover, the prior p.d.f.s used in the analysis with nested sampling are also the same as those used in Chapter 6, listed in Table 6.2. We thus build our new *benchmark* background by simulating a population κ_B of 1764 GR sources with the aforementioned properties. The resulting distribution of TIGER odds ratios for single sources $P(\ln O_{GR}^{modGR}|\kappa_B, \mathcal{I})$, is shown in Fig. 7.1.

7.1.2 The Kolmogorov-Smirnov statistic

The *Kolmogorov-Smirnov (K-S) statistic* [229, 339] D of a random variable x for two sets of i.i.d. samples $d_1 = \{X_i\}_{i=1,\ldots,n}$ and $d_2 = \{X_i'\}_{i=1,\ldots,n'}$ (not necessarily generated by the same distribution), is defined as the distance between
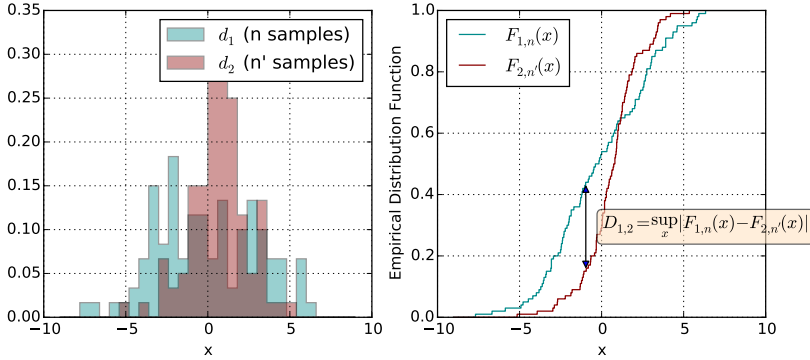
Figure 7.2: *A schematic representation of the K-S statistic. Left: the histograms of two sets of samples, d_1 and d_2. Right: their empirical distribution functions and the K-S statistic $D_{1,2}$ as their infinity norm distance.*

the *empirical distribution functions* $F_{1,n}$ and $F_{2,n'}$ of the two data sets, under the infinity norm $\| \cdot \|_\infty = \sup_x | \cdot |$, *i.e.*:

$$D_{1,2} = \sup_x |F_{1,n}(x) - F_{2,n'}(x)|, \qquad (7.1)$$

where an empirical distribution function $F_n(x)$ is the (normalized) cumulative function of the counting of n observation occurrences over x:

$$F_n(x) = \frac{1}{n} \sum_{i=1}^{n} I_{X_i \leq x}, \quad I_{X_i \leq x} = \left\{ \begin{array}{ll} 1 & \text{if } X_i \leq x \\ 0 & \text{otherwise} \end{array} \right. . \qquad (7.2)$$

This is schematically shown in Fig. 7.2. Note that by definition, $0 \leq D_{1,2} \leq 1$. A small K-S statistic $D_{1,2} \ll 1$ indicates a strong similarity between the two sets of samples, whereas large differences will yield values of $D_{1,2} \approx 1$.

For the purpose of comparing backgrounds populated under different configurations, we will calculate the K-S statistic for the odds ratio random variable, $O_{\text{GR}}^{\text{modGR}}$.[1]

7.2 Tidal deformation

Neutron stars are the most compact objects made of matter that are known to exist. For the purposes of CBC analysis, treating NS as point particles is usually a good approximation, since any matter effects are estimated to be relatively

---

[1]Note that we are **not** performing a *K-S test*, which gives a measure of how likely it is that the two sets of samples originate from the same underlying distribution. In fact we know that they do not! We are only interested in quantifying the similarity between them.
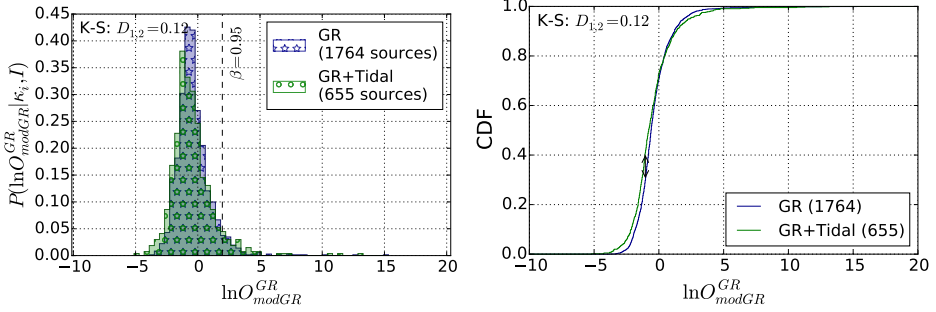
Figure 7.3: *Comparison between a GR background populated with point-particle injections and one populated with MS1 as the equation of state. In both cases TaylorF2 templates were used to simulate and recover the signal. Left: single-source distributions for $P(\ln O_{\mathrm{GR}}^{\mathrm{modGR}} | \kappa_{tidal}, \mathcal{I})$ (green circle-hatched) and $P(\ln O_{\mathrm{GR}}^{\mathrm{modGR}} | \kappa_B, \mathcal{I})$ (blue starred). Right: Empirical distribution function of the same two data sets. The Kolmogorov-Smirnov statistic takes the value $D_{1,2} = 0.12$, quantifying the close similarity of the two distributions. We thus do not expect tidal effects to be a source of systematic errors in this treatment.*

weak. Nevertheless, the lack of knowledge on the true nature and properties of NS matter leaves the strength of such effects undetermined by more than an order of magnitude. In particular, the dominant matter effect on the evolution of a BNS inspiral is caused by the deformation that the tidal field of each NS imposes on its companion. These deformations influence the orbital motion, hence modifying the emitted GW signal. This is described in Sec. 2.6.1. The leading and next-to-leading order tidal corrections to the waveform (up to fractional 1PN order) enter the phase with an overall $\left(\frac{v}{c}\right)^5$ and $\left(\frac{v}{c}\right)^7$ respectively, and are given by the first two terms of Eq. (2.55)

$$\Psi_{tidal}^{1PN} = \quad - \quad \frac{3}{128\eta} \left(\frac{v}{c}\right)^{-5} \sum_{A=1}^{2} \frac{\lambda_A}{M^5 X_A} \left[24\left(12 - 11X_A\right) \left(\frac{v}{c}\right)^{10} \right.$$
$$\left. - \quad \frac{5}{28} \left(3179 - 919X_A - 2286X_A^2 + 260X_A^3\right) \left(\frac{v}{c}\right)^{12} \right]. \quad (7.3)$$

In this section we will try to estimate the impact of tidal effects on TIGER in a worst-case scenario.

The undetermined quantities here are the *tidal deformability parameters* λ_A, $A = 1, 2$ of the two NS or, more conveniently, the dimensionless $\hat{\lambda}_A = \lambda_A / m_A^5$. These are mass dependent parameters, ranging in $\sim 10^2 - 10^5$, with the explicit functional dependence on the mass being determined by the unknown *equation of state*. We choose to simulate a population of sources κ_{tidal}, assuming one of the *stiffest* candidate models, namely MS1 (see Fig. 11.1), to be the true EoS, inducing strong tidal effects.

Since the true neutron star EoS is not known, we will use point-particle templates for recovering the signal. This discrepancy between signal and template may lead to biases, which we hope to counteract by cutting off the analysis at a high frequency of 400 Hz, or equivalently at an orbital velocity of $v/c \sim 0.25$ and a compactness of $GM/(c^2R) \sim 0.07$. Hinderer *et al.* [200] have shown that with second generation GW interferometers, tidal deformation will not be at all measurable below 450 Hz. Thus, such a cut-off will relieve us from the best part of tidal effects in the phase, which occur at high frequencies due to their high PN order, while at the same time will only cost a loss in SNR in the order of 1%. Furthermore, any non-perturbative effects which may occur in the late inspiral, such as tidal disruption of the stars [357, 168] or contact will be also cut off.

After simulating a population of BNS inspirals with the underlying NS EoS being the stiff MS1, we populate a GR background distribution by analyzing with the usual point particle templates always cutting off our analysis at 400 Hz. We then compare against the benchmark background of Sec. 7.1.1 as illustrated in Fig. 7.3. The two distributions look very much alike and as shown in the right panel, the K-S statistic is rather small with a value of $D_{1,2} = 0.12$. This verifies that with the current high-frequency cut-off, the most important type of matter effects will not affect the performance of TIGER. Alternatively, and since the magnitude of the tidal effects is still unknown, one could even try to marginalize over the λ_A parameters within their prior range, in order to reduce possible systematic errors that arise when using point particle templates.

7.3 Waveform discrepancies

In Section 2.4 we saw how different approaches to performing the post-Newtonian expansion have led to different waveform models. We also saw how these models may deviate from one another at different regions of the parameter space [114].

In practice, the Bayesian analysis of the signal must be performed using a template family that keeps a good balance between

- being sophisticated and accurate enough to capture all the important features of a CBC waveform without introducing fundamental biases and

- being simple enough to be generated fast in the frequency domain.

The second point implies a preference towards templates that are generated directly in the frequency domain like TaylorF2, rather than time-domain templates that need to undergo an additional FT stage. However, waveforms that are generated by numerical methods of differential evolution, and are expected to be more accurate, are defined in the time domain. In any case, the real gravitational wave signal will not completely match the template waveforms that we choose to use.

In Chapter 5 we used the TaylorF2 model as a template for the analysis, the same model that was used to simulate the signal. Here we will investigate to
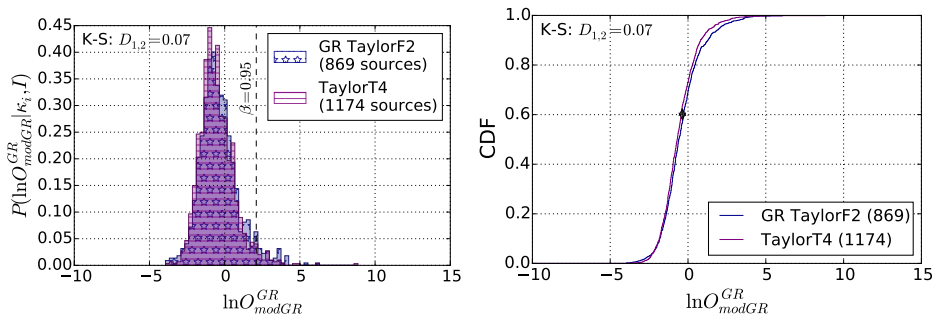
Figure 7.4: *Comparison between a GR background populated with TaylorF2 injections and one populated with TaylorT4 injections. In both cases TaylorF2 templates were used to recover the signal. Left: single-source distributions for $P(\ln O_{\mathrm{GR}}^{\mathrm{modGR}}|\kappa_{T4}, \mathcal{I})$ (purple line-hatched) and $P(\ln O_{\mathrm{GR}}^{\mathrm{modGR}}|\kappa_B, \mathcal{I})$ (blue starred). Right: Empirical distribution functions of the same two data sets. The distributions are indeed very similar, with the K-S statistic taking the value $D_{1,2} = 0.07$, indicating that our analysis is robust against waveform-modeling discrepancies.*

what extent the use of different models for injection and recovery will affect the performance of TIGER, and in particular the background distribution, for the case of BNS sources that we are interested in. We expect that the difference between our model template and exact GR will have a similar effect. The reader should recall the results of [114] mentioned in Section 2.4, which show that both the *effectualness* and the *faithfulness* between different waveform models in the low-mass, zero-spin region of the parameter space, are very close to 1 and in any case > 0.99. These comparisons include EOB-based waveforms that are tuned with NR simulations towards the end of inspiral. Overall, we do expect BNS analysis with TaylorF2 to be sufficiently reliable for our purposes.

It is however crucial to check that such small differences between waveforms will not be interpreted by TIGER as significant GR violations. To this end, we simulate a set of injected GR waveforms using the time-domain TaylorT4 approximant, described in Section 2.4, while keeping the frequency-domain TaylorF2 as the recovery template. A fundamental difference between the two approximants is that TaylorT4 is based on an adaptive numerical (Runge-Kutta) integration of the differential equations of motion Eq. (2.20), while TaylorF2 is based on the assumptions of the stationary phase approximation Eq. (2.29), both calculated to 3.5PN. The setup for the simulations is the same as the one used in Section 7.1.1. After analyzing 1174 events, the single-source background $P(\ln O_{\mathrm{GR}}^{\mathrm{modGR}}|\kappa_{T4}, \mathcal{I})$ is plotted against the TaylorF2 background of Fig. 6.3 in the left panel of Fig. 7.4. A background for $P(\ln {}^{(15)}\mathcal{O}_{\mathrm{GR}}^{\mathrm{modGR}}|\kappa_{T4}, \mathcal{I})$ for catalogues of 15 sources each, is also plotted against the corresponding TaylorF2 background, in the right panel. Judging by the similar shapes of the two backgrounds, it appears that the impact of waveform discrepancies on the performance of TIGER is negligible. To
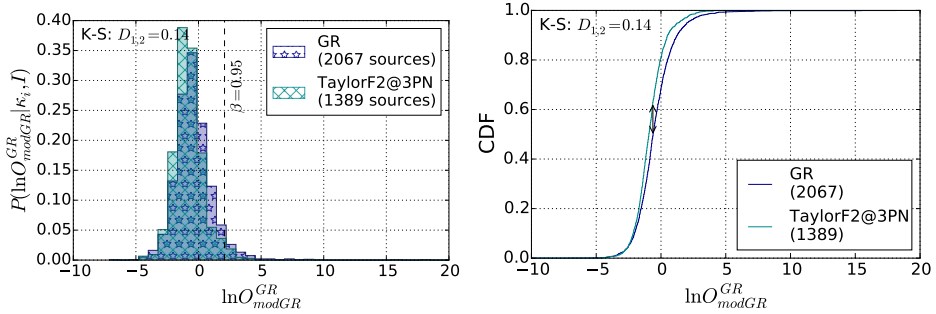
Figure 7.5: *Comparison between a GR background analyzed by using TaylorF2 @ 3.5PN templates (blue starred) and one using TaylorF2 @ 3PN templates (cyan checked), both cut at 400 Hz. In both cases TaylorF2 @ 3.5PN was used to simulate the signals. Left: single-source distributions for $P(\ln O_{\mathrm{GR}}^{\mathrm{modGR}}|\kappa_{+PN}, \mathcal{I})$ and $P(\ln O_{\mathrm{GR}}^{\mathrm{modGR}}|\kappa_B, \mathcal{I})$. Right: Empirical distribution function of the same two data sets. The K-S statistic takes the value $D_{1,2} = 0.14$, implying a sufficiently small sensitivity to missing higher-order terms in the phase.*

quantify this similarity, we calculate the K-S statistic for the two distributions to be 0.07.

7.4   Truncation in the post-Newtonian expansion

Apart from the fundamental differences between different approximants and the exact GR solutions, there is an additional error originating from the incompleteness of the post-Newtonian series. Currently, the phase coefficients are known up to 3.5PN order, and this is the accuracy with which all our simulations and waveform comparisons were done so far.

Since at this moment there is no hint at our disposal that would lead to estimates on higher order PN coefficients, we are restricted to work with the terms that are already available. One may thus investigate what would have happened if one had missed the highest available term at 3.5PN, *i.e.* if one had erroneously set $\psi_7 = 0$ in the template waveforms. Let us truncate the phase expansion of the TaylorF2 template used for recovery at 3PN and let κ_{+PN} describe a population of sources that is exactly the same as the one used in Section 7.1.1. The new subscript is only there to remind us that the injections are simulated up to 3.5PN, one term higher than what is used for recovery. In Fig. 7.5 the new background for $P(\ln O_{\mathrm{GR}}^{\mathrm{modGR}}|\kappa_{+PN}, \mathcal{I})$ is plotted next to the benchmark background, $P(\ln O_{\mathrm{GR}}^{\mathrm{modGR}}|\kappa_B, \mathcal{I})$, and it is evident that any effect induced by the missing PN order is small. In particular, the K-S statistic calculated for these two single-source backgrounds is $D_{B,+PN} = 0.14$. This result can also be interpreted as a very small sensitivity to deviations at 3.5PN order, which is indeed expected,

in accordance with the discussion of Section 5.2. Note however that weak as it may be, our sensitivity at 3.5PN order is still many orders of magnitude better than what was previously achievable with double pulsar observations.

Unless there is a tremendous increase in the values of the coefficients $\psi_i, \psi_i^{(l)}$ at orders of 4PN and higher, one expects that the additional higher-order modifications to the waveform will be less significant than what was missed in the above scenario, and will mostly affect the high-frequency end of the inspiral. The fact that NR waveforms cover the late inspiral and that NR-tuned waveforms show good agreement with their post-Newtonian counterparts further supports the expectation that the high-order corrections will be small. Finally, recall that in our analysis the recovery waveforms are cut at 400 Hz. It is thus reasonable to conclude that, at least within the scope of second generation detectors, TIGER analysis of BNS signals is safe against biases coming from the missing high-PN-order effects.

7.5   Instrumental calibration errors

As in any other experiment, the output of GW detectors is subject to errors, originating from an instrumental mis-calibration of the different hardware components. Such *calibration errors* (CE) are represented as an overall error in the instrument's transfer function $R(f)$ which may severely bias any inference method applied to the data. Nevertheless, the authors of [370] already showed that CE will not significantly deteriorate parameter estimation or model selection methods, using a model based on initial LIGO/Virgo measurements. It remains to be seen whether the impact on TIGER is equally minor.
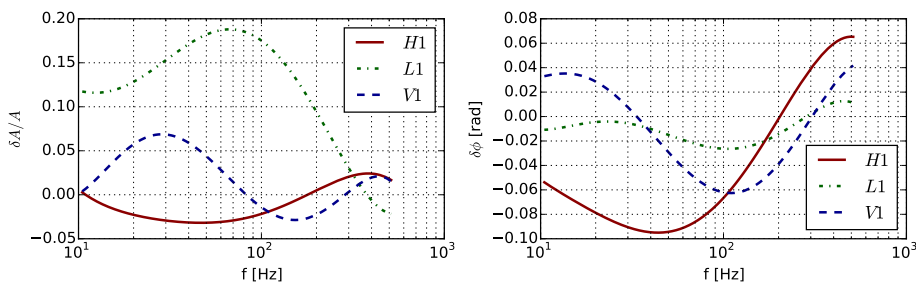
Figure 7.6: *An example realization of calibration errors in the amplitude (left) and phase (right) of the output of the three interferometers H1 (red solid), L1 (green dash-dotted) and V1 (blue dashed), as a function of frequency.*

To this end, we populate a set of sources detected with a network of mis-calibrated interferometers κ_{CE} with a different CE realization for each source. The CEs are simulated separately for each interferometer as errors in both amplitude and
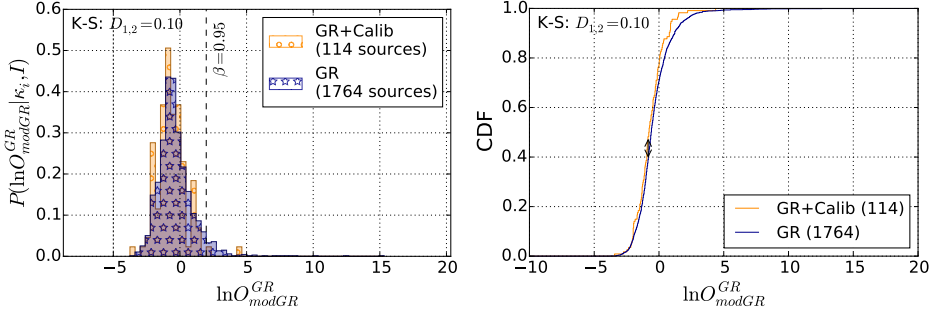
Figure 7.7: *Comparison between GR backgrounds with (brown) and without (blue) calibration errors in the detectors' output. Left: single-source distributions for $P(\ln O_{\mathrm{GR}}^{\mathrm{modGR}}|\kappa_{CE}, \mathcal{I})$ and $P(\ln O_{\mathrm{GR}}^{\mathrm{modGR}}|\kappa_B, \mathcal{I})$. Right: Empirical distribution function of the same two data sets. The K-S statistic takes the value $D_{1,2} = 0.10$.*

phase, following the model of [370] that meets realistic expectations. In particular, we introduce an error in the *measured* transfer function $R_m(f)$ with respect to the *exact* transfer function $R_e(f)$ as

$$R_m(f) = \left[1 + \frac{\delta A}{A}(f)\right] e^{i\delta\phi(f)} \, R_e(f), \tag{7.4}$$

where the profiles of the amplitude and phase errors are smooth functions of f with magnitudes in the order of $\delta A/A \sim 10\%$ and $\delta\phi \sim 3°$ respectively. Errors in the estimated transfer function act on the data $\tilde{d}$ as multiplicative operators in the frequency domain and thus induce errors in the interpretation of both the noise $\tilde{n}(f)$ and the signal $\tilde{h}(f)$ by the same complex factor $\left[1 + \frac{\delta A}{A}(f)\right] e^{i\delta\phi(f)}$. By the definition of the noise PSD in Eq. (1.83), we find that CEs induce an error in the measured noise PSD $S_m(f)$ with respect to the exact noise PSD $S_e(f) = S_n(f)$, that depends on the amplitude error

$$S_m(f) \propto \langle n(f)\, n^*(f)\rangle = \left[1 + \frac{\delta A}{A}(f)\right]^2 S_e(f)\,. \tag{7.5}$$

This illustrates how CEs may indeed wither one's inference methods.

The error-generating process goes as follows: first, we obtain the 1σ CE curves that were measured during the last science runs of the Initial detectors [8, 26] (these are summarised in Table II of [370]); next, using these as the 1σ curves of a Gaussian model for the amplitude $\frac{\delta A}{A}$ and phase $\delta\phi$ errors, we sample 15 points in the frequency space; finally, a CE realization is completed by interpolating these 15 points with a 7th order polynomial in f. An example realization of CEs that were used is illustrated in Fig. 7.6 for the amplitude and phase errors as functions of frequency.

The signals are then analyzed under the false assumption of zero CE by using the same templates as in Sec. 7.1.1. A comparison of this κ_{CE} background with the

benchmark background κ_B where no calibration errors are present is illustrated in Fig. 7.7. The K-S statistic in this case yields $D_{CE,B} = 0.10$, which implies that the effect of instrumental calibration errors on TIGER is indeed negligible.

7.6 Effect of neutron star spins

Until now all TIGER simulations have been restricted to BNS systems whose component neutron stars are assumed to be non-spinning. In reality, neutron stars are observed to be impressively fast-spinning objects, with spin frequencies reaching *e.g.* 716 Hz in the case of PSR J1748-2446ad [197]. In the context of relativistic effects however (see Section 2.4.2), the quantity of interest is the dimensionless spin parameter $\vec{\chi} = \frac{\vec{S}}{m^2}$ which typically takes small values [248], in the order of $\mathcal{O}(10^{-2})$. The fastest spinning neutron star in a BNS system has a dimensional spin amplitude $\chi \sim 0.02$. We thus expect spins in BNS systems to be small, however the currently available observations of such systems are few. In our subsequent analysis we will always populate sources by sampling the component spin-amplitudes χ_1, χ_2 from a Gaussian distribution centred at $\mu_\chi = 0$ and with a standard deviation of $\sigma_\chi = 0.02$, that is

$$\chi_A = \frac{|\vec{S}_A|}{m_A^2} \sim |\mathcal{N}(0, 0.02)|, \quad A = 1, 2. \tag{7.6}$$

This can be seen as a rather conservative choice, since the spin distribution for the observed population is much closer to zero.

According to Eq. (2.38), component spins introduce effects that to leading order enter the GW phase in the 1.5PN coefficient ψ_3. It is interesting to observe that this is the exact same order at which tail effects become measurable. It thus becomes even more important that the spin effects be accounted for in the recovery and disentangled from potential modifications of GR. The need for spins in the recovery templates will become more clear in the following sections.

Introducing spin parameters for both components increases the dimensionality of the parameter space to 15. Needless to say, this extension gives a richer structure to the waveform space and puts a heavy burden on the analysis algorithm. Interestingly enough, an efficient way to capture the essential modifications of the spins may be possible by restricting the spins $\vec{S}_1, \vec{S}_2$ to be aligned/anti-aligned with the orbital angular momentum $\vec{L}$. In what follows, we shall examine how the presence of both (anti-)aligned and generic spins in the simulated signals affects the TIGER background and its efficiency in discriminating a 1.5PN GR violation from spin effects.

7.6.1 Aligned spins

Let us now extend the restricted 9-dimensional CBC parameter space to the *11-dimensional spin-aligned*:

$$\vec{\theta}_{\text{aligned}} = \vec{\theta}_{\text{restr}} \otimes (\chi_1, \chi_2), \quad \chi_A \in [-1, 1]. \tag{7.7}$$

We are now dealing with binaries in which each component may have a non-zero spin, which however is restricted to be parallel to the orbital angular momentum, *i.e.* $\vec{s}_i = \chi_i \hat{L} \parallel \vec{L}$. The two additional spin parameters χ_1, χ_2 are the spin magnitudes, with the sign indicating whether the orientation is the same (aligned) or opposite (anti-aligned) to $\hat{L}$. As a first test we consider a population of GR sources κ_χ with (anti-)aligned spins sampled by using the amplitude distribution of Eq. (7.6) and with a 50-50 probability on each spin being aligned or anti-aligned with $\vec{L}$. For a better comparison with previous results we choose to stick with TaylorF2, since it can accommodate (anti-)aligned spins as shown in Eq. (2.45). We will have to abandon this choice in the next section where generic precessing spins will be considered.

As for the template used for recovery, let us examine two different cases:

S0 (no spins): The same TaylorF2 template that was used in Sec. 7.1.1, using the same priors and with the restricted parameter space of Eq. (5.2) that *assumes zero spins*.

SA (aligned spins): A SpinTaylorF2 template with the extended parameter space of Eq. (7.7) and with a flat prior in the spin-amplitude range $\chi_A \in [-0.1, 0.1]^2$. Other than this extension, it has the same properties as S0.

In Fig. 7.8 we compare the two backgrounds constructed by analyzing the aligned-spin population κ_{aligned} with the templates of S0 and SA, with the benchmark background of Sec. 7.1.1 as reference. This is shown for single-sources and for catalogues of 15 sources. The corresponding K-S statistic for the single-source backgrounds compared against the benchmark background gives 0.33 for S0 and 0.05 for SA. Evidently, if one omits the spin parameters in the analysis of BNS signals, one loses much of the sensitivity in detecting a possible GR violation. On the other hand, if (anti-)aligned spins are accounted for, the background distribution is very much the same as the benchmark background where no spins were considered at all. Let us now see if this statement will still hold if the population of sources has generic spins that are not restricted to a particular orientation.

---

[2]Note that in principle the prior range may only go up to 0.7 which is roughly the upper limit where the most compact NS reaches its break-up point. Less compact NS will already break up at spin values $\chi_A < 0.7$.
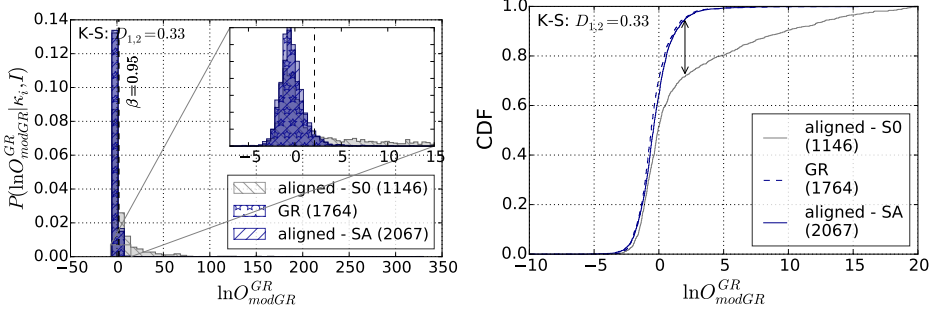
Figure 7.8: *Comparison between background analysis with S0 and SA templates, for a population κ_{aligned} of sources with aligned spins. Left: single-source distributions $P(\ln O_{\text{GR}}^{\text{modGR}}|\kappa_{\chi}, \mathcal{I})$ for S0 (grey) and SA (blue). The tail of S0 is clearly visible and is due to the attempt of recovering signals with spin using zero-spin templates. Right: Empirical distribution function of the same two data sets. The K-S statistic between S0 and either SA or the no-spin benchmark background is quite high, $D_{B,S0} = D_{SA,S0} = 0.33$. However, aligned-spin recovered with SA is very similar to no-spin benchmark background, $D_{B,SA} = 0.05$.*

7.6.2 Generic precessing spins

An astrophysically realistic population of BNS sources should have no restrictions on the orientations of the component spin vectors. It thus seems like a reasonable choice to sample the spin orientations uniformly in the 2-sphere, parametrized by the angular coordinates $(\theta_{\vec{\chi}_A}, \phi_{\vec{\chi}_A})$ with respect to the direction of the *orbital angular momentum* $\hat{z} = \hat{L}_N$ and an arbitrarily chosen x-axis perpendicular to $\hat{z}$ (*e.g.* the intersection of the orbital plane with the lign of sight). Unlike the (anti-)aligned case, where the spin axes remain aligned with $\vec{L}_N$ throughout the entire evolution of the binary, in the generic case, the spins will undergo precession, due to the spin-orbit and spin-spin interactions of Eq. (2.35). The strength of this precession effect crucially depends on the magnitude of the spins' off-axis components and their relative orientation. Our choice of spins will therefore have to correspond to a particular reference time during the binary evolution, which we choose to be t_{init}, the time when the (22)-mode of the signal crosses the $f_{\text{low}} = 20$ Hz low end of the sensitivity band of our detectors.

The probability density on the fully precessing parameter space that will be used for simulating the sources, will then be the product of

- a p.d.f. on the standard non-spinning CBC parameters,
- the Gaussian p.d.f. of Eq. (7.6) on the spin amplitudes χ_A, $i = 1, 2$,
- a uniform density on $\cos\theta_{\vec{\chi}_A} \in [0, 1]$,
- a uniform density on $\phi_{\vec{\chi}_A} \in [0, 2\pi)$.
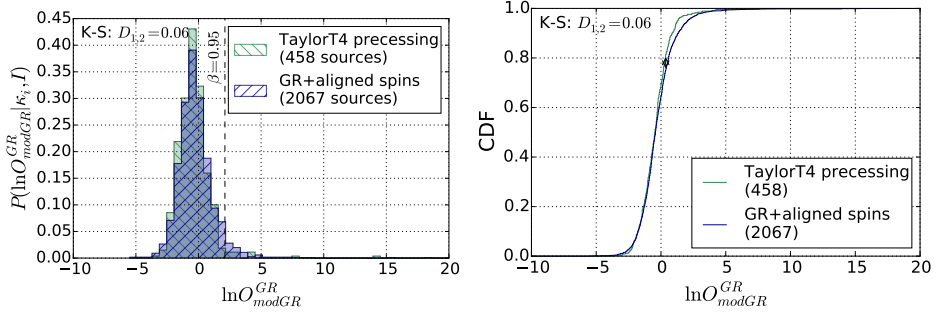
Figure 7.9: *Comparison between background analysis with SA templates, for a κ_χ population of BNS sources with aligned spins based on SpinTaylorF2, and a $\kappa_{\vec{\chi}}$ population of BNS sources with generic (precessing) spins based on SpinTaylorT4. Left: single-source distributions $P(\ln O_{\mathrm{GR}}^{\mathrm{modGR}}|\kappa_\chi, \mathcal{I})$ and $P(\ln O_{\mathrm{GR}}^{\mathrm{modGR}}|\kappa_{\vec{\chi}}, \mathcal{I})$. Right: Empirical distribution function of the same two data sets. The K-S statistic takes the value $D_{1,2} = 0.06$.*

To simulate signals with arbitrary precessing spins a different approximant than SpinTaylorF2 will be used, namely the time-domain SpinTaylorT4, whose spin coefficients are described in Sec. 2.4.2.

Based on the results of Sec. 7.6.1, it is already clear that recovering with zero-spin templates is not a good idea. On the other hand, extending the parameter space in the recovery to include arbitrary spins would significantly increase the computational cost, possibly without yielding a proportional amount of information [371]. Hence we will attempt to use the same *aligned-spin template* of SA that was used in the previous section. The spin-aligned recovery template will not be able to capture any feature of precession such as amplitude modulation (which for small spins are anyway expected to be too weak to make a measurable difference in the waveform). It can however match the main features of the phase evolution introduced by spins.

The results of this analysis are illustrated in Fig. 7.9 and give a clear indication that for the analysis of a BNS population with arbitrary precessing spins, it is enough to use an aligned-spin template. The additional features of non-aligned spins are absorbed in the background but seem to be too weak to modify significantly. In particular, the K-S statistic between the generic-spin $\kappa_{\vec{\chi}}$ background and the aligned-spin κ_χ, both recovered with the aligned-spin SA template, gives $D_{\chi,\vec{\chi}} = 0.08$. From a practical point of view, this is a very successful step towards establishing the good performance of TIGER under realistic conditions.

Figure 7.10: *Comparison between background analysis with SA templates, for a κ_χ population of BNS sources with aligned spins based on SpinTaylorF2, and a κ_{all} population of BNS sources based on SpinTaylorT4, with generic (precessing) spins, tidal effects, and calibration errors incorporated. Left: single-source distributions $P(\ln O_{\mathrm{GR}}^{\mathrm{modGR}}|\kappa_\chi, \mathcal{I})$ and $P(\ln O_{\mathrm{GR}}^{\mathrm{modGR}}|\kappa_{\mathrm{all}}, \mathcal{I})$. Right: Empirical distribution function of the same two data sets. The K-S statistic takes the value $D_{1,2} = 0.05$.*

7.7 Robustness against a combination of effects

So far, TIGER has been shown to perform consistently well under a list of uncontrollable effects of astrophysical (NS spins, precession, tidal deformation), instrumental (calibration errors) or fundamental nature (waveform discrepancies, post-Newtonian truncation). Here, a combination of the effects introduced above will be adopted, and a new background based on the most realistic assumptions will be populated. Finally, the efficiency of TIGER in a particular GR-violating scenario will be assessed, by analyzing a simulated set of realistic non-GR sources.

This final robustness test will be set up by using a population κ_{all} of sources, whose GW signals

- feature tidal effects based on a stiff equation of state (MS1), up to next-to-leading order (5PN, 6PN in phase),

- feature effects of spins sampled from a narrow spin amplitude distribution ($\mathcal{N}(0, 0.02)$) and of random orientation,

- are modelled by a different waveform approximant (SpinTaylorT4) than the one used for recovery (SpinTaylorF2) and

- undergo instrumental calibration errors before being represented in the output data stream.

The resulting background distribution of $P(\ln O_{\mathrm{GR}}^{\mathrm{modGR}}|\kappa_{\mathrm{all}}, \mathcal{I})$ is shown in Fig. 7.10 and is compared against the almost identical GR background with aligned spins of κ_χ. In addition to the GR background, we also populate a set of non-GR sources

κ'_{all} with all the above properties but with an additional parameter-independent -10% shift at 1.5PN in the expansion of Eq. (2.44) as

$$\frac{\mathrm{d}v}{\mathrm{d}t}(v) = \mathcal{G}_{PP}(v) + \mathcal{G}_{tidal}(v) + \delta\xi_3\alpha_3(m_1, m_2, \vec{S}_1, \vec{S}_2)v^{12}, \qquad (7.8)$$

with $\delta\xi_3 = -0.1$ denoting the relative shift at 1.5PN. This will provide an example of how TIGER will be able to detect violations of GR with all the above uncontrollable effects being present. Again, the data are analyzed with the aligned-spin SpinTaylorF2 template SA of Sec. 7.6.1 with a high frequency cut-off at 400 Hz.

In Fig. 7.11 we compare the single-source GR background of $P(\ln O_{\text{GR}}^{\text{modGR}}|\kappa_{\text{all}}, \mathcal{I})$ (dark blue) and $P(\ln O_{\text{GR}}^{\text{modGR}}|\kappa'_{\text{all}}, \mathcal{I})$ (dark red); these are to be contrasted against the benchmark background $P(\ln O_{\text{GR}}^{\text{modGR}}|\kappa_B, \mathcal{I})$ of Fig. 7.1. The same for the odds-ratio of catalogues of 15 sources is shown in Fig. 7.12. The results suggest that the new background is well-behaved and very similar to the benchmark background. Moreover, the GR violation that was used is clearly distinguishable from GR after analyzing 15 detected sources, with an efficiency essentially reaching 100% for any FAP within the statistical uncertainty of the available number of catalogues.

7
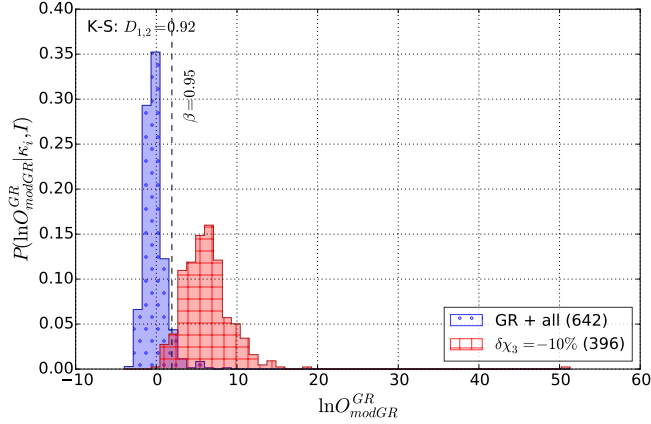
Figure 7.11: *Single-source odds-ratio distributions for GR background $P(\ln O_{\text{GR}}^{\text{modGR}}|\kappa_{\text{all}}, \mathcal{I})$ with all effects present and its GR-violating variant of Eq. (7.8) $P(\ln O_{\text{GR}}^{\text{modGR}}|\kappa'_{\text{all}}, \mathcal{I})$ (dark red). Both sets of sources are analyzed by using the spin-aligned SpinTaylorF2 template (SA).*
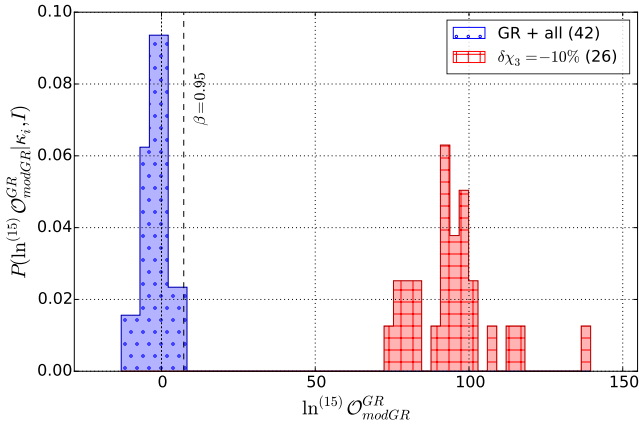
Figure 7.12: *Multi-source odds-ratio distributions for GR background $P(\ln\,{}^{(15)}\mathcal{O}_{\text{GR}}^{\text{modGR}}|\kappa_{\text{all}}, \mathcal{I})$ with all effects present (dark blue) and its GR-violating variant of Eq. (7.8) $P(\ln\,{}^{(15)}\mathcal{O}_{\text{GR}}^{\text{modGR}}|\kappa'_{\text{all}}, \mathcal{I})$, for catalogues of 15 sources each. Both sets of sources are analyzed by using the spin-aligned SpinTaylorF2 template (SA). The two are well separated, suggesting that a typical GR-violating catalogue of 15 sources will be measured way beyond the bulk of the background.*

7
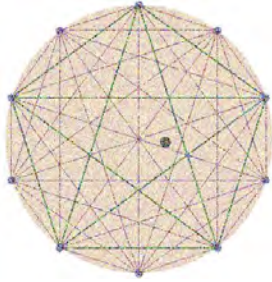
TIGER in real data

> *Knowledge would be fatal. It is the*
> *uncertainty that charms one. A mist*
> *makes things wonderful.*

Oscar Wilde

8.1 Introduction

Let us now busy ourselves with the real-life implementation of TIGER and address the remaining technical issue of analyzing gravitational wave signals in the presence of real noise. There are two main features of real noise, in contrast with the synthetic noise that was used until now, that may further challenge the discriminatory power of our analysis, namely

- *Non-stationarity*: the overall behaviour of each instrument in the network of interferometers will in reality vary over time, yielding a set of PSDs that vary with time. In any calculation involving the noise-weighted inner product Eq. (3.3), such as the calculation of the likelihood, a temporary estimate of each detector's PSD in the vicinity of the arrival time of each signal will be necessary. If not, a wrong assessment of the noise may lead to serious biases in any inference method.

- *Non-Gaussianity*: a standard assumption used when modelling detector noise is that a noise realisation is an observation of a random variable sampled from a product of Gaussian distributions, one for each frequency bin. This assumed Gaussianity does not necessarily hold in reality, due to various instrumental effects as well as environmental factors. A few characteristic categories of non-Gaussianities fall within a general class of
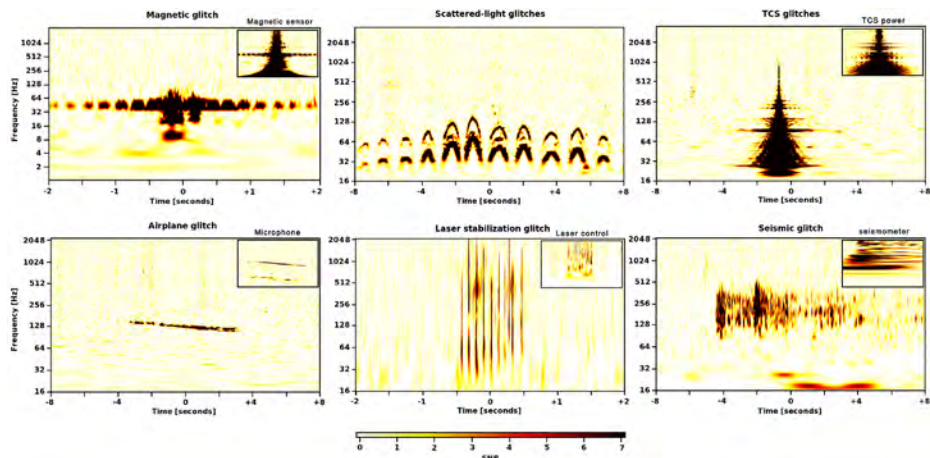
Figure 8.1: *Omega time-frequency spectrograms (see Sec. 8.2.3) of six examples of glitches. Glitch families are identifiable by their unique time-frequency morphology: a 50 Hz power-line glitch also detected by the magnetometers (top left); a series of glitches caused by scattered light induced by seismic activity (top middle); a thermal compensation system (TCS) instability (top right); an airplane event with a clear Doppler effect (bottom left); a glitch in the laser stabilization loop (bottom middle); and an undefined shape due to a seismic event up-converted to higher frequencies (bottom right). Auxiliary channels identifying the glitches are shown as inset plots. Taken from [3].*

8

noise effects termed *glitches*, which can be described as transient "bursts of noise". The identification of such noise effects and their distinction from a GW signal is a crucial task for a robust analysis.

Moreover, resonant lines have not been taken into account (violin modes, drum modes, power supply), which may also exhibit non-stationarity. We do not expect this to affect a broad-band signal such as the BNS signals we consider here.

In this chapter we will see how one would in reality incorporate a time-dependent PSD estimation and how one would treat the possible presence of glitch-like effects in the data, both in the context of CBC data analysis. Some of the most familiar examples of glitch patterns are illustrated in Fig. 8.1 from [3], where their effect on *searches* of GW signals is studied.

Notice for example, in the case of the airplane glitch (lower left), the clear correlation between the detector output and the readout of a co-located microphone sensor. Other types of glitches of different nature may be picked up by a number of auxiliary sensors/data channels which serve as a useful diagnostic tool for characterizing the quality of the data. The technical part of this discussion is the topic of *detector characterization* (DetChar), a detailed discussion of which is outside the scope of this dissertation.

8.2 Data quality and vetoes

There are different ways in which one can deal with bad quality data. If possible one may try to identify a recurring type of noise or glitch and actively mitigate the noisy source itself, as is usually done with lab-related resonances. In many cases however, the noisy source is uncontrollable and most types of glitches occur unexpectedly. This is why the online detector characterization pipelines are continuously analyzing the output of hundreds of channels, in order to characterize data segments and eventually suggest for part of data to be excluded from further analysis (vetoing).

8.2.1 Veto categories

There are five different levels (categories) of vetoing data, which are listed and briefly described below. These are ordered in decreasing order of strength with the most severe being category 1 or CAT1. The interested reader can seek more technical details in [6, 338].

CAT1 : Obvious problems on the detector. CAT1 periods have to be removed to redefine the science data.

CAT2 : Noisy periods where the coupling noise source / GW channel is well established. Triggers are removed before post-processing.

CAT3 : Noisy periods where the coupling is not well understood. The validity of a GW candidate flagged by a CAT3 should be controlled carefully.

CAT4 : Hardware injections used for sensitivity studies. To be removed from the GW candidate list

CAT5 : Advisory flags to track problems on the detector but no direct impact on the GW channel

For selecting good stretches of real data for TIGER simulations, we choose to exclude anything that is CAT4 vetoed or worse.

8.2.2 Segment types

Apart from the general notion of a segment which is simply defined by a start time and an end time, we distinguish the following *types of segments* for a GW interferometer:

Science Segment A connected time interval during which the detector is in *science mode*, *i.e.* it is operational and in a steady state, with its optical cavities locked. By convention, the start time of a science segment needs

to be at least 300 seconds after lock is acquired and the end time at least 10 seconds before lock is lost.

Veto Segment A connected interval within a science segment, during which the veto conditions for one or more veto categories are satisfied. Depending on the veto category $X \in \{1, 2, 3, 4\}$, the segment is tagged as a *CAT-X veto segment*.

Unvetoed Segment A connected interval within a science segment that has no intersection with any veto segment. Similar tagging is applied as for veto segments *e.g.* a CAT-4 unvetoed segment does not contain any CAT-4 veto segments.

Unless stated otherwise, we will always consider the maximal versions of the above types, that is we will restrict to the longest segments that satisfy the above definitions.

8.2.3   Omega spectrograms

A quick empirical way to look for glitches in detector data is by inspecting *omega spectrograms* [124] like the ones illustrated in Fig. 8.1. These are 2-dimensional density plots, produced by tiling the time-frequency space and calculating the normalized energy content of the data in each tile, based on the *Q transform*.

Given a time series of data $x[n]$, $n = 0, \ldots, N - 1$, the (discrete) Q transform is defined as the convolution

$$X[m, l, Q] = \sum_{n=0}^{N-1} x[n] \, w[n - m, l, Q] \, e^{-i \frac{2\pi n l}{N}}, \tag{8.1}$$

where $w[n, l, Q]$ is a time-domain windowing function of characteristic frequency l and quality factor Q. Here the windowing function w in its continuous form is chosen to be the *bisquare window*, which in the Fourier domain reads

$$\tilde{w}(f, \varphi, Q) = \begin{cases} A(1 - (\frac{f}{\Delta f})^2)^2 & , \text{if } |f| < \Delta f, \\ 0 & , \text{if } |f| \geq \Delta f \end{cases}, \tag{8.2}$$

where $\Delta f = \frac{\varphi \sqrt{11}}{Q}$ is the half bandwidth of the tiling and the normalization condition gives $A^2 = \frac{315 Q}{128 \sqrt{11} \varphi}$. The discrete expression can be obtained by substituting $f \to \frac{k f_s}{N}$, $\varphi \to \frac{l f_s}{N}$ and $A \to A f_s^2 / N^2$. This choice of windowing gives a good finite version of an exponential windowing, without having the pathology of infinite tails.

Just like the Fourier transform of a signal yields its content of sinusoids of different frequencies, the Q transform effectively yields its content of burst-like windowed sinusoids of different frequencies and quality factors. For different values of Q,
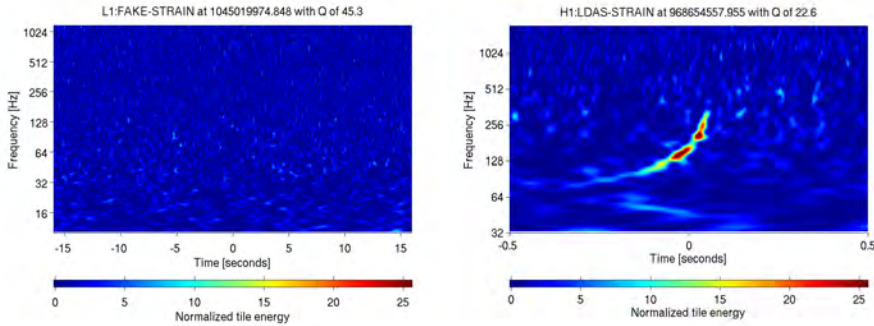
Figure 8.2: *Examples of real data omega-scans for an artificial BNS signal of $\rho = 13.7$ (left) and a NSBH signal of $\rho \simeq 15$ (right). The BNS signal is hundreds of seconds long and the energy that it deposits in the data is so much spread across time that it is not visible by the naked eye. The higher mass NSBH signal on the other hand is much more concentrated in time and is clearly visible in an omega spectrogram.*

one can apply the Q transform on the output signal of the detector, calculate the normalized energy for each tile in the time-frequency space and draw the omega spectogram. The normalization is performed with respect to the expectation value of the noise energy, according to the currently estimated noise PSD.

The omega spectrograms can give good indications for the presence of bursts of noise in the data or possibly the presence of a well localized signal. In Fig. 8.2 two examples of omega spectrograms are displayed, where a CBC GW signal was artificially added in the data and no glitches were present in the noise. The left panel shows the case of a BNS signal with a single-detector SNR of 13.7, which however is not visible since, due to the very long duration of the signal in band ($\mathcal{O}(100)$s), its energy is distributed across many tiles. This is pretty much what real glitch-free noise would look like. To the right however we see quite clearly what looks like a chirp signal, which is in fact a hardware-injection of a coalescing NSBH binary. Notice how the time scale is now much shorter and the waveform is much better localized, due to the higher total mass of the system, giving a dense energy deposition in the time-frequency space.

8.3 Estimating the PSD

A reliable estimate for the true noise PSD is of paramount importance for the purposes of data analysis, since it will affect matched filtering, FAP estimates, likelihood calculation and any other calculation that involves the noise-weighted inner product. For the calculation of the PSD one needs to make use of a sufficiently long unvetoed segment of data that is assumed to contain no contribution from GW signals. Based on the output of detector characterization pipelines, segments of bad quality data are vetoed and excluded. Furthermore, the different

search pipelines [2] can guarantee that no signal is present in a given segment.

We require that the data segment from which the PSD is estimated is at least 512 seconds long and falls within $\mathcal{O}(5)$ minutes before or after the GW event to be analyzed, in order to avoid effects of non-stationarity of the noise. The segment of length l_{seg} seconds is then split into a set of $N_{seg} = \lfloor \frac{l_{seg}}{32} \rfloor$ sub-segments of 32 seconds, for which N_{seg} individual PSDs are calculated $S_n^i(f)$, $i = 1, \ldots, N_{seg}$ by means of Eq. (1.83). The final $S_n(f)$ estimate per frequency bin is derived as the point-wise *median* of the individual $S_n^i(f)$.

An example of a real PSD calculation from SR6-VSR2/3 data was shown in Fig. 1.4. The modelled design sensitivity curves for each detector are plotted with dashed lines, while the corresponding PSDs estimated from real data are plotted with solid lines.

8.4 Simulations and results

In this section the performance of TIGER will be tested with data coming from real detector output. The task is then to populate a GR background distribution by injecting GW signals from BNS systems into real-noise, unvetoed segments of LIGO Hanford (H1), LIGO Livingston (L1) and Virgo (V1) detectors. Many of the unvetoed segments will in fact be too short to either be eligible for a PSD calculation, or even fit a BNS signal (which can be in band for as long as ~ 280 seconds for a $(1,1)M_\odot$ system). Thus, we will be injecting our signals into segments that are at least 1024 seconds long. Moreover, we will naturally assume that no real GW signal is present in the data.

8.4.1 Noise

Since none of the second generation GW interferometers was operational during the time when this study was carried out, there was no real data available from either aLIGO or AdVirgo. This means that, apart from the modelled sensitivity curves and some spectral lines that correspond to known resonances, one did not know in advance what the noise will look like. Nevertheless, one did have real output data from the initial LIGO and Virgo detectors, which can then be *re-coloured* based on the predicted sensitivity curves of their Advanced counterparts [5]. It is not guaranteed that the result will accurately resemble the actual noise of aLIGO and AdVirgo, since various upgrades have been performed and new components have been introduced in the Advanced configuration. It is however an informative first estimate that included both non-stationary and non-Gaussian features.

For this study we use S6-VSR2/3 data from an extensive 2-month epoch between GPS times 966383960 (00:00 GMT 21-08-2010) and 971614865 (00:00 GMT 20-10-2010), which is then re-coloured to follow the *early advanced* noise curves of

aLIGO and AdVirgo shown in Fig. 1.5. These correspond to the sensitivities that are expected to be achieved during the first 4 months of operation (O1). The science segments of this epoch are then vetoed using the original veto segments that the detector characterization pipelines tagged as CAT4. We proceed with the remaining CAT4 unvetoed segments that are at least 1024 seconds long. The cumulative distribution of CAT4 unvetoed segment lengths for the full 2-month stretch of data for all three detectors is plotted in the left panel of Fig. 8.3.
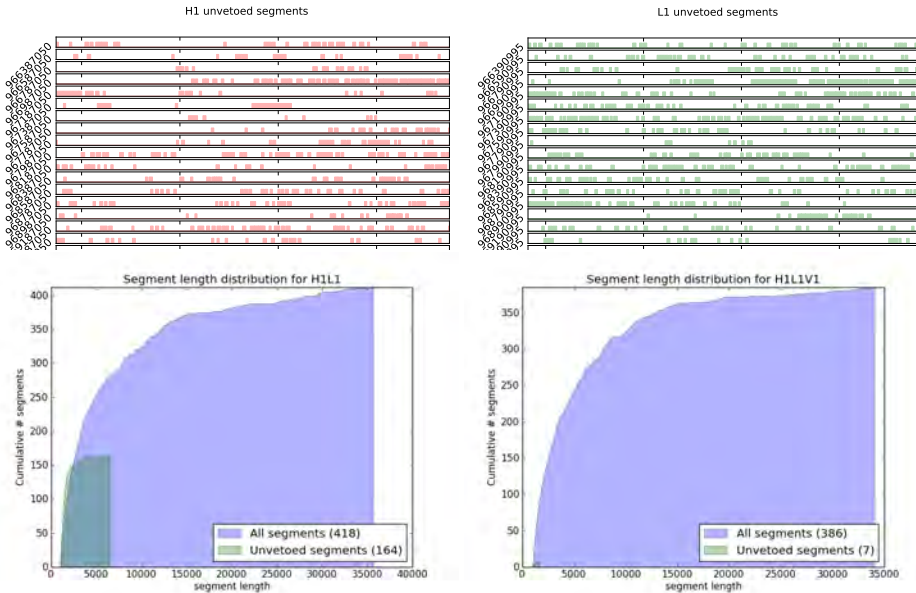
Figure 8.3: *Top: Unvetoed segments in an example stretch of H1 (left) and L1 (right) data. V1 data are much more fragmented and are not shown here. Bottom: Cumulative distribution of science (blue) and CAT-4 unvetoed (green) segment lengths for 2 months of data on double H1-L1 (left) and triple H1-L1-V1 (right) time, during which all detectors were on science mode.*

8.4.2   Timeslides

An additional problem in populating a background of thousands of BNS sources is that of the sparsity of coincident unvetoed time. It will not always be possible to find thousands of long segments that are simultaneously unvetoed for all three detectors. This is already clear by looking at the right panel of Fig. 8.3. In order to solve this issue we can artificially slide the arrival times of the signal at the three detectors with respect to one another, so that unvetoed segments located at different times can be combined.

In practice we populate the collections $T^I = \{t_1^I, t_2^I, \ldots, t_{n_I}^I\}$, $I = H, L, V$ of

candidate injection times (one for each detector) and for each source we form a triple (t^H, t^L, t^V) by randomly sampling T^H, T^L and T^V respectively. We then perform the injection at t^H, t^L and t^V in the data-streams of H, L and V respectively (not forgetting to consistently apply the additional time shift with respect to the center of the earth). The PSD for each detector I is also calculated individually using data from the segment that includes t^I. By using these *timeslides* we significantly enlarge the amount of independent noise realizations on which the background can be populated.

8.4.3   Real-noise GR background

We are now ready to populate our background distribution in real data. A total of 631 GR-consistent sources are simulated and injected into S6-VSR2/3 noise, re-coloured to the Early Advanced noise curve for the H1-L1-V1 network of detectors. Since this is a much less sensitive configuration than the final ZDHP for aLIGO and the BNS-optimized SR for Virgo, we intentionally lower the population's distance range to $D \in [10, 30]$ Mpc, so that most of the sources pass the $\rho_{net} = 8$ threshold[1]. In this case no timeslides were used and it turned out that only a handful of unvetoed segments in triple detector time were longer than 1024 seconds, so the results that follow come from injections in H1 and L1 only. Other than that, the set-up for the simulated signals is the same as the one used in Sec. 7.1.1. For the analysis of the data, again the parameter space, template waveforms and priors used are the ones described in Sec. 7.1.1, again with the exception of the distance prior which is set within the range $[1, 100]$ Mpc.

The resulting background distribution of $\ln O_{\mathrm{GR}}^{\mathrm{modGR}}$ for single sources is shown in Fig. 8.4, together with a scatter plot in the ρ_{net} - $\ln O_{\mathrm{GR}}^{\mathrm{modGR}}$ plane. In the latter, the signals recovered with a Bayes factor of GR against noise less than 32 are coloured in gray; these were cut off from the histogram in the bottom panel. Overall we observe that the background distribution of single-source odds ratios is similar to the ones we saw throughout Chapters 6,7, with the majority of sources falling below zero. We do however observe two outlying events, which will be followed up with a more detailed analysis in Sec. 8.4.4. For FAP values of 0.05 and 0.01, the corresponding $\ln O_{\mathrm{GR}}^{\mathrm{modGR}}$ thresholds are -0.02 and 2.73 respectively. Once the outliers are excluded (which they should, as we shall see below), the new thresholds become -0.30 and 2.15.

8.4.4   Follow-up analysis of outliers

The diagnostic plots of Fig. 8.5 are generated by the Omega pipeline, based on the Q transform that was discussed in Sec. 8.2.3. The time-frequency plane is

---

[1]Of course the distribution is kept uniform in volume, only the range is rescaled.
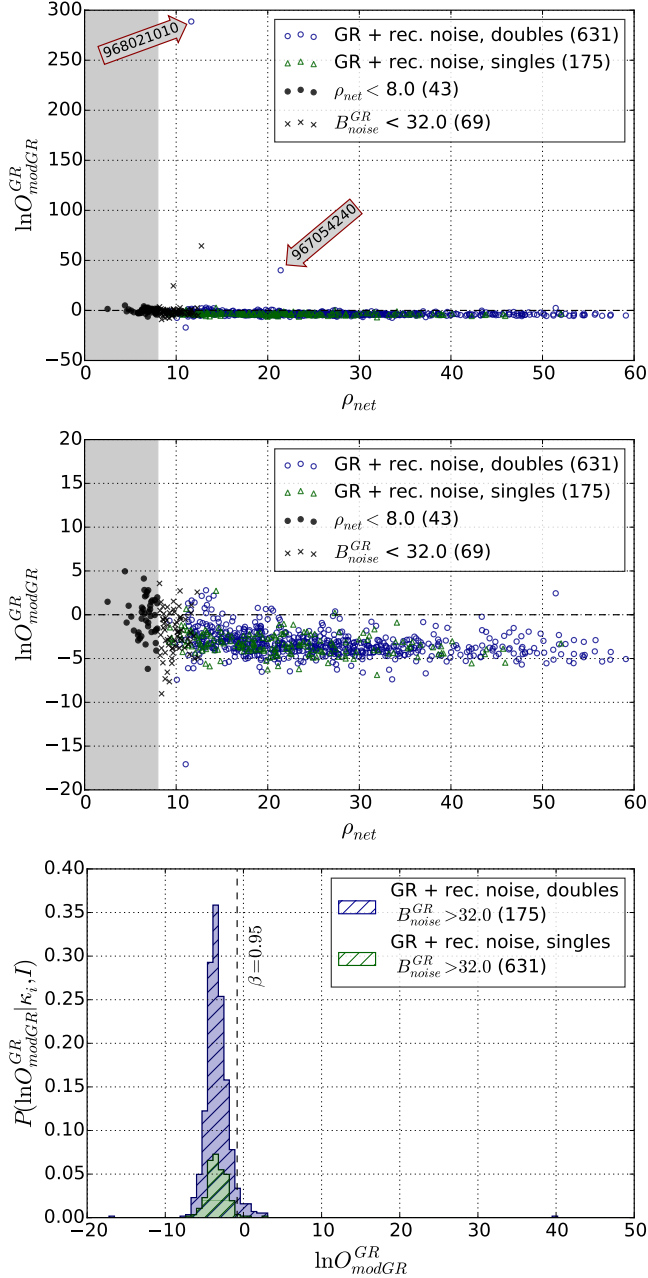
Figure 8.4: *A background populated by injecting 631 simulated BNS signals into real detector noise from S6/VSR3, re-coloured to the Early Advanced noise curve, for a network of two detectors (H,L). Events in single (double) detector time are drawn in green (blue). Top: a scatter plot showing the distribution of sources in the ρ_{net} - $\ln O_{GR}^{modGR}$ plane. Two outliers are clearly visible, which are tagged by their times of coalescence. Middle: the same plotted zoomed in, without the outliers. Bottom: a stacked histogram of the background distribution $P(\ln O_{GR}^{modGR}|\kappa, \mathcal{I})$ of single-source log-odds ratios in single (green) and double (blue) detector time. We notice the presence of two clearly distinguishable outlying events, one at a log-odds ratio of 40 and one at 289!*

tiled according to a minimum acceptable energy mismatch and the normalized energy of the Q-transformed data is calculated for each tile.

Even though the data segments in which the events were injected were not vetoed, one should always double check whether the data look reasonably glitch free. Especially in the case where data are re-coloured to a new noise PSD, there may be artificial amplifications of glitch patterns that were originally missed by the data quality algorithms. Such occurrences have shown up in our analysis and we investigate the data segments enclosing the two most outlying events, injected at GPS times 967054240 and 968021010.
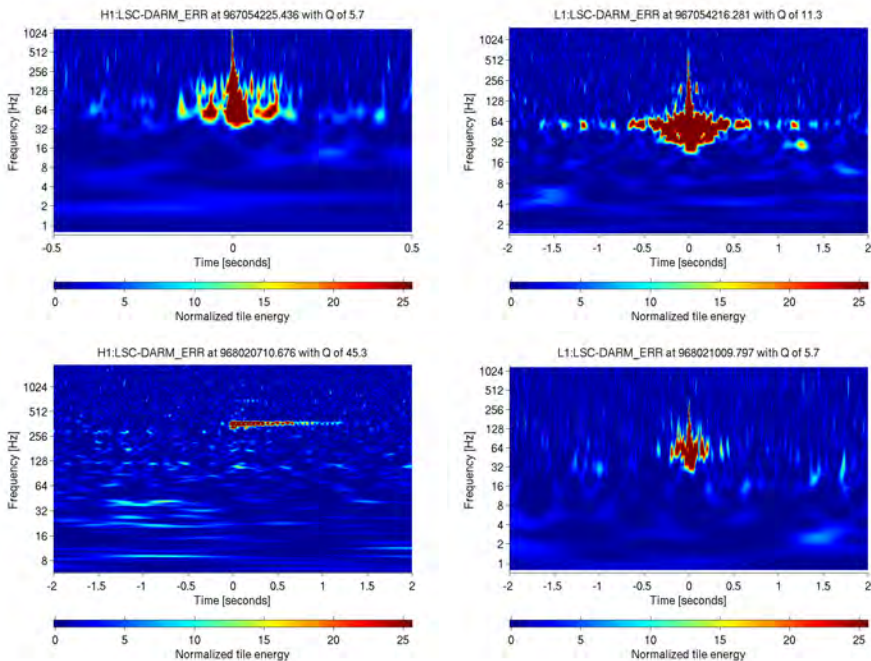
Figure 8.5: *Real data omega-scans capturing glitches that appear within two of the injections' data segments. For these events, TIGER yielded an odds ratio of 40 (top) and 289 (bottom) respectively. Possible glitch candidates in the vicinity of the injections are shown in the data of H1 (left) and L1 (right). In both cases we can see the presence of loud glitches in the data.*

With a quick look in the Omega pipeline diagnostic plots we immediately find loud glitches in the vicinity of each event. In particular, L1 data seem to contain a loud glitch centred at $t = 967054216.281\,\text{s}$, about 24 seconds before the injected time of coalescence of the first outlier and lasting for more than 1 s. A weaker and shorter glitch lasting less than 0.5 s is also found in H1 data 15 seconds before coalescence. Both seem to be correlated with loud triggers in a number of the auxiliary channels that hold data from environmental sensors (seismome-

ters, magnetometers *etc*). Similarly, during the second outlier another glitch appears in the data of L1 centred at $t = 968021009.801$ s and lasting for 0.5 s. Coincidentally, this places the glitch right on the injected time of coalescence, which explains the hugely overestimated odds ratio. After cross checking with the output of the auxiliary channels this glitch seems to be correlated with a loud electromagnetic event. On the other hand, H1 data seem to be glitch-free with a possible candidate only appearing 300 s before coalescence, when the signal is still outside LIGO's frequency range.

Judging from the above diagnostics alone, it is safe to say that in reality such events would not have been taken into consideration for full analysis with TIGER. In a realistic scenario, if such an event occurred, one would exclude it from the TIGER analysis upon examining the omega spectrograms of Fig. 8.5, because these loud events are

- too loud for too shortly to be BNS signals,

- morphologically different from the characteristic shape of a chirp signal *i.e.* concentrated around a central frequency which is increasing with time, like in Fig. 8.2,

- correlated with loud events in one or more auxiliary channels,

and would thus be identified as glitches. Furthermore, the Bayesian analysis algorithms and parameter estimation are affected by the glitches giving unusually multi-modal posterior distributions. One of the possible consequences of a short glitch is a strong bias in the mass posteriors, which is in fact what we observe with the second outlier, whose chirp mass is mis-estimated to be $\mathcal{M}_c > 8M_\odot$. This is in fact yet another reason why the event would have been rejected, since the chirp mass posterior p.d.f. lies way beyond the BNS threshold of $\mathcal{M}_c \leq 1.3M_\odot$.

8.4.5 Future avenues

Different approaches to counteract the existence of glitches in the data are being considered by the GW data analysis community. The most conservative one has already been described, namely to completely exclude data segments that contain glitches from the analysis. In this approach, any detection of a signal that has an overlap with such a segment will not be followed up with TIGER. A second approach would be to ignore only the piece of data that is affected by the glitch, usually referred to as *gating*. In this case, a detected signal overlapping with a glitch would in fact be processed, however the contribution of the overlapping segment to the calculations would be "nullified".

A third, more ambitious approach is to attempt to fit glitches, based on a set of parametrized glitch models [135, 247] before proceeding further with data analysis pipelines. One would then try to remove the glitch by using the best fit

8

parameters for the glitch model and subtracting it from the data. Since the duration of a typical glitch is very short (in the order of a second), compared to BNS signals, and *well localized* in the time-frequency space, this method can be applied in many cases without significantly affecting the follow-up analysis of the signal. Preliminary studies show that glitch fitting can significantly improve parameter estimation and evidence calculations, successfully removing biases induced by the presence of glitches.

8.5 Concluding remarks

In the presence of noise, our ability to directly infer the true nature of a signal is compromised. The success of statistical inference methods that one may employ relies upon the assumption that the stochastic properties of the noise are understood. However, long-term variability and unexpected effects in the noise, mostly due to environmental factors or instrumental misbehaviour, do occur and may severely compromise our inference methods. Non-stationarity of the stochastic properties of the noise, seen as the time-variability of the PSD, most heavily affects very long-duration methods such as continuous-wave (CW) analysis and searches for stochastic backgrounds. On the other hand, the occurrence of brief non-Gaussianities (glitches) will severely contaminate the background in the analysis of short GW signals such as burst search pipelines. Fortunately, our region of interest falls somewhere in-between. BNS signals last long enough to be clearly distinguished from short transient effects of noise and much shorter than the scale of overall variations in the noise PSD.

In this chapter we had an idea of how these two effects of noise can be counteracted for our analysis with TIGER and witnessed how severely can instrumental glitches affect its performance. Since we can never avoid glitches being present in a large sample of long-duration GW sources, it is important that these are identified and excluded from the analysis. However, most of the detector characterization efforts are tailored for the purposes of GW searches, and rightly so. It is then possible that the standards for vetoing a possible glitch event are good enough for search pipelines but not strict enough for a more thorough data analysis with sensitive scientific output. Thus, this investigation also raises the question of a need for an additional veto category, one that is more strict than CAT4 and ensures the rigorous performance of not only search pipelines but also full Bayesian PE or MS pipelines.

Chapter 9
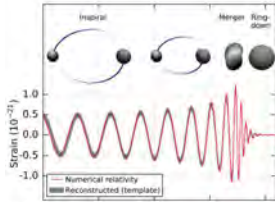
Testing GR: conclusions and future avenues

> *"Ah, gravity, thou art a heartless bitch."*
>
> Sheldon Cooper, The Big Bang Theory

The era of gravitational wave detections has just begun, and a new window with an exciting view is opening for gravitational physics, astrophysics and cosmology. Motivated by the rich dynamical content of GW signals from compact binaries, we have developed a Bayesian inference method dedicated to testing general relativity in its relativistic, strong-field regime. This method is based on assessing the consistency of the phase evolution of the signal with what is predicted by GR-based models. Compared against other methods, it has the advantages of being formulated in a Bayesian framework and that it is not a targeted test that compares GR against a particular alternative, but a rather generic one.

The need for a population of a background distribution may not sound like something that a Bayesian purist would appreciate. However, it is one that cannot be circumvented, mainly due to errors in the calculation of evidences in high-dimensional spaces, that are difficult to tame. In a sense it is a frequentist's cherry on top of a Bayesian cake.

In a proof-of-principle setting of Chapter 6, TIGER was shown to perform well, with a resolution in high post-Newtonian order that is many orders of magnitude better than any gravitational experiment has achieved to date. Several effects of fundamental, astrophysical and instrumental nature were investigated in Chapter 7 and our method was shown to be robust. These effects had to do with waveform discrepancies, finite-order PN truncation, NS spin and tidal effects, instrumental calibration errors. Finally, possible effects of non-Gaussian and

---

Image from [21].

143

non-stationary features that are present in the real noise of GW interferometers were studied in Chapter 8.

For systems with zero spins, the intrinsic parameters that define the phase evolution are the two component masses. When extending the signal space to include systems with non-zero spins, the signal space is enlarged by six additional dimensions. The main contributions to the phase evolution however, come from the instantaneous spins' projections on the axis of total angular momentum. Effects of precession, driven by non-aligned spins modulate the amplitude of the waveform and vary the spins' projections throughout the inspiral. For the weakly precessing BNS systems that we expect to find in nature, the consideration of constant aligned spin components is proven to be sufficient to capture the essential structure of the signal. One therefore only needs to extend one's template waveforms to include (anti-)aligned spins without losing much sensitivity in detecting GR-violating features. On the other hand, when considering NS-BH or BH-BH binaries, one cannot assume that precession effects appear as weak modifications/modulations of the signal, since typical BHs may have nearly extremal spins (above 0.9). These systems will need special treatment that will be briefly discussed below.

9.1 TIGER with binary black holes

In this dissertation we restricted ourselves to consider BNS systems only. There are clear reasons why these should be used as a first step, related to the region in the parameter space that these systems occupy, namely a corner of low mass ratios and low spin magnitudes. Nuisance effects that may appear due to the presence of matter were counteracted by setting a high-frequency cut-off in the analysis. Black holes on the other hand have the advantage of consisting of pure spacetime but may reach extremal spin magnitudes and high mass ratios, in which cases the reliability (in terms of faithfulness and effectualness) of currently available waveform models becomes questionable [114]. Such an inadequacy is bound to cause significant biases in Bayesian model selection methods like TIGER. More accurate EOB-based models tuned with NR waveforms in the late inspiral are currently too computationally expensive to be used as recovery templates, of which millions of waveforms need to be generated.

Zero-spin tests One may however arrive at a first estimate about the performance of TIGER with BBH signals by using existing inexpensive waveform models such as *IMRPhenomB* [36] [1] for *non-spinning* BBH systems. This is

---

[1]IMR stands for *Inspiral-Merger-Ringdown* and "Phenom" indicates the phenomenological nature of this approximant, in the sense that the numerical values of its coefficients are tuned using a set of accurate NR waveforms. The suffix "B" only enumerates the version of this approximant. More sophisticated versions have recently been available, namely IMRPhenomC [322] and IMRPhenomP [191, 324, 325].

actually a frequency-domain approximant, that transcends all three stages of coalescence: inspiral, merger and ringdown. It is described by an analytical expression $h(f) = A(f)e^{-i\Psi(f)}$ in frequency space, with a common phase expression $\Psi(f)$ throughout all three stages, of polynomial form, and a split expression $A(f)$ for the amplitude. The latter is described by the usual chirp form during the inspiral, a function during the merger and an exponential decay during ringdown. More explicitly

$$\mathcal{A}(f) = C\, f^{-7/6} \begin{cases} (f/f_1)^{-7/6}(1+\sum\limits_{i=2,3}\alpha_i v^i) & : & f < f_1 \\ w_m(f/f_1)^{-2/3}(1+\sum\limits_{i=1,2}\epsilon_i v^i) & : & f_1 \leq f < f_2 \\ w_r\mathcal{L}(f,f_2,\sigma) & : & f_2 \leq f < f_3\,, \end{cases} \tag{9.1}$$

$$\Psi(f) = 2\pi f t_c + \varphi_c + \frac{3}{128\,\eta\,v^5}\left(1+\sum_{k=2}^{7}\psi_k v^k\right). \tag{9.2}$$

The phase coefficients ψ_i are given in Table I of [36], together with expressions for the transition frequencies f_1, f_2, f_3 and the amplitude parameter σ. Naively using this as a model waveform, and treating ψ_i as the test parameters for TIGER, we populate the background distribution shown in Fig. 9.1. The main difference in the set-up between these simulations and the ones carried out for BNS is the wide distribution for the sources' total mass M, ranging from $3M_\odot$ to $30M_\odot$. Moreover, we simulate a set of GR-violating scenarios, with the following shifts to the IMR phase coefficients:

A1 a constant 10% shift in the ψ_6 phase coefficient (3PN),

A2 a constant 5% shift in the ψ_6 phase coefficient,

A3 a constant 2.5% shift in the ψ_6 phase coefficient,

B a constant 10% shift in the ψ_7 phase coefficient (3.5PN).

The foreground distributions for these scenarios are plotted against the background in Fig. 9.1. We find that there is remarkable sensitivity in the high-order coefficient $\delta\psi_6$ and much less so in $\delta\psi_7$. We also observe how the efficiency of detecting a deviation in ψ_6 decreases as the relative shift becomes smaller (from 10% to 5% to 2.5%). At this level however, the phenomenological nature of the phase coefficients does not allow for a direct physical interpretation of the above modifications.

Studies with spinning BH In order to extend the TIGER method to studying systems with spinning BHs, we will need to make use of accurate waveform families that cover the highly-spinning, highly-asymmetric corners of the parameter space, the regions where the aforementioned post-Newtonian and phenomenological waveform models perform poorly. Such waveforms have recently become available in the form of

9
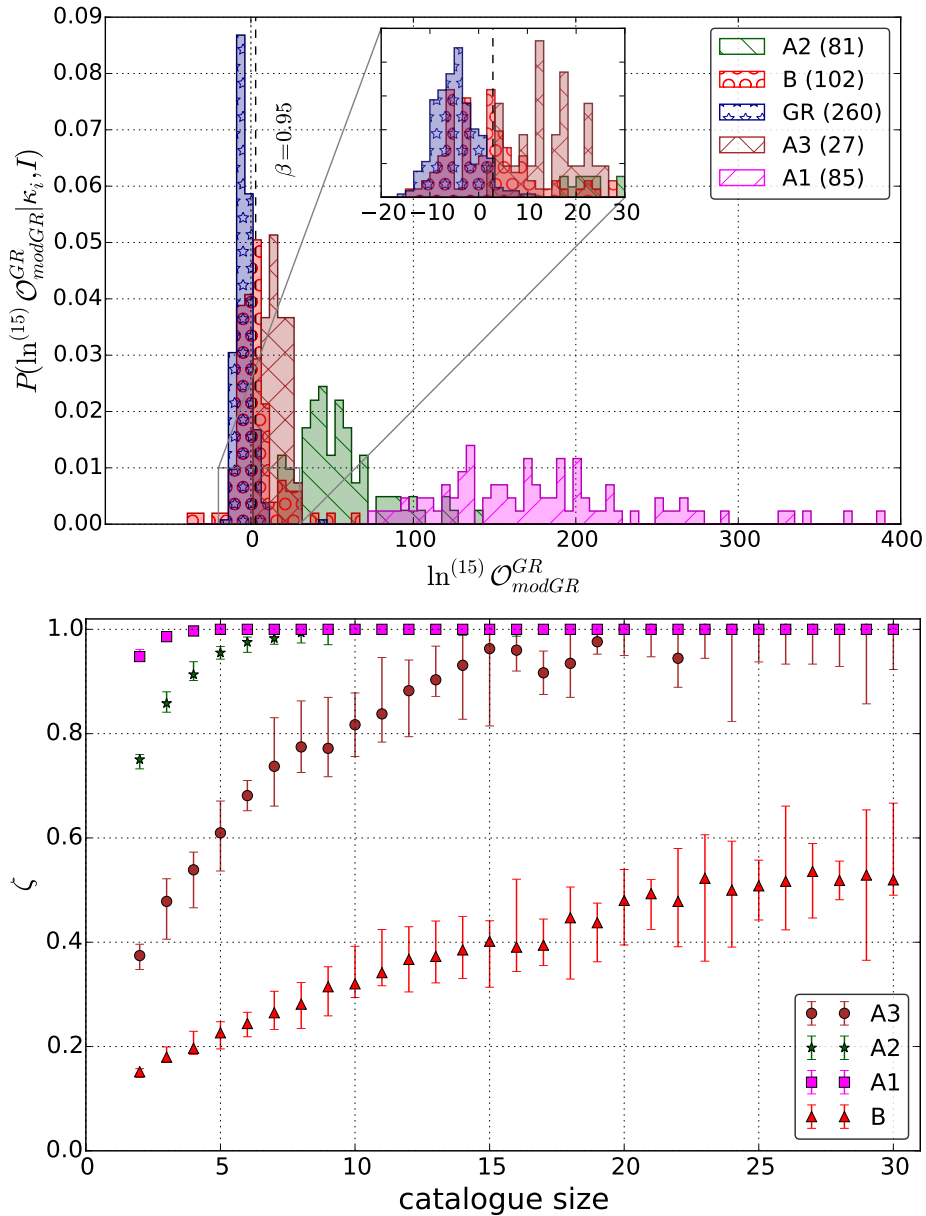
Figure 9.1: *Top: Background (blue) and foreground distributions of the TIGER log-odds-ratio $^{(15)}\mathcal{O}_{\mathrm{GR}}^{\mathrm{modGR}}$ for catalogues of 15 sources each. The foreground histograms correspond to the GR-violating scenarios A1 (purple), A2 (green), A3 (brown) and B (red). Bottom: Efficiency as a function of catalogue size, for the four GR-violating scenarios, using 1000 realizations of partitioning the analyzed sources into catalogues.*

- Effective-one-body models with spins (SEOB), calibrated towards merger by NR waveforms (SEOBNR); these have been developed for non-precessing spins (SEOBNRv1) [350] and generic precessing spins (SEOBNRv2) [285] [2].

- Phenomenological models with spins, that are described by analytic expressions, are also calibrated by NR waveforms, and extend all the way to ringdown. A very recent one is IMRPhenomP [191, 324, 325], which also models generic precessing spins.

- PhenSpin [341, 342], a hybrid model that evolves as SpinTaylorT4 in the inspiral, is matched with a NR-tuned waveform towards plunge and merger, which in turn is matched with the ringdown signal predicted by BH perturbation theory.

SEOBNR waveforms are rather expensive to be used as templates but could easily be used for simulating very realistic signals for injection. Recall that, even though the template waveforms for the analysis do not need to be perfectly accurate as much as they need to be fast to produce, the injected waveforms do need to be as close to reality as possible, if we want to build a reliable background. Regarding the recovery templates, IMRPhenomP can be directly generated in the frequency domain, so it is fast enough, and also crucially captures spin effects, including precession. An interesting question arises regarding the interpretation of parametrized deviations in the phase of IMRPhenom waveforms, as these are phenomenologically derived waveforms whose coefficients have no direct physical interpretation. Alternatively, PhenSpin can also be used; being however a time-domain numerical template it does come with additional computational costs, dominated by those of its SpinTaylorT4 part.

Reduced-order modelling for expensive templates One may in fact be able to use seemingly unaffordable waveform models like SEOBNR as recovery templates, by means of newly developed surrogate modelling methods like *reduced order modelling* (ROM). ROM provides an algorithm of pre-processing the space of templates, in order to produce principal components for the likelihood calculations. This allows for reliable analysis to be made on a signal by only producing a small optimal fraction of the each template waveform. The pre-processing part may be a very long and computationally intense process but it needs to be performed only once per template family. ROM is considered the most promising way to speed up current analysis methods that require the production of millions of waveforms (TIGER being one of them), and to render the use of "expensive" realistic templates affordable in the near future.

---

[2]See references for the restrictions on intrinsic parameters that apply to each waveform model.

9.2   Constraining the graviton's massive dispersion relation

One of the attractive features of TIGER is that it is built to capture generic deviations from GR and as a framework is not tied to any particular alternative theory of gravity. In this section we shall only slightly deviate from this rule and will perform a phenomenological analysis that can indicate whether gravity is mediated by a massive field. The motivation for doing this is simple: although the parameterization of this test is very specific, we will in fact be probing the phenomenology of a wide class of possible theories featuring a massive graviton, and will still remain agnostic to the details of the underlying theory. In fact, we will apply this test of Bayesian parameter estimation to the first direct GW detections, in order to set the most stringent upper bound on the graviton rest mass to date!

9.2.1   Theory and waveform modeling

An interesting class of alternative theories of gravity, the earliest of which were put forward in the 1970s, is one where gravitation is mediated by a massive field [150]. In these "massive graviton" theories, a gravitational wave would propagate slower than light, with a speed of propagation that depends on its frequency/wavelength. Following the standard prescription for a massive dispersion relation

$$E^2 = p^2 c^2 + h^2 c^2 / \lambda_g^2 \,, \tag{9.3}$$

one finds that the speed of a graviton will depend on its wavelength λ as

$$v_g \simeq c \sqrt{1 - (\lambda/\lambda_g)^2} \,, \tag{9.4}$$

in the limit $\lambda \ll \lambda_g$, where $\lambda_g = h/(m_g c)$ is a length scale that can be interpreted as the *Compton wavelength* of the graviton (m_g being its rest-mass).

This massive dispersion relation has a direct effect on the GW phase which is frequency dependent and is accumulated throughout propagation. In [382] Will finds that a GW signal will arrive distorted at the observer (since high-frequency waves will arrive earlier than low-frequency waves); in the frequency domain this is encoded as the extra phase term

$$\delta\Psi_{\mathrm{MG}}(f) = -\frac{\pi^2 \mathcal{M}_c D}{\lambda_g^2 (1+z)} (\pi \mathcal{M}_c f)^{-1} + \varphi_g + t_g f \,. \tag{9.5}$$

Here, z is the cosmological redshift and D is a cosmological distance defined in Eq. (9.6) below. Since the chirping waveform consists of a rich spectrum of frequencies, the effect described by Eq. (9.5) leaves a characteristic frequency-dependent signature whose magnitude can be measured. Prospects for this kind of analysis using Bayesian methods were first studied in [154].

Now, in Eq. (9.5) the second and third term can be absorbed in a re-definition of the measured phase and time of coalescence φ_c and t_c, since the corresponding modifications can be considered uniform for all detectors. The remaining first term has a pre-factor that crucially depends on the Compton length of the graviton λ_g, as well as on the distance to the source. The appropriate cosmological distance parameter D is defined as

$$D = \frac{1+z}{a_0} \int_{t_e}^{t_0} a(t)\, \mathrm{d}t \,, \tag{9.6}$$

where a is the cosmological scale factor, t_e and t_0 are the times of emission and detection and $a_0 = a(t_0)$ is the value of the scale factor at the time of detection (now). To first order in the redshift z, D can be approximated by $D \sim (1-z)\,D_L$, where D_L is the luminosity distance. As a result, our measurement will have an inherent degeneracy with cosmological parameters, which however is weak at low redshifts. In the analysis that follows we will be effectively measuring a parameter l_g defined by

$$\frac{D}{\lambda_g^2(1+z)} = \frac{D_L}{l_g^2} \,, \tag{9.7}$$

i.e. the combination that appears as a distance factor in Eq. (9.5); we shall treat l_g as an additional free parameter in our waveform model. Again, for small redshifts, the quantity l_g will be a good approximation of λ_g and to first order in z one finds $l_g \simeq (1+z)\lambda_g$. Subsequently, for a given cosmological model which fixes the *exact* functional relation between z and D_L (and therefore between D and D_L), we may analytically transform the posterior p.d.f. of l_g to one of λ_g via Eq. (9.7). The result is only weakly sensitive to the choice of ΛCDM cosmological parameters, which here are set to the latest Planck values [28] (Table 4, "TT+lowP+lensing+ext"):

$$H_0 = 67.90\,\mathrm{km\,s}^{-1}\,\mathrm{Mpc}^{-1} \,, \quad \Omega_\Lambda = 0.6935 \,, \quad \Omega_m = 0.3065 \,. \tag{9.8}$$

Existing bounds A good overview of current bounds on the Compton wavelength of the graviton is given in [80], where a clear distinction is also made between bounds of *static* and of *dynamical* nature. Simply put, static bounds originate from the static sector of the gravitational interaction, which would also be affected if gravity was mediated by a massive field. In particular, the static potential would take a Yukawa form $V(r) = -\frac{Gm}{r} e^{-r/\lambda_g}$, where λ_g acts as the effective cut-off scale for gravity. The most stringent *static bound* to date comes from Solar System measurements [346, 382] (and the orbit of Mars in particular), which set the constraint $\lambda_g > 2.8 \times 10^{12}$ km. There exist two more static bounds, one from studying the large-scale galactic cluster dynamics [185] and one from weak lensing observations [126], setting lower bounds at 6.2×10^{19} km and 1.8×10^{22} km respectively, however these result from strongly model-dependent calculations and incorporate assumptions, most notably on thegalactic distribution of dark matter. The systematics introduced by these assumptions can

149

dramatically weaken the lower bound claims. *Dynamical bounds* are related to the dynamical sector of GR and come from observations involving the generation and/or propagation of GWs; we are about to set such a bound in Sec. 9.2.2. Prior to the first GW detection, the only such bound came from observations of binary pulsars and the consistency of their orbital decay rate with GR. If gravitons were massive, the modified propagation of gravitational waves within the binary system would alter the orbital dynamics and would modify the way in which the orbit decays [169]. No such inconsistency was observed in PSR B1534+12 or PSR B1913+16 and a dynamical lower bound was set at 1.6×10^{10} km.

9.2.2   Results

We analysed GW150914 according to the set-up outlined in [23], assuming a uniform prior in the logarithm of λ_g (based on the fact that λ_g is a scale parameter), and using a prior range of $\lambda_g \in [10^{13}, 10^{20}]$ m. Two waveform approximants are mainly used in this analysis, namely the single-spin-precessing IMRPHENOMPv2 [191, 222] and the aligned-spin SEOBNRv2 for which reduced order modeling is employed to speed up the analysis [303]; moreover, the same analysis performed with other waveform models gives similar results.We find that $\lambda_g > 10^{13}$ km, below which value the posterior abruptly drops to practically zero and above which it quickly rises like a sigmoid function to a flat distribution. Because with this particular prior the λ_g posterior is formally unbounded, we can make use of a flat prior in m_g (which translates to $\pi(\lambda_g) \propto 1/\lambda_g^2$) in order to obtain a meaningful 90% confidence lower bound. This is illustrated in Fig. 9.2, where the cumulative posterior distribution on λ_g is plotted. This constraint is tighter than the current lower bound set by Solar System tests [382] by a factor of a few, and translates to a bound on the graviton rest mass of $m_g < 1.24 \times 10^{-22}eV/c^2$. It also beats the only other *dynamical* bound related to GW propagation, the one set by binary pulsars [169], by three orders of magnitude! Additionally, we have calculated the Bayes factor between the GR hypothesis and the *massive dispersion relation* (MDR) hypothesis to be $\ln B_{MDR}^{GR} = 0.52$, slightly in favour of the GR hypothesis.

The same analysis on the second confirmed detection GW151226 yields posteriors on λ_g that are slightly looser than what was already obtained by GW150914; this is largely due to the overall weakness of the former relative to the latter. Since the Compton wavelength of the graviton is a global parameter whose value is expected to be common across all GW signals, we can straightforwardly combine information from both events and arrive at a *combined posterior* p.d.f. for λ_g (and equivalently for m_g), as outlined in Sec. 3.4.3. As expected, the second event does not improve the lower bound of $\lambda_g > 10^{13}$ km, since its posterior is non-informative above that value.

The bound inferred from the current analysis is expected to further tighten in the future, with the detection and analysis of more GW signals from compact binaries. In particular, low-mass BBH systems or neutron star binaries of similar
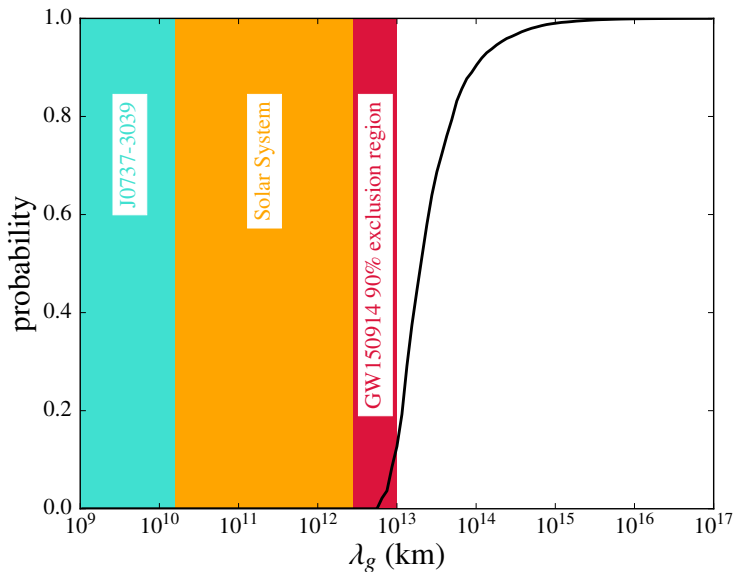
Figure 9.2: *Cumulative posterior distribution for the Compton wavelength λ_g of the graviton, resulting from the analysis of GW150914, and setting a 90% lower bound at 10^{13} km [24]. The new exclusion region based on this measurement is shaded in red and spans almost an order of magnitude. Exclusion regions from the dynamical bound of binary pulsars and the tightest static bound based on Solar System tests are shaded in cyan and orange respectively.*

loudness are expected to contribute valuable information, since much more of the earlier inspiral (where $(\pi \mathcal{M}_c f)^{-1}$ is large) will be in band.

9.3 Testing the no-hair theorem with black hole ringdown

The framework developed in Chapter 5 is not specific to CBC inspiral. In fact it was recently applied to the analysis of simulated GW signals from the BH ringdown stage, that follows a BBH merger [259], for the purpose of testing the no-hair conjecture. The scenario that was investigated was a population of intermediate-mass black hole (IMBH) mergers, whose ringdown signal would be detectable by Einstein Telescope (ET).

The idea is the following: by the master equation of Kerr BH perturbation theory [352, 301, 242], the ringdown signal is a superposition of damped sinusoids,

schematically taking the form

$$h(t) = \frac{M}{D_L} \sum_{l \geq 2, |m| \leq l} A_{l,|m|} \, e^{i(\omega_{lm} + 2\pi i/\tau_{lm})t} \, {}_{-2}Y^{l,m}(\iota, \phi) \,, \qquad (9.9)$$

where ${}_{-2}Y^{l,m}$ consist the functional basis of (-2)-spin-weighted spherical harmonics. These terms are the black hole's superradiant eigenmodes or *quasi-normal modes* (QNM), whose complex eigen-frequencies $\tilde{\omega}_{lm} = \omega_{lm} + i\frac{2\pi}{\tau_{lm}}$ (mode frequencies ω_{lm} and damping times τ_{lm}) are completely characterized by two numbers: the BH mass M and spin J, according to the no-hair conjecture; the relations that give $\omega_{lm}(M,J)$ and $\tau_{lm}(M,J)$ and the QNM amplitudes $A_{l,m}$, have been calculated numerically to good approximation. This means that by measuring more than a pair of QNM parameters, one gets a consistency test of the no-hair conjecture. A violation thereof means that one or more of the QNM parameters does not have the functional dependence on M and J predicted by GR. By parametrizing relative deviations in $\tilde{\omega}_{lm}$, we immediately get a way of applying the TIGER machinery for testing the no-hair conjecture with ringdown signals. It was found that a relative shift of 10% in either the (22)-mode or the (33)-mode frequencies will almost surely be detectable after combining information from about 10 sources, while a 25% relative deviation in the damping time of the (22)-mode is still not likely to be detected after 50 sources are analyzed. However, parameter estimation in a targeted analysis for τ_{22} shows that such a deviation may be constrained to roughly 10% with the same amount of sources. The method is less sensitive to mode frequencies and damping times of the remaining subdominant QNMs.

9.4   Into the future

Before closing Part II of this dissertation, I would like to point out a valid question that naturally arises once one obtains a clear picture of what TIGER will and will not do. TIGER will make a statement about whether the data are consistent with what GR predicts or not. However, if it finds the data to be perfectly consistent with GR, it is not designed to put direct bounds on particular alternative theories of gravity or families thereof. And if it does find inconsistencies between the data and GR, it will not make any statement on the nature of the GR violation.

So, once detections start coming in, how should one follow up results produced by TIGER that point to one direction or the other? If TIGER shows consistency with GR a further step would be to run PE analysis on parametrized deviations, in order to put bounds on modifications of the PN coefficients, and possibly on parameters of alternative theories of gravity. This should be continued as long as the consistency remains clear. If, on the other hand, TIGER indicates a clear violation of GR, one should be prepared to follow it up with tailor-made tests against alternative theories. Not many theories have made exact predictions on

how CBC waveforms are modified, and there is ample work to be carried out in this respect. Those who have, can then be ranked on the basis of their evidence and compared against GR, and marginalized posterior p.d.f.s can be drawn on the non-GR part of their parameter space. It could well be that more than one alternative theories of gravity are favoured over GR, and that for more than one of them we will be able to obtain *lower bounds* on GR-violating parameters (if $\vec{0}$ is left outside of the posterior bulk). Needless to say, claims of falsification of GR should come with great caution and only after any other possible explanation is ruled out; that is, all the implicit assumptions of our model, on the nature of the sources and their environment, on the properties of the detectors, on the waveform models, *etc.*, everything that can be found in our background information $\mathcal{I}$, should be thoroughly studied, or stated as a possible caveat. Of course, there is always the intermediate scenario where the combined odds ratio lies beyond the bulk of the background, but with a FAP that is not low enough to indicate a clear GR violation. The safe thing to do in such a case, would be to wait patiently for more detections to come in, which will eventually drive the combined odds ratio deeper into or further beyond the background.

Part III

The Neutron Star Equation of State

<div style="text-align: right">
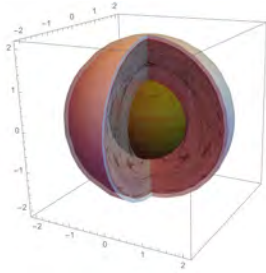
Chapter 10

The physics of neutron stars

</div>

Apart from being the constituent of compact binaries, a neutron star is an extremely interesting astrophysical object in its own right. Holding the title of the most dense stable form of matter known to exist, with densities reaching a few times above that of an atomic nucleus, neutron stars have captured the attention and imagination of the physics community. One of the great unresolved mysteries in modern physics, lying unsettled on the interface of relativistic astrophysics, nuclear physics, particle physics and condensed matter physics, is that of determining the nature and physical properties of the cold interior of a neutron star, where densities reach supranuclear values, unattainable by any current man-made experiment.

Neutron stars, being compact astrophysical objects, take up a special place in a number of efficient mechanisms for the emission of gravitational waves. From a macrophysical perspective, the physics of the NS interior is encoded in the neutron star's *equation of state* (EoS), which describes the way the pressure builds up with increasing density, and thus the way hydrostatic equilibrium is achieved in the interior of the star. Current bounds to the NS EoS have been set by both physical arguments and astrophyiscal observations. However, due to the highly non-trivial nature of the microphysics that describes cold matter at supranuclear densities, as well as the lack of access to such regimes through current laboratory experiments, there is still a high degree of uncertainty in the NS EoS.

It then naturally occurs that a possible GW detection from a system containing a

<div style="text-align: right">

10

</div>

NS may yield valuable information on its physical properties and, in particular, its equation of state. This part of the dissertation is devoted to studying the possible ways in which gravitational waves, emitted during the coalescence of Neutron Star binaries, may yield information on the neutron star EoS, and inventing possible methods that will allow us to extract this information from the observed data.

To date, various methods have been proposed and applied in an attempt to measure NS structure related quantities by means of electromagnetic observations of NS as pulsars. Among those, the following are considered for measuring NS masses, radii, or other matter properties of NS:

- observations of X-ray binaries, in which a NS accretes mass from a companion for measuring masses and possibly radii;

- EM observations of isolated binaries, measurement of quasi-periodic oscillations and NS surface cooling;

- gravitational redshift measurements of spectral lines for constraining compactness M/R;

- pulsar timing with binary pulsars for (i) accurate mass measurements (ii) measurements of spin-orbit coupling and moments of inertia, and (iii) studying pulsar glitches which can give hints on the internal structure and EoS;

- neutrino detections during proto-NS formation in core-collapse SN explosions.

However, in most cases the resolution and systematics of the observations are far from satisfactory if one wishes to put significant constraints on the EoS.

In a distinct category of methods, one should classify the first interesting constraint on "asymmetries" of observed NS, set by the *non-detection* of gravitational waves during the science runs of the initial LIGO and Virgo detectors (most notably for the case of the Crab [1] and Vela [2] pulsars [11, 10, 7]). As we shall see, the methods discussed here will provide an independent way of measuring these properties, being susceptible to a totally different set of systematic uncertainties than the ones based on electromagnetic observations.

Coalescing binary neutron stars, nuclear physics and cosmology   Much effort in GW research has been put on solving the *direct* problem of deriving a gravitational waveform from the known physics. Conversely, lack of knowledge in NS physics results in a certain degree of ambiguity in the waveform. The current uncertainty in the physics underlying the NS EoS provides fertile ground for studying an *inverse* problem, of extracting physics from the analysis of GW signals emitted by BNS systems. In particular, GW data analysis can probe

---

[1]ra: $5^h 34^m 32.0^s$ dec: $22^o, 0', 52.1''$

[2]ra: $8^h 35^m 20.6^s$, dec: $-45^o - 10' - 35.0''$

unexplored territory in nuclear physics and provide invaluable input on the matter properties and composition at supranuclear densities.

Once the NS EoS problem is settled, cosmology gives us yet another inverse problem that we can then solve. Inspiraling BNS systems are known to be *standard sirens*, *i.e.* their *luminosity distance* D_L and *redshift* z can be inferred independently. Moreover, in contrast with EM observations at cosmological distances, there is no need for calibration (equivalent to the "cosmic distance ladder"), since luminosity distance is only found in the GW amplitude, and the intrinsic luminosity is also encoded in the phase via the chirp mass. In the absence of matter, a coalescing binary is characterized by a single scale, given by its chirp mass; this implies that cosmological redshift will have an effect on the entire waveform that is completely degenerate with that of a "redshifted mass" (*i.e.* the source's mass will appear to be larger than its intrinsic value by $1 + z$). In the presence of matter however, this redshift-mass degeneracy is broken by the additional scale introduced by matter effects, so the redshift can indeed be measured independently[3]. This gives us a new, totally independent way of doing cosmography and the potential of independently inferring the values of cosmological parameters $(H_0, \Omega_m, \Omega_\Lambda)$ in the standard ΛCDM model. This avenue was first explored in [261].

In the remainder of this chapter, we will briefly go through the basic physical mechanisms underlying the properties of neutron stars.

10.1 The Neutron Star Equation of State

Even though the prediction of the existence of extremely compact objects made almost solely of neutrons dates as far back as the late 1930s with the pioneering work of Baade and Zwicky [53] and Oppenheimer and Volkoff [278], the first detection of such an object did not occur until 1967 [198]; interestingly enough, an exact modelling of the equation of state at such high densities is yet to be devised. Theoretically, fairly accurate predictions can be made under realistic assumptions up to a certain density regime, starting from the simplest model of an ideal Fermi gas. Let us briefly walk through the crucial features of a realistic EoS, going up the scale of complexity and density, to the point where theoretical uncertainties prohibit any further predictions.

10.1.1 Simple EoS models

At densities where degenerate electrons are still the dominant source of stabilizing pressure, typically at $\rho < 10^{11} \text{g cm}^{-3}$, the EoS of normal matter can be

---

[3]A different way of measuring the redshift is by means of a coincident EM observation. However, this kind of information is expected to be available for only a small fraction ($\sim 10^{-3}$) of the coalescing systems.

approximated, starting from the ideal Fermi gas model. This has its roots in the pioneering work of Chandrasekhar [123], who established the first consistent model for the hydrostatic equilibrium of ideal white dwarfs (WDs). There, the gravitational force was counteracted by the degenerate pressure of the Fermi electron gas. Similarly, in the most simplified model for neutron stars, one considers a cold, degenerate gas of non-interacting neutrons, that dominates the pressure and energy density of the star. As shown in Appendix B, one gets a *polytropic* form for the EoS,

$$P = K\rho_0^\Gamma \, , \tag{10.1}$$

whose validity will of course be restricted to a particular density range. In the non-relativistic limit, $\rho_0 \ll 6 \times 10^{15} \, \mathrm{g \, cm^{-3}}$ the *polytropic coefficients* Γ and K are calculated as: $\Gamma = \frac{5}{3}$, $K = 5.38031 \times 10^3 \, \mathrm{kg^{-2/3} \, m^4 \, s^{-2}}$

10.1.2 EoS at low densities

Building on the simple non-interacting gas model described above, we will now briefly describe the relatively well understood EoS at densities below the density of *neutron drip*, ρ_{drip} (see Sec. 10.1.3). Apart from WD and gas planets, the EoS at such densities describe one of the outmost layers of a NS, known as the *crust*.

The model outlined in Sec. 10.1.1 has been further corrected and enriched by:

1. Electrostatic effects between the charged particles of the fluid. These give a significant correction for WD, but a rather negligible one for NS as matter becomes increasingly neutron-rich.

2. Detailed balance in the β-decay reaction that regulates the fractional abundances in the *n-p-e* mixture.

3. Nucleon-nucleon many-body interactions; these require either the application of semi-empirical models for the nuclear energy, or/and field-theoretic calculations of quantum chromodynamics (QCD) that govern the strong interaction.

4. Different compositions if more species/resonances become stable at high densities (pions, kaons, strange hadrons, etc.). Transitions to energetically favourable compositions result to "softening" of the EoS since more compact stable configurations become available.

The book by Shapiro and Teukolsky (1983) [329] is an excellent guide for the interested reader that wishes to see the details behind the calculations of the listed features.

Since our interest lies in the very high-density regime, we will not discuss the first point, apart from mentioning that it may contribute a non-negligible correction to the NS radius and maximum mass, as it becomes important in the outer, less dense layers of the NS. However, it is instructive to discuss the inverse β-decay, one of the crucial physical processes that makes a NS what it is.

Inverse β-decay Assuming a mixture of the three basic particles e, p, n, that make up all of regular matter, one may derive the conditions of detailed balance for the reaction

$$n^0 + \nu_e \rightleftharpoons p^+ + e^- \tag{10.2}$$

which is an amphidirectional version of the familiar β-decay (in which an anti-neutrino is found on the RHS instead). The outcome will depend on the current state variables of the system, while it is evident that the natural direction of the reaction is to the right, due to the rest-mass difference between m_n and $m_p + m_e$. In a high-density environment however, where the electron Fermi energy is high enough and where the electron fluid is highly degenerate, each additional electron would contribute an energy larger than its rest mass by roughly E_F, due to the Pauli exclusion principle. When working with neutron stars, all three species will be in a highly degenerate state and –electrostatic and nuclear interactions aside– can be modelled as ideal Fermi gases. As shown in Appendix B, the abundance of neutrons can become more than three orders of magnitude larger than that of protons, settling to an asymptotic value of 8 at large densities.

More realistic low-density EoS The above ideal Fermi gas mixture model is good first approximation but, as already mentioned above, is missing key ingredients for a realisitc EoS. More realistic models that include a number of additional features, such as electrostatic forces, semi-empirical formulas for the energy of nuclei, and many-body interactions were developed throughout the 20th century. Recall that at low densities the nucleons are grouped into heavy nuclei, with $^{56}_{26}$Fe being the lowest energy state of matter below $\rho \sim 10^7$ g, at which point the e^- Fermi gas becomes fully relativistic. Then, inverse β-decay kicks in, enriching nuclei with neutrons, which in turn shifts the balance of the fission process towards heavier nuclei.

A few characteristic low-density models are outlined in [329]. In brief, the Thomas–Fermi approach incorporates electrostatic corrections to the EoS and is solved numerically in the Feynmann-Metropolis–Teller model (FMT). The Harrison-Wheeler (HW) EoS considers heavy nuclei that become neutron rich at high densities due to β-equilibrium and is based on a semi-empirical mass formula for $M(A, Z)$, known as the liquid drop model to minimize the energy with respect to (continuous) A and Z; it is considered valid in the region $10^7 \leq \rho \leq 3 \times 10^{11}\,\mathrm{g\,cm^{-3}}$, above which it is smoothly matched to that of a mixture of equilibrium nuclides with free neutron and electron gas (see below). The Baym–Pethick–Sutherland (BPS) EoS uses a more sophisticated mass formula that includes Coulomb lattice corrections and treats A and Z as discrete variables; the latter effect introduces discontinuities in the density wherever a phase transition to a different (A, Z) pair takes place. The BPS EoS closely agrees with HW and is valid for densities below neutron drip $\rho \leq 4.3 \times 10^{11}\,\mathrm{g\,cm^{-3}}$ which are met in the interior of white dwarfs and in the outer crust of neutron stars.

10

10.1.3   EoS at very high densities

Neutron drip   As the inverse β-decay leads to more and more neutron rich nuclei, the effect of intra-nuclear Coulomb forces weakens, and so does the tendency for nuclei heavier than $^{56}_{26}$Fe to break apart. With increasing density, larger and larger nuclei become more energetically favorable, up to a critical point where it becomes energetically favorable for the first neutrons to "drip" out of the nuclei. The onset of this effect, known as the "neutron drip" is at roughly $\rho \sim 3.2 \times 10^{11}\,\mathrm{g\,cm^{-3}}$; above this density, neutrons are found in two phases: both in nuclei and as free particles outside the nuclei in the form of a degenerate Fermi gas. At even higher densities the free neutron gas starts to dominate in pressure and density, until eventually the nuclei begin to dissolve at roughly the nuclear density $\rho_{\mathrm{nucl}} = 2.8 \times 10^{14}\,\mathrm{g\,cm^{-3}}$. Until that regime is reached, the EoS is well described by the Baym–Bethe–Pethick model (BBP) [64].

EoS above nuclear densities   In contrast with EoS calculations at lower densities, the uncertainties at densities much larger than neutron drip become increasingly large, mainly due to the lack of understanding of nucleon-nucleon many-body interactions at this regime. Most notably, the situation becomes largely uncertain when densities reach values a few times larger than nuclear densities $\rho > \rho_{\mathrm{nuc}} \simeq 2.8 \times 10^{14}\,\mathrm{g\,cm^{-3}}$, where nucleons are essentially in touch with each other. Models developed over many decades can be classified into three broad categories: (i) nonrelativistic potential models, (ii) models based on field theoretical approaches, and (iii) models based on the relativistic Dirac-Brueckener-Hartree-Fock approach. Some experimental results are available for symmetric nuclear matter but any naive extrapolation to highly asymmetric cold matter at even higher densities cannot be relied upon.

10.1.4   Neutron star structure and modern EoS models

Contemporary models for the NS EoS at very high densities are based on relativistic field theory or the relativistic Dirac-Brueckner-Hartree-Fock approach, but are even more sophisticated than what is described above, in terms of composition and calculations of nucleon-nucleon interactions. An extensive list of such models can be found e.g. in papers by Lattimer et al. [237], Hinderer et al. [200] and references therein. In Fig. 10.2 a few examples of such models are listed, together with the approach that each model is based on, as well as the matter composition that it considers.

According to the current models, the NS has a structure that subdivides its interior to: (i) the inner core, (ii) the outer core, (iii) the crust and (iv) the envelope. Most of the mass is found in the core, while the much less dense crust typically extends only 1-2 km deep. In the simplest models, the composition of the core (in models where only ordinary matter is considered) is mainly neutrons with a small proton and electron fraction, while the crust consists of a mixture of

neutrons and heavy nuclei. The envelope and an overlaying atmosphere is rich in charged particles and is where most of the observed EM phenomena take place.

Some EoS models predict that a NS's inner core can reach densities that are high enough to populate additional strange species, or excite heavier baryonic resonances. The transition to non-normal matter effectively softens the EoS, since it opens up new channels to lower the total energy of the star. As a consequence, the maximum NS mass in such models is expected to be smaller.

Hyperons Hyperons are baryons that contain at least one strange quark. Such particles can be formed in the NS core by e.g. the inverse decay of a nucleon's u-quark, accompanied by the emission of a meson, when such a process is energetically favored by the conditions in the core. EoS models that predict the formation and co-existence of hyperons with normal matter inside the inner core of NS exhibit a relative softening at high densities. Examples of such models can be found e.g. in [65]. In the investigations that follow, we will be using a hyperonic model that is still consistent with current physical and observational constraints, namely the H4 model described in [234].

Pion condensates Yet another EoS-softening mechanism may occur through the formation of mesons, which may begin to appear e.g. via the reaction $n \rightarrow p + \pi^-$, as soon as this becomes energetically favorable, *i.e.* $\mu_n - \mu_p = \mu_e > m_\pi = 139.6\,\mathrm{MeV}$ (this may occur at supranuclear densities). It can be shown that any such population will consist mainly of pions, the lightest possible type of mesons. Due to their bosonic nature, pions at very low temperatures will form dense Bose-Einstein condensates, in which the bulk kinetic energy/pressure becomes very low. This softens the EoS quite significantly, which is why many of these models have already been excluded by existing observations (see Sec. 10.3).

Superfluidity and superconductivity A well known effect in cold condensed matter physics is that of electron pairing, where Cooper pairs of electrons behave as integer-spin particles (bosons) and form a condensate with near-zero resistance and viscosity. In the interior of neutron stars, the same effect may occur, but this time it is the nucleons that form the fermion pairs. Since the proton density is governed by the electron density, the protons occupy much lower momenta than the neutrons, so pairing mostly happens between p–p and n–n pairs. The proton pairing gives superconductive properties for the charge transfer in the NS interior, while the neutron pairing gives superfluid properties for mass transfer in the star. The equivalent to the Curie temperature below which the pairing is populated, is expected to be in the order of 10^{10}K, which is many orders of magnitude higher than the typical NS temperature. These super-features are held responsible for violent phenomena that seem to occur in observed pulsars and manifest themselves in the form of rotational irregularities or sudden bursts of EM radiation. These types of *glitches* observed in pulsar signals can be explained

by sudden (quantized) reconfigurations of the superconductive (magnetic) or superfluid (rotational) vortex structure in the NS interior.

10.1.5   Quark matter and strangeness

It has been advocated that the inner core of a NS can reach densities high enough that nuclear matter undergoes a phase transition where quarks break free from the nucleons and can be found in a deconfined state. This introduces an entirely different regime for the core, featuring three quark species (u, d, s), that most probably exhibit *color superconductivity* and potentially *color flavour locking*; the strange quark core extends almost out to the surface, and is enveloped in a very thin crust of normal nuclear matter. Such a state of matter would be more stable than any nuclear matter configuration and was conjectured to be the *ultimate state of matter* by Bodmer and Witten, in what is known as the "strange matter hypothesis". A characteristic property of EoS models for strange quark stars, which are the softest ones currently available at high densities, is that pressure drops towards zero at a critical lower density (self-bound stars). In practice, the quark matter EoS are non-differentiably continued by normal matter EoS at lower densities. Realistic SQM models employ perturbative QCD methods; a popular model described in [299] uses the MIT bag model, with an energy per baryon ceiling at $939 \, \text{MeV}$ setting a strict bound on the bag constant $B \leq 94.92 \, \text{MeV} \, \text{fm}^{-3}$. An extensive review of the theory and phenomenology of SQM stars is given by Weber in [376].

10.2   Relativistic stars in hydrostatic equilibrium

Hydrostatic equilibrium configurations for stars in GR can be obtained by applying the EFE Eq. (1.14) after using the fluid's properties to define the stress energy tensor in the RHS. Usually a high degree of freedom is postulated, e.g. for stable spherically symmetric stars one has three Killing vector fields, along which the metric is invariant. Symmetries remove degrees of freedom from the problem and make the solutions easier to derive. Furthermore, we will only consider a perfect fluid, whose stress energy tensor is given by:

$$T_{\mu\nu} = (\rho + P) \, u_\mu u_\nu + P g_{\mu\nu} \, . \tag{10.3}$$

The two state functions that enter the stress-energy tensor, the energy density ρ and pressure P are related; for a given type of matter this relation can be made explicit once its equation of state $P = P(\rho, s)$ is known. Since we will be interested in neutron stars, for which $T \simeq 0$ (or at least much smaller than the Fermi temperature E_F'/k), we shall also use that $s = 0$ everywhere, and thus the entropy dependence is removed and the EoS is fully characterized by knowing $P = P(\rho)$.

10.2.1 The Tolman-Oppenheimer-Volkoff equation

A spherically symmetric metric in its most general form is given by the line element:

$$ds^2 = -e^{2\Phi(t,r)}dt^2 + e^{2\lambda(t,r)}dr^2 + r^2 \overbrace{\left[d\theta^2 + \sin^2\theta\, d\phi^2\right]}^{d\Omega^2}. \qquad (10.4)$$

In the special case when the metric is also static, we have $\frac{\partial\Phi}{\partial t} = \frac{\partial\lambda}{\partial t} = 0$ and we also recover the Schwarzschild metric Eq. (4.3) as the *exterior* (vacuum) solution. In the presence of matter in the star's interior, and for a given initial condition (e.g. mass density ρ_c at $r = 0$), the *interior* solution will give a density profile $\rho(r)$ and pressure profile $P(r)$ depending on the matter EoS, $P = P(\rho)$.

Working towards this derivation, we define the quantity $m(r)$:

$$e^{2\lambda(r)} \equiv \left(1 - \frac{2m(r)}{r}\right)^{-1}. \qquad (10.5)$$

Recall that in Newtonian gravity, the hydrostatic equilibrium is achieved by the cancellation between the pressure gradient and the gravitational force, $\frac{dP}{dr} = -G\frac{m(r)\rho(r)}{r^2}$, on each infinitesimal shell of matter. In GR, the equilibrium equations are derived from the EFE, giving the following system of three independent linear differential equations

$$\frac{dm}{dr} = 4\pi r^2 \rho(r), \qquad (10.6)$$

$$\frac{dP}{dr} = -\frac{\rho(r)\, m(r)\left(1 + \frac{P(r)}{\rho(r)}\right)\left(1 + \frac{4\pi r^3 P(r)}{m(r)}\right)}{r\left(r - 2m(r)\right)}, \qquad (10.7)$$

$$\frac{d\Phi}{dr} = -\frac{1}{\rho(r) + P(r)}\frac{dP}{dr}. \qquad (10.8)$$

The first equation (10.6) tells us that $m(r)$ can be interpreted as the integrated mass within a ball of radius r,

$$m(r) = \int_0^r dr'\, \rho(r')\, 4\pi r'^2. \qquad (10.9)$$

This quantity is not a bare (baryonic) mass (it is not an integral of the local density ρ with the invariant volume element) but also it includes the gravitational binding energy, so that it matches an exterior Schwarzschild solution for a total gravitational mass $M = m(R)$. The second equation (10.7) is known as the *Tolman-Oppenheimer-Volkoff* equation [354, 278, 355] and together with Eq. (10.6) gives a solution for the density and pressure profiles in the star's interior. Finally, in Eq. (10.8) the remaining unknown metric function Φ is directly derived once $\rho(r)$ and $P(r)$ are obtained, and fixes the g_{00} component of the metric.

10

Its integration constant is fixed by the continuity condition with the exterior Schwarzschild metric. Thus, given an explicit expression for the EoS, for a given central density ρ_c or central pressure P_c, the integration of the above system of equations yields a unique solution that defines the equilibrium configuration of the star. In the eyes of gravity, all the details of the complex microphysics that govern the fluid properties at every single point in the star, are encoded in a single function.
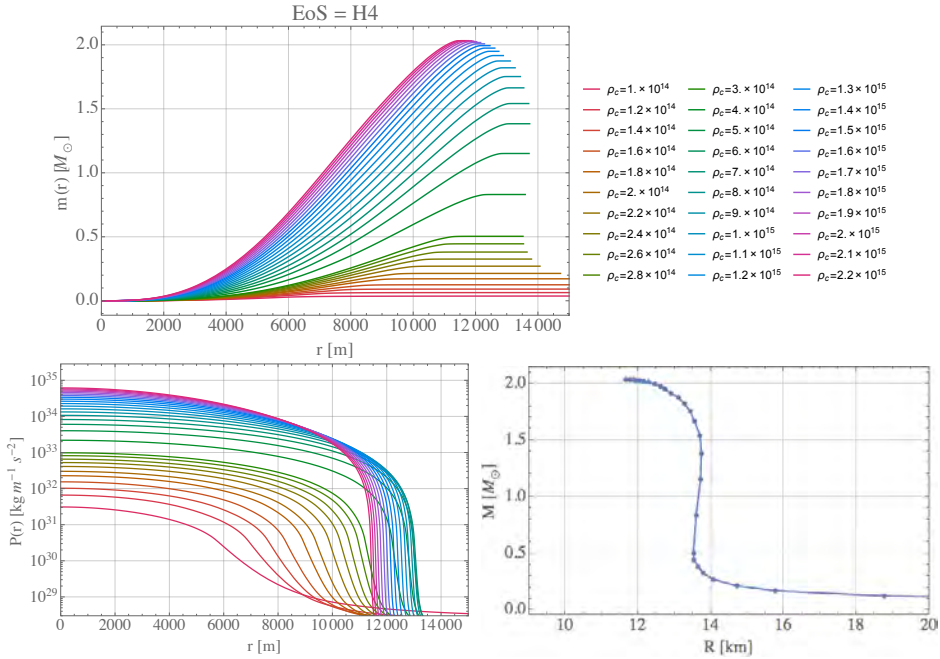
Figure 10.1: *Solutions to the TOV equations using different values for the central density ρ_c as an initial condition, with a particular EoS model. Top: mass enclosed within radius r; the list of central densities used is given on the right, in $\mathrm{g\,cm^{-3}}$. Bottom: pressure as a function of radius (left); total mass M_* of the star plotted against its total radius R_* (right), each point corresponding to a choice for ρ_c. The EoS model used here is H4.*

10.2.2 Stability condition

A star that satisfies the TOV equation is in hydrostatic equilibrium, however it is not guaranteed to be stable under small density or pressure perturbations. In [351, 329] and references therein, it is shown how stability is related to the criterion that the total mass at equilibrium M_* increases with increasing central

EQUATIONS OF STATE

Symbol	Reference	Approach	Composition
FP	Friedman & Pandharipande (1981)	Variational	np
PS	Pandharipande & Smith (1975)	Potential	$n\pi^0$
WFF(1–3)	Wiringa, Fiks & Fabrocine (1988)	Variational	np
AP(1–4)	Akmal & Pandharipande (1997)	Variational	np
MS(1–3)	Müller & Serot (1996)	Field theoretical	np
MPA(1–2)......	Müther, Prakash, & Ainsworth (1987)	Dirac-Brueckner HF	np
ENG	Engvik et al. (1996)	Dirac-Brueckner HF	np
PAL(1–6)	Prakash et al. (1988)	Schematic potential	np
GM(1–3)	Glendenning & Moszkowski (1991)	Field theoretical	npH
GS(1–2)	Glendenning & Schaffner-Bielich (1999)	Field theoretical	npK
PCL(1–2)	Prakash, Cooke, & Lattimer (1995)	Field theoretical	$npHQ$
SQM(1–3)......	Prakash et al. (1995)	Quark matter	$Q\,(u, d, s)$

NOTE.—"Approach" refers to the underlying theoretical technique. "Composition" refers to strongly interacting components (n = neutron, p = proton, H = hyperon, K = kaon, Q = quark); all models include leptonic contributions.

Figure 10.2: *Table with a few representative EoS models, based on different approaches and matter compositions; taken from [237].*

density ρ_c (or pressure P_c) as

$$\text{stable: } \frac{\mathrm{d}M_*}{\mathrm{d}\rho_c} > 0\,, \quad \text{unstable: } \frac{\mathrm{d}M_*}{\mathrm{d}\rho_c} \leq 0\,. \qquad (10.10)$$

The main idea behind the stability criterion (10.10) is that the occurrence of a small density perturbation that compresses the star should induce an increase in the energy (mass) of the star; should the contrary be true, the star would uncontrollably roll down towards lower energy configurations, with its central density continuously increasing. One thus finds that the central density ρ_c or pressure P_c, or NS mass M_*, for which $\mathrm{d}M_*/\mathrm{d}\rho_c = 0$ (turning point), marks the onset of instability for a given equation of state. This is illustrated in the plots of Fig. 10.1, where the TOV equations are solved numerically for the EoS model known as H4 [234]. There is of course the possibility that the turning point is only one of the local maxima, and that the instability criterion is only satisfied locally; at even higher densities stability may be re-established. This implies that the population of stars that reaches the region of instability will immediately migrate to the next stable region of its EoS. For instance, this is what happens past the stability region of white dwarfs: once a WD becomes unstable, the configuration makes a violent transition (collapse) into the next stable region of the EoS at much higher central densities, which corresponds to a NS.

10

10.3   Constraints from theory and observation

The main constraints on the NS EoS are given by the following theoretical bounds:

- maximal compactness in GR
- causality and the speed of sound

and the following observational bounds:

- largest measured NS mass
- largest measured spin
- largest measured redshift.

10.3.1   Maximally compact star

According to the TOV equation, a matter configuration can achieve hydrostatic equilibrium in GR only if it can be supported by the pressure predicted by its EoS. In GR however, the EoS itself cannot be arbitrarily stiff: any block of matter that becomes as compact as a sphere of its Schwarzschild radius (or inner Kerr horizon if it is rotating) immediately collapses into a black hole. The outer less dense shells will inevitably follow, since there is no more pressure to support them. Thus, a maximum compactness condition $m(r)/r < 1/2$ is imposed throughout the star's interior, up to its surface ($M/R < 1/2$); this is shown as the excluded region in the upper left corner of Fig. 10.3.

10.3.2   Causality

An EoS that respects causality cannot predict a supra-luminal speed of sound anywhere in the NS interior, at least for the mass range for which the NS is stable. This imposes a physical constraint on the isentropic EoS function $P(\rho)$, which has to satisfy (in geometric units)

$$c_s = \sqrt{\frac{\mathrm{d}P}{\mathrm{d}\rho}} \leq 1 \,. \tag{10.11}$$

An additional assumption is that, by *Le Chatelier's principle*, the pressure is a monotonically non-decreasing function of density, *i.e.*

$$\frac{\mathrm{d}P}{\mathrm{d}\rho} \geq 0 \tag{10.12}$$

The combination of Eq. (10.11) and (10.12) allowed Rhoades and Ruffini [314] to develop a formalism that predicts an overall maximum allowed NS mass, within

the uncertainty on the EoS. Given a density range $\rho_1 \leq \rho \leq \rho_2$ for which the EoS is unknown but still respects causality, and assuming that the EoS is known outside this range, the EoS that maximizes the NS mass is the one that is marginally causal in the low-end, until it reaches $P(\rho) = P(\rho_2)$ and remains constant at this value, up to $\rho = \rho_2$.

10.3.3 Measuring masses

Accurate measurements of large NS masses alone can in fact exclude EoS models that predict maximum NS masses that are smaller than the largest measured mass. In 2013 Antoniadis et al. [44] reported the measurement of a neutron star mass $2.01 \pm 0.04 M_\odot$ for a pulsar in a NS-WD binary PSR J0348+0432 [4]. This observation already excludes many of the softest EoS models, among which most of the SQM models. In the MIT bag model described in Sec. 10.1.5 a choice of $B = 57.39\,\mathrm{MeV\,fm^{-3}}$, $m_s = 50\,\mathrm{MeV}$ and $\alpha_c = 0.6$ gives one of the stiffest SQM models often referred to as *SQM3*, whose maximum mass falls just within the errors of the measurement.
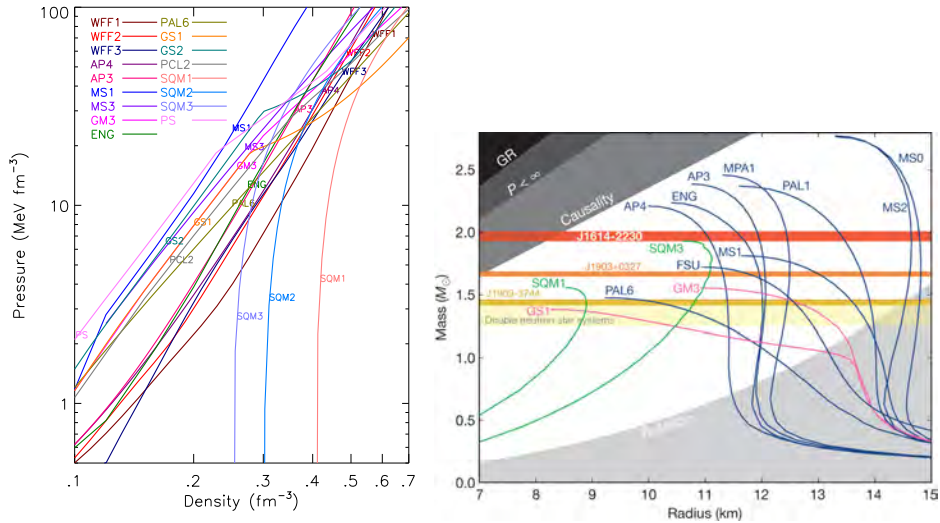
Figure 10.3: *Left: the defining $P(\rho)$ function for a list of EoS models, from Lattimer (2012) [238]. Notice how the SQM models are self-bound, giving vanishing pressure at finite non-zero density values. Right: $M(R)$ curves for several different NS EoS, from Demorest et al. (2010) [155]. Different bounds are shown in the labelled shaded regions. The horizontal bands represent the mass measurements for the three most massive NS observed. An EoS whose maximum mass lies below the measured value is ruled out.*

---

[4]ra: $03^h 48^m 43^s.639000(4)$, dec: $+04^o 32' 11''.4580(2)$

10.3.4   Rotation

Neutron stars are well known for both their compactness and their rapid rotation. Due to conservation of angular momentum, during the formation of a NS that follows the collapse of a much bigger rotating star, the newly formed NS may often happen to rotate as fast as a few hundreds times per second. A large population of *millisecond pulsars* has been observed in the radio and microwave EM spectrum.

The rotational frequency for a NS of a given mass M is approximately limited by the Keplerian frequency $f_K(M; \text{EoS})$ of a test particle co-rotating on a circular orbit, along the equator of the NS surface. Depending on the details of the EoS, the maximum frequency has an explicit dependence on the mass. This relation has been approximated very accurately by an empirical formula, obtained with numerical simulations using a relativistic NS model [330, 331, 189].

$$f_K \simeq C \, \left(\frac{M}{M_\odot} \right)^{1/2} \left(\frac{R}{10 \, \text{km}} \right)^{-3/2} \,, \qquad C = 1.08 \, \text{kHz} \,. \tag{10.13}$$

This relation, that involves both the mass and the radius of the *non-rotating* configuration, is universal and does not seem to depend on the details of the EoS.

Currently, the fastest spinning NS that has been accurately measured has a rotation frequency of $\sim 716 \, \text{Hz}$. This allows us to set a constraint on the space of EoS, that excludes all models whose mass-shedding limit due to rotation is set at a frequency less than the highest observed one. The corresponding bound is illustrated as the excluded region in the lower right part of the mass-radius plot of Fig. 10.3.

For SQM models the empirical formula is also valid but for a different value of the C constant, which in this case is larger, $C_{\text{SQM}} = 1.15 \, \text{kHz}$. These are self-bound models with $R \to 0$ as $M \to 0$, as can be seen in the representative curves of the SQM family that start from the bottom left corner of the M–R plane in Fig. 10.3.

10.3.5   Direct gravitational wave detection: a new hope

The big variety of approaches and compositions in existing EoS models, and the parametric freedom that each of those may entail, yield a plethora of consistent EoS candidates that is only partly represented in the table of Fig. 10.2. Furthermore, a more intuitive picture of the variety of models is given in Fig. 10.3, where the interesting problem to be solved is clearly illustrated. In the left panel we see the defining $P(\rho)$ function of different EoS models, and in the right one we see the M–R curves that the different models predict, together with exclusion regions given by the aforementioned set of bounds.

It is evident that, due to the unknown physics above nuclear densities, there is still a large degree of uncertainty in the determination of both the microphysics

and the macrophysical properties of the EoS, even after all available theoretical and observational constraints are applied. In the next chapter, we shall see that GW detections with AdVirgo and aLIGO may contribute significantly in putting futher constraints on the space of NS EoS. This will be achieved by analysing GW signals from coalescing NS binaries and by simultaneously measuring the NS mass and at least one additional EoS-sensitive quantity, most notably the *tidal deformability parameter.* Other potential observables that will also aid in inferring the EoS are the NS radius/compactness, the moment of inertia or spin-induced quadrupolar moment, as well as features that characterize the post-merger behaviour (resonant frequencies, lifetime of hypermassive NS, etc.).

The EoS signature on GW signals is rather fine, hence the discriminatory power of individual observations of this sort crucially depends on the strength of the signal, *i.e.* on the SNR. At a first glance it seems that only with an unrealistically loud BNS event will we be able to obtain a sufficiently accurate measurement. However, we shall see how, given a solid Bayesian formulation of the problem, information from many low-SNR detections can be statistically combined into tight, significant constraints.

10

10

Chapter 11

Three roads to the neutron star EoS

"New shit has come to light!"

The Dude, The Big Lebowski

11.1 Introduction

In this chapter, we study the possibility of inferring the neutron star equation of state using detected GW signals generated during the inspiral of binary neutron star systems. To this end we shall develop Bayesian analysis methods, along the lines of Sec. 3.2, and will perform a number of numerical experiments to test their potential, in the context of second generation ground-based interferometers.

The possibility of measuring the neutron star EoS with gravitational wave observations of BNS coalescences has recently been the subject of extensive investigation. Here, the first complete, realistic data analysis effort is presented, giving a credible assessment of EoS measurability in the era of second generation GW detectors. The dominant matter effect that may contribute with a measurable signature in the GW signal is the tidal deformation effect of Sec. 2.6.1, that enters the phase $\Phi(t)$ as in Eq. (2.56). Recall that the tidal deformability is expressed by a parameter λ, which is related to the NS mass m and radius $R(m)$ through $\lambda(m) = (2/3)k_2(m)R^5(m)$, where k_2 is the second Love number. This quantity determines the magnitude of the effect in the gravitational waveform. Although the leading order tidal effects enter the phase at high apparent post-Newtonian order (first appearing alongside the 5PN phase contribution), these corrections come with a large prefactor: $\lambda(m_A)/M^5 \propto (R_A/M)^5 \sim 10^2 - 10^5$ (with M the total mass of the binary), so that they may be observable with advanced detectors.

The potential of detecting tidal effects in the early inspiral ($f_{gw} < 450$ Hz) was studied in a Fisher matrix analysis by Hinderer et al. [200], based on prior 1PN calculations performed in [170, 368]. During this stage, tidal effects can be safely treated as small perturbations on the orbital evolution of the binary (that is accurately described by post-Newtonian waveforms), and are sensitive to the details of the NS equation of state. They have shown that λ_A are only measurable for very loud BNS sources and only for the stiffest EoS in the case of second generation GW detectors. Read *et al.*, using waveforms hybridized with input from NR simulations and Fisher matrix analysis, estimated that with a single close-by source (at a distance of ~ 100 Mpc), the neutron star radius could be constrained to 10% [309]. In a similar study for multiple detected sources, Markakis *et al.* [255] concluded that a similar accuracy as in [309] could be attained with 3 sources that have low signal-to-noise ratio (SNR). Lackey *et al.* performed a similar analysis for NSBH, which also indicated encouraging prospects [233]. Damour, Nagar and Villain [147] extended the calculation of tidal effects to higher order, namely 2.5 PN beyond their Newtonian contribution in an effective one-body setting, and demonstrated a Fisher matrix calculation, in a parametrization where the tidal deformability λ is approximated as a linear function of the NS mass. By extending the EOB calculation to high order, the tidal contribution to the phase can be trusted up to the very end of the inspiral. This approximation is sufficiently good for most known EoS, within the range of mass values under consideration. We follow this approach in one of our methods and perform a full Bayesian analysis on a series of simulations using realistic sets of BNS sources.

Here, it is important to note that, even though an analytical Fisher matrix approach may be a good first estimate of what can be achieved with a given detector sensitivity, its validity restricts to the regime of high SNR [132, 358, 396]. Especially in problems with a rich parameter space, the estimates derived by a Fisher matrix analysis are by no means reliable at low SNR and are often too optimistic. In the case of second generation GW detectors however, the majority of detections are expected to lie close to the detection threshold (SNR$\simeq 8$). Thus, it is desirable to obtain results from Bayesian studies, using realistic simulated sources, and in a realistic data analysis setting, as will be demonstrated below. In what follows, we shall see how performing a full Bayesian analysis on the data from multiple GW detections from BNS inspirals can significantly enhance one's ability to measure the NS EoS. Two qualitatively different methods indicate that, given a few tens of detections, and assuming non-spinning BNS systems, one can extract significant information about the tidal deformability and discriminate between a soft, a moderate and a stiff EoS, using the Advanced LIGO-Virgo network of detectors. We will extend the investigation to systems consisting of spinning NS, and will include higher order tidal effects as calculated in [147], as well as contributions from quadrupole-monopole effects [181]. An important part of this work is summarized in [152, 35]. In a recent Bayesian study, Lackey et al. [235] showed how similar results could be obtained by performing

11

parameter estimation on $\tilde{\Lambda}$, a combination of the tidal deformability parameters and masses of the two component NS (essentially what appears as the leading order coefficient), which is claimed to be the optimal one in terms of uncertainty and correlations [200].

Sources will be distributed in an astrophysically realistic way, leading to the distribution of SNRs that we expect to see towards 2018. Two different Bayesian analysis methods will be investigated:

HR: *Hypothesis ranking* within a finite list of different theoretical EoS, and

PE: *Parameter estimation* on parameters that characterize the EoS and are common across all sources.

The first method is based on Bayesian model selection (Sec. 3.4.1), that trivially allows one to combine information from multiple sources so as to arrive at a stronger result. To do the same with PE, *global parameters* need to be identified that do not vary from source to source; these will be simply taken to be coefficients in a polynomial expansion of $\lambda(m)$ in powers of $(m - m_0)/M_\odot$, where m_0 is some reference mass. A similar analysis in terms of parameter estimation was recently performed by Lackey and Wade [235]. The latter authors modeled the EoS as piecewise polytropes, allowing them to arrive at statements on the measurability of pressure as a function of density and neutron star radius as a function of mass. The PE method also has the advantage that physical priors such as causality can more easily be folded in.

Of necessity, we will use relatively simple waveform approximants, as otherwise the simulated data analysis problem would have been intractable with existing methods and computational infrastructure. Much effort is being put into large-scale numerical simulations of the spacetimes of coalescing BNS, especially of the late inspiral [56, 57, 73, 203, 307, 305]. The resulting waveforms are "hybridized" by matching them onto post-Newtonian or effective one-body waveforms, so that the earlier inspiral is also represented. While such waveforms represent the state of the art in our understanding of BNS coalescence, producing a single one of them can take weeks. By contrast, high quality parameter estimation requires millions of waveforms to be compared with the data (see [364] and references therein). A full solution of the problem of inferring the EoS from BNS detections will likely involve a combination of constructing phenomenological or "tuned" waveform models with input from numerical relativity [341, 342, 285, 349, 324, 191, 325], and significantly speeding up the analysis of the data, *e.g.* through the use of Reduced Order Modeling; see [303, 119] and references therein. In that regard we note the recent work by Bernuzzi *et al.* [72], who derived an effective one-body model that accurately describes tidal effects close to merger for a number of different EoS, matching results from numerical simulations essentially to within the numerical uncertainties.

The main concern regarding the reliability of methods that rely on effects taking place during the inspiral, is that of the validity of the existing point-particle

11

(PP) inspiral waveform models close to merger. This was already pointed out in [200] (together with some less important sources of errors) and studied in detail in [372], where the authors demonstrate that significant biases arise due to the discrepancies between the different (PN) waveform approximants at high frequencies. Indeed the true PP waveform may not agree with any of the existing models to sufficient accuracy. Furthermore, the possibility of obtaining significant input from numerical relativity (NR) would require a large set of lengthy simulations that go hundreds of cycles deep into the inspiral; such an effort is currently unfeasible. The author is very much aware of this issue and does not claim the current analysis to correspond to an ideal scenario to its last detail[1]. However, based on results of [307, 203], we do expect that the predicted contribution of the matter effects to the waveform is close to reality and that the main part of the systematics originates from the point-particle sector. In particular, an important observation made by Read *et al.* [307], had to do with the "distinguishability" $||\delta h|| \equiv \sqrt{\langle h_2 - h_1 | h_2 - h_1 \rangle}$ in terms of the usual PSD-weighted inner product $\langle \cdot | \cdot \rangle$ for waveforms h_1, h_2 of the same family but differing in their parameter values, in this case λ. As can be seen in their Fig. 12, the dependence of $||\delta h||$ on changes in λ is very similar for PN approximants and for hybridized numerical relativity (NR) waveforms. Thus we are confident that already by using PN approximants we can *accurately predict* how well we will be able to infer the EoS, once the accurate PP waveforms become available for use in data analysis algorithms. The current analysis will also inform the waveform modeling, NR and data analysis communities as to what can reasonably be expected in terms of scientific output, once their considerable efforts come to fruition.

We will consider three different effects that take place during a BNS inspiral and affect the orbital evolution of the binary and thus the GW waveform emitted by the system, namely (i) tidal deformations induced by the companion's gravitational field, (ii) the coupling of spin induced quadrupole moment and (iii) the physical contact between the two finite-sized stars, which we consider to signify the end of the coherent GW emission of the inspiral.

The remainder of this chapter is structured as follows. In 11.2 we introduce the waveform model and the EoS-related contributions from the two effects mentioned above. Before diving into the methods, a general set-up for the simulations is given in Sec. 11.3. The main body of this work lies in Sec. 11.4.1 and 11.5.1, where two different Bayesian methods are studied, for inferring the NS EoS using realistic sets of GW detections. There, details of the methodologies are discussed and results from a series of simulations for each of the three approaches are demonstrated. A brief note on the EoS information content of BNS signals is given in Sec. 11.6, and possible sources of inference bias are explored in Sec. 11.7, before reaching a discussion on current and future developments in Chapter 12.

---

[1]In this study, we will consistently use a single waveform approximant (TaylorF2), both for simulating the signals and as templates for the analysis, in order to avoid such biases.

11.2 Waveform modelling

11.2.1 Post-Newtonian waveform for point particle

For the modelling of our BNS inspiral waveforms, we will be using a post-Newtonian approximation, where the evolution of the orbit is expressed in terms of an expansion in powers of v/c, v being the instantaneous characteristic orbital velocity of the binary, $v = (\pi M f_{gw})^{1/3}$, f_{gw} being twice the orbital frequency and $M = m_1 + m_2$ being the total mass.

More specifically, we employ the *stationary phase approximation* (SPA) to obtain an analytical expression for the waveform directly in the frequency domain (FD), the TaylorF2 waveform defined in Sec. 2.4. The GW polarizations are then expressed as

$$\tilde{h}(f) = A(f)e^{i\Psi_{PP}(f)} \tag{11.1}$$

where the *amplitude* $A(f)$ and *phase* $\Psi_{PP}(f)$ in the "point-particle case" take the form of Eq. (2.27), (2.28) and (2.29).

Throughout the whole study, we will again only assume quasi-circular orbits. We will not take into account post-Newtonian corrections in the waveform amplitude. On the other hand, we make use of the expansion coefficients in the phase that are calculated up to 3.5 post-Newtonian order [50], including spin-orbit, spin-spin and self-spin-spin interactions which enter at 1.5 PN, 2PN and 2PN order in the phase $\Psi_{PP}(f)$ respectively [114, 295, 262] as given explicitly in Sec. 2.4. When moving away from the simple "point-particle" scenario, to a finite-sized matter distribution, as in the case of a BNS system, the expression for the phase evolution in Eq. (2.28) will be enriched with additional terms, whose magnitudes depend on each component's internal structure.

11.2.2 Matter effects and equations of state

Based on the discussion of Sec. 2.6, we will enrich the waveform phase structure with two additional matter effects that will be present and potentially measurable in coalescing BNS systems. These will be (i) the effects of tidal-induced deformation on each NS by the gravitational field of its companion, and (ii) the contribution of the additional spin-induced quadrupole moment of each (spinning) NS. Furthermore, a more realistic termination condition than f_{LSO} will be chosen below.

In the series of numerical simulation experiments that will be presented, three different EoS models are considered, namely MS1 [267], H4 [234] and SQM3 [299]. These can be seen as representatives of stiff (MS1), moderate (H4) and soft (SQM3) equations of state, the distinguishability among which we are aiming to investigate. The defining $P(\rho)$ functions and the derived mass-radius graphs of the three EoS considered here, can be seen in Fig. 10.1 and Fig. 10.3.

11

Tidal deformations   In order to incorporate the effects of tidal deformability in the GW phasing, we will be using the tidal terms calculated up to 2.5PN beyond leading order, as shown in Eq. (2.56). Since three individual EoS will be considered for our numerical experiments, we will need to known how to calculate the tidal deformability parameter λ as a function of the NS mass m. Instead of solving the differential equations "on the fly", it will be enough to interpolate the different $\lambda(m; \text{EoS})$ curves with a quartic polynomial fit

$$\lambda(m; \text{EoS}) = \sum_{i=0}^{4} a_i^{\text{EoS}} m^i \tag{11.2}$$

using a set of points that lie within the mass region of interest. The fitting is done once and for all and the calculation of λ using the fitted polynomial will speed up the analysis of the HR method. The values of the fitted polynomial coefficients are given in Table 11.1 and the corresponding curves and residuals are shown in Fig. 11.1. We see that the uncertainties introduced by the fitting, (in the order of $0.01 \times 10^{-23} \text{s}^{-5}$) are quite small in comparison with the differences between the three EoS, as well as with the statistical errors that we expect to see in the analysis.

EoS	$a_0 \, [10^{-24}\text{s}^5]$	$a_1 \, [10^{-17}\text{s}^4]$	$a_2 \, [10^{-12}\text{s}^3]$	$a_3 \, [10^{-7}\text{s}^2]$	$a_4 \, [10^{-3}\text{s}]$
MS1	6.0437	1.1206	-2.0384	1.3264	-3.2735
H4	2.0486	0.88919	-1.6739	1.2290	-4.4138
SQM3	-15.319	1.1693	-2.3354	2.2036	-8.6594

Table 11.1: *Quartic polynomial fitted coefficients for the three representative EoS.*

11.2.3   Universal relations between NS matter properties

Much attention has recently been drawn to a set of phenomenological relations that have been established between different physical mass-dependent parameters of neutron stars, namely the moment of inertia I, the second Love number k_2, the quadrupole moment q [390, 391], and the compactness $\mathcal{C}$ [258]. The claim is that these relations hold irrespectively of the EoS at hand.

We shall make use of these relations to reduce the problem of inferring the EoS to a single parameter problem, that is, knowledge of one of the above parameters implies knowledge of any other EoS-related parameter that may enter our model. In particular, we make use of the *Love–Q* relation (Eq. (54) and Table I of [391] to obtain an expression of the form $a(\lambda, m)$, as well as a *Love–$\mathcal{C}$* relation, to obtain the NS compactness and radius $R(\lambda, m) = m/\mathcal{C}(\lambda, m)$. Both these relations will help adding realistic effects, without increasing the dimensionality of our parameter space by unifying the parameters of the tidal effects, Q-M effects and radii for each component NS.
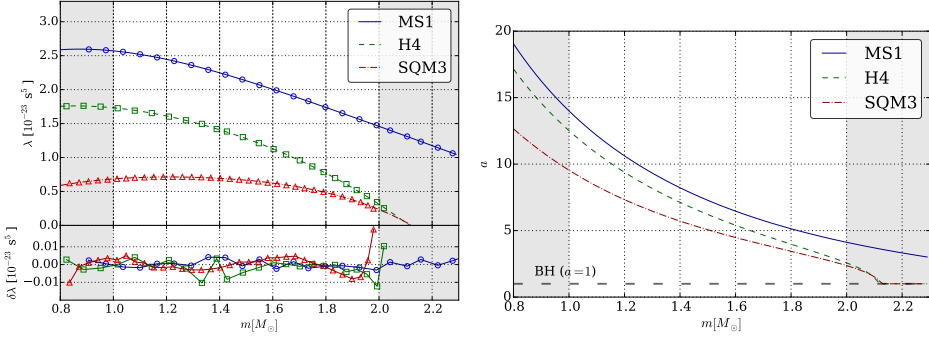
Figure 11.1: *Left: The tidal deformability parameter $\lambda(m)$ as a function of neutron star mass for three different EoS: a soft one (SQM3), a moderate one (H4), and a stiff one (MS1). Curves are fitted quartic polynomials, whose residuals are shown in the lower subplot. Only masses within the unshaded region $[1, 2]M_\odot$ will be considered. Right: The quadrupole parameter $a(m)$ as a function of neutron star mass for the three different EoS. The horizontal dashed line indicates the value for black holes, which is $a = 1$.*

Quadrupole-monopole effects   The second matter effect that we will incorporate in the waveform is that of the spin-induced quadrupole moment, that enters the waveform phase as in Eq. (2.64). The magnitude of this effect is determined by the NS spin χ and the QM parameter a, which depends on the NS mass in a way that is dictated by the EoS. For computing $a(m)$, we make use of the recently discovered phenomenological *Love-Q* relation [390, 391], which is believed to hold irrespective of the EoS and allows us to calculate a directly, given a value for λ,

$$
\begin{aligned}
\ln a(m) = \; & 0.194 + 0.0936 \ln \frac{\lambda}{m^5} + 0.0474 \left(\ln \frac{\lambda}{m^5} \right)^2 \\
& -4.21 \times 10^{-3} \left(\ln \frac{\lambda}{m^5} \right)^3 + 1.23 \times 10^{-4} \left(\ln \frac{\lambda}{m^5} \right)^4 .
\end{aligned}
$$

The systematic errors that may rise due to this assumption are expected to be much smaller than the statistical uncertainties met in this study. The relative fractional errors due to the universal fit were estimated in [391] for several EoS to be at the 1% level. Together with Eqs. (2.63) and (2.64), this then allows us to compute the QM contribution to the phase. The resulting $a(m)$ curves for the three EoS models of interest are illustrated in the right panel of Fig. 11.1. QM contributions to the phase are expected to be sub-dominant compared to the tidal effects of Sec. 2.6.1, even for relatively fast spinning NS, as shown in Fig. 11.3.

11

Termination of the waveform at contact   In the recent simulations [152, 235], the waveform was cut off at a frequency corresponding to the last stable circular orbit (LSO) in the point particle limit, given by

$$f_{\text{LSO}} = \frac{1}{6^{3/2}\pi M}. \tag{11.3}$$

However, as we shall see below, it will often happen that the two neutron stars attain physical contact before the corresponding distance between the components is reached. We will instead impose the cut-off

$$f_{\text{cut}} = \min\{f_{\text{LSO}}, f_{\text{contact}}\}, \tag{11.4}$$

where, using Kepler's third law, the "contact frequency" is given by

$$f_{\text{contact}} = \frac{1}{\pi}\left(\frac{M}{R(m_1) + R(m_2)}\right)^{1/2}. \tag{11.5}$$

We stress that the termination condition (11.4) is still a relatively heuristic one (not taking into consideration effects of tidal deformation, tidal disruption, Roche lobes, spins, etc.), but is crucially more realistic than termination at f_{LSO}. Moreover, the length of the waveform itself carries physical information [254], in this case on the EoS, which we wish to incorporate [2]. On the other hand, shorter waveforms have a smaller number of cycles from which information can be extracted; when we come to the results of our simulations we will see which effect wins out.

In order to compute the radii $R(m_1)$, $R(m_2)$, we again make use of a recently discovered phenomenological relation, this time between the compactness $\mathcal{C} = m/R$ and λ; this is the *Love-$\mathcal{C}$* relation, Eqn. (4) of Maselli *et. al* [258]

$$\mathcal{C} = 0.371 - 3.91 \times 10^{-2}\ln\frac{\lambda}{m^5} + 1.056 \times 10^{-3}\left(\ln\frac{\lambda}{m^5}\right)^2. \tag{11.6}$$

For a given EoS (*i.e* a given relationship $\lambda(m)$), the above expression gives us $R(m)$, from which the contact frequency (11.5) is obtained. The relative error in the compactness (and hence in the radius) due to the fit of Eq. (11.6) was found to be at the 2% level, implying a relative error of 1% in the contact frequency.

Fig. 11.2 shows the dependence of f_{LSO} and f_{contact} on component masses m_1, m_2 for the EoS considered above. Note how in the astrophysically relevant range $m_A \in [1, 2]\, M_\odot$, $A = 1, 2$, it often happens that $f_{\text{contact}} < f_{\text{LSO}}$, especially for low masses and for the stiffer EoS (MS1) which can support larger neutron star radii. In order to get an impression of the magnitude of the matter effects, we show

---

[2]It seems reasonable to expect that termination at our f_{cut} will be sufficiently indicative of the in reality more complicated but nevertheless dramatic changes in the waveform evolution that will occur around that frequency, and which should indeed carry information about the EoS [56, 57, 73, 203, 307, 305].
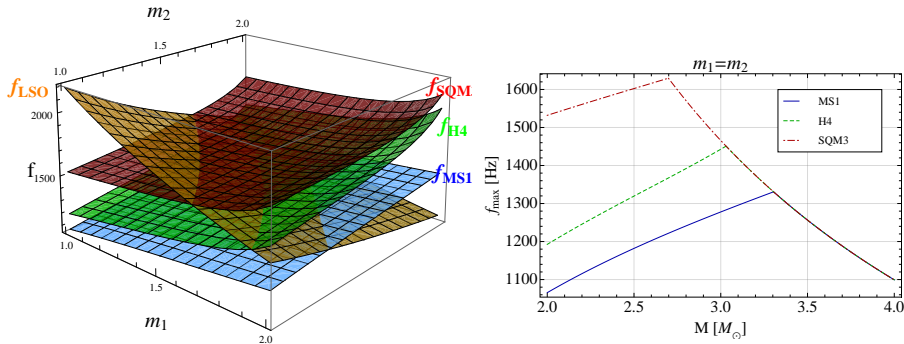
Figure 11.2: *Left: The frequencies f_{LSO} and $f_{contact}$ as functions of m_1, m_2 for the EoS shown in Fig. 11.1. Right: Maximum frequency cut-off as a function of total mass for equal-mass binaries, for the same three EoS. Observe how the stiffer EoS signals will be cut short earlier in the inspiral than the softer ones, for low-mass systems.*

in Fig. 11.3 the evolution of the different matter terms introduced in the phase, as the inspiral frequency increases. The system is a typical $(1.35, 1.35)$ $M_{\odot}$ BNS system following a stiff EoS (MS1), with relatively high NS spins ($\chi_1 = \chi_2 = 0.1$). The effect scales linearly with λ and quadratically with the spin amplitudes; the high spin values are chosen in order to show a visible effect in the phase, which is still rather small, compared to the tidal effects.

11.3 Simulations set-up

In the sections that follow, we investigate two qualitatively different Bayesian methods that can be used to acquire information on the NS EoS, given a set of GW detections from BNS coalescence. These are potential post-detection methods that should be applied on events that are verified BNS detections. The BNS nature of the detected source may be established by a mass-related criterion, such as the $\mathcal{M}_c < 1.3$ $M_{\odot}$ criterion proposed in [32]. However it is possible that imposing such a high-mass restriction on the detections to be processed, could potentially exclude sources holding decisive information related to the NS EoS (e.g. a high-mass NS that would provide strong evidence against a set of soft EoS). Therefore, one would definitely benefit from using a combination of criteria of different nature; one that may incorporate evidence of a post-merger meta-stable object, or an electromagnetic (EM) signature matching one of a BNS coalescence [348, 204]. Here however, we will not be concerned with selection criteria and will assume that all our sources are guaranteed to be BNS coalescences.

The computational methods used for the analysis of the simulated data are based on the *nested sampling* algorithm of Sec. 3.3.2, which can produce both the *evidence* for a waveform model and a set of *posterior samples* of its parameter
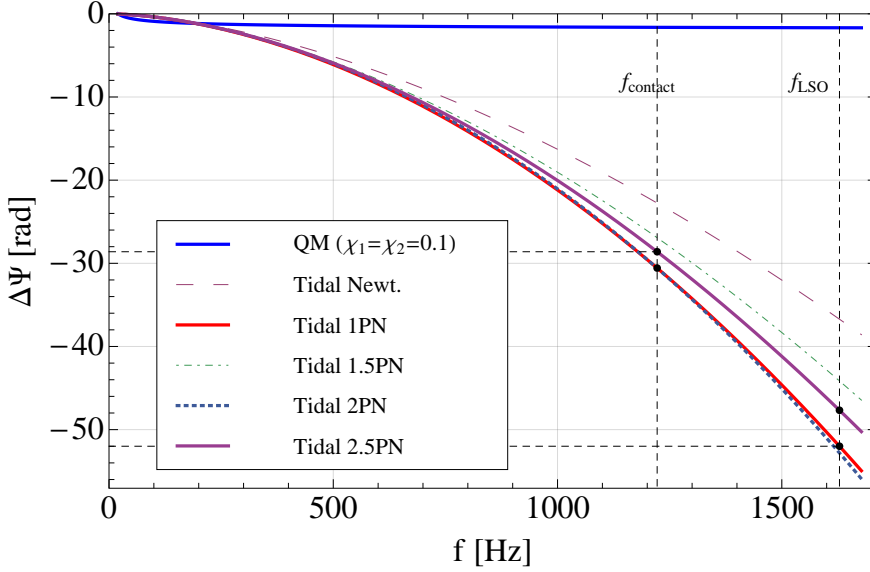
Figure 11.3: *Phase contributions of the QM effect and tidal effects up to different PN orders as functions of GW frequency for a* $(1.35, 1.35)M_\odot$ *binary with a stiff EoS (MS1). The QM contribution from each NS scales quadratically with its spin and is shown here for* $\chi_1 = \chi_2 = 0.1$. *The dashed vertical lines indicate the contact and LSO frequencies.*

space. These two kinds of output will play a central role in the inference methods that will be studied.

To give a figurative description, the *HR method* comprises a set of Bayesian Model Selection tests, while the *PE method* performs Bayesian Parameter Estimation on a set of EoS-related parameters; a third *functional inference method* (FI) outlined in Appendix C, is currently under development as an attempt to formulate Bayesian non-parametric inference on the global functional dependence of one source parameter (λ) on another (m). All methods have the feature of seamlessly combining information from multiple detections into a unique result, therefore effectively improving the discriminatory power of the network of GW interferometers on the EoS, as more and more sources are detected.

A common set-up will be used in the simulations that will be performed for all methods, so that their behaviour can be judged on common grounds. This entails choices for both the parameters of the simulated and noise and signals (injection), as well as the ones for the templates used in the analysis algorithm (recovery). Different scenarios for underlying NS mass and spin distributions will be investigated; the choices for these and all other parameters of the set-up are described below.

11.3.1 Injections set-up

Mass distribution   For the injected mass parameters we consider two different scenarios for the distributions of m_A:

MU : a uniform mass distribution in the range $[1, 2]\,M_\odot$

MG : a Gaussian distribution centred at $\mu_m = 1.35 M_\odot$ with a standard deviation of $\sigma_m = 0.05 M_\odot$, restricted within $[1, 2] M_\odot$

The latter scenario is motivated by currently available mass measurements on NS binaries, see e.g. Kiziltan et al. [227].

Spin distribution   For the injected spin parameters we consider three different scenarios for the distributions of the dimensionless (anti-)aligned spin magnitudes χ_1, χ_2:

S0 : zero spins,

S02 : a Gaussian distribution centred at $\mu_\chi = 0$, with a standard deviation of $\sigma_\chi = 0.02$,

S05 : a Gaussian distribution centred at $\mu_\chi = 0$, with a standard deviation of $\sigma_\chi = 0.05$.

Positive (negative) spin values will correspond to spins $\vec{S_A}$ that are aligned (anti-aligned) with the orbital angular momentum $\vec{L}$. Note that in the case of zero spins, the quadrupole-monopole effect is not present.

The choice for small spin values is motivated by the observed population of spins in NS binaries [248] and is a rather conservative one, since by the time of coalescence NS will have spun down further. However, it would be precarious to assume that the properties of the observed population of NS will be identical to those of the coalescing BNS populations that will be detected with GW interferometers, since different sets of selection effects may be in play for EM and GW observations. This cautionary note refers to both the underlying NS spin and mass distributions.

Other injection parameters   The simulated signals will be added coherently into simulated Gaussian and stationary noise, for the network of an AdVirgo detector at Cascina, Italy and two aLIGO detectors at Hanford, WA, and Livingston, LA, based on the design sensitivity noise PSDs shown in Fig. 1.4 (SR and ZDHP respectively). As for the remaining CBC parameters, the orientation ι, polarization ψ and sky-location (θ, ϕ) angles will be distributed uniformly in the sphere, the phase at coalescence ϕ will be uniform in $[0, \pi)$ and the distance r will be sampled uniformly in volume (*i.e.* $\propto r^2 \mathrm{d}r$) and, unless stated otherwise will range in $[100, 250]$ Mpc.

11

11.3.2 Recovery set-up

For analysing the data, again a Gaussian, stationary noise model will be used, based on the design aLIGO and AdVirgo noise PSDs for calculating likelihoods. Analysis will initiate at a lower frequency of 40 Hz and will terminate at f_{cut}, with a sampling rate of 4096 Hz.

Unless stated otherwise, the mass prior will be uniform in $[1, 2] M_\odot$ and, whenever applicable, the prior for the (anti-)aligned spin amplitude will be uniform in $[-0.1, 0.1]$. Here too, the angular parameters (ι, ψ) and (θ, ϕ) are assigned priors uniform in the sphere and the distance prior will range in $[100, 250]$ Mpc, using a logarithmic prior. The time of coalescence parameter t_c will range within 10 ms before and after the injected time of coalescence. The priors used for additional EoS-related parameters will be described separately below.

As we shall see, the prior density distribution for the component masses will play an important role. In principle we could take this to be always the same as the mass distribution for the injections. However, we would then implicitly be assuming that the astrophysical mass distribution of neutron stars in binaries will be reliably known in the advanced detector era. At the time of writing only 9 double neutron star systems have been observed, sometimes with large error bars on the measured masses; it seems unlikely that this situation will improve dramatically in the next few years. We also note the differing results for observationally based estimates of the mass distribution in BNS systems; for example, $(\mu_m, \sigma_m) = (1.37 \, M_\odot, 0.042 \, M_\odot)$ in Valentim *et al.* [356] and $(\mu_m, \sigma_m) = (1.33 \, M_\odot, 0.13 \, M_\odot)$ in Kiziltan *et al.* [227], the difference partially being due to the use of different subsets of the known systems based on the reliability of individual mass measurements. Finally, it is possible that due to selection biases, the distribution of masses in electromagnetically observed neutron star binaries will not be identical to the mass distribution in BNS coalescences detected by Advanced LIGO and Virgo. For these reasons, we will mostly assume a flat component mass prior with $m \in [1, 2] \, M_\odot$. However, in Sec. 11.7 we will also briefly investigate what happens if the astrophysical distribution of masses of neutron stars in binaries can be assumed known after all.

As for the nested sampling algorithm itself, 1024 live points and 200 MCMC points will be used for sampling the parameter space. The termination condition is the same as in Sec. 6.3, namely $dZ < 0.1$.

11.4 Hypothesis Ranking

11.4.1 Method

Given a discrete set of (finitely many) EoS models $\{M_1, \cdots, M_K\}$, we will be interested in ranking them, in the light of data $d_1, \cdots, d_N$ coming from a set of N BNS GW detections. The ranking process will be one on the set of hypotheses

$\{H_i\}_{i=1,\cdots,K}$, where the hypothesis H_i states that model M_i is the true model for the NS EoS and defines a family of waveforms $\tilde{h}^{(i)}(f;\vec{\theta})$.

Each model predicts a unique way in which the tidal deformability parameter λ, the quadrupole parameter a and the NS radius R depend on the mass m of the neutron star. This was illustrated e.g. in Figs. 11.1 and 11.2 for a representative set of candidate equations of state. Therefore the set of parameters $\vec{\theta}$ is the standard set of CBC parameters (5.2) and is the same across all waveform families, however the calculated values for $\lambda_A = \lambda(m_A; M_i)$, $a_A = a(m_A; M_i)$ and $R_A = R(m_A; M_i)$ differ. The general form of the waveform given by Eq. (11.1), (2.27) and (2.29), together with the spin, tidal and QM contributions Eq. (2.45), (2.56), (2.64) and the waveform termination condition (11.4), yield a waveform model $\tilde{h}^{(i)}(f;\vec{\theta})$ associated with the hypothesis H_i.

Now, once we have data from a verified BNS detection we can compute the evidence $P(d|H_i,\mathcal{I})$ for each model hypothesis H_i, using the corresponding waveform family $\tilde{h}^{(i)}(f;\vec{\theta})$ as templates for analysing the data. The *likelihood* of a (Fourier transformed) data set $\tilde{d}(f)$ on a given point $\vec{\theta}$ of the parameter space, for the model hypothesis H_i, is given by the integral of Eq. (3.12)

$$p(d|\vec{\theta},H_i,\mathcal{I}) = \mathcal{N} \exp\left[-2\int_{f_{\text{low}}}^{f_{\text{high}}} df \frac{|\tilde{d}(f)-\tilde{h}^{(i)}(f;\vec{\theta})|^2}{S_n(f)}\right], \qquad (11.7)$$

where $\mathcal{N}$ is a normalization factor, and $S_n(f)$ is the detector's one-sided noise power spectral density. [3] We set the low frequency cut-off at $f_{\text{low}} = 40$ Hz, and the high-frequency cut-off at $f_{\text{high}} = f_{\text{cut}}$ given in Eq. (11.4). The *evidence* of the data for each individual model is given by the prior-weighted integral of the likelihood over the parameter space

$$P(d|H_i,\mathcal{I}) = \int d\vec{\theta}\, p(\vec{\theta}|\mathcal{I})\, p(d|H_i,\vec{\theta},\mathcal{I})\,. \qquad (11.8)$$

We will numerically compute $P(d|H_i,\mathcal{I})$ by using the nested sampling algorithm. Then the odds ratio O_j^i for any pair of models H_i, H_j is directly computed as the ratio of the models' posteriors

$$O_j^i = \frac{P(H_i|d,\mathcal{I})}{P(H_j|d,\mathcal{I})} = \frac{P(H_i|\mathcal{I})}{P(H_j|\mathcal{I})}\frac{P(d|H_i,\mathcal{I})}{P(d|H_j,\mathcal{I})} \qquad (11.9)$$

Assuming a set of N independent detections $d = d_1,\ldots,d_N$ one can rewrite the odds ratio as in Eq. (3.33), using Bayes' theorem and the multiplication rule for independent random variables as

$$^{(N)}O_j^i = \frac{P(H_i|\mathcal{I})}{P(H_j|\mathcal{I})} \prod_{n=1}^{N} \frac{P(d_n|H_i,\mathcal{I})}{P(d_n|H_j,\mathcal{I})}, \qquad (11.10)$$

---

[3]For a network of multiple detectors with uncorrelated noise, the multiplication rule Eq. (3.30) may be used to express the overall likelihood as a product of likelihoods for individual detectors.

where $P(H|\mathcal{I})$ is the probability that quantifies our prior belief in the hypothesis H, in the absence of any GW data. Note that it is often convenient to work with the *logarithms* of the odds ratios, as we will also do here. For the purpose of this study, we show no prior preference for any model over the rest, and will thus set the priors for all hypotheses to be equal to each other (*i.e.* the prior ratio in Eq. (11.10) for any pair of hypotheses equals 1)

$$P(H_i|\mathcal{I}) = P(H_j|\mathcal{I}) \quad \forall i, j \in 1, \ldots, K \, . \tag{11.11}$$

We will refer to $^{(N)}O_j^i$ as the *combined odds ratio for N sources* between hypotheses H_i and H_j. According to Eq. (11.10), if $^{(N)}O_j^i > 1$ (equivalently $\ln {}^{(N)}O_j^i > 0$), then the data favors the hypothesis H_i over the hypothesis H_j. By comparing the evidences of all hypotheses considered, we arrive at an overall ranking for the set of hypotheses $\{H_i\}_{i=1,\ldots,K}$, where the highest ranked model is the one assigned with the largest posterior probability, given the observed data.

It is important to note that

1. Even if the true equation of state were in the set H_i, $i = 1, \ldots, K$, one should not necessarily expect it to end up at the top of the ranking; this is due to the effects of noise and the fact that the majority of detected sources will have low signal-to-noise ratios (SNRs). The evidences for the different hypotheses, and thus the odds ratios should be treated as statistics over the random variable d. Thus one should not expect to obtain a definite result when calculating the odds ratios for a given set of detections; the purpose of the simulations described in the following section is to explore the behaviour of the combined odds ratio statistic.

2. In practice, the correct equation of state will probably not be in the finite set H_i, $i = 1, \ldots, K$. Nevertheless, one may expect the highest-ranked hypothesis to be close to the true one.

Here a notion of *closeness* or distance in a space of functions is implied; this can be defined by *e.g.* employing the L^2 norm $||f|| = (\int |f|^2 d\mu)^{1/2}$. The integration measure μ need not be uniform in mass (*i.e.* in principle $d\mu \neq dm$), but should rather reflect the amount of information that is collected from each infinitesimal mass interval. That is, if two functions differ significantly at a mass interval where no sources are found, but are almost equal elsewhere, then the "distance" between them should be small. In this sense, an appropriate notion of distance between EoS would depend on the NS mass-distribution. Here however, the set of functions $\lambda_{(i)}(m)$ that we consider are clearly distinguishable across the mass interval of interest $[1, 2]M_\odot$ and admit a strict ordering in terms of stiffness.

11.4.2   Simulations and results

We wish to demonstrate the ability to distinguish at least between a stiff, a moderate and a soft EoS, which will be represented by the models MS1, H4 and

11

SQM3 respectively. Our simulated signals will be generated according to these three models. For the analysis of the data we will use the same three models, as well as the point particle (PP) model, in which no tidal effects are present ($\lambda = 0$). In this way we will arrive to results for hypothesis ranking on the set of hypotheses $\{H_{PP}, H_{SQM3}, H_{H4}, H_{MS1}\}$, for 3 realistic sets of BNS sources.

Since this is meant to be a post-detection analysis, two additional conditions are imposed on the simulated signals, in order to ensure that the sources that participate in the analysis would have been detected in real science run conditions:

1. An optimal signal-to-noise-ratio cutoff of $8 \leq \rho_{opt} \leq 30$. The lower cutoff is chosen as the nominal threshold for detection, whereas the high cutoff excludes unlikely loud events that may yield overly optimistic results; and

2. A post-analysis signal-to-noise Bayes factor cutoff of $\ln B^{\mathrm{signal}}_{\mathrm{noise}} \geq 32$ on the point particle template [4] (roughly corresponding to a detected SNR of 8).

The latter implies that any signal that is distant enough from the manifold of point particle signals $\tilde{h}^{PP}(f; \vec{\theta})$ so as not to be confidently detected by the PP template, is discarded. This may inevitably introduce a small bias disfavoring hard EoS models, as the waveforms generated by those models will deviate the most from their PP counterparts.

We populate a set of simulated sources by choosing astrophysically motivated scenarios, based on combinations of the mass [MG, MU] and spin [S0, S02, S05] distribution scenarios of Sec. 11.3.1. Ideally one would like to look at the impact of the different matter effects, for each of the population scenarios and each of the model EoS individually. However, the corresponding simulations are computationally expensive if one wants to have good statistics. For this reason, we proceed as follows:

- First we set the spins to zero both in injections (S0) and templates. We generate results for injected component masses according to the uniform MU, and then the Gaussian MG population scenario; however, in both cases the mass prior in our Bayesian analysis is taken to be uniform on $[1, 2]\,M_\odot$. Again because of computational cost, we only make this comparison for the case where the EoS in the signals is MS1, *i.e.* the stiffest equation of state considered in this paper.

- Next we specialize to the more astrophysically motivated Gaussian distribution for the component masses (still keeping a uniform prior in the analysis), and we also switch on spins. In the injections, we distribute the latter according to the S02 and S05 scenarios, while in the templates we let the prior on the spins be uniform on the interval $[-0.1, 0.1]$, to reflect the ignorance about spins we will in practice have. Since in this case we are

---

[4]The detection efforts themselves can not take the unknown EoS effects into account, and searches are done with point particle templates.

including all the aforementioned astrophysical effects, we generate results not only for MS1, but for H4 and SQM3 as well.

Results are presented in terms of the natural logarithm of the odds ratio $\ln^{(N)} O_j^i$, since quantities like the evidence typically take very large values.

Masses: MU (uniform), MG (Gaussian); no spins

We examine how the ranking statistics $^{(N)}O_j^i$ are distributed after having combined information from 20 BNS detections ($N = 20$) drawn from a uniform mass distribution. The resulting distribution of $\ln^{(20)}O_{MS1}^i$ for this set of simulations, using MS1 as the true EoS, is shown in the cumulative plot of Fig. 11.4.
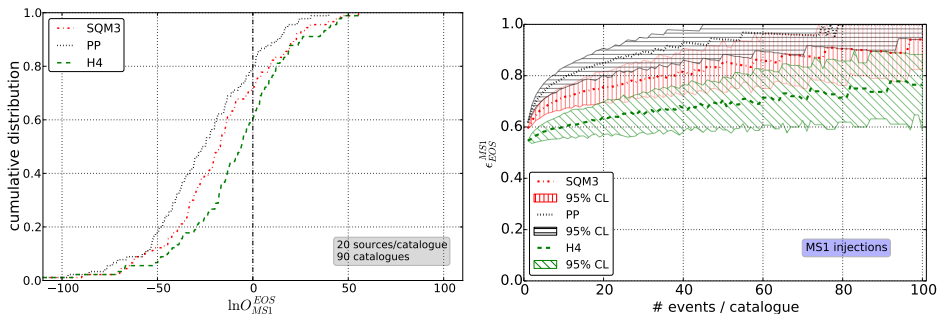

Figure 11.4: *Hypothesis ranking results for a population of sources with component NS masses sampled from a uniform mass distribution in $[1, 2]\,M_\odot$ and with zero spins. Left: cumulative distribution for the combined odds ratio between the underlying EoS (MS1) and the other three candidate models (PP, SQM3, H4), for 90 independent catalogs of 20 sources each. Negative values correctly favor MS1. Right: the fraction of correct rankings $\epsilon_{\mathrm{EOS}}^{\mathrm{MS1}}$ as a function of catalog size. A set of 1,800 sources is partitioned into catalogs in 1,000 different ways; medians are drawn as thick lines and 95% confidence intervals are shown as shaded regions.*

We let the injections have MS1 as their EoS, and we compute the log odds ratios $\ln^{(20)}O_{\mathrm{MS1}}^{\mathrm{EOS}}$ for catalogs of 20 sources each, where, in turn, "EOS" stands for PP, SQM3, and H4. Examples of the cumulative distributions of these log odds ratios are shown in the left panel of the figure. In the absence of detector noise, one would have $\ln^{(20)}O_{\mathrm{MS1}}^{\mathrm{EOS}} < 0$ in all three cases, since any EoS different from the correct one (MS1) would be deprecated. What we see is that $\ln^{(20)}O_{\mathrm{MS1}}^{\mathrm{PP}} < 0$ for about 80% of the catalogs, while $\ln^{(20)}O_{\mathrm{MS1}}^{\mathrm{H4}} < 0$ in about 60% of the cases. Note that H4 is the most similar to MS1, followed by SQM3 and PP; and indeed, the log odds ratios obtained tend to correctly rank the EoS in this way. This is similar to what one sees in the top right panel of Fig. 2 of our earlier work [152], where tidal effects were considered up to 1PN beyond leading order and termination was set to f_{LSO}. However, despite the fact that in the present work we take tidal effects to much higher order, the left tails of the cumulative log odds

ratio distributions stretch to less negative values. This can be explained by the different termination of the waveforms, which for the EoS and mass distributions we consider tends to be at contact rather than LSO (see Fig. 3). For a typical system with component masses $(1.35, 1.35) \, M_\odot$ and equation of state MS1, the termination frequency is $f_{\text{contact}} = 1222$ Hz whereas $f_{\text{LSO}} = 1629$ Hz, so that the signal contains less information on tidal effects (which manifest themselves at high frequency) than in [152]. Indeed, as can be seen in Fig. 11.3, the higher-order tidal effects due to their alternating signs do not significantly change the number of cycles in the phase, though they will add some structure because they come with different powers of v; on the other hand, termination at contact seems to have a much stronger effect, cutting the tidal phase short (in this example by roughly 15 radians). The QM effect is much weaker and is not expected to give a significant contribution to the inference.

It is also of interest to observe how the performance of this method improves as the number of detected sources increases. We expect the *fraction of correct rankings* between the true model and any of its competitors to gradually increase with the catalog size. Such a trend is indeed exhibited in the right panel of Fig. 11.4, which shows the fraction $\epsilon_{\text{EOS}}^{\text{MS1}}$ of catalogs for which MS1 is ranked higher than, respectively, H4, SQM3 and PP (*i.e.* $\ln^{(20)} O_{\text{MS1}}^{\text{EOS}} < 0$ where "EOS" is, in turn, PP, SQM3, and H4), as a function of the number of sources per catalog. This is a good hint in favour of posterior consistency of the current method, which implies that for N large enough, the success of hypothesis ranking will converge to 100%. A variance over this statistic is also expected when partitioning a finite number of sources into catalogues; a curve corresponding to the median of $\epsilon_{\text{EOS}}^{\text{MS1}}$ and a band corresponding to its 95% confidence interval based on 1,000 partitioning realizations are drawn for each EoS, as N runs from 0 to 100. We see the same trend as in the left panel: H4, being the most similar to MS1, is ranked below MS1 the least often, and PP, being the most dissimilar, the most often. We note that in going to a higher number of sources per catalog, we start experiencing small number statistics; with a total of 1,800 sources available, at 100 sources per catalog only 18 independent catalogs can be composed. However, if we assume that the distribution of the 1,800 single-source odds ratios is representative of the underlying distribution, we can safely say that the results are free from statistical artifacts.

Next, in Fig. 11.5 we look at the case where the spins are still zero in injections and templates, but the injected masses are distributed according to a Gaussian (MG) with $\mu_m = 1.35 \, M_\odot$ and $\sigma_m = 0.05 \, M_\odot$. Unlike in Fig. 11.4, in the left panel showing the cumulative distributions of the log odds ratios, *we now consider catalogs of 100 sources each*, which turns out to be necessary to approach the discriminatory power we had with a uniform mass distribution. Even then, H4, the EoS that most closely resembles the injected MS1, is not distinguishable from it: the probability that MS1 gets ranked above H4 is approximately the same as the probability that H4 ends up above MS1.

11
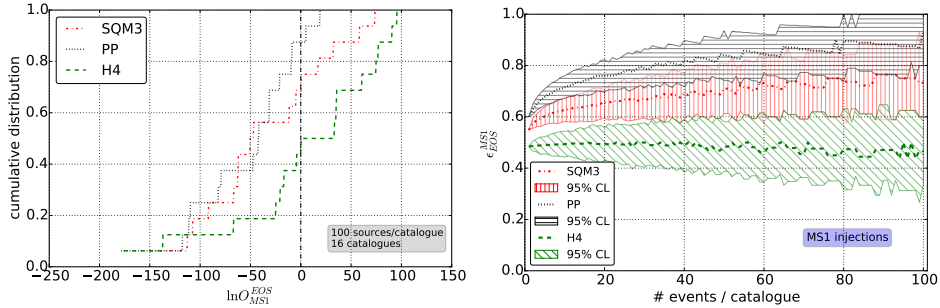
Figure 11.5: *Same as Fig. 11.4 but in this case for a population of NS following the Gaussian mass distribution MG with a strong peak around $1.35\,M_\odot$. Here however, the left panel shows cumulative distribution of the combined odds ratio for catalogs of 100 sources.*

Masses: MG (Gaussian); Spins: S0, S02, S05

We now specialize to the astrophysically better motivated Gaussian distribution for the injected component masses (but sticking to a uniform mass prior in our analyses), and we switch on (anti-)aligned spins χ_A, $A = 1, 2$. In the injections, the spins are sampled according to the scenarios S0 ($\chi_A = 0$), S02 ($\sigma_\chi = 0.02$) and S05 ($\sigma_\chi = 0.05$), while in the templates, we also use (anti-)aligned spins with priors that are uniform in $\chi_A \in [-0.1, 0.1]$. This time we give results for injections where the EoS is MS1, H4, and SQM3, respectively.

S0 The results for non-spinning sources (S0) are summarised in Fig. 11.6. From top to bottom, the injections follow MS1, H4, and SQM3, respectively. In the left panels we see examples of cumulative distributions of $\ln{}^{(100)}\mathcal{O}_{\rm inj}^{\rm EoS}$ for independent catalogs of 100 sources each, where "inj" is the injected equation of state, while "EOS" is, in turn, taken to be each of the other three EoS considered. Recall that a negative value of the log-odds ratio favours the correct hypothesis.

In the right panels of Fig. 11.6 we again vary the number of sources per catalog, and show the fraction $\epsilon_{\rm EoS}^{\rm inj}$ of times that the injected equation of state is ranked higher than each of the other three EoS in turn. For a given number of sources per catalog, we partition individual sources into catalogs in 1,000 different ways and look at the medians and 95% confidence intervals of the $\epsilon_{\rm EOS}^{\rm inj}$.

We observe that, in the case of a stiff EoS (MS1), the true model is most often favoured against SQM3 and PP. The median fraction of correct rankings with 20 (100) combined sources is 70% (90%) against SQM3 and 76% (93%) against PP. However, similarly to what we saw in Fig. 11.5, we see that the runner-up model H4 is favored as often as MS1; the ranking statistics do not seem to improve with catalog size, so again we see that MS1 and H4 are indistinguishable in this case.
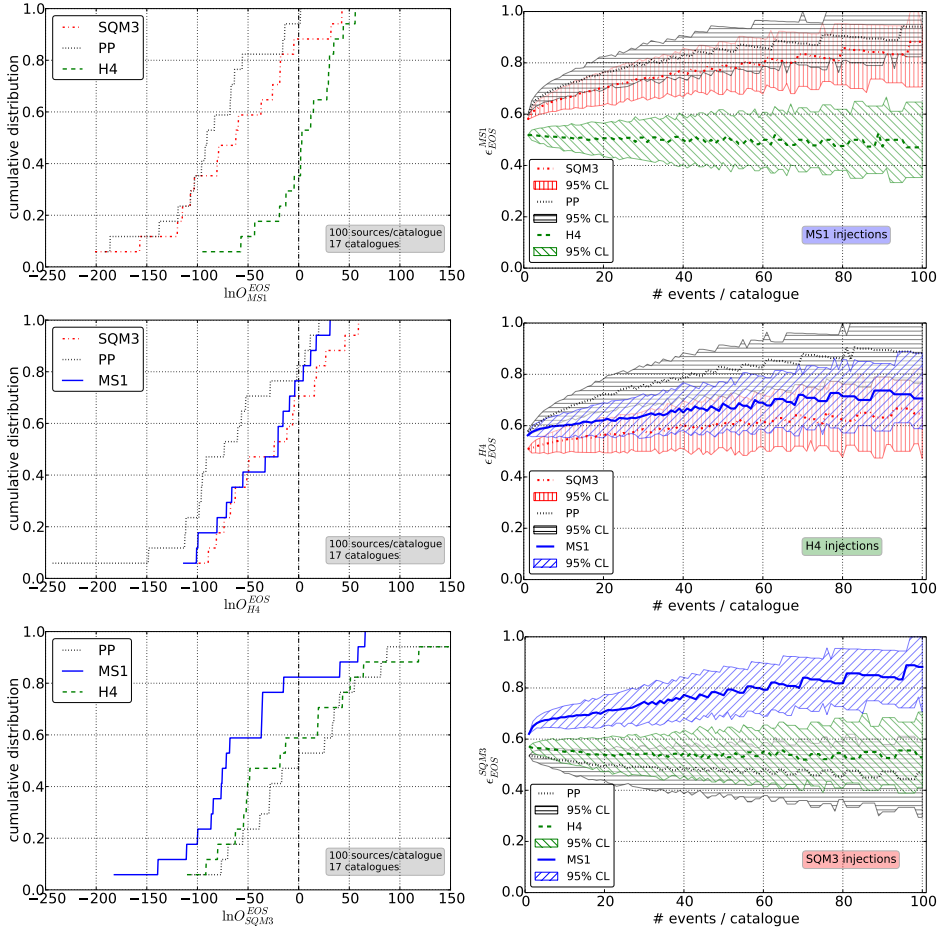
Figure 11.6: *On the left: cumulative distribution plots for the odds-ratio ranking statistic between a model EoS and the one used in the simulated signal (top: MS1, middle: H4, bottom: SQM3). The odds ratios are calculated after combining sets (catalogues) of 100 distinct sources. On the right: the dependence of the ratio of correct rankings on the catalogue size. Error bars represent 95% confidence intervals calculated by simulating 1,000 different partitioning realizations on the full set of useful sources.*

11

If the true model is a moderate EoS (H4), it will correctly be ranked higher than the runner-up (SQM3) 66% of the time after 100 sources are combined. MS1 is actually more deprecated than the soft SQM3, which shows that MS1 and H4 are much better distinguishable in this case, in contrast with what we saw in the top panels. This is an interesting result that hints towards a possible presence of a bias favouring a softer EoS. A similar feature will be observed and studied further in Sec. 11.5.
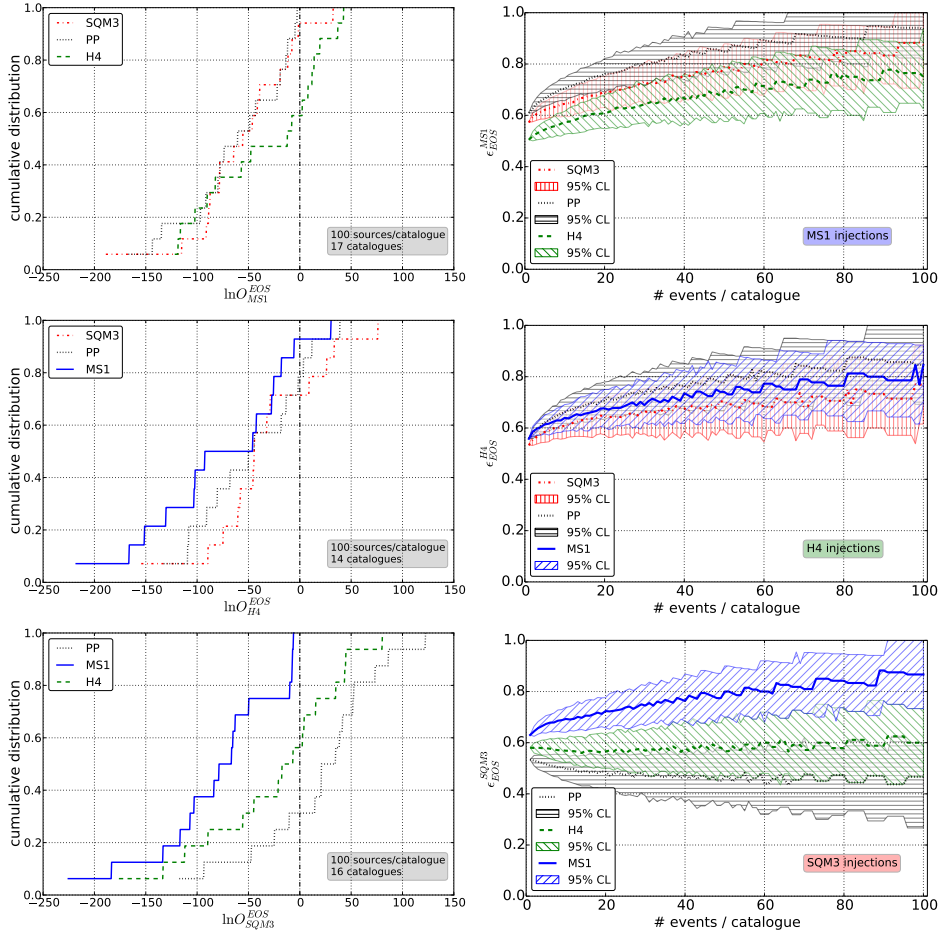
Figure 11.7: *Same as Fig. 11.6, but for sources with (anti-)aligned spin sampled from a Gaussian distribution with $\mu_\chi = 0$ and $\sigma_\chi = 0.02$.*

Finally, if the true model is a soft EoS (SQM3), the stiff MS1 is, as expected, the most deprecated, and with 100 combined sources will be correctly disfavoured 90% of the time. The moderate H4 is very weakly deprecated and even with 100 sources the fraction of correct rankings only reaches 55%, while there also seems to be a small bias towards favouring PP, with a negative trend as more sources are combined.

S02   Similar results for aligned-spins with magnitudes sampled from a normal distribution centred at zero, with a standard deviation of $\sigma_\chi = 0.02$ are summarized in Fig. 11.7. The waveform templates for analysing the data also have the two aligned spin components as free parameters, again with a uniform prior in

11

$\chi_A \in [-0.1, 0.1]$.

Let us first compare the results for MS1 (top panels in Fig. 11.7) with the ones for Gaussian distributed masses but zero spins in injections (Figs. 11.5 and 11.6). Looking at the $\epsilon_{\mathrm{EOS}}^{\mathrm{MS1}}$, we infer that EoS again tend to be ranked correctly according to "stiffness" and similarity to MS1, and we even see some improvement in the discernibility of H4 from MS1, especially as the number of sources per catalog goes to 100.

For H4 injections (middle panels in Fig. 11.7), the medians of $\epsilon_{\mathrm{EOS}}^{\mathrm{H4}}$ are still ordered, with the median of $\epsilon_{\mathrm{PP}}^{\mathrm{H4}}$ staying above that of $\epsilon_{\mathrm{MS1}}^{\mathrm{H4}}$, which in turn trumps $\epsilon_{\mathrm{SQM3}}^{\mathrm{H4}}$. However, H4 being in between MS1 and SQM3 in stiffness (see Fig. 11.1), the 95% uncertainty intervals of the $\epsilon_{\mathrm{EOS}}^{\mathrm{H4}}$ show considerable overlap; although H4 is ranked above each of the other EoS reasonably frequently, the internal ranking is less clear but still PP seems to be the most deprecated.

Finally, for SQM3 (bottom panels), this being the softest EoS other than the PP model, the stiff MS1 tends to be deprecated reasonably strongly, but it is hard to distinguish SQM3 from either H4 or PP. Note again the slightly downward trend in the median of $\epsilon_{\mathrm{PP}}^{\mathrm{SQM3}}$ with increasing number of sources per catalog; this may indicate a small bias.

S05 Similar results for aligned-spins with magnitudes sampled from a normal distribution with $\mu_\chi = 0$ and $\sigma_\chi = 0.05$. Again, the waveform templates have the two aligned spins as free parameters, with a uniform prior in $\chi_A \in [-0.1, 0.1]$. Here too, we see similar results for the distinguishability between the different EoS as in the previous two scenarios. The $\epsilon_{\mathrm{EoS}}^{\mathrm{inj}}$ curves are ranked as expected but the inference is again poorer than one would hope for. Most notably, we see hints of possible bias that may *e.g.* be responsible for the non-deprecation of H4 when MS1 is used as the underlying EoS in the top-right panel.

11.5 Parameter Estimation

11.5.1 Method

In this section we introduce a second method for inferring the NS EoS, based on Bayesian parameter estimation. As implied by the title, we first need to formulate the inference problem in a parametrized way. A clear advantage of hypothesis ranking was that information from multiple detections can trivially be combined. In measuring parameters, we will want to do the same. The obvious choice of simply formulating the problem as one of inference on the central EoS-related parameters λ_A that enter the waveform model, is problematic if we want to eventually combine information from multiple detections. The reason is that λ is a source-dependent parameter and in particular it depends on the NS mass; therefore, it would make no sense to combine measurements of an observable
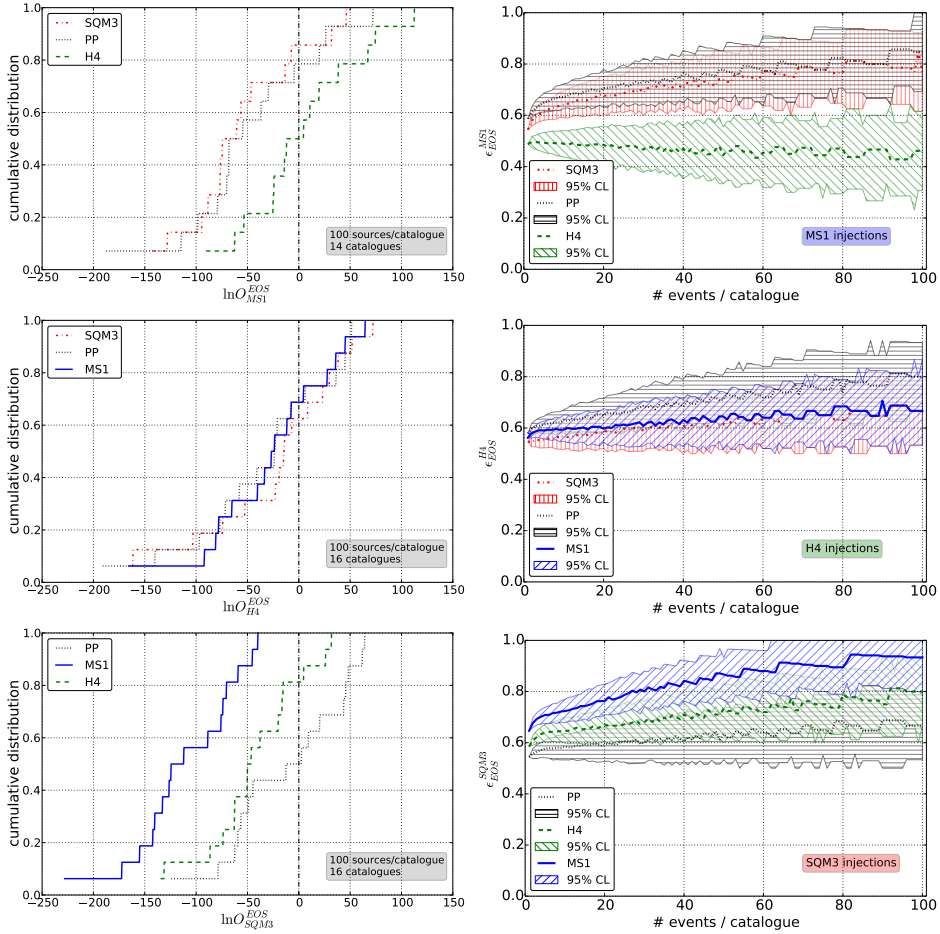
Figure 11.8: *Same as Fig. 11.6, but for sources with (anti-)aligned spin sampled from a Gaussian distribution with $\sigma = 0.02$, centered at 0.*

that depends on incidental details of the sources. Instead one needs to identify observables that only depend on the EoS; we will attempt to infer the dependence of λ on the NS mass and, if possible, in a parametrized way.

One example of such a parametrization would be a Taylor expansion of $\lambda(m)$ around a reference mass m_0, as was suggested by Damour *et al.* [147]

$$\lambda(m) = \sum_{j=0}^{j_{\max}} \frac{1}{j!} c_j \left(\frac{m - m_0}{M_\odot} \right)^j . \tag{11.12}$$

This will result in a set of *global parameters*, the expansion coefficients c_i, which

are common across the entire set of detected sources. [5] We shall adopt this parametrization of the equation of state; in our preliminary work [152] we restricted ourselves to a first-order approximation, where the functions $\lambda(m)$ are modelled by straight lines

$$\lambda_{\text{lin}}(m; c_0, c_1) = c_0 + c_1(m - m_0) \,. \tag{11.13}$$

Our choice for the reference mass m_0 will always be $1.4 M_\odot$, motivated by the increased density of observed NS masses around that value. Here, we will mostly examine the case of a quadratic expansion

$$\lambda_{quad}(m; c_0, c_1) = c_0 + c_1(m - m_0) + \frac{c_2}{2}(m - m_0)^2 \,. \tag{11.14}$$

Already at zero-th order, the value of c_0 (*i.e.* the value of λ at $1.4 M_\odot$) is indicative of the stiffness of the EoS. Since this value will be inferred from detected systems of masses that lie within a wide range, an important assumption of the quadratic method is that the true EoS can be well approximated by a quadratic function, within the range of the observed NS masses.

Note that since the true EoS will almost surely not be characterized by a linear or quadratic $\lambda(m)$ function, the *true value* of the global parameters c_0, c_1 and c_2 is not well defined. For a given BNS population with a given NS mass distribution, one can treat the EoS parameters themselves as random variables and define their expectation value. This will be further studied in Sec. 11.7.

The parameter space will now be extended to take the form

$$\vec{\theta} = \{\vec{\theta}_{\text{CBC}}, \vec{\theta}_{\text{EOS}}\} \tag{11.15}$$

where $\vec{\theta}_{\text{CBC}}$ is the usual set of CBC parameters given in Eq. (5.2) and $\vec{\theta}_{\text{EOS}}$ is the set of parameters that define the EoS. Our EoS-extended waveform model will be constructed by mapping the new global parameters $\vec{\theta}_{\text{EOS}}$ and the masses m_A to the tidal deformability parameters λ_A of Eq. (2.56)

$$\lambda_A = \lambda_{EOS}(m_A; \vec{\theta}_{EOS}) \,. \tag{11.16}$$

An example of such a mapping is given in Eq. (11.14). The posterior p.d.f. over the entire parameter space of each BNS system can be obtained by means of a numerical algorithm like nested sampling, which will be employed here. Now, the *likelihood* function is defined as

$$p(d|\vec{\theta}_{\text{CBC}}, \vec{\theta}_{EOS}, \mathcal{I}) = \mathcal{N} \exp\left[-2 \int_{f_{\text{low}}}^{f_{\text{high}}} df \frac{|\tilde{d}_n(f) - \tilde{h}_{EOS}(f; \vec{\theta}_{\text{CBC}}, \vec{\theta}_{EOS})|^2}{S_n(f)}\right] \,, \tag{11.17}$$

---

[5]Here again it seems that we need to assume a single-branched equation of state. This will be further discussed in Section 12.1.

where $\mathcal{N}$ is a normalization factor, $\tilde{d}_n(f)$ is the Fourier transformed data and $S_n(f)$ is the detector's one-sided noise power spectral density. [6]   The template $\tilde{h}_{EOS}(f; \vec{\theta}_{\mathrm{CBC}}, \vec{\theta}_{EOS})$ is the modelled gravitational waveform in the frequency domain, for a given set of (source-dependent) binary parameters $\vec{\theta}_{\mathrm{CBC}}$ and (global) EoS-related parameters $\vec{\theta}_{EOS}$. The limits of integration are taken to be $f_{\mathrm{low}} = 40\mathrm{Hz}$ and $f_{\mathrm{high}} = f_{\mathrm{cut}}$.

Once the likelihood function on the parameter space is sampled well enough, the nested sampling algorithm allows us to obtain a good estimate of the posterior pdf, $p(\vec{\theta}_{\mathrm{CBC}}, \vec{\theta}_{EOS} | d, \mathcal{I})$. Since we are only interested in the EoS-related parameters $\vec{\theta}_{EOS}$, the rest can be marginalized over

$$p(\vec{\theta}_{EOS} | d, \mathcal{I}) = \int_{\Sigma_{\mathrm{CBC}}} \mathrm{d}\vec{\theta}_{\mathrm{CBC}} \, p(\vec{\theta}_{\mathrm{CBC}}, \vec{\theta}_{EOS} | d, \mathcal{I}). \tag{11.18}$$

In order to combine information from N independent detections $\{d_1, \ldots, d_N\}$, one may again make use of Bayes rule and the multiplication rule for the independent random variables $d_1, \ldots, d_N$

$$\begin{aligned} p(\vec{\theta}_{EOS} | d_1, \ldots, d_N, \mathcal{I}) &= p(\vec{\theta}_{EOS} | \mathcal{I}) \prod_{n=1}^{N} \frac{p(\vec{\theta}_{EOS} | d_n, \mathcal{I})}{p(\vec{\theta}_{EOS} | \mathcal{I})} \\ &= p(\vec{\theta}_{EOS} | \mathcal{I})^{N-1} \prod_{n=1}^{N} p(\vec{\theta}_{EOS} | d_n, \mathcal{I}) \end{aligned} \tag{11.19}$$

which shows how the posterior on the global parameters is updated by the posterior-to-prior ratio for each source that gets detected.

It is instructive here to justify the possibility of inferring more than two global parameters, as in the case of a model that characterizes the EoS by quadratic polynomials $\lambda_{quad}(m; c_0, c_1, c_2)$. For any given BNS source, the number of real EoS observables is always 2, since the quantities that fully describe the waveform beyond point-particle are λ_1 and λ_2. It follows that any attempt to do parameter estimation on a set of three parameters that are functions of λ_1 and λ_2 will lead to a 1-dimensional degeneracy in the likelihood (*i.e.* there is a 1-dimensional family of quadratic functions that pass through a set of 2 points on the $m - \lambda$ plane). However, for two BNS sources of different masses and/or spins, these degeneracies will generically not foliate the space of global parameters in the same way; thus, it is expected that degeneracies of this sort will be lifted as the variety of detected sources increases.

Alternative parameterizations   Finally, we should note that one is free to choose other ways of parametrizing the problem, as long as one has a way to map the global EoS parameters $\vec{\theta}_{\mathrm{EOS}}$ to the source-dependent λ_A parameters,

---

[6]For a network of multiple detectors with uncorrelated noise, the multiplication rule may be used to express the overall likelihood as a product of likelihoods for individual detectors.

given the component masses m_A. More specifically, a physically well motivated parametrization is acquired by adopting a family of piecewise polytropic models for the NS EoS. These are models where the interior of the NS is characterized by a (small) number of polytropic EoS of the form

$$P(\varepsilon) = K_i \varepsilon^{1+1/n_i} \quad , \quad \varepsilon_{i-1} < \varepsilon \le \varepsilon_i \,, \tag{11.20}$$

where different polytropic indices n_i are valid in different ranges of the energy density ε (and most of the pre-factors K_i are fixed by continuity conditions). As discussed in [308], even a simple such model with two free parameters is sufficient to cover closely enough the existing set of candidate EoS.

Yet another possibility is the set of parameters related to the *constant speed of sound* model that attempts to describe the macrophysics of a hybrid NS interior [39]. As long as one can directly map the set of global parameters to a function $\lambda(m)$, one can directly perform Bayesian inference techniques on these parameters and possibly apply any physical or observational constraints, or even a prior p.d.f. that may be in one's disposal.

These considerations deserve elaborate investigations that are outside the scope of the current thesis. It is however interesting to note that translating from one parameterization $\vec{\theta}_{\mathrm{EOS}}$ to another $\vec{\theta}'_{\mathrm{EOS}}$ is only a matter of performing a simple transformation [7] and using the transformation law for probability densities

$$p(\vec{x}) = p(\vec{y}) \left| \frac{\partial \vec{y}}{\partial \vec{x}} \right| \,, \quad \vec{x} \leftrightarrow \vec{y}. \tag{11.21}$$

If we denote by φ, φ' the mappings

$$\varphi : (\vec{\theta}_{\mathrm{EOS}}, m_A) \to (\lambda_A, m_A), \quad \varphi' : (\vec{\theta}'_{\mathrm{EOS}}, m_A) \to (\lambda_A, m_A) \tag{11.22}$$

then $\varphi^{-1} \circ \varphi'$ gives the desired transformation. In practice, the most flexible choice would be to simply parameterize the templates used in our numerical algorithm by the λ_A's, and leave the transformation to whichever set of global parameters we wish to use to be worked out in the post-processing stage of the analysis. The posterior information contained in the results will in any case remain intact.

11.5.2 Simulations and results

For the global EoS-related parameters, namely $\{c_0, c_1, c_2\}$ in the quadratic approximation to $\lambda(m)$ as in Eq. (11.13) and Eq. (11.14) respectively, the priors are chosen to be uniform in $c_0 \in [0, 5] \times 10^{-23} s^5$, $c_1 \in [-2.5, 0] \times 10^{-23} s^5$, and $c_2 \in [-3.7, 0] \times 10^{-23} s^5$. In the mass regime of interest, this choice of ranges can accomodate all the EoS in Fig. 2 of [200]. As it turns out, in the quadratic approximation only the leading-order coefficient c_0 can be measured with any kind

---

[7]Extra care is needed in cases where this transformation is not bijective.

of accuracy. Nevertheless, one has $c_0 = \lambda(m_0)$, with m_0 some fixed reference mass (which we take to be $1.4\,M_\odot$), and as can be seen in Fig. 2 of Hinderer *et al.*, which shows nearly 20 different predictions for $\lambda(m)$, valuable information could be gleaned from just that one number.

We will impose additional conditions on the simulated signals, similarly to those of Sec. 11.4.2, before accepting a detected source for analysis:

1. The optimal network SNR should be: $8 \leq \rho_{\mathrm{net}} \leq 30$ and

2. A post-analysis signal-to-noise Bayes factor cutoff of $\ln B^{\mathrm{signal}}_{\mathrm{noise}} \geq 32$.

As before, we consider the following cases:

- Spins are zero both in injections and templates; regarding the mass distributions, we compare results for an MU population with what one gets with an MG population. However, for the templates we do not assume knowledge of the astrophysical mass distribution, sticking to a uniform mass prior on $[1, 2]\,M_\odot$. We will also compare between terminating the waveform at f_{LSO} or f_{cut}.

- Next we again consider both MU and MG mass distributions, but now we switch on spins. In the simulated population, the latter follow the scenarios S0, S02 and S05, while in the templates the priors for the spins are uniform on $[-0.1, 0.1]$.

Thus, there are several different variable features that may affect the analysis, (frequency cutoff, mass/spin distribution) and we shall introduce them gradually so that their individual effects on the main result, namely the posterior p.d.f. of c_0 can be better understood. To give a more detailed picture of the analysis, further extensive results will be shown in plots, but only for the *benchmark* set-up, that uses f_{cut} as a waveform termination condition, MU for the mass distribution and no spins.

Masses: MU, MG; no spins

We first consider an S0 population of BNS sources, where the component bodies are non-spinning ($\chi_A = 0$, $A = 1, 2$); we also do not include spins in our recovery templates. In particular, this means that the quadrupole-monopole effect does not come into play, and neither do the spin-orbit and spin-spin terms of Eq. (2.45), starting at 1.5PN and 2PN respectively.

A summary of the parameter estimation results for c_0, for a set of sources whose mass distribution follows the uniform scenario MU, is shown in Fig. 11.9.

The median and 95% confidence intervals as functions of N give a first impression of how the combined posterior is progressively updated each time a new source
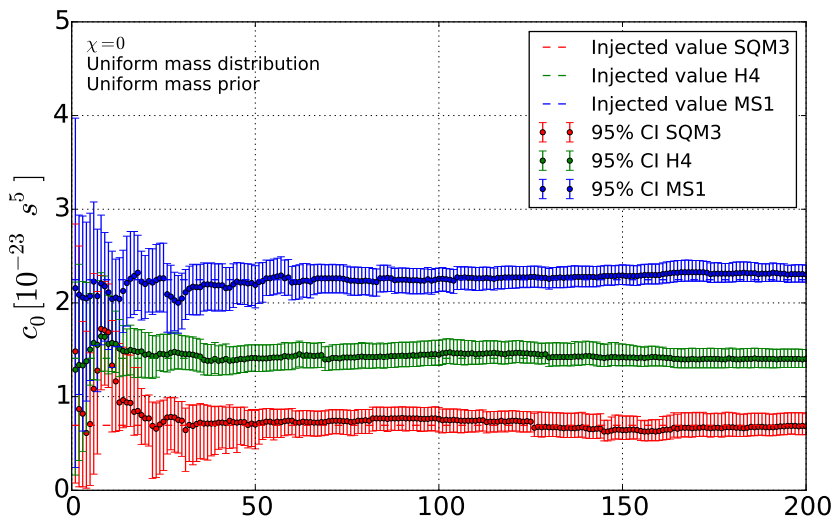
Figure 11.9: *Median and 95% confidence intervals of the combined marginalized posterior $p(c_0|\{d_i\}_{i=1,\ldots,N},\mathcal{I})$ for the zero-th order expansion coefficient c_0 as a function of the number of detected sources. The waveforms extend up to f_{cut}, the sources are non-spinning with m_1, m_2 drawn from a uniform mass distribution. The different colors indicate the EoS used in three different sets of simulated waveforms, with the horizontal dashed lines marking the 'true value' of c_0 in each case.*

is detected and incorporated in the analysis. We observe that in each of the scenarios studied here, the combined posterior distribution will eventually peak around a certain value of c_0, with a few tens of detected sources.

We point out however, that the remaining EoS-related global parameters, c_1 and c_2 are not well measurable by themselves, at least given the number of sources available in these sets of simulations. An example of the 1D posterior evolution for c_1 and c_2, corresponding to the plot of Fig. 11.9, is given in Fig. 11.10. Even so, the information on $c_0 = \lambda(m_0)$ alone is enough to significantly narrow down the true EoS.

The plots of Figs. 11.9 and 11.10 show median values and confidence intervals which are good representatives of the posterior distribution but still yield little information about the shape of the p.d.f.. The p.d.f.s were estimated and combined using a kernel density estimator (KDE) with a Gaussian kernel on the posterior points of each source, and making use of Silverman's rule to optimize the bandwidth. In Fig. 11.11 a set of plots is shown, that illustrate the marginalized posterior p.d.f. of c_0 (top), c_1 (middle) and c_2 (bottom) after having combined data from 50 sources whose underlying EoS is MS1 (left), H4 (center) and SQM3 (right). In the same plots we can also see in green the single-source posterior p.d.f. of the last source that was analysed, generated using a KDE on its posterior points (around 5000 per source). We see that (at least for the best inferred

11
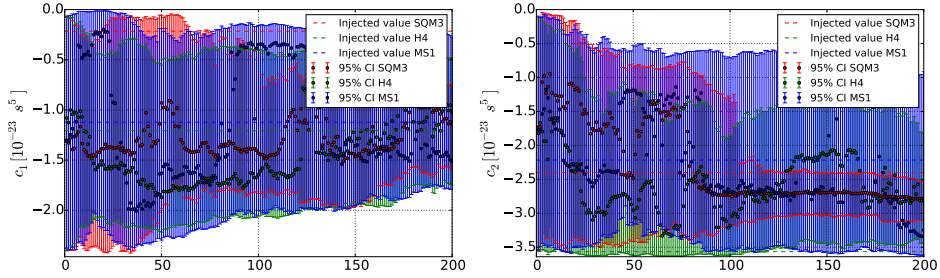
Figure 11.10: *Evolution of the medians and 95% confidence intervals in the measurement of the higher-order coefficients c_1 and c_2 in the quadratic approximation to $\lambda(m)$, for the case of spinning injections. The behavior for non-zero injected spins and/or gaussian mass distribution is qualitatively the same.*

parameter c_0), even if a single-source measurement gives large uncertainties and is not peaked around the true value, the combination of information from tens of sources will eventually drive the combined posterior to converge to the correct value.
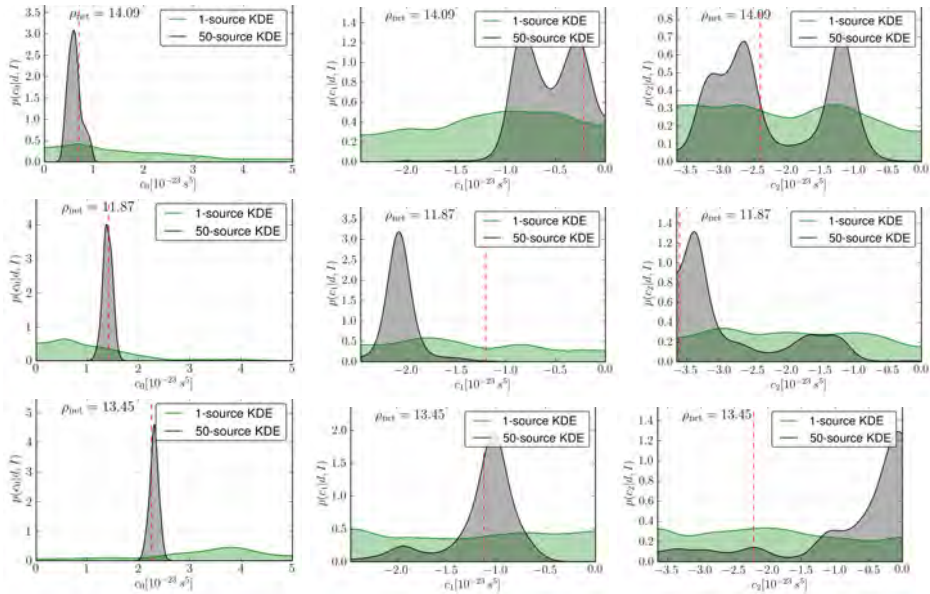
Figure 11.11: *Example of posterior p.d.f. plots for c_0 (left), c_1 (centre) and c_2 (right), after combining information from 50 sources (black curve) using a Gaussian kernel density estimator. The p.d.f. of the last added source is also shown (green curve) and its SNR is given at the top left corner. The underlying EoS used are from top to bottom: SQM3, H4 and MS1, and the "true values" are drawn as red vertical lines.*

Since the EoS cannot be characterized by a single parameter, it is also useful to look at two-dimensional posteriors for pairs of the global parameters (or even three-dimensional if possible); this way one can also check for correlation patterns that are not visible in single-parameter p.d.f.s. A typical set of two-dimensional combined posteriors is shown in Fig. 11.12, in which the contours represent the 95% confidence areas of the c_0-c_1, c_1-c_2 or c_0-c_2 combined PDF each time a set of 10 new sources is combined, with the curves being drawn more solid as the number of combined sources increases. The innermost, darkest drawn contours correspond to the 95% CI after 50 sources have been analysed. We see that c_0
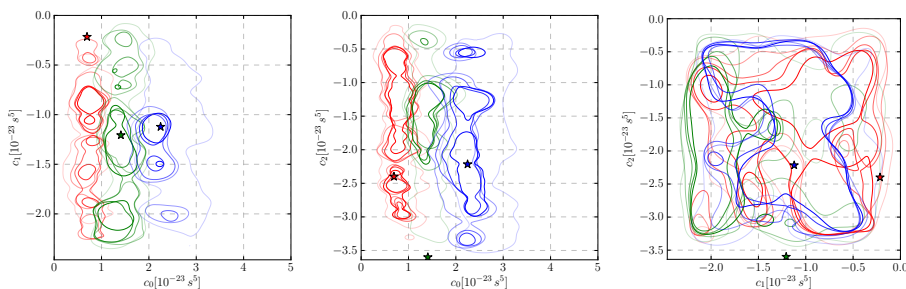
Figure 11.12: *Example of two-dimensional posterior plots for the three pairs of global variables c_0-c_1 (left), c_0-c_2 (centre), c_1-c_2 (right), after 50 sources have been analysed. The injected EoS are MS1 (blue), H4 (green) and SQM3 (red), with stars marking their corresponding "true values". The 95% confidence contours are drawn for each 10 sources that are added to the analysis in increasingly solid color, the most solid one corresponding to 50 combined sources.*

does not appear to be significantly correlated with either c_1 or c_2.

Next, we turn to the scenario where the simulated population of sources has an underlying Gaussian mass distribution MG, with $\mu_m = 1.35\,M_\odot$ and $\sigma_m = 0.05\,M_\odot$. Again the spins parameters are always set to zero in both injection and recovery waveforms.

Results on the evolution of the posterior medians and 95% confidence intervals for c_0 with increasing number of detections are shown in Fig. 11.13. We see that a good separation between MS1, H4, and SQM3 doesn't occur until > 100 sources have become available, and large systematic biases appear. As explained below, this is related to the continued use of a flat prior on the component masses, a distribution which now has a significant mismatch with the astrophysical one. The effect of the mass prior is further investigated in Sec. 11.7.

Masses: MU, MG; Spins: S0, S02, S05

We now move on to a more realistic set of scenarios where NS spins are not neglected, but are added as additional free parameters in our recovery model,
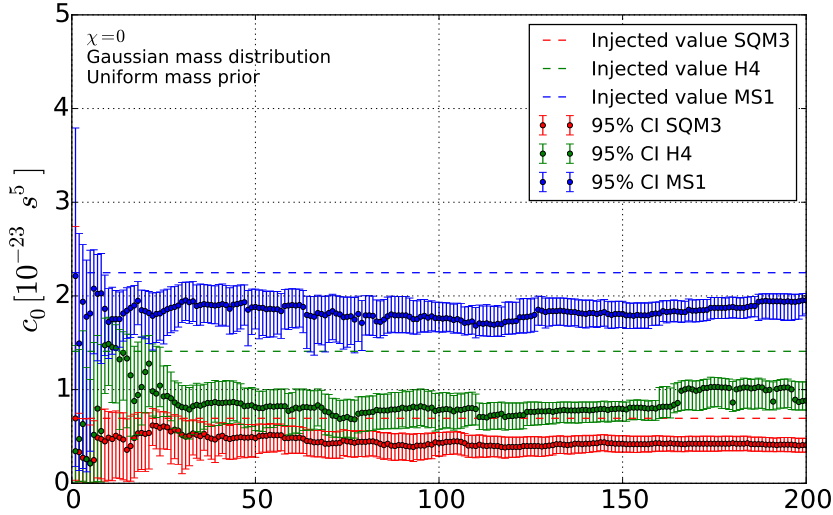
Figure 11.13: *Same as Fig. 11.9 but this time the component NS masses of the simulated population are drawn from a Gaussian mass distribution (MG). There is clear evidence of systematic bias in all three sets of sources: the posterior p.d.f.s converge significantly far from the horizontal dashed lines that mark the underlying 'true value' of c_0 in each case.*

with a uniform prior on their magnitudes ranging in $\chi_A \in [-0.1, 0.1]$ (we again restrict to spins (anti-)aligned with $\vec{L}$) A set of plots similar to that of Fig. 11.9 is panelled in Fig. 11.14, where combinations of the different mass distributions MU (left) and MG (right) with spin amplitude distributions S0 (top), S02 (middle) and S05 (bottom) were used for sampling the parameters of the simulated sources.

Judging from the behaviour of the median and 95% confidence intervals as the number of combined sources increases we arrive at the following conclusions.

1. The posterior p.d.f.s seem to be consistently wider than the ones obtained in the no-spin analysis. This is to be expected: when adding spin parameters in the recovery templates we enlarged the parameter space by two additional dimensions, thus seeding additional correlations between intrinsic parameters and making the parameter space harder to sample. The delicate measurement of matter effects is thus affected by additional statistical errors, which slow down the convergence of *e.g.* the c_0 posterior.

2. There is clear presence of a bias that again appears when the NS population follows a peaked mass distribution; weak signs of bias are also present when the mass distribution is uniform. The magnitude of this bias varies slightly across the right panels of Fig. 11.14 and in some cases it is not as evident as in Fig. 11.13, mainly due to the wider error bars. Two possible sources of bias will be investigated in the following section.
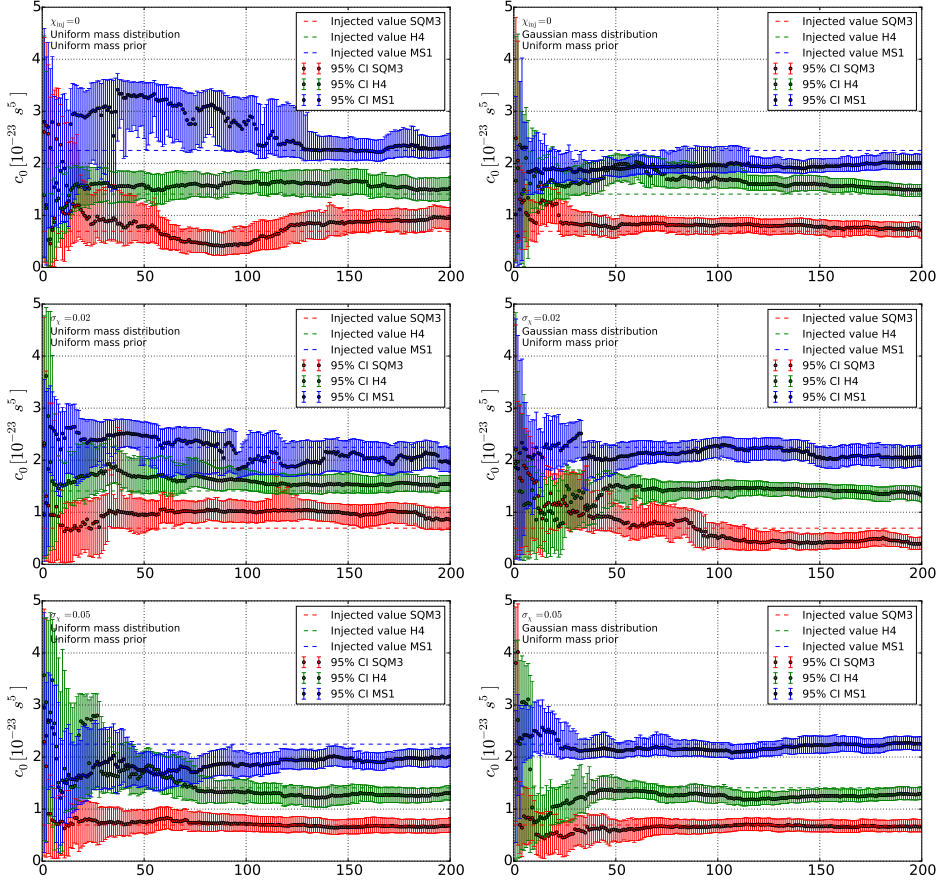
Figure 11.14: *Same as Fig. 11.9, but for populations of BNS systems whose mass and spin distributions follow different scenarios; for recovery, templates have (anti-)aligned spins with uniform priors $\chi_A \in [-0.1, 0.1]$. The component masses m_1, m_2 are sampled from a uniform (left) or a Gaussian (right) distribution. The (anti-)aligned spin amplitudes are either set to zero (top) or sampled from a Gaussian distribution with $\sigma_\chi = 0.02$ (middle) or $\sigma_\chi = 0.05$ (bottom).*

11.6   EoS Information Content of BNS signals

11

With different EoS-related effects introducing mass-dependent contributions to the phase, throughout the entire inspiral, it would be useful to quantify the gain in inference yielded by each source of information. In this section we briefly discuss the information yield of a BNS system related to the EoS parameters.
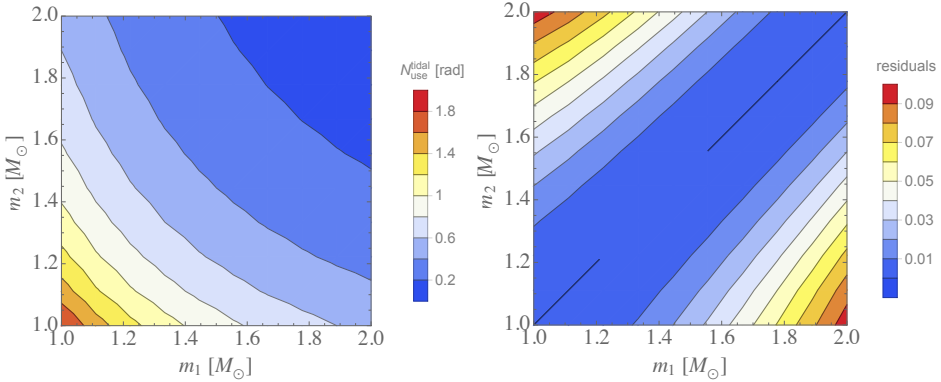
Figure 11.15: *Left: Number of useful tidal cycles as a function of the component masses. It is a monotonically decreasing function of mass, and the dependence seems to be primarily on the chirp mass parameter $\mathcal{M}_c$. Right: For each point in m_1-m_2 we assume $N_{\mathrm{use}}^{\mathrm{tidal}}$ to be the same as for the point with an identical $\mathcal{M}_c$ but with $q = 1$, and calculate the residual. The EoS used here is MS1.*

11.6.1   Number of Useful Cycles

Typically, most of the phase contribution of matter effects is attributed to tidal effects, which appear at high PN order and therefore are stronger at high frequencies. However, one may identify two competing factors that define how each part of the waveform contributes to the measurability of EoS-related parameters. The first factor is, of course the phase contribution of tidal (and Q-M) effects, as demonstrated in section 2.6.2. The second factor is the set of sensitivity curves of the detectors used. It is thus instructive to estimate the number of *useful cycles* $\mathcal{N}_{\mathrm{use}}$ Eq. (2.33) contributed by the matter effects, which is a quantity that counts the accumulated phase multiplied by a PSD-weighted factor. As can be seen in Fig. 11.16, even though the bulk of the tidal phase is accumulated at high frequencies, the low detector sensitivities at this frequency range may render the effect unmeasurable.

As a first note, it is interesting to see that this quantity almost reduces to a function of the chirp mass of the system. This becomes evident in Fig. 11.15, where the number of useful cycles is plotted in the $m_1 - m_2$ plane, along with a family of lines of constant $\mathcal{M}_c$. The relative uncertainty introduced by assuming $\mathcal{N}_{\mathrm{use}}^{\mathrm{tidal}} = \mathcal{N}_{\mathrm{use}}^{\mathrm{tidal}}(\mathcal{M}_c(m_1, m_2))$, plotted in Fig. 11.15 is less than 5% in the best part of the parameter space and less than 10% for $q \sim 2$, the largest mass ratios considered here.

Keeping this in mind, we now fix the mass-ratio to that of equal-mass systems ($q = 1$ or $\eta = 0.25$) and examine how the useful cycles accumulate as a function of frequency, for a set of $\mathcal{M}_c$ values. This is plotted in Fig. 11.16, starting at 40 Hz and terminating at f_{cut}. The extension to f_{LSO} (plotted with faint lines)

gives us an idea of how much information is lost due to the fact that the waveform terminates upon contact. In the same plot we also show the number of useful cycles $\mathcal{N}_{\mathrm{QM}}$ contributed by the Q-M phase terms.
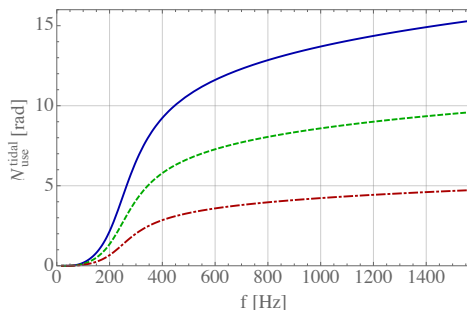
Figure 11.16: *Number of useful cycles for the tidal and QM effects in the phase as a function of frequency, for a BNS system of $(1.4, 1.4)\, M_\odot$ and for three EoS: SQM3 (red dash-dotted), H4 (green dashed) and MS1 (blue solid).*

11.7 Sources of bias

11.7.1 Underlying mass distribution vs mass prior

Unlike with our evidence calculations, in the case of posterior density functions it is relatively easy to "re-weight" the sampling of parameter space so as to make $p(\vec{\theta}_{\mathrm{CBC}}, \{c_j\}|d, \mathcal{I})$ correspond to different priors on the parameters [364]. The degradation in the estimation of c_0 (and for that matter, hypothesis ranking) happened when we changed the way the component masses in the injections were distributed. Hence it is of interest to study the effect of the prior on the masses in particular.

Let us pretend to have perfect knowledge of the astrophysical mass distribution – in our example a Gaussian with $\mu_m = 1.35\, M_\odot$ and $\sigma_m = 0.05\, M_\odot$ – and take the prior on m_1, m_2 to be identical to it. In the case of zero spins, the result is shown in the left panel of Fig. 11.17. We see that the significant biases we encountered in Fig. 9 have largely gone away. In the right panel of Fig. 11.17 we also include spins as before; here too, the biases seen earlier are strongly mitigated, though the larger parameter space to be probed still causes larger statistical errors.

This is not a typical case of a "prior-dominated" inference on a parameter, since the bias originates from a bad choice of priors for different parameters (m_1, m_2) than the one that we are interested in (c_0). Two important details that make this bad choice manifest itself as a bias in the c_0 posteriors are the following. First, there is the fact that the parameters λ_A, through which c_0 is inferred, have an implicit dependence on the masses m_A. The c_0 posterior is determined by the

205
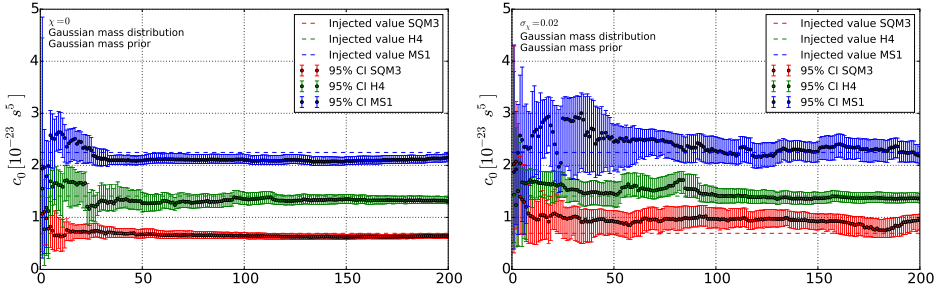
Figure 11.17: *Same as Fig. 11.14 but using the true underlying mass priors (Gaussian in both cases) by reweighting the posterior points. We see how the prominent bias observed earlier largely goes away.*

posterior on the m–λ plane for each component NS, and if the masses are biased then so is the inferred $\lambda(m)$ curve. Second, since c_0 is treated as an independent parameter, the bias enters through the mass prior, in the process of marginalizing over m_1 and m_2, consistently for each source, and is therefore a persistent bias that will not average out as the number of sources increases.

In conclusion, the biases we see in the estimation of c_0 mostly result from the mismatch between the mass distribution for the sources and the prior distribution of component masses in the Bayesian analysis of the data. The relatively small remaining biases that occur when the injected mass distribution is the same as the prior can be attributed to the quadratic approximation for $\lambda(m)$ used in the template waveforms, and the fact that when most of the masses are in a narrow interval, less of the underlying tidal deformability function is being probed by the sources.

Finally, the small residual bias that can be observed not only in the right panel of Fig. 11.17 but also in the left panels of Fig. 11.14, where the mass distribution was uniform, is due to the corresponding spin distributions. Spin parameters χ_A enter the phase at 1.5 PN onwards, and are known to have significant correlations with the mass ratio η, which in turn is found in the tidal terms. Consequently, a discrepancy between the injected spin distribution and the recovery (uniform) spin prior will introduce a bias in EoS parameters through the χ-η correlation.

11.7.2   Treatment of PE method as an unbiased estimator

Starting with a given prior p.d.f., the product of our PE method is a sequence of p.d.f.s on the space of global EoS parameters. The main aim of such inference methods is to deliver fast convergence and posterior consistency, *i.e.* the posterior p.d.f.s should converge to a highly peaked distribution around the "true value" predicted by the underlying model (if such a point exist); if the underlying model provides an *underlying distribution* rather than a single value, then the sequence

of p.d.f.s should converge to that distribution.

Strictly speaking, there is no "true value" for the polynomial coefficients c_0, c_1, c_2, since the Taylor expansion coefficients that were quoted are only local infinitesimal quantities around the reference mass m_0. On the other hand, by applying parameter estimation on each BNS inspiral signal, we probe pairs of points in the m-λ plane, with which we effectively infer an *interpolation* of the underlying $\lambda(m)$ curve. Depending on the distribution of NS masses, a particular region of the mass prior will be probed; such a mass-distribution dependency will result in a posterior distribution which may well deviate from the Taylor expansion values that can be calculated via Eq. (11.14) and Table 11.1. In other words, the PE method is not an *unbiased estimator* of these values[8]. However, within the scope of this study, we will content ourselves with the peak of the distribution converging to the *expectation value* of the underlying distribution on c_j with an increasing accuracy, to the level where the different models are clearly distinguishable from each other.

The expectation value of a mass-dependent parameter θ is defined as its mean value over m_1-m_2 pairs under the underlying mass distribution f

$$\bar{\theta} = \int_{1M_\odot}^{2M_\odot} \mathrm{d}m_1 \int_{1M_\odot}^{2M_\odot} \mathrm{d}m_2 \, \hat{\theta}(m_1, m_2) \, f(m_1) \, f(m_2) \tag{11.23}$$

where by $\hat{\theta}$ we denote the measured value of θ given a pair of masses. For instance, if we used the linear approximation to parameterize the space of EoS models, then a BNS system with $m_1 \neq m_2$ would uniquely define a set of parameters $\{\hat{c}_0, \hat{c}_1\}$; these are the ones that yield a line that passes from the two points on the m-λ plane predicted by the underlying EoS model

$$\hat{c}_0(m_1, m_2) = \lambda(m_2) + \frac{\lambda(m_1) - \lambda(m_2)}{m_1 - m_2}(m_0 - m_2), \tag{11.24}$$

$$\hat{c}_1(m_1, m_2) = \frac{\lambda(m_1) - \lambda(m_2)}{m_1 - m_2}. \tag{11.25}$$

To demonstrate how much the expectation value $\bar{c}_0$ can differ from the corresponding Taylor expansion coefficient, depending on the underlying mass distribution, we plot $\bar{c}_0$ for the Gaussian family of mass distributions in Fig. 11.18. The two axes represent the mean μ_m and standard deviation σ_m of the underlying Gaussian mass distribution $\mathcal{N}(\mu_m, \sigma_m)$, for which the expectation value is calculated. A *uniform* mass distribution is represented as the limit of $\sigma_m \to \infty$ for any value of μ_m, so the top border of the plot, corresponding to $\sigma_m = 1M_\odot$ already gives a good approximation for it; the $N(1.35, 0.05)$ scenario studied above corresponds to the point marked in white. Indeed, we see that the differences between expectation values for different mass distributions are relatively minor, in comparison with the differences between the three EoS models considered. The

---

[8]This is also why one should not expect the posterior to converge to a delta function in the limit of infinitely many detections.
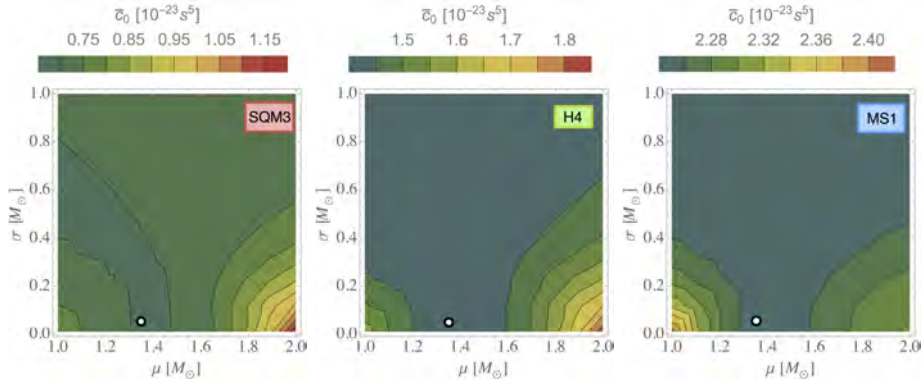
Figure 11.18: *Expectation value for c_0, calculated as in Eq. (11.23), for a population of sources following an underlying Gaussian mass function, as a function of the mean μ_m and standard deviation σ_m and for the three EoS, SQM3 (left), H4 (centre), MS1(right). The uniform distribution MU can be seen as the limit of infinite σ_m and is approximated by the top edge of the plots; the Gaussian distribution MG corresponds to the white mark at $(1.35, 0.05)$.*

Taylor expansion coefficient c_0 for MS1 is $2.248 \times 10^{-23} \mathrm{s}^5$, for H4 $1.409 \times 10^{-23} \mathrm{s}^5$ and for SQM3 $0.694 \times 10^{-23} \mathrm{s}^5$, which are sufficiently close to the expectation values $\bar{c}_0$, as long as the mass function is not highly peaked close to the edges of the mass prior. However, as our inference method combines more and more information from a large number of observations, even these minor differences may give an apparent bias, if the Taylor expansion coefficients are naively interpreted as the "true values" of the models.

11

Chapter 12

Discussion and outlook

12.1 Conclusions

For many decades, the elusive equation of state of neutron star matter has remained one of the biggest open problems of astrophysics. With the detection of GW signals from coalescing NS binaries, we will have a new source of unique information, with which we may probe the NSs' internal structure.

The astrophysicists will thus gain a better understanding of the underlying physical mechanisms that hold a NS together, the composition of NSs, their habits and life cycle, and will be able to collect ''demographics'' on their population throughout the Universe. More information of similar importance can be obtained by detecting GWs sourced by isolated NSs (quakes, mountains, etc.), as well as by observing and correlating simultaneous GW and EM events. Moreover, a possible correlation between GW detection from NS binaries and EM detections of certain types of gamma-ray bursts will shed light on determining the origin of the latter, for which the exact mechanisms are still unknown.

Apart from the impact on astrophysics, by significantly constraining the NS EoS we will also feed invaluable input to nuclear physics community, on the composition and properties of cold matter at a so far inaccessible regime of supranuclear densities. For instance, we may be able to give answers to: whether a phase transition takes place, of what type and at what densities; whether our observations are compatible with different matter compositions, the formation of condensates,

the presence of Kaons, Hyperons, etc.; whether any of our theoretical approaches to nuclear interactions are indeed valid in this high-density regime. It could also reveal a long sought for connection between NS binary coalescence and a nuclear process of rapid neutron capturing, known as the *r-process*. The extreme conditions during a BNS merger may provide a fertile environment for nuclei of heavy isotopes to be formed by means of the r-process. If sufficient fraction of the mass escapes as ejecta, then the population of BNS mergers (together with core-collapse supernovae) could account for the missing part of the observed abundances of some heavy isotopes in our Universe. And of course it may well be that NS matter is not the ultimate final state before gravitational collapse into a black hole. Indications of the existence of an even more compact or exotic kind of stellar object (*e.g.* a *boson star*) could pave the way for a series of unexpected discoveries in the future.

Knowledge of the NS EoS will also open new horizons for cosmology, by establishing BNS systems as *self-calibrating standard sirens*, with which one will be able to perform simultaneous measurements of luminosity distances and redshifts. These measurements will have direct implications to cosmography and cosmology, providing us with a new independent way of estimating the parameters of the standard cosmological model, free of the intrinsic systematics of the cosmic distance ladder. This kind of analysis was put forward by Messenger & Read [261] and was further explored recently in [153], where the authors find that the knowledge of the NS EoS allows to measure the Hubble parameter H_0, the matter energy parameter Ω_m and the dark energy parameter Ω_Λ – the basic ingredients of the Friedman equation in a ΛCDM cosmology.

In this part of the dissertation we developed and studied Bayesian analysis methods in a realistic setting, in order to obtain a realistic estimate of the potential of EoS inference with the upcoming network of AdVirgo and aLIGO detectors.

Hypothesis ranking   The first is a hypothesis ranking method, based on Bayesian model selection within a set of competing candidate EoS models. It is shown that this method seems to be giving results that converge towards favouring the true underlying EoS model as the number of analyzed signals increases, and that the ranking also respects the order of "stiffness" in the set of candidate models. There are however cases where the convergence is not as fast as one would hope for. To a certain extent, this is due to a combination of inherent uncertainties of different origins, the control of which could lead to a more efficient performance with faster convergence. Apart from the expected statistical uncertainties due to noise, a very prominent source of uncertainty is of numerical origin. Let us recall that the essence of this method is the calculation of Bayes factors for the signal hypotheses for a number of different EoS models. Now, the numerical calculation of the evidence integral with nested sampling is subject to errors, which may be non-negligible in our high-dimensional parameter space. The size of the errors depends on the parameter values chosen for the nasted sampling algorithm, most crucially the number of *live points*, the number of *MCMC points*

and the termination condition. Here we have chosen $N_{\text{live}} = 1024$, $N_{\text{MCMC}} = 200$ and $dZ = 0.1$. In Fig. 4 of Veitch & Veccio (2009) [366], the authors show how the standard deviation of a $\log B$ calculation varies with the number of live points and MCMC points used. For our choices the standard deviation is estimated to be of $\mathcal{O}(1)$; moreover, it would need $\sim 10^4$ live points and at least 500 MCMC points in order to reach a desirable error of less than 0.1. However, given the large amount of simulations that needed to be run in order to obtain sufficiently good statistics, such an increase in either N_{live} or N_{MCMC} would significantly increase the computational cost. Of course, in a real-life analysis, one will only need to perform a small set of runs per detected signal, and will thus have enough resources to increase one's performance goal.

Parameter estimation In the second method the space of EoS was parametrized based on the shape of the $\lambda(m)$ function, so that Bayesian parameter estimation would produce posterior p.d.f.s and put constraints on the EoS parameters space. This method is able to distinguish between typically soft, medium and stiff EoS after combining information from a few tens of sources. In the chosen parametrization, where the $\lambda(m)$ function is represented by a parabola, most of the information is channeled into the posterior of c_0, the zeroth order coefficient which gives the value of λ at $1.4\,M_\odot$. Even this piece of information alone can significantly constrain the NS EoS and rule out the majority of currently competing models. As seen in the plots of Sec. 11.5.2, the 95% confidence regions of the posterior p.d.f. shrink as more sources are detected and tend to peak around the expected value.

Functional Inference A third road to the neutron star EoS, a Bayesian *non-parametric* method, is currently under development and is described in Appendix C. The purpose of this third, more generic method is to infer the functional dependence of λ on m, without restricting to a certain parametrization scheme. Instead it makes use of any piece of information that each source provides for the value of λ over any given mass m (or mass bin m_i). Therefore, depending on the underlying mass distribution, mass regions that are probed better will yield a more informative λ posterior p.d.f., while results are more uncertain in mass regions where less NS are found.

A source of systematic errors, which is common to all three methods, is related to the underlying distribution of NS masses and was discussed in Sec. 11.7.1. An interesting workaround consists in folding in information from the already analyzed signals, and updating the mass prior p.d.f. every time a new source is detected. This parallel inference on the underlying distribution of masses would be the object of a Bayesian non-parametric study and is left for future work.

An interesting question arises when one considers the possibility of there being more than one population of NS that, due to a certain divergence in their evolutionary paths, may be described by different EoS (*i.e.* by multi-branched $P(\rho)$,

$M(R)$, $\lambda(m)$ functions). This scenario is possible and has been considered in theoretical studies (and also encompasses the possibility of there being a very light BH population, within the NS mass range). The question is then, if such a multi-branched scenario exists, *e.g.* featuring two distinct populations of NSs, would it manifest itself in the above methods? Clearly, the results given by the HR method could reveal no such information, unless of course that particular multi-branched EoS is explicitly prescribed as a candidate model. With the PE method, one would expect to find such evidence in the form of a persistent multi-modal posterior p.d.f., given enough detections that would statistically cover both populations. The relative posterior weights of the peaks would then reflect the relative abundancy of BNS systems whose components belong to either branch. However, information from systems where the two populations mix will be difficult to interpret. Finally, the non-parametric FI method would directly reveal two distinct branches in the $\lambda(m)$ posterior plot. Such a population study is outside the scope of this dissertation but is worth mentioning nonetheless.

12.2   Future avenues

Arbitrary spins   The current studies started in a proof-of-principle setting, where only non-spinning NS were considered, and were extended to a setting where spins were aligned or anti-aligned with orbital angular momentum. Naturally, the next stage would be to completely discard any restriction on the spin direction (while keeping the spin magnitudes at astrophysical realistic values), which would also allow for precessional effects to kick in. Such an extension will have consequences on our inference that are twofold: On the one hand, the parameter space will be largely extended and, given the correlations between parameters at high-PN orders, the statistical uncertainties for any Bayesian method are expected to grow. On the other hand, allowing for precession to take place will give additional structure to the waveform, especially through amplitude modulation; this will help in lifting any degeneracies between spin parameters and mass or matter-related parameters. Therefore, for recovery one should employ a template family that captures well the principal features of precession in the waveform.

Input from numerical relativity simulations   Significant amount of work has been devoted to studying high-order effects that appear towards the end of the inspiral, as well as the merger and post-merger behaviour of BNS systems, using Numerical Relativity (NR) waveforms [309, 307, 72, 57, 345, 305, 202, 203]. The production of such waveforms relies on computationally heavy simulations, which can currently cover a few tens of cycles prior to merger. Even though the magnitude of EoS-related effects during the early inspiral is believed to be reliably estimated by the existing analytical methods [147, 307, 203], a detailed comparison with accurate solutions from NR simulations, where no approxima-

tions need to be considered, is in order. More importantly, the discrepancy between the point-particle parts of different PN approximants at high frequencies, where tidal effects yield the best part of their signal, may lead to serious biases when trying to infer the EoS; this was already mentioned in [200] and was explicitly demonstrated in [372]. Furthermore, the non-linear behaviour of tidal effects becomes increasingly important towards the end of the inspiral and needs to be further investigated both analytically and numerically, for different EoS models. Therefore, it will be of great benefit for the robustness of any inference method to obtain reliable inspiral waveforms with input from NR simulations. As a bonus, a systematic study with NR waveforms will also allow us to fold in information from the post-merger phase. Independent studies [72, 345] have shown that the post-merger spectrum can reveal characteristic peaks that are related to matter effects and are sensitive to the EoS. A detailed investigation towards this direction is currently under way. Finally, a coincident or subsequent EM observation of a burst and the expected afterglow, coming from the environment of the merger and the ejected mass, will also hold information related to the EoS, as shown e.g. in [347, 204].

Importance of high-frequency sensitivity: squeezed light In Sec. 11.6, it was shown how potentially useful information is suppressed due to the limited detector sensitivity at high frequencies. The noise curves used for the current study correspond to the SR (AdVirgo) and ZDHP (aLIGO) configurations for a network of three second generation interferometers at design sensitivity. There is however the prospect for further improvement of the sensitivity at high frequencies, by implementing the quantum-enhancing technology of *squeezed light* [4]. For a certain set of sources such a modification may actually decrease the observed SNR, due to a noise increase at low frequencies. However, this may eventually be avoided by implementing frequency-dependent squeezing [225]. In any case, the re-distribution of sensitivity will surely enhance tidal-related measurements. In Fig. 12.1 we compare both the corresponding noise PSDs and the non-normalized number of useful cycles of the tidal phase for a $(1.4, 1.4)M_\odot$ BNS system at 100 Mpc, when a single advanced detector is used with and without sqeezed light.

Einstein Telescope The next generation of gravitational wave detectors is already under investigation. A comprehensive design study document was published in 2011 [1] describing the Einstein Telescope (ET), a proposed third generation underground cryogenic GW detector, consisting of three V-shaped co-located interferometers. The advanced technology that will be used for ET will lead to an improvement in sensitivity over the second generation of detectors by almost an order of magnitude overall, and even more at low frequencies. The left plot of Fig. 12.1 shows the expected noise PSD in comparison with those of AdVirgo and aLIGO and their squeezed-light upgrades. Such an improvement in sensitivity will dramatically increase the detection rate for coalescing compact binaries (with a BNS reach in the order of a Gpc), it will give a fairly large number of high-

12
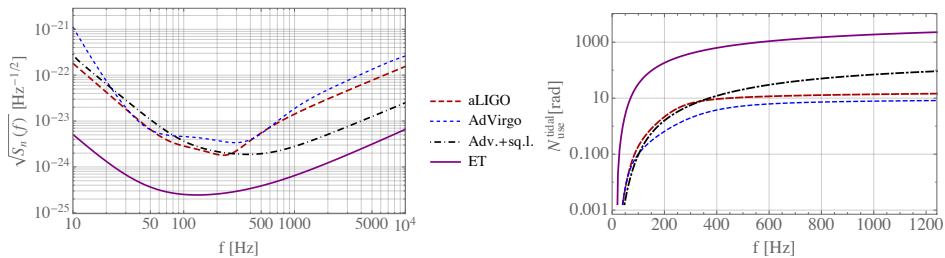
Figure 12.1: *Left: Noise PSDs for AdVirgo and aLIGO, their squeezed light upgrade, and Einstein Telescope. The gain in the high frequency band is clearly visible. Right: Number of useful tidal cycles for the same set of detectors, for a $(1.4, 1.4)M_\odot$ BNS inspiral at a distance of $100\,\mathrm{Mpc}$. The high-frequency upgrades are expected to significantly increase the sensitivity to EoS signatures in the waveform.*

SNR detections per year, and will give an overall boost to our EoS-measuring capabilities. On the right plot of Fig. 12.1 we also see the non-normalized number of useful tidal cycles for a $(1.4, 1.4)M_\odot$ BNS system at 100 Mpc as detected by ET. Preliminary studies indicate that with a couple of months' worth of ET data, the EoS parameters can be constrained with a $\sim 10\%$ accuracy. Finally, ET will be able to carry out the task of constraining cosmological parameters with thousands of BNS inspirals being detected over the course of a few years of operation.

Appendices

Post-Newtonian equations of motion

In the post-Newtonian approximation the equations of motion for the two-body problem in the center-of-mass frame take the form

$$\frac{\mathrm{d}\vec{v}}{\mathrm{d}t} = -\frac{GM}{\|\vec{x}\|^2}\left[(1+A)\hat{x} + B\,\vec{v}\right] + O\left(\frac{1}{c^8}\right). \tag{A.1}$$

Here, $\vec{v} = \dot{\vec{x}}$ is the velocity related to the separation vector $\vec{x} = \vec{x}_1 - \vec{x}_2$ between the two point masses. The quantities A and B have been calculated to 3.5PN order [88] and are explicitly given by the following expressions

$$
\begin{aligned}
A = {}& \frac{1}{c^2}\left\{-\frac{3\dot{r}^2\eta}{2} + v^2 + 3\eta v^2 - \frac{GM}{r}(4+2\eta)\right\} \\
&+ \frac{1}{c^4}\left\{\frac{15\dot{r}^4\eta(1-3\eta)}{8} - \frac{9\dot{r}^2\eta v^2}{2} + 6\dot{r}^2\eta^2 v^2 + 3\eta v^4 - 4\eta^2 v^4\right. \\
&\qquad \left. + \frac{GM}{r}\left[-\dot{r}^2(2+25\eta+2\eta^2) + \left(-\frac{13\eta}{2}+2\eta^2\right)v^2\right] + \frac{G^2M^2}{r^2}\left(9+\frac{87\eta}{4}\right)\right\} \\
&+ \frac{1}{c^5}\left\{-\frac{GM}{r}\dot{r}v^2\frac{24\eta}{5} - \frac{G^2M^2}{r^2}\dot{r}\frac{136\eta}{15}\right\} \\
&+ \frac{1}{c^6}\left\{\dot{r}^6\left(\frac{-35\eta}{16}+\frac{175\eta^2}{16}-\frac{175\eta^3}{16}\right) + \dot{r}^4 v^2\left(\frac{15\eta}{2}-\frac{135\eta^2}{4}+\frac{255\eta^3}{8}\right)\right. \\
&\qquad + \dot{r}^2 v^4\left(-\frac{15\eta}{2}+\frac{237\eta^2}{8}-\frac{45\eta^3}{2}\right) + v^6\left(\frac{11\eta}{4}-\frac{49\eta^2}{4}+13\eta^3\right) \\
&\qquad + \frac{GM}{r}\left[\dot{r}^4\left(79\eta-\frac{69\eta^2}{2}-30\eta^3\right) + \dot{r}^2 v^2\left(-121\eta+16\eta^2+20\eta^3\right)\right. \\
&\qquad\quad \left. + v^4\left(\frac{75\eta}{4}+8\eta^2-10\eta^3\right)\right] \\
&\qquad + \frac{G^2M^2}{r^2}\left[\dot{r}^2\left(1+\frac{32573\eta}{168}+\frac{11\eta^2}{8}-7\eta^3+\frac{615\eta\pi^2}{64}-110\eta\ln\left(\frac{r}{r_0'}\right)\right)\right.
\end{aligned}
$$

A

$$+v^2\left(-\frac{26987\eta}{840}+\eta^3-\frac{123\eta\pi^2}{64}+22\eta\ln\left(\frac{r}{r_0'}\right)\right)\Big]$$

$$+\frac{G^3M^3}{r^3}\left[-16-\frac{437\eta}{4}-\frac{71\eta^2}{2}+\frac{41\eta\pi^2}{16}\right]\Big\}$$

$$+\frac{1}{c^7}\left\{\frac{GM}{r}\left[112\eta\dot{r}^5-\dot{r}^3v^2\left(114\eta+12\eta^2\right)+\dot{r}v^4\left(\frac{366\eta}{35}+12\eta^2\right)\right]\right.$$

$$+\frac{G^2M^2}{r^2}\left[\dot{r}^3\left(\frac{294\eta}{5}+\frac{376\eta^2}{5}\right)+\dot{r}v^2\left(\frac{692\eta}{35}-\frac{724\eta^2}{15}\right)\right]$$

$$+\frac{G^3M^3}{r^3}\left[\frac{3956\eta}{35}+\frac{184\eta^2}{5}\right]\Big\}, \tag{A.2}$$

$$B=\frac{1}{c^2}\left\{-4\dot{r}+2\dot{r}\eta\right\}$$

$$+\frac{1}{c^4}\left\{\left(\frac{9\eta}{2}+3\eta^2\right)\dot{r}^3-\left(\frac{15\eta}{2}+2\eta^2\right)\dot{r}v^2+\frac{GM}{r}\left(2+\frac{41\eta}{2}+4\eta^2\right)\dot{r}\right\}$$

$$+\frac{1}{c^5}\left\{\frac{8\eta v^2}{5}\frac{GM}{r}+\frac{24\eta}{5}\frac{G^2M^2}{r^2}\right\}$$

$$+\frac{1}{c^6}\left\{15\dot{r}^5\left(-\frac{3\eta}{8}+\eta^2+\frac{\eta^3}{4}\right)+\dot{r}^3v^2\left(12\eta-\frac{111\eta^2}{4}-12\eta^3\right)\right.$$

$$+\dot{r}v^4\left(-\frac{65\eta}{8}+19\eta^2+6\eta^3\right)$$

$$+\frac{GM}{r}\left[\dot{r}^3\left(\frac{329\eta}{6}+\frac{59\eta^2}{2}+18\eta^3\right)-\dot{r}v^2\left(15\eta+27\eta^2+10\eta^3\right)\right]$$

$$+\frac{G^2M^2}{r^2}\dot{r}\left[-4-\frac{18169\eta}{840}+25\eta^2+8\eta^3-\frac{123\eta\pi^2}{32}+44\eta\ln\left(\frac{r}{r_0'}\right)\right]\Big\}$$

$$+\frac{1}{c^7}\left\{\frac{GM}{r}\left[-v^4\left(\frac{626\eta}{35}+\frac{12\eta^2}{5}\right)+\dot{r}^2v^2\left(\frac{678\eta}{5}+\frac{12\eta^2}{5}\right)-120\eta\dot{r}^4\right]\right.$$

$$+\frac{G^2M^2}{r^2}\left[v^2\left(\frac{164\eta}{21}+\frac{148\eta^2}{5}\right)-\dot{r}^2\left(\frac{82\eta}{3}+\frac{848\eta^2}{15}\right)\right]$$

$$+\frac{G^3M^3}{r^3}\left(-\frac{1060\eta}{21}-\frac{104\eta^2}{5}\right)\Big\}. \tag{A.3}$$

A

Modeling the neutron star equation of state

B.1 Statistical physics reminder

In a relativistic context it is instructive to describe all thermodynamic quantities in a local inertial frame, *comoving* with the fluid. This is known as the *Local Comoving Lorentz Frame* (LCLF). In the LCLF we define the *baryon density* n, the *total energy density* ε and *entropy density* s, the *energy per baryon* $\frac{\varepsilon}{n}$ and *entropy per baryon* $\frac{s}{n}$. The first law of thermodynamics then gives:

$$\eth Q = \mathrm{d}\left(\frac{\varepsilon}{n}\right) + P\,\mathrm{d}\left(\frac{1}{n}\right)\,, \tag{B.1}$$

where $\eth Q$ is the amount of heat transferred into the system, P is the pressure and $\frac{1}{n}$ is the volume per baryon. For a fluid element in equilibrium at temperature T we also have:

$$\eth Q = T\,\mathrm{d}s \Rightarrow \mathrm{d}\left(\frac{\varepsilon}{n}\right) = -P\,\mathrm{d}\left(\frac{1}{n}\right) + T\,\mathrm{d}s\,. \tag{B.2}$$

The energy density is then a function of number density and entropy density: $\varepsilon = \varepsilon(n, s)$. For *multi-component systems*, where m different species of particles co-exist, with number densities n_i and *concentrations*

$$Y_i = \frac{n_i}{n}\,, \qquad i = 1,\ldots,m\,. \tag{B.3}$$

Note that concentrations sum to unity and the total energy density is now $\varepsilon = \varepsilon(n_i, s)$ or equivalently $\varepsilon = \varepsilon(Y_i, n, s)$, and Eq. (B.2) becomes:

$$\mathrm{d}\left(\frac{\varepsilon}{n}\right) = -P\,\mathrm{d}\left(\frac{1}{n}\right) + T\,\mathrm{d}s + \sum_i \mu_i \mathrm{d}Y_i\,, \tag{B.4}$$

where μ_i is the *chemical potential* for the species i, the quantity that defines the energy contribution per particle addition and thus regulates the abundance of the species. For instance, in NS formation models, where the produced neutrinos

propagate freely and are free to escape to infinity, the corresponding chemical potential would be $\mu_{\nu_i} = 0$ for neutrinos of any flavour ($i = e, \mu, \tau$).

We now have a definition for the statistical conjugates to the state functions $1/n$, s, Y_i:

$$P = n^2 \frac{\partial(\varepsilon/n)}{\partial n} \qquad \text{(volume conjugate)} \qquad \text{(B.5)}$$

$$T = \frac{\partial(\varepsilon/n)}{\partial s} \qquad \text{(entropy conjugate)} \qquad \text{(B.6)}$$

$$\mu_i = \frac{\partial(\varepsilon/n)}{\partial Y_i} = \frac{\partial \varepsilon}{\partial n_i} \qquad \text{(species concentration conjugate)}. \qquad \text{(B.7)}$$

B.2 Models

B.2.1 Preliminaries

Starting from the simple model of a completely degenerate ideal Fermi gas in equilibrium, and by gradually introducing non-trivial components to the system, we will show a number of theoretically predicted equations of state by explicitly calculating expressions for the state functions of density, energy and pressure. In Appendix B.1, the reader will find a brief overview of the basics of statistical physics and thermodynamics that are necessary to describe the properties of matter in thermodynamic equilibrium.

We recall that for a particle species i with degeneracy factor (number of polarizations) g_i, and number density in phase space $\frac{d\mathcal{N}_i}{d\mathcal{V}_{\mathrm{ph}}}$, the *distribution function* f_i plays the role of the dimensionless probability density of the species in phase space and is defined as

$$\frac{d\mathcal{N}_i}{d\mathcal{V}_{\mathrm{ph}}} = \frac{g_i}{h^3} f_i(\vec{x}, \vec{p}, t) \,, \qquad \text{(B.8)}$$

where h is Planck's constant. Then the number density of the species gives the normalization of the distribution function:

$$n_i = \int \frac{g_i}{h^3} f_i(\vec{x}, \vec{p}, t) \mathrm{d}^3 p \,, \qquad \text{(B.9)}$$

The species' state functions such as the *energy* density ϵ and the *pressure* P are given by

$$\epsilon_i(\vec{x}, t) = \int E \frac{g_i}{h^3} f_i(\vec{x}, \vec{p}, t) \mathrm{d}^3 p \,, \qquad \text{(B.10)}$$

$$P_i(\vec{x}, t) = \frac{1}{3} \int p v \frac{g_i}{h^3} f_i(\vec{x}, \vec{p}, t) \mathrm{d}^3 p \,. \qquad \text{(B.11)}$$

The ideal Fermi gas The ideal fermi gas is a physical description of a fluid of a given density, consisting of non-interacting fermions at a given temperature T. Thermodynamically, its distribution function at equilibriium is governed by the Fermi-Dirac probability density function,

$$f(E) = \frac{1}{e^{\frac{(E-\mu)}{kT}} + 1} \,. \tag{B.12}$$

The Fermi energy $E_F = \mu$ is determined by the *chemical potential* μ and the *Fermi momentum* is defined via the dispersion relation:

$$p_F = \frac{\sqrt{E_F^2 - m^2 c^4}}{c^2} \,. \tag{B.13}$$

Alternatively the dimensionless *relativity parameter* $x = \frac{p}{mc^2}$ is often used.

The two asymptotic limits of low and high temperature give:

$T = 0$ the completely degenerate ideal Fermi gas:

$$f(E) = \left\{ \begin{array}{ll} 1, & \text{if } E \leq E_F \\ 0, & \text{if } E > E_F \end{array} \right. , \tag{B.14}$$

$kT \gg \mu$ the Maxwell-Boltzmann distribution:

$$f(E) \propto e^{\frac{\mu - E}{kT}} \,. \tag{B.15}$$

B.2.2 Simple EoS models

In the most simplified model for neutron stars, one considers a degenerate gas of non-interacting neutrons, which will indeed, at high densities, dominate the pressure and energy density of the star. Here we continue the discussion of Section 10.1.1 in more detail. Assuming a completely degenerate (cold) Fermi gas of neutrons, the distribution function of Eq. (B.14), combined with Eq. (B.10) and (B.11) gives:

$$\varepsilon_n = \frac{m_n^4 c^5}{3 \hbar^3} \chi(x_{n,F}) \,, \quad P_n = \frac{m_n^4 c^5}{3 \hbar^3} \phi(x_{n,F}) \,, \tag{B.16}$$

where we have defined the dimensionless functions:

$$\chi(x) = \frac{1}{8\pi^2} \left[x\sqrt{1 + x^2} \left(\frac{2x^2}{3} - 1 \right) + \ln(x + \sqrt{1 + x^2}) \right] \,, \tag{B.17}$$

$$\phi(x) = \frac{1}{8\pi^2} \left[x\sqrt{1 + x^2} \left(1 + 2x^2 \right) - \ln(x + \sqrt{1 + x^2}) \right] \,. \tag{B.18}$$

A closer look at Eq. (B.16) reveals that a self gravitating configuration of a neutron Fermi gas can sustain a much more compact structure than what the

B

electron gas could. Quite interestingly, in this model, one gets a *polytropic* form for the EoS:

$$P = K \rho_0^{\Gamma} \tag{B.19}$$

whose validity will of course be restricted to a particular density range.

For the ideal neutron Fermi gas the *polytropic coefficients* Γ and K can be calculated in the relativistic and non-relativistic limits:

- Non-relativistic neutron gas, $\rho_0 \ll 6 \times 10^{15}$ g cm^{-3}:

$$\Gamma = \frac{5}{3} \,, K = \frac{3^{2/3} \pi^{4/3} \hbar^2}{5 \, m_n^{8/3}} = 5.38031 \times 10^3 \, \mathrm{kg}^{-2/3} \, \mathrm{m}^4 \, \mathrm{s}^{-2} \tag{B.20}$$

- Ultra relativistic neutron gas, $\rho_0 \gg 6 \times 10^{15}$ g cm^{-3}:

$$\Gamma = \frac{4}{3} \,, K = \frac{3^{1/3} \pi^{2/3} \hbar c}{4 \, m_n^{4/3}} = 1.22928 \times 10^{10} \, \mathrm{kg}^{-1/3} \, \mathrm{m}^3 \, \mathrm{s}^{-2} \tag{B.21}$$

For a typical NS, densities are expected to be restricted to values where the neutron gas is essentially nonrelativistic. [1]

B.2.3 EoS at low densities

Here, we continue the discussion of Section 10.1.2 on the *inverse β-decay* in more detail.

Inverse β-decay   Assuming a mixture of the three basic particles e, p, n, that make up all of regular matter, one may derive the conditions of detailed balance for the reaction

$$n^0 + \nu_e \rightleftharpoons p^+ + e^- \tag{B.22}$$

which is an amphidirectional version of the familiar β-decay (in which an anti-neutrino is found on the RHS instead). The outcome will depend on the current state variables of the system, while it is evident that the natural direction of the reaction is to the right, due to the rest-mass difference between m_n and $m_p + m_e$. In a high-density environment however, where the electron Fermi energy is high enough and where the electron fluid is highly degenerate, each additional electron would contribute an energy larger than its rest mass by roughly E_F, due to the Pauli exclusion principle. When working with neutron stars, all three species will be in a highly degenerate state and –electrostatic and nuclear interactions aside– will behave as ideal Fermi gases.

---

[1] By contrast, an electron gas becomes relativistic at much lower densities, $\rho_0 > 10^7$ g cm^{-3}.

In equilibrium, where additionally we consider $ds = 0$ and $dn = 0$, we get from Eq. (B.4) $\sum_i \mu_i dY_i = 0$ and, given that neutrinos can escape freely from the system, we also have $\mu_{\nu_e} = 0$, so:

$$\mu_n = \mu_e + \mu_p \,. \tag{B.23}$$

Furthermore, charge neutrality implies that:

$$n_e = n_p \Rightarrow p_{e,F} = p_{p,F} \Rightarrow m_e \, x_{e,F} = m_p \, x_{p,F} \,. \tag{B.24}$$

Thus the unknown parameters reduce to a single unknown chemical potential, or relativistic parameter x. By combining Eq. (B.23), (B.13) and (B.24), one arrives at the equation of state via the parametric equations:

$$P = \frac{c^5}{\hbar^3} \left[m_n^4 \, \phi(x_{n,F}(x)) + m_p^4 \, \phi(x_{p,F}(x)) + m_e^4 \, \phi(x_{e,F}(x)) \right] \,, \tag{B.25}$$

$$\varepsilon = \frac{c^5}{\hbar^3} \left[m_n^4 \, \chi(x_{n,F}(x)) + m_p^4 \, \chi(x_{p,F}(x)) + m_e^4 \, \chi(x_{e,F}(x)) \right] \,, \tag{B.26}$$

$$n = \frac{2c^3}{3\pi^2 \hbar^3} \left[m_n \, x_{n,F}(x) + m_p \, x_{n,F}(x) \right] \tag{B.27}$$

By setting $x_n = 0$ we obtain the threshold values when neutrons start to appear, in which case Eq. (B.23), combined with Eq. (B.24) and (B.27) yields a baryon (proton) density of $n(x_{n=0}) \simeq 7.352 \times 10^{30} \text{cm}^{-3}$, or a mass density $\rho_0(x_n = 0) \simeq 1.230 \times 10^7 \text{g cm}^{-3}$. The general solution above this threshold density gives the proton-to-neutron ratio shown in Fig. B.1, where we see that the ratio decreases to a minimum before increasing to the asymptotic value $\frac{1}{8}$ in the limit of infinite momentum/density.
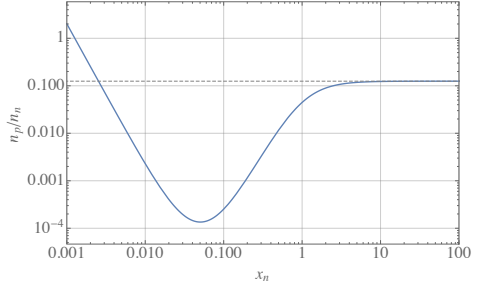
Figure B.1: *Proton-neutron ratio as a function of neutron relativistic parameter x_n. Asymptotic value is $n_p/n_n = 1/8$, while a global minimum is reached at $x_n = 5.04055 \times 10^{-2}$, $n_p/n_n = 1.35726 \times 10^{-4}$.*

B

B

Functional Inference: a third road to the NS EoS

C.1 Functional Inference: Method

Let us now discuss a third Bayesian method with which we attempt to directly infer the functional form of $\lambda(m)$, which characterizes the EoS. It is a non-parametric Bayesian inference method, in the sense that the EoS will not be described/modelled by a particular parametrized family as was done in Sec. 3.4.2; instead, the inference will be made on the full space of functions. The observable in this case is the function $\lambda(m)$ itself, rather than a set of real-valued parameters.

Again, the output that contains the information for a source s is the *posterior* p.d.f., which in this case will be marginalized over all binary parameters except for the masses m_A and tidal deformabilities λ_A,

$$p(m_1, m_2, \lambda_1, \lambda_2 | d, \mathcal{I}).$$

The intermediate product that we wish to derive for a given detection, is a family of posterior p.d.f.s, $p_m(\lambda | d, \mathcal{I})$, which, for each mass value m (or mass *bin*), yields a probability distribution on the value of λ, given the data d of a single source. Then, we shall make use of Bayes' law for each member of the family, as was done in Sec. 11.5 in order to make it possible to combine information from multiple sources

$$p_m(\lambda | d, \mathcal{I}) \quad = \quad \frac{p_m(d | \lambda, \mathcal{I}) p_m(\lambda | \mathcal{I})}{p_m(d | \mathcal{I})} \ . \tag{C.1}$$

Each such posterior p_m is expected to converge to a δ-function centered around the true value of λ over m, as predicted by the underlying EoS.

Naturally, not all sources can give the same amount of information (if any) for each mass or mass bin considered. Indeed, given an observation of a source i, the

Appendix C. Functional Inference: a third road to the NS EoS

posterior density $p_m(\lambda|d,\mathcal{I})$ over a mass m is given by the marginalization

$$p_m(\lambda|d,\mathcal{I}) = \sum_{m_i} p_m(\lambda_i|m_i, d_i, \mathcal{I})\, p(m_i|d_i, \mathcal{I})\,, \tag{C.2}$$

where by i we index a particular NS, and where $p(m_i|d_i, \mathcal{I})$ is simply the marginalized posterior of the NS mass. The first factor $p_m(\lambda_i|m_i, d_i, \mathcal{I})$ represents the posterior p.d.f. of λ over m, given the observed data d_i and the knowledge that the mass of the NS is equal to m_i. It can be argued that the set of all realistic EoS predicts a correlation between values of λ over neighbouring masses. At this stage we will not take such correlations into account; we will also consider mass bins that are wide enough

Now we consider two different cases that apply in the limit of no prior correlations between the values of λ at different masses:

- If $m_i \in m$, then clearly we have $p_m(\lambda|m_i, d_i, \mathcal{I}) = p^{(i)}(\lambda_i|m_i, d_i, \mathcal{I})$.

- If $m_i \notin m$, then we have no information over m and the prior is returned: $p_m(\lambda|m_i, d_i, \mathcal{I}) = p_m(\lambda|\mathcal{I})$.

In the continuum limit the marginalization is given by

$$p_m(\lambda|d_i, \mathcal{I}) = \int \mathrm{d}m_i\, p_m(\lambda|m_i, d_i, \mathcal{I})\, p(m_i|d_i, \mathcal{I})\,, \tag{C.3}$$

and in the limit of no correlations between the values of λ at different masses, the first factor limits to a $\delta(m_i - m)p^{(i)}(\lambda_i|m_i, d_i, \mathcal{I})$. In practice however, the continuous mass variable is grouped into bins, and thus for data analysis purposes the categorical expression is more appropriate. Furthermore, there do exist correlations between the values of λ at different masses, since for example (due to physical restrictions) $\lambda(m)$ needs to be a continuous function that cannot vary too wildly as the mass varies. Then one may define a correlation function $C_\lambda(m; m')$ that acts as a kernel that propagates information of $p(\lambda|m', d, \mathcal{I})$ from the neighbouring points of m to $p_m(\lambda|d, \mathcal{I})$. This however will not be quantified here and is deferred for a future study.

The above expressions hold for example in the case of a NSBH binary system, where information on the tidal parameter λ is obtained from a single NS component per source. Some modification is required when BNS systems are considered, since for each source s that is associated with a given data set d_s, there are two pairs of m and λ parameters, one for each component NS. Eqn. Eq. (C.2) is modified to a marginalization over the m_1 - m_2 plane:

$$p_m(\lambda|d,\mathcal{I}) = \sum_{m_1, m_2} p_m(\lambda|m_1, m_2, d, \mathcal{I})\, p(m_1, m_2|d, \mathcal{I})\,, \tag{C.4}$$

C

where $p(m_1, m_2|d, \mathcal{I})$ is the marginalized 2D posterior of the component masses. Here the factor $p_m(\lambda|m_1, m_2, d, \mathcal{I})$ represents the posterior p.d.f. of λ over m, given the observed data d from a BNS source and the knowledge that the component masses are equal to m_1 and m_2. We consider four cases regarding the values of m_1, m_2 with respect to m:

- $m_1 \in m$, $m_2 \notin m$: then $p_m(\lambda|m_1, m_2, d, \mathcal{I}) = p(\lambda_1 = \lambda|m_1, m_2, d, \mathcal{I})$

- $m_1 \notin m$, $m_2 \in m$: then $p_m(\lambda|m_1, m_2, d, \mathcal{I}) = p(\lambda_2 = \lambda|m_1, m_2, d, \mathcal{I})$

- $m_1 \notin m$, $m_2 \notin m$: then the prior is returned, $p_m(\lambda|m_1, m_2, d, \mathcal{I}) = p(\lambda|m, \mathcal{I})$

- $m_1 \in m$, $m_2 \in m$: then we assign

$$p_m(\frac{\lambda_1 + \lambda_2}{2}|m_1, m_2, d, \mathcal{I}) = p(\frac{\lambda_1 + \lambda_2}{2}|m_1, m_2, d, \mathcal{I})$$

The last case is the less trivial one. It corresponds to both masses of the posterior point taking values within the same mass bin m, in which case we can assume $m_1 \simeq m_2$. But if the masses are the same, then this implies $\lambda_1 \simeq \lambda_2$, which is generally not satisfied by the posterior points. However, from the expression Eq. (2.56) giving the tidal contribution to the phase, we observe that when $\eta = 0.25$, $X_A = 0.5$, the resulting contribution *in each PN order* is of the form $(\lambda_1 + \lambda_2)$ times a constant. Therefore, when $m_1 = m_2$, there exists a 1-dimensional degeneracy in the λ_1-λ_2 plane, in the calculation of the waveform (and therefore the likelihood) and thus, we are free to choose the only set of values for which the function $\lambda(m)$ is single-valued. This corresponds to the point $(\lambda_1', \lambda_2') = (\frac{\lambda_1 + \lambda_2}{2}, \frac{\lambda_1 + \lambda_2}{2})$.

The above argument does not hold for the QM effects in the phase and the above waveform degeneracy is lifted when these are taken into account. However, as shown in Sec. 11.6, the best part of the information on the EoS comes from the tidal effects and thus, this approximation is well justified.

It is noteworthy that, since the chirp mass $\mathcal{M}_c$ is a very accurately estimated parameter (with a relative error of $O(10^{-3})$), and since

$$\frac{\partial m_1(\mathcal{M}_c, \eta)}{\partial \eta} \leq 0 \,, \ \frac{\partial m_2(\mathcal{M}_c, \eta)}{\partial \eta} \geq 0 \,,$$

it follows that up to a small error,

$$\mathrm{supp}\, p(m_1|d, \mathcal{I}) \cap \mathrm{supp}\, p(m_2|d, \mathcal{I}) = \{1.1487 \bar{\mathcal{M}}_c\} \,, \tag{C.5}$$

where $\bar{\mathcal{M}}_c$ is the estimated peak of the chirp mass posterior, and where the RHS corresponds to the $m_1 = m_2$ value in the equal-mass case, $\eta = 0.25$. In other words, almost the entire m_1 posterior is located at larger masses than the entire

m_2 posterior. This means that the two component NS of each source contribute to (almost) disjoint subsets of the family of posteriors.

The final step is to combine information from multiple observations to obtain the final posterior family of p.d.f.s, $p_m(\lambda|\{d_s\}_{s \in S}, \mathcal{I})$. When combining information from multiple sources $s \in \mathcal{S} = 1, \ldots, N$ one needs to take into account all the possibilities of each of the observed masses $\{m_{s1}, m_{s2}\}_{s \in S}$ being within or outside any of the mass bins considered. Let $m \in I_m$ which represents the family of masses or mass bins, and denote by $p^{(sA)}(\lambda, m|d_s, \mathcal{I})$, $A = 1, 2$ the posterior p.d.f. of $p(\lambda_{sA} = \lambda, m_{sA} = m|d_s, \mathcal{I})$ for the s-th source.

$$
\begin{aligned}
p_m(\lambda|\{d_s\}_{s \in S}, \mathcal{I}) &= \frac{p_m(\{d_s\}_{s \in S}|\lambda, \mathcal{I}) p_m(\lambda|\mathcal{I})}{p_m(\{d_s\}_{s \in S}|\mathcal{I})} \quad (\text{C.6}) \\
&= p_m(\lambda|\mathcal{I}) \prod_{s \in S} \frac{p_m(d_s|\lambda, \mathcal{I})}{p_m(d_s|\mathcal{I})} \\
&= p_m(\lambda|\mathcal{I}) \prod_{s \in S} \frac{p_m(\lambda|d_s, \mathcal{I})}{p_m(\lambda|\mathcal{I})}, \quad \forall m \in I_m.
\end{aligned}
$$

Now, making use of the marginalization process for each source, as described above, we see that when the s-th source is added, the current prior (i.e. the posterior after $s-1$ detections) is updated

- by $p^{(s1)}(\lambda|m_{s1} \in m, d_s, \mathcal{I})/p_m(\lambda|\mathcal{I})$ with a probability weight of $p(m_{s1} \in m|d_s, \mathcal{I})$,

- by $p^{(s2)}(\lambda|m_{s2} \in m, d_s, \mathcal{I})/p_m(\lambda|\mathcal{I})$ with a probability weight of $p(m_{s2} \in m|d_s, \mathcal{I})$, and

- by the identity with a probability weight of $p(m_{s1} \notin m, m_{s2} \notin m|d_s, \mathcal{I})$.

Finally we obtain:

$$
\begin{aligned}
p_m(\lambda|\{d_s\}_{s \in S}, \mathcal{I}) =& p_m(\lambda|\mathcal{I}) \prod_{s \in S} \left[\frac{p^{s1}(\lambda, m|d_s, \mathcal{I})}{p_m(\lambda|\mathcal{I})} \right. \\
&\left. + \frac{p^{s2}(\lambda, m|d_s, \mathcal{I})}{p_m(\lambda|\mathcal{I})} + p(m_{s1} \notin m, m_{s2} \notin m|d_s, \mathcal{I}) \right], \quad (\text{C.7})
\end{aligned}
$$

where we managed to obtain an expression for the combined posterior in terms of the two-dimensional posteriors on the λ-m plane for each component.

C.2 Functional Inference: Preliminary Results

Serving as a proof-of-principle demonstration, some preliminary results are shown in Fig. C.1 after combining information from 30 relatively loud BNS sources
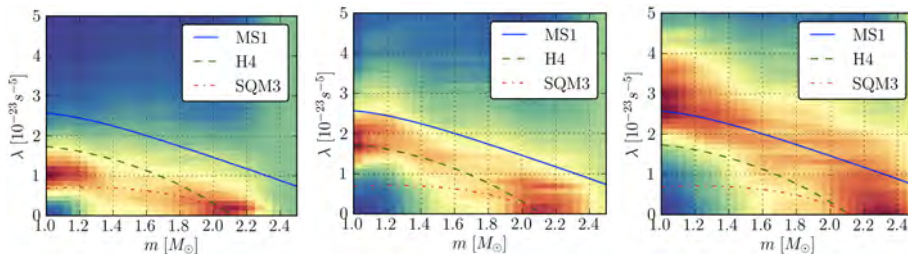
Figure C.1: *Functional inference posterior on $\lambda(m)$ after analyzing a set of 30 BNS sources with one of three EoS: SQM3 (left), H4 (centre) and MS1 (right). The posterior density profile is drawn above each mass bin, with denser regions (red) representing more posterior weight for the corresponding values of λ.*

with $8 < \rho_{\text{net}} < 30$, with the underlying EoS being SQM3 (left), H4 (centre) and MS1 (right). The mass distribution is taken to be uniform in $[1, 2]\, M_\odot$ and the NS components are non-spinning. The template waveforms used for recovery also have spins set to zero but have the tidal deformabilities λ_1 and λ_2 as additional free parameters with a uniform prior in $[0, 5 \times 10^{-23}]\, \text{s}^5$. The posterior probabilities are shown in color and are normalized per mass bin, i.e. for each mass bin m, the posterior p.d.f. of $\lambda(m)$ is drawn on the corresponding column. We clearly see that the posterior densities tend to accumulate around the underlying EoS in each case, so posterior consistency is indeed achieved. [1]

As an additional by-product, one may integrate the posterior probability along each of the candidate EoS in order to obtain a ranking figure of merit:

$$\mathcal{F}_{\text{EoS}} \propto \int \mathrm{d}m \, p_m(\lambda(m; \text{EoS})|\{d_s\}_{s \in S}, \mathcal{I}) \,. \tag{C.8}$$

An arbitrary number of candidate EoS models can thus be directly compared against each other with no extra computational cost. We show results from the analysis of Fig. C.1 in Table C.1, where we see that the candidate models are ranked correctly.

rec \ inj	SQM3	H4	MS1
SQM3	0.628	0.385	0.234
H4	0.547	0.539	0.273
MS1	0.306	0.423	0.489

Table C.1: $\mathcal{F}_{\text{EoS}}$ *scores of the three candidate EoS models after combining 30 BNS sources.*

---

[1]The slight apparent bias towards zero in the can be attributed to the one-sidedness of the contributions of correlations as one approaches the edges of the m-λ plane.

C

BIBLIOGRAPHY

[1] Einstein telescope, design study document. `http://www.et-gw.eu/etdsdocument/`.

[2] The LSC-Virgo White Paper on Gravitational Wave Searches and Astrophysics. 2014. `https://dcc.ligo.org/LIGO-T1400054/public`.

[3] J. Aasi et al. The characterization of Virgo data and its impact on gravitational-wave searches. *Class.Quant.Grav.*, 29:155002, 2012.

[4] J. Aasi et al. Enhancing the sensitivity of the LIGO gravitational wave detector by using squeezed states of light. *Nature Photon.*, 7:613–619, 2013.

[5] J. Aasi et al. Prospects for Localization of Gravitational Wave Transients by the Advanced LIGO and Advanced Virgo Observatories. 2013.

[6] J. Aasi et al. Characterization of the LIGO detectors during their sixth science run. 2014.

[7] J. Aasi et al. Narrow-band search of continuous gravitational-wave signals from Crab and Vela pulsars in Virgo VSR4 data. *Phys. Rev.*, D91(2):022004, 2015.

[8] J. Abadie et al. Calibration of the LIGO Gravitational Wave Detectors in the Fifth Science Run. *Nucl.Instrum.Meth.*, A624:223–240, 2010.

[9] J. Abadie et al. Predictions for the Rates of Compact Binary Coalescences Observable by Ground-based Gravitational-wave Detectors. *Class.Quant.Grav.*, 27:173001, 2010.

[10] J. Abadie et al. Beating the spin-down limit on gravitational wave emission from the Vela pulsar. *Astrophys. J.*, 737:93, 2011.

[11] B. Abbott et al. Beating the spin-down limit on gravitational wave emission from the Crab pulsar. *Astrophys.J.*, 683:L45–L50, 2008.

[12] B. P. Abbott et al. Astrophysical Implications of the Binary Black-Hole Merger GW150914. *Astrophys. J.*, 818(2):L22, 2016.

[13] B. P. Abbott et al. Binary Black Hole Mergers in the first Advanced LIGO Observing Run. 2016.

[14] B. P. Abbott et al. Calibration of the Advanced LIGO detectors for the discovery of the binary black-hole merger GW150914. 2016.

[15] B. P. Abbott et al. Characterization of transient noise in Advanced LIGO relevant to gravitational wave signal GW150914. 2016.

[16] B. P. Abbott et al. GW150914: First results from the search for binary black hole coalescence with Advanced LIGO. 2016.

[17] B. P. Abbott et al. GW150914: Implications for the stochastic gravitational wave background from binary black holes. *Phys. Rev. Lett.*, 116(13):131102, 2016.

[18] B. P. Abbott et al. GW150914: The Advanced LIGO Detectors in the Era of First Discoveries. *Phys. Rev. Lett.*, 116(13):131103, 2016.

[19] B. P. Abbott et al. GW151226: Observation of Gravitational Waves from a 22-Solar-Mass Binary Black Hole Coalescence. *Phys. Rev. Lett.*, 116(24):241103, 2016.

[20] B. P. Abbott et al. Localization and broadband follow-up of the gravitational-wave transient GW150914. *Submitted to: Astrophys. J. Lett.*, 2016.

[21] B. P. Abbott et al. Observation of Gravitational Waves from a Binary Black Hole Merger. *Phys. Rev. Lett.*, 116(6):061102, 2016.

[22] B. P. Abbott et al. Observing gravitational-wave transient GW150914 with minimal assumptions. 2016.

[23] B. P. Abbott et al. Properties of the binary black hole merger GW150914. 2016.

[24] B. P. Abbott et al. Tests of general relativity with GW150914. 2016.

[25] B. P. Abbott et al. The Rate of Binary Black Hole Mergers Inferred from Advanced LIGO Observations Surrounding GW150914. 2016.

[26] T. Accadia et al. Virgo calibration and reconstruction of the gravitational wave strain during VSR1. *J.Phys.Conf.Ser.*, 228:012015, 2010.

[27] T. Adamo and E. Newman. The Kerr-Newman metric: A Review. *Scholarpedia*, 9:31791, 2014.

[28] P. A. R. Ade et al. Planck 2015 results. XIII. Cosmological parameters. 2015.

[29] E. G. Adelberger. New tests of Einstein's equivalence principle and Newton's inverse-square law. *Classical and Quantum Gravity*, 18:2397–2405, July 2001.

[30] S. Adrian-Martinez et al. High-energy Neutrino follow-up search of Gravitational Wave Event GW150914 with ANTARES and IceCube. 2016.

[31] M. Agathos. Operator Product Expansion in 2D Lorentzian Quantum Gravity. *Master Thesis, Utrecht University*, 2011.

[32] M. Agathos, W. Del Pozzo, T. G. F. Li, C. V. D. Broeck, J. Veitch, et al. TIGER: A data analysis pipeline for testing the strong-field dynamics of general relativity with gravitational wave signals from coalescing compact binaries. *Phys.Rev.*, D89(8):082001, 2014.

[33] M. Agathos, W. Del Pozzo, T. G. F. Li, C. van den Broeck, J. Veitch, and S. Vitale. Testing General Relativity Using Gravitational Waves from Binary Neutron Stars: Effect of Spins. In K. Rosquist, editor, *Thirteenth Marcel Grossmann Meeting: On Recent Developments in Theoretical and Experimental General Relativity, Astrophysics and Relativistic Field Theories*, pages 1710–1712, Jan. 2015.

[34] M. Agathos et al. In prep. 2015.

[35] M. Agathos, J. Meidam, W. Del Pozzo, T. G. F. Li, M. Tompitak, et al. Constraining the neutron star equation of state with gravitational wave signals from coalescing binary neutron stars. 2015.

[36] P. Ajith, M. Hannam, S. Husa, Y. Chen, B. Bruegmann, et al. Inspiral-merger-ringdown waveforms for black-hole binaries with non-precessing spins. *Phys.Rev.Lett.*, 106:241101, 2011.

[37] M. Alcubierre. *Introduction to 3+1 Numerical Relativity*. Oxford University Press, 2008.

[38] R. Aldrovandi and J. G. Pereira. *Teleparallel Gravity*. 2013.

[39] M. G. Alford, S. Han, and M. Prakash. Generic conditions for stable hybrid stars. *Phys.Rev.*, D88(8):083013, 2013.

[40] J. Alsing, E. Berti, C. M. Will, and H. Zaglauer. Gravitational radiation from compact binary systems in the massive Brans-Dicke theory of gravity. *Phys.Rev.*, D85:064041, 2012.

[41] L. Amarilla and E. F. Eiroa. Shadow of a Kaluza-Klein rotating dilaton black hole. Phys. Rev. D, 87(4):044057, Feb. 2013.

[42] J. Ambjørn, A. Görlich, J. Jurkiewicz, and R. Loll. *Quantum Gravity via Causal Dynamical Triangulations*, page 723. 2014.

[43] J. Ambjørn and R. Loll. Non-perturbative Lorentzian quantum gravity, causality and topology change. *Nuclear Physics B*, 536:407–434, Dec. 1998.

[44] J. Antoniadis, P. C. Freire, N. Wex, T. M. Tauris, R. S. Lynch, et al. A Massive Pulsar in a Compact Relativistic Binary. *Science*, 340:6131, 2013.

[45] J. Antoniadis, M. van Kerkwijk, D. Koester, P. Freire, N. Wex, et al. The relativistic pulsar-white dwarf binary PSR J1738+0333 I. Mass determination and evolutionary history. *Mon.Not.Roy.Astron.Soc.*, 423:3316, 2012.

[46] T. Appelquist, A. Chodos, and P. Freund. *Modern Kaluza-Klein theories*. Frontiers in physics. Addison-Wesley Pub. Co., 1987.

[47] R. Arnowitt, S. Deser, and C. W. Misner. Dynamical Structure and Definition of Energy in General Relativity. *Physical Review*, 116:1322–1330, Dec. 1959.

[48] K. Arun, A. Buonanno, G. Faye, and E. Ochsner. Higher-order spin effects in the amplitude and phase of gravitational waveforms emitted by inspiraling compact binaries: Ready-to-use gravitational waveforms. *Phys.Rev.*, D79:104023, 2009.

[49] K. Arun, B. R. Iyer, M. Qusailah, and B. Sathyaprakash. Testing post-Newtonian theory with gravitational wave observations. *Class.Quant.Grav.*, 23:L37–L43, 2006.

[50] K. Arun, B. R. Iyer, B. Sathyaprakash, and P. A. Sundararajan. Parameter estimation of inspiralling compact binaries using 3.5 post-Newtonian gravitational wave phasing: The Non-spinning case. *Phys.Rev.*, D71:084008, 2005.

[51] K. G. Arun and A. Pai. Tests of General Relativity and Alternative theories of gravity using Gravitational Wave observations. *Int.J.Mod.Phys.*, D22:1341012, 2013.

Bibliography

[52] G. A. B. Review of Publications- Schwerkraft und Weltall by Pascual Jordan. JRASC, 48:154, Aug. 1954.

[53] W. Baade and F. Zwicky. Cosmic Rays from Super-novae. *Proceedings of the National Academy of Science*, 20:259–263, May 1934.

[54] D. C. Backer and R. W. Hellings. Pulsar timing and general relativity. ARA&A, 24:537–575, 1986.

[55] S. Baessler, B. R. Heckel, E. Adelberger, J. Gundlach, U. Schmidt, et al. Improved Test of the Equivalence Principle for Gravitational Self-Energy. *Phys.Rev.Lett.*, 83:3585, 1999.

[56] L. Baiotti, T. Damour, B. Giacomazzo, A. Nagar, and L. Rezzolla. Analytic modelling of tidal effects in the relativistic inspiral of binary neutron stars. *Phys.Rev.Lett.*, 105:261101, 2010.

[57] L. Baiotti, T. Damour, B. Giacomazzo, A. Nagar, and L. Rezzolla. Accurate numerical simulations of inspiralling binary neutron stars and their comparison with effective-one-body analytical models. *Phys.Rev.*, D84:024017, 2011.

[58] S. Balmelli and P. Jetzer. Effective-one-body Hamiltonian with next-to-leading order spin-spin coupling. *Phys.Rev.*, D91(6):064011, 2015.

[59] E. Barausse and A. Buonanno. Extending the effective-one-body Hamiltonian of black-hole binaries to include next-to-next-to-leading spin-orbit couplings. *Phys.Rev.*, D84:104027, 2011.

[60] E. Barausse, A. Buonanno, and A. Le Tiec. The complete non-spinning effective-one-body metric at linear order in the mass ratio. *Phys.Rev.*, D85:064010, 2012.

[61] B. Barker and R. O'Connell. Effect of the rotation of the central body on the orbit of a satellite. *Phys.Rev.*, D10:1340–1342, 1974.

[62] B. Barker and R. O'Connell. Center of inertia and coordinate transformations in the postNewtonian charged N body problem in gravitation. *J.Math.Phys.*, 20:1427–1434, 1979.

[63] T. W. Baumgarte and S. L. Shapiro. *Numerical Relativity: Solving Einstein's Equations on the Computer.* June 2010.

[64] G. Baym, H. A. Bethe, and C. J. Pethick. Neutron star matter. *Nuclear Physics A*, 175:225–271, Nov. 1971.

[65] I. Bednarek, P. Haensel, J. Zdunik, M. Bejger, and R. Manka. Hyperons in neutron-star cores and two-solar-mass pulsar. *Astron.Astrophys.*, 543:A157, 2012.

[66] J. D. Bekenstein. Relativistic gravitation theory for the MOND paradigm. *Phys.Rev.*, D70:083509, 2004.

[67] K. Belczynski, V. Kalogera, and T. Bulik. A Comprehensive study of binary compact objects as gravitational wave sources: Evolutionary channels, rates, and physical properties. *Astrophys.J.*, 572:407–431, 2001.

[68] J. Beltran Jimenez and A. L. Maroto. A cosmic vector for dark energy. *Phys.Rev.*, D78:063005, 2008.

[69] J. Beltran Jimenez and A. L. Maroto. Cosmological electromagnetic fields and dark energy. *JCAP*, 0903:016, 2009.

[70] J. Beltran Jimenez and A. L. Maroto. Viability of vector-tensor theories of gravity. *JCAP*, 0902:025, 2009.

[71] E. A. Bergshoeff, O. Hohm, and P. K. Townsend. Massive Gravity in Three Dimensions. *Phys.Rev.Lett.*, 102:201301, 2009.

[72] S. Bernuzzi, A. Nagar, T. Dietrich, and T. Damour. Modeling the dynamics of tidally-interacting binary neutron stars up to merger. 2014.

[73] S. Bernuzzi, A. Nagar, M. Thierfelder, and B. Brugmann. Tidal effects in binary neutron star coalescence. *Phys.Rev.*, D86:044030, 2012.

[74] C. P. L. Berry and J. R. Gair. Linearized f(R) gravity: Gravitational radiation and Solar System tests. Phys. Rev. D, 83(10):104022, May 2011.

[75] E. Berti, A. Buonanno, and C. M. Will. Estimating spinning binary parameters and testing alternative theories of gravity with LISA. *Phys.Rev.*, D71:084025, 2005.

[76] E. Berti, A. Buonanno, and C. M. Will. Testing general relativity and probing the merger history of massive black holes with LISA. *Class.Quant.Grav.*, 22:S943–S954, 2005.

[77] E. Berti, V. Cardoso, and C. Will. Black hole spectroscopy with LISA. *AIP Conf.Proc.*, 873:82–88, 2006.

[78] E. Berti, V. Cardoso, and C. M. Will. On gravitational-wave spectroscopy of massive black holes with the space interferometer LISA. *Phys.Rev.*, D73:064030, 2006.

[79] E. Berti et al. Testing General Relativity with Present and Future Astrophysical Observations. *Class. Quant. Grav.*, 32:243001, 2015.

[80] E. Berti, J. Gair, and A. Sesana. Graviton mass bounds from space-based gravitational-wave observations of massive black hole populations. *Phys. Rev.*, D84:101501, 2011.

[81] E. Berti, L. Gualtieri, M. Horbatsch, and J. Alsing. Light scalar field constraints from gravitational-wave observations of compact binaries. *Phys.Rev.*, D85:122005, 2012.

[82] B. Bertotti, L. Iess, and P. Tortora. A test of general relativity using radio links with the Cassini spacecraft. *Nature*, 425:374, 2003.

[83] H. A. Bethe and G. Brown. Contribution of high-mass black holes to mergers of compact binaries. *Astrophys.J.*, 517:318, 1999.

[84] J. Binney, N. Dowrick, A. Fisher, and M. Newman. The Theory of critical phenomena: An Introduction to the renormalization group. 1992.

[85] T. Binnington and E. Poisson. Relativistic theory of tidal Love numbers. *Phys.Rev.*, D80:084018, 2009.

[86] A. Biswas and K. R. S. Mani. Relativistic perihelion precession of orbits of Venus and the Earth. *Central European Journal of Physics*, 6:754–758, Sept. 2008.

[87] L. Blanchet. Radiative gravitational fields in general relativity. 2. Asymptotic behaviour at future null infinity. *Proc.Roy.Soc.Lond.*, A409:383–399, 1987.

[88] L. Blanchet. Gravitational Radiation from Post-Newtonian Sources and Inspiralling Compact Binaries. *Living Rev.Rel.*, 17(2), 2014.

Bibliography

[89] L. Blanchet, A. Buonanno, and G. Faye. Higher-order spin effects in the dynamics of compact binaries. II. Radiation field. *Phys.Rev.*, D74:104034, 2006.

[90] L. Blanchet, A. Buonanno, and G. Faye. Tail-induced spin-orbit effect in the gravitational radiation of compact binaries. *Phys.Rev.*, D84:064041, 2011.

[91] L. Blanchet, A. Buonanno, and G. Faye. Third post-Newtonian spin-orbit effect in the gravitational radiation flux of compact binaries. *ASP Conf.Ser.*, 467:215, 2013.

[92] L. Blanchet and T. Damour. Radiative gravitational fields in general relativity I. general structure of the field outside the source. *Phil.Trans.Roy.Soc.Lond.*, A320:379–430, 1986.

[93] L. Blanchet, T. Damour, and G. Esposito-Farese. Dimensional regularization of the third postNewtonian dynamics of point particles in harmonic coordinates. *Phys.Rev.*, D69:124007, 2004.

[94] L. Blanchet, T. Damour, G. Esposito-Farese, and B. R. Iyer. Gravitational radiation from inspiralling compact binaries completed at the third post-Newtonian order. *Phys.Rev.Lett.*, 93:091101, 2004.

[95] L. Blanchet, T. Damour, G. Esposito-Farese, and B. R. Iyer. Dimensional regularization of the third post-Newtonian gravitational wave generation from two point masses. *Phys.Rev.*, D71:124004, 2005.

[96] L. Blanchet, G. Faye, B. R. Iyer, and B. Joguet. Gravitational wave inspiral of compact binary systems to 7/2 postNewtonian order. *Phys.Rev.*, D65:061501, 2002.

[97] L. Blanchet and B. R. Iyer. Third postNewtonian dynamics of compact binaries: Equations of motion in the center-of-mass frame. *Class.Quant.Grav.*, 20:755, 2003.

[98] L. Blanchet and B. R. Iyer. Hadamard regularization of the third post-Newtonian gravitational wave generation of two point masses. *Phys.Rev.*, D71:024004, 2005.

[99] L. Blanchet, B. R. Iyer, and B. Joguet. Gravitational waves from inspiralling compact binaries: Energy flux to third postNewtonian order. *Phys.Rev.*, D65:064005, 2002.

[100] L. Blanchet and G. Schaefer. Gravitational wave tails and binary star systems. *Class.Quant.Grav.*, 10:2699–2721, 1993.

[101] D. Blas and H. Sanctuary. Gravitational Radiation in Horava Gravity. *Phys.Rev.*, D84:064004, 2011.

[102] L. Bod, E. Fischbach, G. Marx, and M. Naray-Ziegler. One hundred years of the Eotvos experiment. 1991.

[103] A. Bohé, G. Faye, S. Marsat, and E. K. Porter. Quadratic-in-spin effects in the orbital dynamics and gravitational-wave energy flux of compact binaries at the 3PN order. 2015.

[104] L. Bovens and S. Hartmann. *Bayesian Epistemology*. Oxford scholarship online. OUP Oxford, 2004.

[105] V. B. Braginskiĭ and V. I. Panov. Verification of the Equivalence of Inertial and Gravitational Mass. *Soviet Journal of Experimental and Theoretical Physics*, 34:463, 1972.

[106] C. Brans and R. Dicke. Mach's principle and a relativistic theory of gravitation. *Phys.Rev.*, 124:925–935, 1961.

[107] R. Breton, V. Kaspi, M. McLaughlin, M. Lyutikov, M. Kramer, et al. The Double Pulsar Eclipses I: Phenomenology and Multi-frequency Analysis. *Astrophys.J.*, 747:89, 2012.

[108] R. P. Breton, V. M. Kaspi, M. Kramer, M. A. McLaughlin, M. Lyutikov, et al. Using the double pulsar eclipses to probe fundamental physics. *AIP Conf.Proc.*, 983:469–473, 2008.

[109] G. Bretthorst. *Bayesian Spectrum Analysis and Parameter Estimation*. Lecture Notes in Statistics. Springer New York, 2013.

[110] E. Brigham. *The fast Fourier transform.* Prentice-Hall signal processing series. Prentice-Hall, 1974.

[111] A. E. Broderick, T. Johannsen, A. Loeb, and D. Psaltis. Testing the No-Hair Theorem with Event Horizon Telescope Observations of Sagittarius A*. *Astrophys.J.*, 784:7, 2014.

[112] H. A. Buchdahl. Non-linear Lagrangians and cosmological theory. MNRAS, 150:1, 1970.

[113] A. Buonanno and T. Damour. Effective one-body approach to general relativistic two-body dynamics. *Phys.Rev.*, D59:084006, 1999.

[114] A. Buonanno, B. Iyer, E. Ochsner, Y. Pan, and B. Sathyaprakash. Comparison of post-Newtonian templates for compact binary inspiral signals in gravitational-wave detectors. *Phys.Rev.*, D80:084043, 2009.

[115] A. Buonanno, Y. Pan, J. G. Baker, J. Centrella, B. J. Kelly, et al. Toward faithful templates for non-spinning binary black holes using the effective-one-body approach. *Phys.Rev.*, D76:104049, 2007.

[116] A. Buonanno, Y. Pan, H. P. Pfeiffer, M. A. Scheel, L. T. Buchman, et al. Effective-one-body waveforms calibrated to numerical relativity simulations: Coalescence of non-spinning, equal-mass black holes. *Phys.Rev.*, D79:124028, 2009.

[117] M. Burgay, N. D'Amico, A. Possenti, R. Manchester, A. Lyne, et al. An Increased estimate of the merger rate of double neutron stars from observations of a highly relativistic system. *Nature*, 426:531–533, 2003.

[118] W. Campbell, J. Macek, and T. Morgan. Relativistic Time Dependent Multipole Analysis for Scalar, Electromagnetic, and Gravitational Fields. *Phys.Rev.*, D15:2156–2164, 1977.

[119] P. Canizares, S. E. Field, J. Gair, V. Raymond, R. Smith, et al. Accelerated gravitational-wave parameter estimation with reduced order modeling. 2014.

[120] S. M. Carroll. *Spacetime and geometry. An introduction to general relativity.* 2004.

[121] S. M. Carroll, V. Duvvuri, M. Trodden, and M. S. Turner. Is cosmic speed - up due to new gravitational physics? *Phys.Rev.*, D70:043528, 2004.

[122] B. Carter. Axisymmetric Black Hole Has Only Two Degrees of Freedom. *Phys.Rev.Lett.*, 26:331–333, 1971.

[123] S. Chandrasekhar. Xlviii. the density of white dwarf stars. *Journal of Astrophysics and Astronomy*, 15(2):105–109, 1994.

Bibliography

[124] S. Chatterji, L. Blackburn, G. Martin, and E. Katsavounidis. Multiresolution techniques for the detection of gravitational-wave bursts. *Class.Quant.Grav.*, 21:S1809–S1818, 2004.

[125] C. W. Chou, D. B. Hume, T. Rosenband, and D. J. Wineland. Optical Clocks and Relativity. *Science*, 329:1630–, Sept. 2010.

[126] S. R. Choudhury, G. C. Joshi, S. Mahajan, and B. H. J. McKellar. Probing large distance higher dimensional gravity from lensing data. *Astropart. Phys.*, 21:559–563, 2004.

[127] P. T. Chrusciel. 'No hair' theorems: Folklore, conjectures, results. *Contemp.Math.*, 170:23–49, 1994.

[128] I. Ciufolini, A. Paolozzi, and C. Paris. Overview of the LARES Mission: orbit, error analysis and technological aspects. *Journal of Physics Conference Series*, 354(1):012002, Mar. 2012.

[129] I. Ciufolini, A. Paolozzi, E. C. Pavlis, J. C. Ries, R. Koenig, R. A. Matzner, G. Sindoni, and H. Neumayer. Towards a One Percent Measurement of Frame Dragging by Spin with Satellite Laser Ranging to LAGEOS, LAGEOS 2 and LARES and GRACE Gravity Models. Space Sci. Rev., 148:71–104, Dec. 2009.

[130] G. M. Clemence. The Relativity Effect in Planetary Motions. *Reviews of Modern Physics*, 19:361–364, Oct. 1947.

[131] G. Cognola, M. Gastaldi, and S. Zerbini. On the stability of a class of modified gravitational models. *Int.J.Theor.Phys.*, 47:898–910, 2008.

[132] T. Cokelaer. Parameter estimation of inspiralling compact binaries in ground-based detectors: Comparison between Monte Carlo simulations and the Fisher information matrix. *Class.Quant.Grav.*, 25:184007, 2008.

[133] E. Corinaldesi and A. Papapetrou. Spinning test particles in general relativity. 2. *Proc.Roy.Soc.Lond.*, A209:259–268, 1951.

[134] N. Cornish, L. Sampson, N. Yunes, and F. Pretorius. Gravitational Wave Tests of General Relativity with the Parameterized Post-Einsteinian Framework. *Phys.Rev.*, D84:062003, 2011.

[135] N. J. Cornish and T. B. Littenberg. BayesWave: Bayesian Inference for Gravitational Wave Bursts and Instrument Glitches. 2014.

[136] D. Cox and D. Hinkley. *Theoretical Statistics*. Taylor & Francis, 1979.

[137] D. Cox and H. Miller. *The Theory of Stochastic Processes*. Science paperbacks. Taylor & Francis, 1977.

[138] T. Damour and G. Esposito-Farese. Tensor - scalar gravity and binary pulsar experiments. *Phys.Rev.*, D54:1474–1491, 1996.

[139] T. Damour, B. R. Iyer, and B. Sathyaprakash. Frequency domain P approximant filters for time truncated inspiral gravitational wave signals from compact binaries. *Phys.Rev.*, D62:084036, 2000.

[140] T. Damour, P. Jaranowski, and G. Schaefer. Dimensional regularization of the gravitational interaction of point masses. *Phys.Lett.*, B513:147–155, 2001.

[141] T. Damour, P. Jaranowski, and G. Schaefer. Equivalence between the ADM-Hamiltonian and the harmonic coordinates approaches to the third postNewtonian dynamics of compact binaries. *Phys.Rev.*, D63:044021, 2001.

[142] T. Damour and A. Nagar. Faithful effective-one-body waveforms of small-mass-ratio coalescing black-hole binaries. *Phys.Rev.*, D76:064028, 2007.

[143] T. Damour and A. Nagar. Comparing Effective-One-Body gravitational waveforms to accurate numerical data. *Phys.Rev.*, D77:024043, 2008.

[144] T. Damour and A. Nagar. Effective One Body description of tidal effects in inspiralling compact binaries. *Phys.Rev.*, D81:084016, 2010.

[145] T. Damour and A. Nagar. The Effective One Body description of the Two-Body problem. *Fundam.Theor.Phys.*, 162:211–252, 2011.

[146] T. Damour, A. Nagar, and S. Bernuzzi. Improved effective-one-body description of coalescing nonspinning black-hole binaries and its numerical-relativity completion. *Phys.Rev.*, D87(8):084035, 2013.

[147] T. Damour, A. Nagar, and L. Villain. Measurability of the tidal polarizability of neutron stars in late-inspiral gravitational-wave signals. *Phys.Rev.*, D85:123007, 2012.

[148] V. C. de Andrade, L. Blanchet, and G. Faye. Third postNewtonian dynamics of compact binaries: Noetherian conserved quantities and equivalence between the harmonic coordinate and ADM Hamiltonian formalisms. *Class.Quant.Grav.*, 18:753–778, 2001.

[149] P. de Laplace, F. Truscott, and F. Emory. *A Philosophical Essay on Probabilities*. A Philosophical Essay on Probabilities. Wiley, 1902.

[150] C. de Rham. Massive Gravity. *Living Rev. Rel.*, 17:7, 2014.

[151] B. de Wit. Supergravity. *ArXiv High Energy Physics - Theory e-prints*, Dec. 2002.

[152] W. Del Pozzo, T. G. F. Li, M. Agathos, C. Van Den Broeck, and S. Vitale. Demonstrating the feasibility of probing the neutron star equation of state with second-generation gravitational wave detectors. *Phys.Rev.Lett.*, 111(7):071101, 2013.

[153] W. Del Pozzo, T. G. F. Li, and C. Messenger. Cosmological inference using gravitational wave observations alone. 2015.

[154] W. Del Pozzo, J. Veitch, and A. Vecchio. Testing General Relativity using Bayesian model selection: Applications to observations of gravitational waves from compact binary systems. *Phys.Rev.*, D83:082002, 2011.

[155] P. Demorest, T. Pennucci, S. Ransom, M. Roberts, and J. Hessels. Shapiro Delay Measurement of A Two Solar Mass Neutron Star. *Nature*, 467:1081–1083, 2010.

[156] S. Doeleman and G. Bower. Approaching the Event Horizon through VLBI Imaging of Sagittarius A*. *Galactic Center Newsletter*, 18:6–12, July 2004.

[157] M. Dominik, K. Belczynski, C. Fryer, D. Holz, E. Berti, et al. Double Compact Objects I: The Significance of the Common Envelope on Merger Rates. *Astrophys.J.*, 759:52, 2012.

[158] F. W. Dyson, A. S. Eddington, and C. Davidson. A Determination of the Deflection of Light by the Sun's Gravitational Field, from Observations Made at the Total Eclipse of May 29, 1919. *Royal Society of London Philosophical Transactions Series A*, 220:291–333, 1920.

Bibliography

[159] A. S. Eddington. The total eclipse of 1919 May 29 and the influence of gravitation on light. *The Observatory*, 42:119–122, Mar. 1919.

[160] A. Einstein. Erklarung der Perihelionbewegung der Merkur aus der allgemeinen Relativitatstheorie. *Sitzungsber. preuss.Akad. Wiss., vol. 47, No.2, pp. 831-839, 1915*, 47:831–839, 1915.

[161] A. Einstein. Näherungsweise Integration der Feldgleichungen der Gravitation. *Sitzungsberichte der Königlich Preußischen Akademie der Wissenschaften (Berlin), Seite 688-696.*, pages 688–696, 1916.

[162] A. Einstein. Über Gravitationswellen. *Sitzungsberichte der Königlich Preußischen Akademie der Wissenschaften (Berlin), Seite 154-167.*, pages 154–167, 1918.

[163] C. W. F. Everitt, D. B. DeBra, B. W. Parkinson, J. P. Turneaure, J. W. Conklin, M. I. Heifetz, G. M. Keiser, A. S. Silbergleit, T. Holmes, J. Kolodziejczak, M. Al-Meshari, J. C. Mester, B. Muhlfelder, V. G. Solomonik, K. Stahl, P. W. Worden, W. Bencze, S. Buchman, B. Clarke, A. Al-Jadaan, H. Al-Jibreen, J. Li, J. A. Lipa, J. M. Lockhart, B. Al-Suwaidan, M. Taber, and S. Wang. Gravity probe b: Final results of a space experiment to test general relativity. *Phys. Rev. Lett.*, 106:221101, May 2011.

[164] J. A. Faber and F. A. Rasio. Binary Neutron Star Mergers. *Living Rev.Rel.*, 15:8, 2012.

[165] H. Falcke, F. Melia, and E. Agol. Viewing the shadow of the black hole at the galactic center. *Astrophys.J.*, 528:L13, 2000.

[166] G. Faye, L. Blanchet, and A. Buonanno. Higher-order spin effects in the dynamics of compact binaries. I. Equations of motion. *Phys.Rev.*, D74:104033, 2006.

[167] R. D. Ferdman, I. H. Stairs, M. Kramer, M. A. McLaughlin, D. R. Lorimer, et al. A precise mass measurement of the intermediate-mass binary pulsar PSR J1802-2124. *Astrophys.J.*, 711:764–771, 2010.

[168] V. Ferrari, L. Gualtieri, and F. Pannarale. Neutron star tidal disruption in mixed binaries: the imprint of the equation of state. *Phys.Rev.*, D81:064026, 2010.

[169] L. S. Finn and P. J. Sutton. Bounding the mass of the graviton using binary pulsar observations. *Phys. Rev.*, D65:044022, 2002.

[170] E. E. Flanagan and T. Hinderer. Constraining neutron star tidal Love numbers with gravitational wave detectors. *Phys.Rev.*, D77:021502, 2008.

[171] P. C. Freire, N. Wex, G. Esposito-Farese, J. P. Verbiest, M. Bailes, et al. The relativistic pulsar-white dwarf binary PSR J1738+0333 II. The most stringent test of scalar-tensor gravity. *Mon.Not.Roy.Astron.Soc.*, 423:3328, 2012.

[172] J. F. Friedman and N. Stergioulas. *Rotating relativistic stars*. Cambridge University Press, Cambridge, 2013.

[173] A. Friedmann. Über die Möglichkeit einer Welt mit konstanter negativer Krümmung des Raumes. *Zeitschrift fur Physik*, 21:326–332, Dec. 1924.

[174] M. Frigo and S. Johnson. The design and implementation of fftw3. *Proceedings of the IEEE*, 93(2):216–231, Feb 2005.

[175] Y. Fujii and K.-i. Maeda. *The Scalar-Tensor Theory of Gravitation*. July 2007.

[176] T. Futamase and Y. Itoh. The post-Newtonian approximation for relativistic compact binaries. *Living Rev.Rel.*, 10:2, 2007.

[177] M. Gai, A. Vecchiato, A. Riva, M. Lattanzi, A. Sozzetti, et al. Astrometric tests of General Relativity in the Solar system. *J.Phys.Conf.Ser.*, 490:012240, 2014.

[178] L. Gergely, Z. Perjes, and M. Vasuth. Spin effects in gravitational radiation back reaction. 2. Finite mass effects. *Phys.Rev.*, D57:3423–3432, 1998.

[179] L. A. Gergely. Second postNewtonian radiative evolution of the relative orientations of angular momenta in spinning compact binaries. *Phys.Rev.*, D62:024007, 2000.

[180] L. A. Gergely. Spin spin effects in radiating compact binaries. *Phys.Rev.*, D61:024035, 2000.

[181] L. A. Gergely and Z. Keresztes. Gravitational radiation reaction in compact binary systems: Contribution of the quadrupole - monopole interaction. *Phys.Rev.*, D67:024020, 2003.

[182] L. A. Gergely, Z. I. Perjes, and M. Vasuth. Spin effects in gravitational radiation back reaction. 1. The Lense-Thirring approximation. *Phys.Rev.*, D57:876–884, 1998.

[183] L. A. Gergely, Z. I. Perjes, and M. Vasuth. Spin effects in gravitational radiation back reaction. 3. Compact binaries with two spinning components. *Phys.Rev.*, D58:124001, 1998.

[184] H. Goenner. Some remarks on the genesis of scalar-tensor theories. *Gen.Rel.Grav.*, 44:2077–2097, 2012.

[185] A. S. Goldhaber and M. M. Nieto. Mass of the graviton. *Phys. Rev. D*, 9:1119–1121, Feb 1974.

[186] S. Gossan, J. Veitch, and B. Sathyaprakash. Bayesian model selection for testing the no-hair theorem with black hole ringdowns. *Phys.Rev.*, D85:124056, 2012.

[187] P. Haensel, M. Salgado, and S. Bonazzola. Equation of state of dense matter and maximum rotation frequency of neutron stars. A&A, 296:745, Apr. 1995.

[188] P. Haensel and J. L. Zdunik. A submillisecond pulsar and the equation of state of dense matter. Nature, 340:617–619, Aug. 1989.

[189] P. Haensel, J. L. Zdunik, M. Bejger, and J. M. Lattimer. Keplerian frequency of uniformly rotating neutron stars and strange stars. *Astron. Astrophys.*, 502:605–610, 2009.

[190] W.-b. Han and S.-l. Liao. PSR J0337+1715: an appropriate laboratory for testing the Nordtvedt effect. 2014.

[191] M. Hannam, P. Schmidt, A. Bohé, L. Haegel, S. Husa, et al. Simple Model of Complete Precessing Black-Hole-Binary Gravitational Waveforms. *Phys.Rev.Lett.*, 113(15):151101, 2014.

[192] H. Hassanieh, P. Indyk, D. Katabi, and E. Price. Simple and practical algorithm for sparse fourier transform. In *Proceedings of the Twenty-third Annual ACM-SIAM Symposium on Discrete Algorithms*, SODA '12, pages 1183–1194. SIAM, 2012.

[193] S. Hawking. Gravitational radiation from colliding black holes. *Phys.Rev.Lett.*, 26:1344–1346, 1971.

[194] S. Hawking. Black holes in general relativity. *Commun.Math.Phys.*, 25:152–166, 1972.

[195] F. W. Hehl, P. von der Heyde, G. D. Kerlick, and J. M. Nester. General relativity with spin and torsion: Foundations and prospects. *Rev. Mod. Phys.*, 48:393–416, Jul 1976.

[196] G. Heidbreder. *Maximum Entropy and Bayesian Methods Santa Barbara, California, U.S.A., 1993.* Fundamental Theories of Physics. Springer, 1996.

[197] J. W. Hessels, S. M. Ransom, I. H. Stairs, P. C. C. Freire, V. M. Kaspi, et al. A radio pulsar spinning at 716-hz. *Science*, 311:1901–1904, 2006.

[198] A. Hewish, S. Bell, J. Pilkington, P. Scott, and R. Collins. Observation of a rapidly pulsating radio source. *Nature*, 217:709–713, 1968.

[199] T. Hinderer. Tidal Love numbers of neutron stars. *Astrophys.J.*, 677:1216–1220, 2008.

[200] T. Hinderer, B. D. Lackey, R. N. Lang, and J. S. Read. Tidal deformability of neutron stars with realistic equations of state and their gravitational wave signatures in binary inspiral. *Phys.Rev.*, D81:123016, 2010.

[201] P. Horava. Quantum Gravity at a Lifshitz Point. *Phys.Rev.*, D79:084008, 2009.

[202] K. Hotokezaka, K. Kyutoku, H. Okawa, M. Shibata, and K. Kiuchi. Binary Neutron Star Mergers: Dependence on the Nuclear Equation of State. *Phys.Rev.*, D83:124008, 2011.

[203] K. Hotokezaka, K. Kyutoku, and M. Shibata. Exploring tidal effects of coalescing binary neutron stars in numerical relativity. *Phys.Rev.*, D87(4):044001, 2013.

[204] K. Hotokezaka and T. Piran. Mass ejection from neutron star mergers: different components and expected radio signals. *Mon.Not.Roy.Astron.Soc.*, 450:1430, 2015.

[205] S. A. Huggett and K. P. Tod. *An Introduction to Twistor Theory.* Aug. 1994.

[206] K. Ioka and K. Taniguchi. Gravitational waves from inspiralling compact binaries with magnetic dipole moments. *Astrophys.J.*, 537:327, 2000.

[207] L. Iorio. Towards a 1% measurement of the Lense-Thirring effect with LARES? *Advances in Space Research*, 43:1148–1157, Apr. 2009.

[208] L. Iorio. Will the recently approved LARES mission be able to measure the Lense-Thirring effect at 1%? *General Relativity and Gravitation*, 41:1717–1724, Aug. 2009.

[209] L. Iorio. Withdrawal: 'a new type of misconduct in the field of the physical sciences: The case of the pseudonyms used by i. ciufolini to anonymously criticize other people's works on arxiv' by l. iorio. *Journal of the Association for Information Science and Technology*, 65(11):2375–2375, 2014.

[210] W. Israel. Event horizons in static vacuum space-times. *Phys.Rev.*, 164:1776–1779, 1967.

[211] W. Israel. Event horizons in static electrovac space-times. *Commun.Math.Phys.*, 8:245–260, 1968.

[212] K. Itô. *An Introduction to Probability Theory.* Cambridge University Press, 1984.

[213] Y. Itoh and T. Futamase. New derivation of a third postNewtonian equation of motion for relativistic compact binaries without ambiguity. *Phys.Rev.*, D68:121501, 2003.

[214] T. Jacobson. Einstein-aether gravity: A Status report. *PoS*, QG-PH:020, 2007.

[215] P. Jaranowski and G. Schaefer. Radiative 3.5 postNewtonian ADM Hamiltonian for many body point - mass systems. *Phys.Rev.*, D55:4712–4722, 1997.

[216] E. Jaynes and G. Bretthorst. *Probability Theory: The Logic of Science.* Cambridge University Press, 2003.

[217] H. Jeffreys. An invariant form for the prior probability in estimation problems. *Proceedings of the Royal Society of London. Series A, Mathematical and Physical Sciences*, 186(1007):453–461, 1946.

[218] H. Jeffreys. *The Theory of Probability.* OUP Oxford, 1998.

[219] V. Kalogera, K. Belczynski, C. Kim, R. W. O'Shaughnessy, and B. Willems. Formation of Double Compact Objects. *Phys.Rept.*, 442:75–108, 2007.

[220] I. Kamaretsos, M. Hannam, and B. Sathyaprakash. Is black-hole ringdown a memory of its progenitor? *Phys.Rev.Lett.*, 109:141102, 2012.

[221] R. P. Kerr. Gravitational field of a spinning mass as an example of algebraically special metrics. *Phys.Rev.Lett.*, 11:237–238, 1963.

[222] S. Khan, S. Husa, M. Hannam, F. Ohme, M. Pürrer, X. Jiménez Forteza, and A. Bohé. Frequency-domain gravitational waves from nonprecessing black-hole binaries. II. A phenomenological model for the advanced detector era. *Phys. Rev.*, D93(4):044007, 2016.

[223] L. E. Kidder. Coalescing binary systems of compact objects to postNewtonian 5/2 order. 5. Spin effects. *Phys.Rev.*, D52:821–847, 1995.

[224] L. E. Kidder, C. M. Will, and A. G. Wiseman. Spin effects in the inspiral of coalescing compact binaries. *Phys.Rev.*, D47:4183–4187, 1993.

[225] H. Kimble, Y. Levin, A. B. Matsko, K. S. Thorne, and S. P. Vyatchanin. Conversion of conventional gravitational wave interferometers into QND interferometers by modifying their input and / or output optics. *Phys.Rev.*, D65:022002, 2002.

[226] B. Kiziltan. Reassessing The Fundamentals: New Constraints on the Evolution, Ages and Masses of Neutron Stars. *AIP Conf.Proc.*, 1379:41–47, 2011.

[227] B. Kiziltan, A. Kottas, M. De Yoreo, and S. E. Thorsett. The Neutron Star Mass Distribution. *Astrophys.J.*, 778:66, 2013.

[228] D. Koller and N. Friedman. *Probabilistic Graphical Models: Principles and Techniques.* Adaptive computation and machine learning. MIT Press, 2009.

[229] A. N. Kolmogorov. *Grundbegriffe der Wahrscheinlichkeitsrechnung.* Springer, Berlin, 1933.

[230] H. Komatsu, Y. Eriguchi, and I. Hachisu. Rapidly rotating general relativistic stars. I - Numerical method and its application to uniformly rotating polytropes. *Mon.Not.Roy.Astron.Soc.*, 237:355–379, 1989.

[231] M. Kramer, I. H. Stairs, R. Manchester, M. McLaughlin, A. Lyne, et al. Tests of general relativity from timing the double pulsar. *Science*, 314:97–102, 2006.

[232] W. G. Laarakkers and E. Poisson. Quadrupole moments of rotating neutron stars. *Astrophys.J.*, 512:282–287, 1999.

[233] B. D. Lackey, K. Kyutoku, M. Shibata, P. R. Brady, and J. L. Friedman. Extracting equation of state parameters from black hole-neutron star mergers. I. Nonspinning black holes. *Phys.Rev.*, D85:044061, 2012.

Bibliography

[234] B. D. Lackey, M. Nayyar, and B. J. Owen. Observational constraints on hyperons in neutron stars. *Phys.Rev.*, D73:024021, 2006.

[235] B. D. Lackey and L. Wade. Reconstructing the neutron-star equation of state with gravitational-wave detectors from a realistic population of inspiralling binary neutron stars. 2014.

[236] L. D. Landau and E. M. Lifshitz. *The classical theory of fields.* 1975.

[237] J. Lattimer and M. Prakash. Neutron star structure and the equation of state. *Astrophys.J.*, 550:426, 2001.

[238] J. M. Lattimer. The nuclear equation of state and neutron star masses. *Ann.Rev.Nucl.Part.Sci.*, 62:485–515, 2012.

[239] J. M. Lattimer and M. Prakash. What a Two Solar Mass Neutron Star Really Means. 2010.

[240] R. Laureijs et al. Euclid Definition Study Report. 2011.

[241] U. J. Le Verrier. Theorie du mouvement de Mercure. *Annales de l'Observatoire de Paris*, 5:1, 1859.

[242] E. Leaver. An Analytic representation for the quasi normal modes of Kerr black holes. *Proc.Roy.Soc.Lond.*, A402:285–298, 1985.

[243] D. E. Lebach, B. E. Corey, I. I. Shapiro, M. I. Ratner, J. C. Webber, A. E. E. Rogers, J. L. Davis, and T. A. Herring. Measurement of the Solar Gravitational Deflection of Radio Waves Using Very-Long-Baseline Interferometry. *Physical Review Letters*, 75:1439–1442, Aug. 1995.

[244] G. Lemaître. Un Univers homogène de masse constante et de rayon croissant rendant compte de la vitesse radiale des nébuleuses extra-galactiques. *Annales de la Société Scientifique de Bruxelles*, 47:49–59, 1927.

[245] T. Li, W. Del Pozzo, S. Vitale, C. Van Den Broeck, M. Agathos, et al. Towards a generic test of the strong field dynamics of general relativity using compact binary coalescence. *Phys.Rev.*, D85:082003, 2012.

[246] T. Li, W. Del Pozzo, S. Vitale, C. Van Den Broeck, M. Agathos, et al. Towards a generic test of the strong field dynamics of general relativity using compact binary coalescence: Further investigations. *J.Phys.Conf.Ser.*, 363:012028, 2012.

[247] T. B. Littenberg and N. J. Cornish. BayesLine: Bayesian Inference for Spectral Estimation of Gravitational Wave Detector Noise. *Phys.Rev.*, D91(8):084034, 2015.

[248] D. Lorimer. Binary and Millisecond Pulsars. *Living Rev.Rel.*, 11:8, 2008.

[249] D. Lovelock. The Einstein tensor and its generalizations. *J.Math.Phys.*, 12:498–501, 1971.

[250] A. Lundgren and R. O'Shaughnessy. Single-spin precessing gravitational waveform in closed form. *Phys.Rev.*, D89(4):044021, 2014.

[251] A. Lyne, M. Burgay, M. Kramer, A. Possenti, R. Manchester, et al. A Double - pulsar system - A Rare laboratory for relativistic gravity and plasma physics. *Science*, 303:1153–1157, 2004.

[252] D. J. C. Mackay. *Information Theory, Inference and Learning Algorithms.* Oct. 2003.

[253] M. Maggiore. *Gravitational Waves: Volume 1: Theory and Experiments*. Gravitational Waves. OUP Oxford, 2007.

[254] I. Mandel, C. P. Berry, F. Ohme, S. Fairhurst, and W. M. Farr. Parameter estimation on compact binary coalescences with abruptly terminating gravitational waveforms. *Class.Quant.Grav.*, 31:155005, 2014.

[255] C. Markakis, J. S. Read, M. Shibata, K. Uryū, J. D. Creighton, et al. Inferring the neutron star equation of state from binary inspiral waveforms. pages 743–745, 2010.

[256] S. Marsat, L. Blanchet, A. Bohé, and G. Faye. Gravitational waves from spinning compact object binaries: New post-Newtonian results. 2013.

[257] M. Martinelli, E. Calabrese, F. De Bernardis, A. Melchiorri, L. Pagano, et al. Constraining Modified Gravity with Euclid. *Phys.Rev.*, D83:023012, 2011.

[258] A. Maselli, V. Cardoso, V. Ferrari, L. Gualtieri, and P. Pani. Equation-of-state-independent relations in neutron stars. *Phys.Rev.*, D88(2):023007, 2013.

[259] J. Meidam, M. Agathos, C. Van Den Broeck, J. Veitch, and B. Sathyaprakash. Testing the no-hair theorem with black hole ringdowns using TIGER. *Phys.Rev.*, D90(6):064009, 2014.

[260] F. Melia and H. Falcke. The supermassive black hole at the galactic center. *Ann.Rev.Astron.Astrophys.*, 39:309–352, 2001.

[261] C. Messenger and J. Read. Measuring a cosmological distance-redshift relationship using only gravitational wave observations of binary neutron star coalescences. *Phys. Rev. Lett.*, 108:091101, 2012.

[262] B. Mikoczi, M. Vasuth, and L. A. Gergely. Self-interaction spin effects in inspiralling compact binaries. *Phys.Rev.*, D71:124043, 2005.

[263] M. Milgrom. A Modification of the Newtonian dynamics as a possible alternative to the hidden mass hypothesis. *Astrophys.J.*, 270:365–370, 1983.

[264] C. K. Mishra, K. Arun, B. R. Iyer, and B. Sathyaprakash. Parametrized tests of post-Newtonian theory using Advanced LIGO and Einstein Telescope. *Phys.Rev.*, D82:064010, 2010.

[265] C. W. Misner, K. S. Thorne, and J. A. Wheeler. *Gravitation*. 1973.

[266] J. Moffat. Scalar-tensor-vector gravity theory. *JCAP*, 0603:004, 2006.

[267] H. Mueller and B. D. Serot. Relativistic mean field theory and the high density nuclear equation of state. *Nucl.Phys.*, A606:508–537, 1996.

[268] R. C. Myers and M. J. Perry. Black holes in higher dimensional space-times. *Annals of Physics*, 172:304–347, Dec. 1986.

[269] W. Nelson, J. Ochoa, and M. Sakellariadou. Gravitational Waves in the Spectral Action of Noncommutative Geometry. *Phys.Rev.*, D82:085021, 2010.

[270] E. Newman and A. Janis. Note on the Kerr spinning particle metric. *J.Math.Phys.*, 6:915–917, 1965.

[271] E. T. Newman, R. Couch, K. Chinnapared, A. Exton, A. Prakash, et al. Metric of a Rotating, Charged Mass. *J.Math.Phys.*, 6:918–919, 1965.

[272] S. Nissanke and L. Blanchet. Gravitational radiation reaction in the equations of motion of compact binaries to 3.5 post-Newtonian order. *Class.Quant.Grav.*, 22:1007–1032, 2005.

Bibliography

[273] S. Nojiri and S. D. Odintsov. Modified Gauss-Bonnet theory as gravitational alternative for dark energy. *Phys.Lett.*, B631:1–6, 2005.

[274] G. Nordström. On the Energy of the Gravitation field in Einstein's Theory. *Koninklijke Nederlandse Akademie van Wetenschappen Proceedings Series B Physical Sciences*, 20:1238–1245, 1918.

[275] K. Nordtvedt. Equivalence Principle for Massive Bodies. II. Theory. *Physical Review*, 169:1017–1025, May 1968.

[276] K. Nordtvedt. Testing relativity with laser ranging to the moon. *Phys.Rev.*, 170:1186–1187, 1968.

[277] K. J. Nordtvedt and C. M. Will. Conservation Laws and Preferred Frames in Relativistic Gravity. II. Experimental Evidence to Rule Out Preferred-Frame Theories of Gravity. *Astrophys.J.*, 177:775–792, 1972.

[278] J. R. Oppenheimer and G. M. Volkoff. On massive neutron cores. *Phys. Rev.*, 55:374–381, Feb 1939.

[279] R. O'Shaughnessy, B. Farr, E. Ochsner, H.-S. Cho, C. Kim, et al. Parameter Estimation of Gravitational Waves from Nonprecessing BH-NS Inspirals with higher harmonics: Comparing MCMC posteriors to an Effective Fisher Matrix. *Phys.Rev.*, D89:064048, 2014.

[280] R. W. O'Shaughnessy, C. Kim, T. Frakgos, V. Kalogera, and K. Belczynski. Constraining population synthesis models via the binary neutron star population. *Astrophys.J.*, 633:1076–1084, 2005.

[281] B. J. Owen, H. Tagoshi, and A. Ohashi. Nonprecessional spin orbit effects on gravitational waves from inspiraling compact binaries to second postNewtonian order. *Phys.Rev.*, D57:6168–6175, 1998.

[282] F. Ozel, D. Psaltis, R. Narayan, and A. S. Villarreal. On the Mass Distribution and Birth Masses of Neutron Stars. *Astrophys.J.*, 757:55, 2012.

[283] A. Pai and K. Arun. Singular value decomposition in parametrised tests of post-Newtonian theory. *Class.Quant.Grav.*, 30:025011, 2013.

[284] Y. Pan, A. Buonanno, A. Taracchini, M. Boyle, L. E. Kidder, et al. Stability of nonspinning effective-one-body model in approximating two-body dynamics and gravitational-wave emission. *Phys.Rev.*, D89(6):061501, 2014.

[285] Y. Pan, A. Buonanno, A. Taracchini, L. E. Kidder, A. H. Mroué, et al. Inspiral-merger-ringdown waveforms of spinning, precessing black-hole binaries in the effective-one-body formalism. *Phys.Rev.*, D89(8):084006, 2014.

[286] P. Pani and E. Berti. Slowly rotating neutron stars in scalar-tensor theories. *Phys.Rev.*, D90(2):024025, 2014.

[287] A. Papapetrou. Spinning test particles in general relativity. 1. *Proc.Roy.Soc.Lond.*, A209:248–258, 1951.

[288] G. Pappas and T. A. Apostolatos. Multipole Moments of numerical spacetimes. 2012.

[289] G. Pappas and T. A. Apostolatos. Revising the multipole moments of numerical spacetimes, and its consequences. *Phys.Rev.Lett.*, 108:231104, 2012.

[290] R. Penrose. Asymptotic properties of fields and space-times. *Phys.Rev.Lett.*, 10:66–68, 1963.

[291] R. Penrose. Zero rest mass fields including gravitation: Asymptotic behavior. *Proc.Roy.Soc.Lond.*, A284:159, 1965.

[292] R. Penrose. Twistor Algebra. *Journal of Mathematical Physics*, 8:345–366, Feb. 1967.

[293] P. Peters. Gravitational Radiation and the Motion of Two Point Masses. *Phys.Rev.*, 136:B1224–B1232, 1964.

[294] E. Poisson. Gravitational waves from inspiraling compact binaries: The Quadrupole moment term. *Phys.Rev.*, D57:5287–5290, 1998.

[295] E. Poisson and C. M. Will. Gravitational waves from inspiraling compact binaries: Parameter estimation using second postNewtonian wave forms. *Phys.Rev.*, D52:848–855, 1995.

[296] J. Polchinski. *String Theory*. June 2005.

[297] R. V. Pound and G. A. Rebka. Gravitational red-shift in nuclear resonance. *Phys. Rev. Lett.*, 3:439–441, Nov 1959.

[298] R. V. Pound and G. A. Rebka. Apparent weight of photons. *Phys. Rev. Lett.*, 4:337–341, Apr 1960.

[299] M. Prakash, J. Cooke, and J. Lattimer. Quark - hadron phase transition in protoneutron stars. *Phys.Rev.*, D52:661–665, 1995.

[300] W. H. Press, B. P. Flannery, and S. A. Teukolsky. *Numerical recipes. The art of scientific computing*. 1986.

[301] W. H. Press and S. A. Teukolsky. Perturbations of a Rotating Black Hole. II. Dynamical Stability of the Kerr Metric. *Astrophys.J.*, 185:649–674, 1973.

[302] F. Pretorius. Evolution of Binary Black-Hole Spacetimes. *Physical Review Letters*, 95(12):121101, Sept. 2005.

[303] M. Pürrer. Frequency domain reduced order models for gravitational waves from aligned-spin compact binaries. *Class.Quant.Grav.*, 31(19):195010, 2014.

[304] M. Pürrer, M. Hannam, P. Ajith, and S. Husa. Testing the validity of the single-spin approximation in inspiral-merger-ringdown waveforms. *Phys.Rev.*, D88:064007, 2013.

[305] D. Radice, L. Rezzolla, and F. Galeazzi. High-Order Numerical-Relativity Simulations of Binary Neutron Stars. 2015.

[306] S. Ransom, I. Stairs, A. Archibald, J. Hessels, D. Kaplan, et al. A millisecond pulsar in a stellar triple system. 2014.

[307] J. S. Read, L. Baiotti, J. D. E. Creighton, J. L. Friedman, B. Giacomazzo, et al. Matter effects on binary neutron star waveforms. *Phys.Rev.*, D88:044042, 2013.

[308] J. S. Read, B. D. Lackey, B. J. Owen, and J. L. Friedman. Constraints on a phenomenologically parameterized neutron-star equation of state. *Phys.Rev.*, D79:124032, 2009.

[309] J. S. Read, C. Markakis, M. Shibata, K. Uryū, J. D. Creighton, et al. Measuring the neutron star equation of state with gravitational wave observations. *Phys.Rev.*, D79:124033, 2009.

[310] H. S. Reall. Higher dimensional black holes. *Int.J.Mod.Phys.*, D21:1230001, 2012.

Bibliography

[311] H. Reissner. Über die Eigengravitation des elektrischen Feldes nach der Einsteinschen Theorie. *Annalen der Physik*, 355:106–120, 1916.

[312] G. Renzetti. Are higher degree even zonals really harmful for the LARES/LAGEOS frame-dragging experiment? *Canadian Journal of Physics*, 90:883–888, Aug. 2012.

[313] G. Renzetti. First results from LARES: An analysis. New A, 23:63–66, Oct. 2013.

[314] C. E. Rhoades and R. Ruffini. Maximum mass of a neutron star. *Phys. Rev. Lett.*, 32:324–327, Feb 1974.

[315] H. Robertson. Kinematics and World-Structure. *Astrophys.J.*, 82:284–301, 1935.

[316] H. Robertson. Kinematics and World-Structure. 2. *Astrophys.J.*, 83:187–201, 1935.

[317] H. Robertson. Kinematics and World-Structure. 3. *Astrophys.J.*, 83:257–271, 1936.

[318] P. Roll, R. Krotkov, and R. Dicke. The Equivalence of inertial and passive gravitational mass. *Annals Phys.*, 26:442–517, 1964.

[319] C. Rovelli. Loop Quantum Gravity. *Living Reviews in Relativity*, 11, July 2008.

[320] F. Ryan. Gravitational waves from the inspiral of a compact object into a massive, axisymmetric body with arbitrary multipole moments. *Phys.Rev.*, D52:5707–5718, 1995.

[321] F. D. Ryan. Spinning boson stars with large selfinteraction. *Phys.Rev.*, D55:6081–6091, 1997.

[322] L. Santamaria, F. Ohme, P. Ajith, B. Bruegmann, N. Dorband, et al. Matching post-Newtonian and numerical relativity waveforms: systematic errors and a new phenomenological model for non-precessing black hole binaries. *Phys.Rev.*, D82:064016, 2010.

[323] R. Scaramella et al. Euclid space mission: a cosmological challenge for the next 15 years. 2015.

[324] P. Schmidt, M. Hannam, and S. Husa. Towards models of gravitational waveforms from generic binaries: A simple approximate mapping between precessing and non-precessing inspiral signals. *Phys.Rev.*, D86:104063, 2012.

[325] P. Schmidt, F. Ohme, and M. Hannam. Towards models of gravitational waveforms from generic binaries II: Modelling precession effects with a single effective precession parameter. *Phys.Rev.*, D91(2):024043, 2015.

[326] B. F. Schutz. *A First Course in General Relativity.* Feb. 1985.

[327] K. Schwarzschild. On the gravitational field of a mass point according to Einstein's theory. *Sitzungsber.Preuss.Akad.Wiss.Berlin (Math.Phys.)*, 1916:189–196, 1916.

[328] A. Sesana, J. Gair, E. Berti, and M. Volonteri. Reconstructing the massive black hole cosmic history through gravitational waves. *Phys.Rev.*, D83:044036, 2011.

[329] S. L. Shapiro and S. A. Teukolsky. *Black holes, white dwarfs, and neutron stars: The physics of compact objects.* 1983.

[330] S. L. Shapiro, S. A. Teukolsky, and I. Wasserman. Implications of the millisecond pulsar for neutron star models. ApJ, 272:702–707, Sept. 1983.

[331] S. L. Shapiro, S. A. Teukolsky, and I. Wasserman. Testing nuclear theory using the 0.5 MS pulsar. Nature, 340:451, Aug. 1989.

[332] S. S. Shapiro, J. L. Davis, D. E. Lebach, and J. S. Gregory. Measurement of the solar gravitational deflection of radio waves using geodetic very-long-baseline interferometry data, 1979˘1999. *Phys. Rev. Lett.*, 92:121101, Mar 2004.

[333] M. Shibata. *Numerical Relativity*. World Scientific Publishing Co, 2016.

[334] M. Shibata and K. Taniguchi. Coalescence of Black Hole-Neutron Star Binaries. *Living Rev.Rel.*, 14:6, 2011.

[335] D. Sivia and J. Skilling. *Data analysis: a Bayesian tutorial*. Oxford science publications. Oxford University Press, 2006.

[336] D. S. Sivia, W. I. F. David, K. S. Knight, and S. F. Gull. An introduction to Bayesian model selection. *Physica D Nonlinear Phenomena*, 66:234–242, June 1993.

[337] J. Skilling. Nested sampling. *AIP Conference Proceedings*, 735(1):395–405, 2004.

[338] J. Slutsky, L. Blackburn, D. Brown, L. Cadonati, J. Cain, et al. Methods for Reducing False Alarms in Searches for Compact Binary Coalescences in LIGO Data. *Class.Quant.Grav.*, 27:165023, 2010.

[339] N. Smirnov. Table for estimating the goodness of fit of empirical distributions. *Ann. Math. Statist.*, 19(2):279–281, 06 1948.

[340] T. P. Sotiriou. 6+1 lessons from f(R) gravity. *Journal of Physics Conference Series*, 189(1):012039, Oct. 2009.

[341] R. Sturani, S. Fischetti, L. Cadonati, G. Guidi, J. Healy, et al. Complete phenomenological gravitational waveforms from spinning coalescing binaries. *J.Phys.Conf.Ser.*, 243:012007, 2010.

[342] R. Sturani, S. Fischetti, L. Cadonati, G. Guidi, J. Healy, et al. Phenomenological gravitational waveforms from spinning coalescing binaries. 2010.

[343] Y. Su, B. R. Heckel, E. Adelberger, J. Gundlach, M. Harris, et al. New tests of the universality of free fall. *Phys.Rev.*, D50:3614–3636, 1994.

[344] H. Tagoshi, A. Ohashi, and B. J. Owen. Gravitational field and equations of motion of spinning compact binaries to 2.5 postNewtonian order. *Phys.Rev.*, D63:044006, 2001.

[345] K. Takami, L. Rezzolla, and L. Baiotti. Spectral properties of the post-merger gravitational-wave signal from binary neutron stars. *Phys. Rev.*, D91(6):064001, 2015.

[346] C. Talmadge, J. P. Berthias, R. W. Hellings, and E. M. Standish. Model Independent Constraints on Possible Modifications of Newtonian Gravity. *Phys. Rev. Lett.*, 61:1159–1162, 1988.

[347] M. Tanaka and K. Hotokezaka. Radiative Transfer Simulations of Neutron Star Merger Ejecta. *Astrophys. J.*, 775:113, 2013.

[348] M. Tanaka, K. Hotokezaka, K. Kyutoku, S. Wanajo, K. Kiuchi, et al. Radioactively Powered Emission from Black Hole-Neutron Star Mergers. *Astrophys.J.*, 780:31, 2014.

[349] A. Taracchini, A. Buonanno, Y. Pan, T. Hinderer, M. Boyle, et al. Effective-one-body model for black-hole binaries with generic mass ratios and spins. *Phys.Rev.*, D89(6):061502, 2014.

[350] A. Taracchini, Y. Pan, A. Buonanno, E. Barausse, M. Boyle, et al. Prototype effective-one-body model for nonprecessing spinning inspiral-merger-ringdown waveforms. *Phys.Rev.*, D86:024011, 2012.

[351] J.-L. Tassoul. *Theory of rotating stars.* 1978.

[352] S. A. Teukolsky. Perturbations of a rotating black hole. 1. Fundamental equations for gravitational electromagnetic and neutrino field perturbations. *Astrophys.J.*, 185:635–647, 1973.

[353] K. S. Thorne. Multipole expansions of gravitational radiation. *Reviews of Modern Physics*, 52:299–340, Apr. 1980.

[354] R. C. Tolman. *Relativity, Thermodynamics, and Cosmology.* 1934.

[355] R. C. Tolman. Static solutions of einstein's field equations for spheres of fluid. *Phys. Rev.*, 55:364–373, Feb 1939.

[356] R. Valentim, E. Rangel, and J. Horvath. On the mass distribution of neutron stars. 2011.

[357] M. Vallisneri. Prospects for gravitational wave observations of neutron star tidal disruption in neutron star / black hole binaries. *Phys.Rev.Lett.*, 84:3519, 2000.

[358] M. Vallisneri. Use and abuse of the Fisher information matrix in the assessment of gravitational-wave parameter-estimation prospects. *Phys.Rev.*, D77:042001, 2008.

[359] H. van Dam and M. Veltman. Massive and mass-less yang-mills and gravitational fields. *Nuclear Physics B*, 22(2):397 – 411, 1970.

[360] C. Van Den Broeck and A. S. Sengupta. Binary black hole spectroscopy. *Class.Quant.Grav.*, 24:1089–1114, 2007.

[361] C. Van Den Broeck and A. S. Sengupta. Phenomenology of amplitude-corrected post-Newtonian gravitational waveforms for compact binary inspiral. I. Signal-to-noise ratios. *Class.Quant.Grav.*, 24:155–176, 2007.

[362] M. Vasuth, Z. Keresztes, A. Mihaly, and L. A. Gergely. Gravitational radiation reaction in compact binary systems: Contribution of the magnetic dipole - magnetic dipole interaction. *Phys.Rev.*, D68:124006, 2003.

[363] A. Vecchiato, M. G. Lattanzi, B. Bucciarelli, M. T. Crosta, F. de Felice, et al. Testing general relativity by micro-arcsecond global astrometry. *Astron.Astrophys.*, 399:337–342, 2003.

[364] J. Veitch, V. Raymond, B. Farr, W. Farr, P. Graff, et al. Parameter estimation for compact binaries with ground-based gravitational-wave observations using the LALInference software library. *Phys.Rev.*, D91(4):042003, 2015.

[365] J. Veitch and A. Vecchio. Assigning confidence to inspiral gravitational wave candidates with Bayesian model selection. *Class.Quant.Grav.*, 25:184010, 2008.

[366] J. Veitch and A. Vecchio. Bayesian coherent analysis of in-spiral gravitational wave signals with a detector network. *Phys.Rev.*, D81:062003, 2010.

[367] R. F. C. Vessot, M. W. Levine, E. M. Mattison, E. L. Blomberg, T. E. Hoffman, G. U. Nystrom, B. F. Farrel, R. Decher, P. B. Eby, C. R. Baugher, J. W. Watts, D. L. Teuber, and F. D. Wills. Test of relativistic gravitation with a space-borne hydrogen maser. *Phys. Rev. Lett.*, 45:2081–2084, Dec 1980.

[368] J. Vines, E. E. Flanagan, and T. Hinderer. Post-1-Newtonian tidal effects in the gravitational waveform from binary inspirals. *Phys.Rev.*, D83:084051, 2011.

[369] J. E. Vines and E. E. Flanagan. Post-1-Newtonian quadrupole tidal interactions in binary systems. *Phys.Rev.*, D88:024046, 2013.

[370] S. Vitale, W. Del Pozzo, T. G. Li, C. Van Den Broeck, I. Mandel, et al. Effect of calibration errors on Bayesian parameter estimation for gravitational wave signals from inspiral binary systems in the Advanced Detectors era. *Phys.Rev.*, D85:064034, 2012.

[371] S. Vitale, R. Lynch, P. Graff, and R. Sturani. Use of gravitational waves to measure alignment of spins in compact binaries. 2015.

[372] L. Wade, J. D. E. Creighton, E. Ochsner, B. D. Lackey, B. F. Farr, et al. Systematic and statistical errors in a bayesian approach to the estimation of the neutron-star equation of state using advanced gravitational wave detectors. 2014.

[373] R. V. Wagoner. Scalar tensor theory and gravitational waves. *Phys.Rev.*, D1:3209–3216, 1970.

[374] R. M. Wald. *General relativity*. 1984.

[375] A. G. Walker. On milne's theory of world-structure. *Proceedings of the London Mathematical Society*, s2-42(1):90–127, 1937.

[376] F. Weber. Strange quark matter and compact stars. *Prog.Part.Nucl.Phys.*, 54:193–288, 2005.

[377] S. Weinberg. *Gravitation and Cosmology: Principles and Applications of the General Theory of Relativity*. July 1972.

[378] S. Weinberg. Ultraviolet divergences in quantum theories of gravitation. In S. W. Hawking and W. Israel, editors, *General Relativity: An Einstein centenary survey*, pages 790–831, 1979.

[379] J. M. Weisberg and J. H. Taylor. Relativistic binary pulsar B1913+16: Thirty years of observations and analysis. *ASP Conf.Ser.*, 328:25, 2005.

[380] J. Wess and J. Bagger. *Supersymmetry and Supergravity*. 1992.

[381] C. Will. *Theory and Experiment in Gravitational Physics*. Cambridge University Press, 1993.

[382] C. M. Will. Bounding the mass of the graviton using gravitational wave observations of inspiralling compact binaries. *Phys. Rev.*, D57:2061–2068, 1998.

[383] C. M. Will. Generation of postNewtonian gravitational radiation via direct integration of the relaxed Einstein equations. *Prog.Theor.Phys.Suppl.*, 136:158–167, 1999.

[384] C. M. Will. Post-Newtonian gravitational radiation and equations of motion via direct integration of the relaxed Einstein equations. III. Radiation reaction for binary systems with spinning bodies. *Phys.Rev.*, D71:084027, 2005.

Bibliography

[385] C. M. Will. The Confrontation between General Relativity and Experiment. *Living Rev.Rel.*, 17:4, 2014.

[386] C. M. Will and J. Nordtvedt, Kenneth. Conservation Laws and Preferred Frames in Relativistic Gravity. I. Preferred-Frame Theories and an Extended PPN Formalism. *Astrophys.J.*, 177:757, 1972.

[387] C. M. Will and A. G. Wiseman. Gravitational radiation from compact binary systems: Gravitational wave forms and energy loss to second postNewtonian order. *Phys.Rev.*, D54:4813–4848, 1996.

[388] J. Williams, X. Newhall, and J. Dickey. Relativity parameters determined from lunar laser ranging. *Phys.Rev.*, D53:6730–6739, 1996.

[389] A. Wiseman. Coalescing binary systems of compact objects to (post)Newtonian**5/2 order. 4V: The Gravitational wave tail. *Phys.Rev.*, D48:4757–4770, 1993.

[390] K. Yagi and N. Yunes. I-Love-Q. *Science*, 341:365–368, 2013.

[391] K. Yagi and N. Yunes. I-Love-Q Relations in Neutron Stars and their Applications to Astrophysics, Gravitational Waves and Fundamental Physics. *Phys.Rev.*, D88(2):023009, 2013.

[392] N. Yunes, A. Buonanno, S. A. Hughes, M. Coleman Miller, and Y. Pan. Modeling Extreme Mass Ratio Inspirals within the Effective-One-Body Approach. *Phys.Rev.Lett.*, 104:091102, 2010.

[393] N. Yunes and S. A. Hughes. Binary Pulsar Constraints on the Parameterized post-Einsteinian Framework. *Phys.Rev.*, D82:082002, 2010.

[394] N. Yunes and L. C. Stein. Non-Spinning Black Holes in Alternative Theories of Gravity. *Phys.Rev.*, D83:104002, 2011.

[395] V. Zakharov. Linearized gravitation theory and the graviton mass. *JETP Lett.*, 12:312, 1970.

[396] M. Zanolin, S. Vitale, and N. Makris. Application of asymptotic expansions of maximum likelihood estimators errors to gravitational waves from binary mergers: the single interferometer case. *Phys.Rev.*, D81:124048, 2010.

[397] J. Zinn-Justin. Quantum field theory and critical phenomena. *Int.Ser.Monogr.Phys.*, 113:1–1054, 2002.

ACRONYMS

EOB Effective One-Body.

EoS Equation of State.

ET Einstein Telescope.

FAP False Alarm Probability.

FD Frequency Domain.

FI Functional Inference.

FLRW Friedman-Lemaitre-Robertson-Walker.

FT Fourier Transform.

GR General Relativity.

GW Gravitational Wave.

HR Hypothesis Ranking.

IID Independent Identically Distributed.

IMBH Intermediate-Mass Black Hole.

IMC Input Mode Cleaner.

ISCO Innermost Stable Circular Orbit.

K-S Kolmogorov-Smirnov.

KDE Kernel Density Estimator.

LAL LIGO Algorithm Library.

LCLF Local Comoving Lorentz Frame.

LIGO Laser Interferometric Space Antenna.

LLR Lunar Laser Ranging.

LQG Loop Quantum Gravity.

LSO Last Stable Orbit.

MCMC Markov Chain Monte Carlo.

ADM Arnowit-Deser-Misner.

BBH Binary Black Hole.

BH Black Hole.

BHNS Black Hole Neutron Star.

BNS Binary Neutron Star.

CBC Compact Binary Coalescence.

CDT Causal Dynamical Triangulations.

CE Calibration Errors.

CI Confidence Interval.

d.o.f. degrees of freedom.

DIRE Direct Integration of Relaxed Einstein equations.

E-H Einstein-Hilbert.

EEP Einstein's Equivalence Principle.

EFE Einstein Field Equations.

EM Electromagnetic.

MS Model Selection.

MWEG Milky Way Equivalent Galaxy.

NCG Noncommutative Geometry.

NP Non-parametrics.

NR Numerical Relativity.

NS Neutron Star.

ODE Ordinary Differential Equation.

PDE Partial Differential Equation.

PDF Probability Density Function.

PE Parameter Estimation.

PK Post-Keplerian.

PM Post-Minkowskian.

PN Post-Newtonian.

PP Point Particle.

pPE parametrized Post-Einsteinian.

pPN parametrized Post-Newtonian.

PSD Power Spectral Density.

QCD Quantum Chromodynamics.

QM Quadrupole-Monopole.

QNM Quasi-Normal Mode.

ROM Reduced-Order Modeling.

SEP Strong Equivalence Principle.

SMBH Super-Massive Black Hole.

SNR Signal-To-Noise Ratio.

SPA Stationary Phase Approximation.

SQM Strange Quark Matter.

SR Science Run.

ST Scalar-Tensor.

SVT Scalar-Vector-Tensor.

TD Time Domain.

TIGER Test Infrastructure for GEneral Relativity.

TOA Time Of Arrival.

TOV Tolman-Oppenheimer-Volkoff.

TT Transverse Traceless.

UTC Coordinated Universal Time.

UV Ultraviolet.

v.f. vector field.

VSR Virgo Science Run.

VT Vector-Tensor.

WD White Dwarf.

WEP Weak Equivalence Principle.

ZDHP Zero-Detuned High-Power.

SUMMARY

So much universe, and so little time.

Sir Terry Pratchett

In 2015 the world of science celebrated the 100-year "birthday" of the General Theory of Relativity, a theory of gravity put forward by Albert Einstein in a trilogy of historical papers published in 1915. His effort to reconcile gravity with Special Relativity, leading to a geometric theory of gravity, culminated into the formulation of the theory's fundamental equations in November 1915, now commonly known as the *Einstein equations*. In an unexpected twist of fate it was around that time in fall of 2015 when we verified (within the utmost secrecy of the LIGO-Virgo Collaboration) the *first direct detection of gravitational waves*, one of the fundamental (and notoriously elusive) features of Einstein's theory. The news broke in early 2016, 100 years after Einstein first predicted the *existence* of gravitational waves. The world was more or less agog, and whether people grasped the actual importance of this discovery or not, it was celebrated by all as yet another scientific breakthrough of mankind. But why does this long-anticipated discovery qualify as such an important milestone in modern physics and what are its actual implications to our understanding of the Universe and the laws of nature? In an attempt to answer this question without resorting to equations or plots, so as to keep the next few pages as non-technical as a summary deserves to be, I find that a philosophical detour may be efficient in giving the necessary perspective.

The Cave

In Plato's allegory of *The Cave*, one finds a group of people chained down from birth, forced to face towards the inside of a dark cave, not being able to directly

see what happens around them or outside the cave walls. They can only observe shadows, created by a fire that burns somewhere in the cave, and projected upon the wall in front of them. And through these shadows they try to infer what reality is like; what living things look like, how they behave, etc. However, like any projection, shadows do not reveal the complete picture: *e.g.* given a shadow's size, the chained cannot calculate the true object's size without knowing the distances between the fire, the object and the wall; in fact they most likely cannot even conceive the sheer notion of fire or shadow.

This allegory not only reveals Plato's acknowledgement of the restricted emperical means of his time, but most importantly it sets the grounds for a very profound, epistemological view of reality, by stressing the essential connection between the real world and what is accessible to us through observation. And indeed, our limited means of observation may withhold crucial information from us, without which our understanding of the world around us is incomplete. Whether mankind will ever be able to access all channels of information that the physical world is endowed with or whether it is doomed to be forever blind to some of them, is a deep philosophical question, but whatever the answer, the best we can do is to keep on exploring.

And we have done so for thousands of years, gazing at the night sky, studying the motions of celestial bodies, performing experiments and building equipment with which we can measure physical quantities to ever-increasing precision. Within the last four centuries, using telescopes and light as our main observational channel to the Universe, we have familiarized ourselves with our solar system, our stellar neighbourhood, our host galaxy and the ones beyond it, all the way out to the deep space, billions of light years away. But even though light may dominate our senses as human beings, it is merely the fire in our cosmic Cave, casting "shadows" upon our hi-tech telescopes. After decades of efforts, we now have the tools to explore what lies beyond the walls of our Cave.

General Relativity and Gravitational Waves

Gravitational waves are cosmic messengers, carriers of information on the *geometry of spacetime* around the source that emitted them. Their existence is a direct consequence of Einstein's General Relativity (GR), a theory that interprets gravitation as nothing else but a manifestation of the *curvature of spacetime*, the stage upon which all events that we witness around us take place. For instance, free-body trajectories in the vicinity of a massive gravitating body (*e.g.* the planetary orbits around the Sun, or the trajectory of a stone thrown upwards from the surface of the Earth) appear to be curved not because of a gravitational *force* acting on them as in Newton's theory of gravity, but only because spacetime itself becomes curved in the presence of mass. One may picture it as an elastic sheet that gets deformed when a heavy object is placed on top of it.

The generalization of a straight line in a curved space setting, where straight lines do not always exist, is called a *geodesic*. These are exactly the curves followed by objects that perform free motion.

Space is not anymore a static entity, but rather a dynamical one; it curves and twists and evolves dynamically as stuff move around in it, and this evolution is determined by the Einstein equations. The same equations tell us that when that same mass that curves spacetime performs accelerated motion (*e.g.* while orbit-

Orbit of a planet around its star in Newtonian gravity (top) and General Relativity (bottom). Notice how the curvature of space causes a small but characteristic modification in the orbit.

ing around another massive object), the changes in curvature induced by that motion can generate ripples in the geometry of space which propagate outwards with the speed of light; these ripples are what we call gravitational waves (GWs). What GWs do is stretch and squeeze the dimensions of spacetime itself and this effect is what physicists have been trying to measure for 100 years. So now that we have done it, we have essentially "unlocked" a whole new sense to the Universe, we can *feel the vibes* in the fabric of spacetime itself.

The biggest challenge when trying to detect gravitational waves is the weakness of the signals we are looking for. On the right hand side of Einstein's equations, which describes the matter content that causes spacetime to curve, one finds an overall prefactor $\frac{8\pi G}{c^4} \simeq 2 \times 10^{-43} \, \mathrm{m\,kg^{-1}\,s^{-2}}$. This means that every kilogram of mass will curve spacetime by a similarly tiny amount; in other words, spacetime is an extremely hard thing to bend! In terms of GW production, a back-of-the-envelope calculation shows that no conceivable man-made experimental setup can generate a GW signal that is sufficiently strong to be detected. But then, the only alternative is to resort to GW sources provided by nature itself (and she is indeed rather generous in that respect). Once again, we need to turn our eyes (or "ears") towards the depths of outer space, and try to eavesdrop on some of the most violent, cataclysmic events in the history of the Universe.

Sources of Science

Amongst the most promising candidate sources of GWs, one finds the family of coalescing compact binaries. These are binary systems consisting of Black Holes or Neutron Stars in tight orbits around their common center of mass. For millions of years these systems kept emitting GWs in a very quiet but steadily
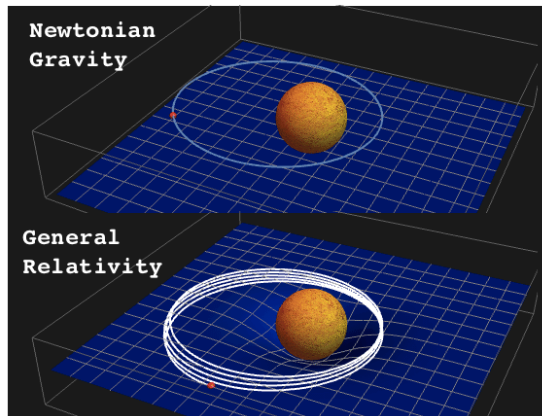
increasing rate. The energy drained in this way slowly pulled the system closer and closer together in an accelerating rate, until the two companions eventually merged together in a crescendo of GW emission, forming a black hole as final product. Black holes are the most compact objects that can possibly exist in the Universe, with neutron stars coming second best. Black holes can be formed as the end result of total gravitational collapse, when a star cannot support its self-gravitating mass by means of controlled, "conventional" processes of nuclear fusion. If the star is sufficiently massive, it eventually ends its life in a supernova explosion, leaving behind a compact remenant as the product of its collapse. That remenant can be a black hole or a neutron star.

Although they are not made of matter but should rather be conceived as pure curved spacetime, black holes have mass, usually thought of as concentrated in their (geometric) center, a point known to host a so called "singularity", where quantities like curvature become infinite. Gravity around such a singularity, and out to a surface known as the *horizon*, is so strong that not even light can escape it. What exactly takes place at or just next to the singularity remains a fundamental open question in physics. What makes black holes even more fascinating from the observational point of view is that the vicinity of a black hole horizon is a place where physical phenomena can be strongly affected by both gravity and quantum mechanics. Now at a fundamental level, GR and quantum mechanics are notoriously incompatible with each other, and if one wishes to reconcile the two theories or perhaps abandon features of one in favour of the other, then the observation of phenomena around a black hole would provide key information that may eventually lead to a unified theroy of Quantum Gravity.

Neutron stars on the other hand are made of matter in its most highly compressed state, at the final stage before total gravitational collapse. In the interior of a neutron star, matter can reach densities that are a few times higher than the denisties found in an atomic nucleus. If the Earth was as dense as a neutron star, it would have had the size of a golf ball! Neutron stars are typically slightly more massive than the Sun, and in a neutron star binary one finds two such objects orbiting each other hundreds of times per second, at a distance of a few tens of kilometers, before they finally merge into a single black hole. And of course, by observing astrophysical phenomena at such extreme conditions, we can infer the properties of matter at regimes that were so far inaccessible to us. This is the subject of Part III of the current dissertation.

A prelude to the future

About 1.3 billion years ago, in a galaxy far far away, two massive black holes were engaged in a tight orbit around their common center of mass. This close encounter was destined to come to a climax whereby these Netherlands-sized objects, each weighing at around 30 Suns, would collide with inconceivable violence at a speed close to the speed of light and merge into a single black hole. Within the last 0.2 seconds of this death-spiral a mass equal to 3 Suns was radiated away as *pure*

energy in the form of gravitational waves. For comparison with human scales, note that just 1 kilogram of pure energy would be enough to cover the demands of a city like Amsterdam for months. About 1.3 billion years later, life on Earth had just started to operate a network of two GW detectors that were finally sensitive enough to detect a gravitational wave that was just passing through. And so they did. Mankind listened to the first audible note in the eternal cosmic symphony of gravitational waves.

It soon became clear that this was a signal from the merger of two black holes. As discussed above, it can be argued that GR is not the ultimate theory of gravity and that at extreme regimes, such as one where two black holes or neutron stars collide, we may be able to witness its breaking point. Now in the context of GR, we have accurate models that describe what a GW signal emitted by a coalescing binary should look like. So if GR is in fact violated, then the detected GW signal will differ from the one that our model predicts and, if that difference is large enough, our analysis will identify the violation of GR. This sort of investigation was the subject of Part II of this dissertation, where a complete analysis pipeline was developed and tested for this purpose. After analyzing the first GW detection, we found no inconsistency with general relativity, and we thus placed upper bounds on possible violations thereof. We now know that so far GR passes the test in a regime that was never probed before.

Similar detections in the future will reveal a wealth of information on the nature of gravity, on the properties, the formation, and the population of black holes and neutron stars throughout the Universe, and much more. Soon we may be able to sense the bursts of GW radiation coming from the deep interior of supernova explosions, or even the GW "echo" from the Big Bang itself.

My first draft of this summary ended with the statement that the *"first detection of gravitational waves will be a triumph for science and mankind"*. One year and one triumph later, I do not dare make firm predictions on what nature may have in store for us in the near or distant future. And this is in fact the most exciting thing about living the dawn of gravitational wave physics.
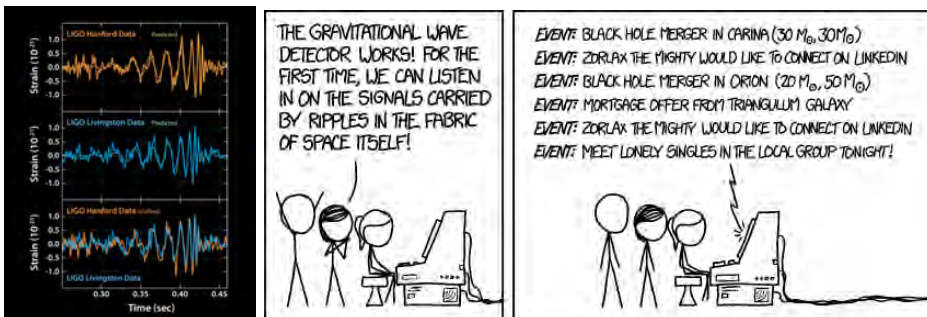
Credits: LIGO, xkcd comics [www.xkcd.com]

ACKNOWLEDGEMENTS

These last few years have been an incredible journey through life for me, at both a personal and a professional level. Through the sad and joyful times, the stressful and the exhilarating moments, the desperate failures and the little victories, the integral of feelings leaves me with the impression that I have grown and matured in so many different ways that it becomes impossible to see myself as the same guy who embarked on this journey more than four years ago. But there are a few individuals who not only stood by my side like invariable frames of reference, but indeed contributed so strongly to this transformation, that are effectively part of it. And these individuals I would like to thank seperately and collectively in the disproportionately few lines that follow.

First and foremost I want to thank my supervisor Chris Van Den Broeck, who showed me the difference between being a physicist and being a Scientist. Chris, I owe you every single experience point that I've gained throughout these years; and a crate of tobacco. I am sure we will keep working together for years to come and I'm already looking forward to whatever comes next. A big thank you to my promotor and group leader, Jo van den Brand, you are indeed a true leader and a source of energy for the entire group, I don't know how you do it but it works. Thanks for having me on board!

During my stay at Nikhef I was fortunate enough to collaborate and interact with a wonderful group of individuals in the Gravity group, I owe a big thankyou to each and every one of you. Tjonnie, you were the best office-mate I could've asked for and a truly brilliant scholar, hope Hong Kong will not be as distant as it sounds. In the meantime let's work on that high tone shall we? Walter, John, Salvo, Jeroen, it was a great pleasure and honor working with you and of course hanging out any chance we got, let's keep doing both of that! To my colleagues at the Nikhef Gravity group Joris, Laura, Mark, Matthieu, Reinier, Kazuhiro, David, Gideon, you've been such a great gang, I'll really miss the physics discussions, the companionship, the coffee chats and all the fun stuff! Many thanks also go to the less junior colleagues, Alessandro, Henk Jan, Eric, Jan-Willem, you were a constant source of knowledge and wisdom, and always available for the most insightful discussions. Rob, thanks for all the discussions and all the good times we've had over the years. Manouk, your dudeness, thanks for showing me the way once again! Alis, it's been great having you in *our* floor, I was very happy to waste your time when you "had to work". You're

good sailor. Not as good as Luca though. The Nikhef people, Pantso, Stergios, Giuseppe, Nagme, Nika, Antonio, Serena, Enrico, Priscilla, Vassili, Rolf and everyone else, thanks for making Nikhef such a great, vibrant, interesting place!

I feel blessed to have been surrounded by such an incredible group of friends with whom I shared so much throughout the years. Wilco my man, Christina, what can I say, it's been so awesome, let's build a bigger drone or just go to Corfu and settle down for good. Willem my favorite guy and now Nikolas, it keeps adding up, doesn't it? To the Utrecht gang, Alekos, Iris, Yannis, Vass, apart from being amazing friends, you've also been the best hosts ever, can't wait to return the hostpitality! Yannis, Stavros, Kostas, Theo, Bessy, Suzette, Nikos, Katerina, Elena, Andrei, Anna, Sergiu, Suus, Thomas, Louisa, Anna, Ruben, Ori, we had so much fun together, I almost wish I didn't have this stupid PhD to finish and just spend more time with you guys! To Lukie, my faithful canine companion, you're a true bastard, but still by far the smartest dog I know! Thank you for turning those hours of my life into a purposeless playtime! Many thanks also to Leo and Alessandra and Daan for all the interesting and relaxing discussions during our long walks, thanks Fiocci for keeping Lukie busy in the meantime. Special thanks to Artemis, Panagiotis and all the other homies too.

To my friends and relatives in Greece who still make my life wonderful and give me things to look forward to, Jonny, Sophia, Lia, Danai, Maria, Nouna, Constantinos, Kots, Michalis, Michalis, Eleni, Louis, Stella, Sophia, Pantelis, Maria and Chris, Kleanthi and Odysseas. Antonis and Kostas, the world may crumble to pieces (already happening) but we'll still be here joking about it like there's no tomorrow. Stavros, Arapis and the Athens gang, there's nothing more refreshing than just hanging out together, axolotl style. To my new bball buddies, Vassilis, Aristos, Konstantinos, and everyone else, thanks for keeping me sane during the most hectic few months of my life. Special thanks to Elena and all the fun and hard-working people at TEDxThessaloniki for the uber-awesome experience, I will never forget! And to my former professors and mentors, Metallinos, Thymis, Zoupanos, Anagnostopoulos and more, whatever I have achieved so far, I owe it to you.

To my family, for your support, for everything you've done for me, for your love and encouragement and trust in me, for making me who I am, I will be forever grateful. I hope I'm making you proud and happy, and I wish we could all grow as old as (grandpa) pappous Michalis and exaggerate about all this to our great grandchildren.

Last but not least... Stella, the brightest star in my Universe, my binary companion in life, partner, accomplice, my other half. You were always there for me, you were always caring, patient, forgiving, supportive, an endless source of energy and inspiration. You are my muse and the love of my life.

A lot of things happened since 2011 on several fronts, and my journey, as well as everyone else's that I know, did not lack its ups and downs. But I know for sure that at least I will remember it as a journey that ended with a ton of fireworks.

Thanks to everybody.